Micronozzle Performance

A Numerical and Experimental Study

Chaggai S. Ganani

Delft University of Technology

TU Delft

Micronozzle Performance

A Numerical and Experimental Study

by

Chaggai S. Ganani

In partial fulfillment of the requirements for the degree of
Master of Science in Aerospace Engineering

at Delft University of Technology

To be defended on Thursday May 9, 2019 at 2:00 PM.

Student number: 4293126

Thesis committee:

Ir. B. T. C. Zandbergen,	Delft University of Technology, Committee Chair
Dr. A. Cervone,	Delft University of Technology, Daily Supervisor
Ir. K. J. Cowan MBA,	Delft University of Technology

TU Delft Delft University of Technology

Acknowledgements

Although the Master thesis is an individual assignment a lot of people have contributed in some form or another for which I would like to thank everyone. Nonetheless I would like to extend my special thanks to the following people: Firstly, I would like to thank my supervisor Dr. A. Cervone for all the help he provided during this thesis. He provided me with valuable feedback and was always available to brainstorm solutions.
Secondly, I would like to thank all the people from micropropulsion research group for providing welcome insights and support.
Furthermore, Dr H.W. van Zeijl, who provided invaluable support and knowledge during the fabrication of the micronozzles.
I would like to thank J. Pearl and E. Vesper for providing support with the various OpenFOAM issues.
Additionally, I would also like to voice my appreciation to all the students in the master room of the space engineering department for providing a very pleasant working environment. And lastly, I want to thank my family who supported me all the way through in too many ways to describe.

Abstract

Micropropulsion is universally considered to be a key technology enabling nano- and pico- satellites to perform more complex missions. However, past research has shown that nozzle efficiencies at the microscale are far inferior to their macro scale counterparts.

These low nozzle efficiencies can be attributed to the relative high viscous losses caused by the low throat Reynolds numbers ($Re_t < 1000$) associated with this microscale. Micronozzles at this scale will generally require throat widths smaller than 300 µm and because of it cannot be manufactured with an axi-symmetric geometry. As a result most micronozzles at this scale are so called planar nozzles where the nozzle profile is extruded normal to the nozzle profile plane and need to be manufactured using MEMS techniques.

Various research efforts have been performed trying to identify methods to mitigate these viscous losses. This thesis study investigates the impact of various alternative nozzle geometries on the nozzle performance through numerical simulations. The numerical simulations evaluate the steady state micronozzle performance, through the use of an open-source (OpenFOAM), 3D Navier-Stokes based solver, with nitrogen gas as the working fluid. The investigated nozzle geometries are linear nozzles with various divergence angles (θ_{out} = 15°, 30°, 45°) and aerospike nozzles truncated at various lengths ($\%_{trunc}$ = 20%, 40%, 60%).

The results of these simulations found that the linear nozzle with θ_{out} = 30° outperformed all the other nozzles for $Re_t > 1200$. Below this Reynolds number the θ_{out} = 45° nozzle outperforms all other nozzles. In contrast to past research it was found that the best aerospike nozzle performed on average 24.7% worse for the thrust efficiency, 15.5% worse for the discharge coefficient, and 14.4% worse for the specific impulse efficiency compared to the best linear nozzle.

This lower performance of the aerospike nozzles was attributed to excessive losses caused by flow expansion in the etch direction, past and over the edge of the spike center body. Based on these results a novel nozzle geometry was designed where the depth of the spike body was increased while the nozzle convergent was kept the same depth. This double depth aerospike geometry was investigated for h_{spike} = 200 − 1000 µm and, averaged over the entire range of investigated Reynolds numbers resulted in 25.9% higher thrust efficiency, 2.0% lower discharge coefficient, and 39.2% higher specific impulse efficiency with respect to the single depth aerospike nozzles. Therefore, these double depth aerospike nozzles outperform even the best linear nozzles considered in this study.

In addition to the numerical study on the various nozzle geometries, select geometries were manufactured. Furthermore, an experimental setup was prepared for experimental testing of said nozzles to validate the numerical results. This nozzle fabrication encountered various complications which resulted in the inability to complete experimental testing in this thesis project. However, a new production flow was designed, using photo-resist instead of a silicon dioxide hardmask for the DRIE etching. This resulted in a more reliable, accurate, quicker, and cheaper production flow that can be used for the future.

Contents

List of Figures

List of Tables

Nomenclature

CFD	Computational Fluid Dynamics
CFL	Courant Friedrichs Lewy
CR100	Class 100 cleanroom
DAQ	Data Acquisiton
DRIE	Deep Reactive Ion Etching
DSMC	Direct Simulation Monte Carlo
DSP	Double Side Polished
EKL	Else Kooi Laboratory
IC	Integrated Circuit
IPA	IsoPropyl Alcohol
JANAF	Joint Army Navy NASA Air Force
LPM	Low Pressure Microthruster
LTS	Local Time Stepping
NASA	National Aeronautics and Space Administration
NI	National Instruments
OpenFOAM	Open source Field Operation And Manipulation
PCB	Printed Circuit Board
PCG	Preconditioned Conjugate Gradient
PECVD	Plasma Enhanced Chemical Vapor Deposition
PIV	Particle Image Velocimetry
PTFE	PolyTetraFluorEthylene
RIE	Reactive Ion Etching
TMAC	Tangential Momentum Accommodation Coefficient
TU Delft	Delft University of Technology
TVD	Total Variation Diminishing
VLM	Vaporizing Liquid Microthruster

List of Symbols

Symbol	Physical parameter	Unit
$\%_{trunc}$	Truncation percentage	–
A_s	Sutherland constant	Pas/K
A_t	Throat area	m^2
A_e	Exit area	m^2
C_D	Discharge coefficient	–
C_F	Thrust coefficient	–
c_p	Specific heat	$J/(molK)$
c^*	Characteristic velocity	m/s
D	Diameter	m
D_h	Hydraulic diameter	m
E	Internal energy	J
F_{meas}	Simulated/measured thrust	N
F_{1D}	Ideal rocket theory thrust	N
g_0	Gravitional acceleration at sea level	m/s^2
e	Specific internal energy	J/kg
h	Specific enthalpy	$J/(molK)$
h_e	Exit depth	m
h_{spike}	Aerospike center body depth	m
h_t	Throat depth	m
$\mathbf{I}$	Identity Matrix	–
I	Turbulence intensity	–
I	Current	A
I_{sp}	Specific impulse	s
$I_{sp_{meas}}$	Simulated/measured specific impulse	s
$I_{sp_{1D}}$	Ideal rocket theory specific impulse	s
Kn	Knudsen number	–
Kn_{avg}	Average knudsen number	–
Kn_{local}	Local knudsen number	–
Kn_t	Throat knudsen number	–
k	Heat transfer coefficient	$W/(m^2K)$
k	Turbulence kinetic energy	m^2/s^2
k_B	Boltzmann constant	$m^2kg/(sK)$
L	Characteristic flow length	m
L_{align}	Of-axial thrust fraction	–
L_{nozzle}	Nozzle length	m
l	Aerospike characteristic length	m
l	Turbulence length scale	m
l_{mag}	Pivotpoint-magnetic coil length	m
l_{nozzle}	Pivotpoint-nozzle interface length	m
M	Mach number	–
Ma	Mach number	–

M_e	Exit Mach number	–
m	Molecular mass	kg
$\dot{m}$	Massflow	kg/s
$\dot{m}_{meas}$	Simulated/measured massflow	kg/s
$\dot{m}_{1D}$	Ideal rocket theory massflow	kg/s
$\boldsymbol{n}$	Normal vector	–
n_{thrust}	Thrust component of normal vector $\boldsymbol{n}$	–
Pr	Prandtl number	–
p	Perimeter	m
p	Pressure	Pa
p_c	Chamber pressure	Pa
p_e	Exit pressure	Pa
p_∞	Freestream pressure	Pa
p_{inlet}	Nozzle inlet pressure	Pa
Q	Volumetric flow rate	m^3/s
R	Specific gas constant	$J/(kgK)$
$\Re$	Universal gas constant	$J/(molK)$
R_a	Convergent curvature radius	m
R_t	Throat curvature radius	m
Re	Reynolds number	–
Re_t	Throat Reynolds number	–
s	Specific entropy	$J/(molK)$
T	Temperature	K
T_0	Sutherland reference temperature	K
T_g	Gas temperature	K
T_i	Incident flow temperature	K
T_r	Reflected flow temperature	K
T_w	Wall temperature	K
T_s	Sutherland temperature	K
t	Time	s
$\mathbf{U}$	Velocity vector	m/s
$\mathbf{U}_g$	Gas velocity vector	m/s
$\mathbf{U}_w$	Wall velocity vector	m/s
U	Velocity	m/s
V	Velocity	m/s
V_i	Incident flow velocity	m/s
V_r	Reflected flow velocity	m/s
V_w	Wall velocity	m/s
W_t	Throat width	m
W_{in}	Nozzle inlet width	m
W_e	Nozzle exit width	m
α	Angelino angle	deg
α	Thermal diffusivity	m^2/s
γ	Specific heat constant	–
ε	Expansion area ratio	–
ε_{div}	Nozzle divergence loss	–
ε_F	Force application fraction	–
η_F	Thrust efficiency	–

$\eta_{I_{sp}}$	Specific Impulse efficiency	–
θ_{in}	Convergence half angle	deg
θ_{out}	Divergence half angle	deg
κ	Thermal conductivity	$W/(mK)$
λ	Molecular mean free path	m
ρ	Density	kg/m^3
μ	Dynamic viscosity	Pas
μ	Mach angle	deg
μ_0	Sutherland reference dynamic viscosity	Pas
ν	Prandtl-Meyer angle	deg
ν_e	Prandtl-Meyer angle at exit plane	deg
σ_T	Thermal accommodation coefficient	–
σ_v	Tangential momentum accommodation coefficient	–
$\boldsymbol{\tau}$	Viscous stress tensor	Pa
Ψ	Compressibility	s^2/m^2
ω	Specific turbulence dissipation rate	$1/s$

1 Introduction

In modern spaceflight a trend has prevailed to make satellites smaller and smaller while still maintaining the capabilities of their larger counterparts. The capabilities are maintained by applying the concept of distributed space systems. This led to Cube and PocketQube satellites becoming more interesting for the general market, as a distributed space system made from these micro-satellites has the potential to significantly reduce the cost of accessing space.

However, one of the limiting factors in a widespread implementation of small format satellites is the lack of an efficient micro propulsion systems. The addition of a propulsion system increases the mission capabilities of these satellites by enabling orbit manoeuvres, orbit maintenance, and formation flying.

In the past Delft University of Technology (TU Delft) has successfully demonstrated two nano-satellites with the Delfi-C3 and the Delfi-n3Xt. The latter of the two demonstrated the T3μPS cold gas micro-propulsion system in orbit. Currently further miniaturization efforts are made to develop and launch Delfi-PQ, a pico-satellite, which plans to demonstrate two different micro-propulsion systems.

These two systems are the Vaporizing Liquid Microthruster (VLM) and the Low Pressure Micro-resistojet (LPM). As the names suggest the VLM vaporizes a liquid, often water, and expels the gaseous products through a nozzle to generate thrust. The LPM uses propellants at a pressure of 300 Pa or less, heats them up and expels them through slots. Propulsion systems miniaturized to the scale of Delfi-PQ have brought various challenges with them. One of these challenges are the micronozzles, used in the VLM, having considerably lower nozzle efficiencies compared to their macronozzle counterparts [1].

Across the globe there have been various research groups working on improving these micronozzle efficiencies. A great number of studies have been focused on altering the nozzle geometry, which aims to mitigate the viscous losses that have been identified as the main cause of the low efficiencies [2]. Furthermore, the majority of these studies have been performed through numerical means as obtaining accurate results from experimental tests is a difficult, time consuming, and costly endeavor [3, 4]. The lack of experimental data also leads to a lack of widespread validation of the obtained numerical results.

Therefore, this thesis project aims to investigate alternative nozzle geometries through numerical

and experimental means, focusing on evaluating nozzle performances and validating numerical results.

From the research aim as defined above the main research objective is formulated:

The research objective is to help improve the understanding of better performing micronozzle geometries and make recommendations for future improvements for the micronozzle performance, such that future microsatellites are enabled to perform more complicated missions, by identifying suitable ways to analyze the flowfield, analyzing the flowfield in alternative micronozzle geometries, and experimentally testing and validating the performance of said geometries.

The term micronozzle has been used for a very wide range of nozzles. For this thesis project a nozzle is considered to be a micronozzle if the design thrust is in the micro to milli newton range. Generally to fulfill this thrust level the nozzle throat diameter has to be below 300 µm and such this will also be taken as a requirement for the definition of a micronozzle. These small throat dimensions result in small Reynolds numbers in the throat. Reynolds numbers below 1000 are of particular interest as microthrusters will frequently have to operate in this regime and the nozzle efficiency losses are the most pronounced here [4]. The Reynolds number referred to in this thesis study is always the throat Reynolds number unless otherwise mentioned. The Reynolds number can be calculated using:

$$Re = \frac{\rho V D}{\mu} = \frac{\dot{m} D}{\mu A} \tag{1.1}$$

Where ρ is the density of the flow, V the flow velocity, μ is the dynamic viscosity of the flow, $\dot{m}$ is the massflow, A is the cross-sectional area of the flow channel, and D the diameter of the channel. Whenever the channel is not circular, D is the hydraulic diameter which is calculated using:

$$D_h = \frac{4A}{p} \tag{1.2}$$

Where D_h is the hydraulic diameter, and p is the perimeter of the cross-section.

Resulting from the definition of micronozzles, which dictates throat diameters of less than 300 µm, micronozzles cannot be manufactured through conventional means. Consequently all the nozzles in this research, and most other studies from literature on this topic, consider planar nozzles. Thus, a micronozzle is a 2D nozzle profile which is extruded normal to the nozzle profile plane to get a 3D planar nozzle. The majority of the micronozzles produced use silicon etching to generate the depth of the nozzle profile. As a result the direction normal to the nozzle profile plane is also called the etch direction.

Based on the background information the following research questions have been formulated that need to be answered to meet the research objective:

1. Are the computational results in the literature in line with the experimental results and with what accuracy?
    (a) What are the flowfield characteristics of the selected geometries?
    (b) What is the best way to analyze the flowfield, taking into account availability of resources such as time, cost and availability at the university?
    (c) What are the most valuable variables to look for in a flowfield to assess its performance?

2. Can alterations to the nozzle geometry improve the performance, and if yes what alterations are recommended?

    (a) Is there a relationship between the characteristics of the flowfield and the experimental performance of the micronozzles and how can this relation be used to improve future designs?

    (b) How do the performances of the different geometries relate to each other?

To answer these questions the various nozzle geometries that are selected for investigation are treated in Chapter 2. In this chapter the selection is justified and the design process is explained. Numerical simulations of these nozzle geometries follows the selection. The numerical setup and methodology that is used for these simulations are treated in Chapter 3. Next in Chapter 4 the results that were obtained through the numerical study will be presented and analyzed. As the aim is to use experimental testing to validate the numerical simulations the micronozzles need to be produced. The methodology used to fabricate the nozzles is treated in Chapter 5. Additionally, this chapter also treats various lessons learned and problems encountered during the production. Unfortunatelly the problems encountered during the fabrication of the micronozzles led to the inability to complete the experimental tests within the time and cost budget of the thesis. As a result no experimental tests could be performed and Chapter 6 covers the experimental setup and methodology as would have been used for the experimental tests. After the experimental setup Chapter 7 presents the conclusions and recommendations drawn from the research.

2

Nozzle Geometries

Before any numerical or experimental research can take place the nozzle geometries have to be selected. In this chapter the nozzle geometries are selected and the reasoning behind the design choices are elaborated.

2.1. Geometry types

In the literature regarding micronozzle efficiencies a great deal of research has been performed into micronozzle geometries and their influence on the nozzle performance. Throughout this literature the linear nozzle, a planar nozzle using the nozzle profile of a conical nozzle, has been a frequent topic of research. This is due to the fact that unlike conventional macro nozzles a bell nozzle does not significantly improve the performance yet does complicate the manufacturing [5, 6]. Therefore, the linear nozzle has become the most used and researched geometry for micronozzles. Consequently because of its easy manufacturability, reasonable performance, and the large library of research available the linear nozzle became the industries standard.

Recent studies have started to conduct research into linear aerospike nozzles and initial numerical results are encouraging [7–10]. By having an external flow which is not bound by an upper or lower wall in the etch direction, one can negate a significant portion of the viscous losses leading to improved performance.

Based on this information it was decided that for this study a variety of linear nozzles will be investigated to function as a baseline "conventional" micronozzle design. Next to the linear nozzles a variety of aerospike nozzles will be studied to further investigate the potential these nozzles showed in past research.

2.2. Design parameters

As one of the goals of this research is to compare the micro aerospike performance to that of the linear nozzle, it is of key importance that the design parameters for both nozzles are as similar as possible to single out the geometric factor in the performance. However, before one can assign values to the design parameters one has to identify these parameters. The parameters which are of interest for this study were identified and can be found in Table 2.1. Figs. 2.1 and 2.2 visually repre-

sent these parameters. In this table the truncation length is only applicable to the aerospike nozzles. Furthermore, note that while both nozzles have a throat radius of curvature R_t the radius is at a very different location. For the linear nozzle the radius of curvature is located at a critical location, the area of choked flow. However, for the aerospike nozzle this curvature is further upstream and together with R_a it forms the channel in the convergent of the aerospike nozzle. As the usecase for R_t in the two nozzles is so different it will not be kept constant between the two nozzle geometries.

Table 2.1: Nozzle design variables

variable	symbol
Convergence half angle	θ_{in}
Divergence half angle	θ_{out}
Throat width	W_t
Throat curvature Ratio	$\frac{2 \cdot R_t}{W_t}$
Convergence curvature Ratio	$\frac{R_a}{W_{in}}$
Inlet width	W_{in}
Nozzle length	L_{nozzle}
Area ratio	$\varepsilon = \frac{A_e}{A_t} = \frac{W_e}{W_t}$
Truncation percentage	$\%_{trunc}$

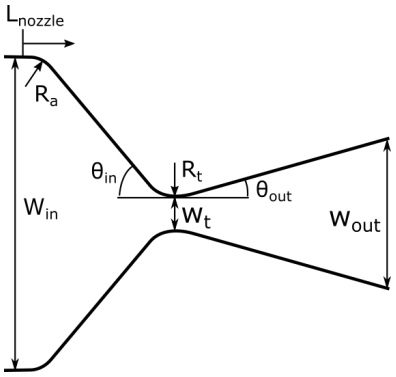

Figure 2.1: Parameter definition for the linear nozzle

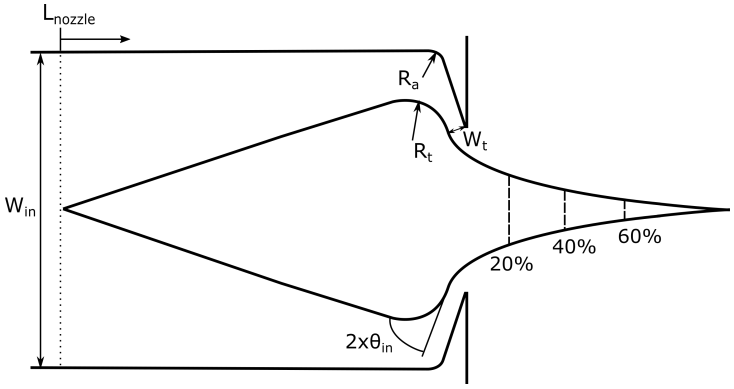

Figure 2.2: Parameter definition for the aerospike nozzle

This study is done to both further the field of micronozzles but also help the development of the Vaporizing Liquid Microthruster (VLM) of Delft University of Technology (TU Delft). From the TU Delft a few requirements were imposed on the design of the VLM and thus on the nozzles and their design parameters. These requirements are as followed:

VLM-NOZZLE-1 The design throat width shall be 45 µm wide.

VLM-NOZZLE-2 The inlet width W_{in} shall be 3000 µm to be compatible with previous work

VLM-NOZZLE-3 The nozzle depth shall be 100 µm to be compatible with previous work.

VLM-NOZZLE-4 The nozzle length (combined convergent and divergent length) of the linear nozzle shall not exceed 3245 µm

VLM-NOZZLE-5 The the chamber pressure shall not exceed 3 bar.

The first four requirements came forth from earlier designs of the VLM as presented in the study of Silva et al. [11]. The dimensions from this article were taken as requirements such that the new nozzles are comparable and compatible with the previous VLM nozzles. The fifth requirement was based on some upper level requirements from the Delfi-PQ project.

With these requirements in mind the nozzles were designed. The linear nozzles, as the baseline nozzle geometry, are designed first, followed by the design of the aerospike nozzles.
Keeping the design parameters equal between the nozzles, combined with the fact that an aerospike nozzle necessitates the use of two nozzle throats will lead to aerospike nozzles that are significantly larger than their linear nozzle counterparts. The aerospike will be so large that it will be larger than requirement Item **VLM-NOZZLE-3** states that the linear nozzle is allowed to be.

To make well-informed design decisions the literature regarding micronozzle research is consulted. Xiangming et al. [12] presented an orthonormal numerical study, which provided indications on the nozzle performance impact of the various design parameters:

- The half convergence angle θ_{in} has no influence on performance for angles higher than 40°
- The radius of curvature R_a does not have significant effect on performance as long as it is present (no data reported for $R_a = 0$).
- Throat curvature ratios ($\frac{2 \cdot R_t}{W_t}$) larger than 1 do not seem to give diminished performance. This is contrary to the reported behavior in macronozzles as reported by [13, 14]
- A larger inlet width of a nozzle leads to a higher thrust and specific impulse
- The parameters that have a large influence on performance are the expansion ratio and the divergence half angle.

With this reported behavior of micronozzles, and the imposed requirements, the design of the nozzle profiles can be made.

2.3. Linear nozzle geometries

From the information gathered in Section 2.2 it can be concluded that for linear nozzles the most influential factors are the inlet width W_{in}, the divergence half angle θ_{out}, and the expansion ratio ε. The inlet width for the nozzle design is fixed at 3000 µm as set by **VLM-NOZZLE-2** and can therefore not be used in the scope of this research as a variable for investigation. The remaining two parameters, the expansion ratio and the divergence half angle, can be varied. From these two variables the divergence half angle was selected to be varied for the linear nozzle designs. This was decided based on the fact that varying divergence half angles have been extensively investigated in the literature [4, 10, 12, 15–19]. Thus, by numerically and experimentally investigating nozzles with varying divergence half angles comparisons can be drawn to this past research.

The decision to not vary both the expansion ratio and the divergence half angle was made based on budgetary and scheduling reasons which would only allow for the production of a total of six nozzle varieties.

With the divergence half angle selected as the variable of investigation the expansion ratio remains constant. This constant expansion ratio was calculated by assuming a nozzle chamber and exit pressure and applying Eq. (2.1)[20]. Where A_e is the nozzle exit area, A_t is the throat area, γ is the

specific heat ratio, p_e is the pressure at the exit plane of the nozzle, p_c is the pressure in the upstream nozzle chamber and Γ is the Van den Kerckhove function defined by Eq. (2.2)[20].

$$\varepsilon = \frac{A_e}{A_t} = \frac{\Gamma}{\sqrt{\frac{2\gamma}{\gamma-1}\left(\frac{p_e}{p_c}\right)^{\frac{2}{\gamma}}\left(1-\left(\frac{p_e}{p_c}\right)^{\frac{\gamma-1}{\gamma}}\right)}} \tag{2.1}$$

$$\Gamma = \sqrt{\gamma}\left(\frac{2}{\gamma+1}\right)^{\frac{\gamma+1}{2(\gamma-1)}} \tag{2.2}$$

For the chamber and exit pressure values of $3 \cdot 10^5$ Pa and 1000 Pa were selected respectively, this leads an area ratio of 16.971. These pressures were driven by the requirements as presented in Section 2.2. Firstly, the design chamber pressure was selected such that future endeavors would be able to use the maximum expected chamber pressure of 3 bar as stated by **VLM-NOZZLE-5**. The lower pressure was selected such that the pressure ratio would be as high as possible, without the longest linear nozzle exceeding the length requirement **VLM-NOZZLE-4**, while still being a round number to aid in analytical analysis.

Three angles of 15, 30, and 45 degrees were selected for the divergence half angle. The reasoning for the choice of these angles is two-fold.
Firstly, these angles of 15, 30, and 45 were frequently investigated in numerical research with experimental validation of the results being very scarce [17, 18, 21–23]. Thus experimentally studying these nozzles would add to the body of experimental verification data.
Secondly, by selecting these three angles one is able to draw parallels to macro scale nozzles where nozzles with divergence half angles of 15° are most often applied. The reason for the usage of this divergence angle are the relatively low divergence losses encountered combined with the short nozzle divergent length. The nozzle divergence loss, ε_{div}, can be analytically approximated according to Eq. (2.3) [20].

$$\varepsilon_{div} = 1 - \frac{1 + cos(\theta_{out})}{2} \tag{2.3}$$

From this equation one can find that a nozzle with a divergence angle of 15° will lose 1.7% of its momentum thrust due to divergence effects. Increasing the divergence angle to 20° will increase this loss to 3%, while using an angle of 10° results in 0.76% losses. From this one might argue that smaller divergence angles are better as less divergence losses occur. However, the divergence half angle also heavily influence the nozzle length, and with it the nozzle weight. For an axisymmetric nozzle, with a unit throat diameter, and an area expansion ratio of 10, one can find that the divergent length of the nozzle will be 3.07 for $\theta_{out} = 10°$, 2.02 for $\theta_{out} = 15°$, and 1.49 for $\theta_{out} = 20°$. Similar to the divergence losses the nozzle divergent length is not linearly dependent on the divergence half angle. Due to this nonlinear dependency a nozzle with a divergence angle of 15° will provide the best combined performance of small divergence losses and a short nozzle.

In contrast to this trend in macro nozzles, past micronozzle research [4, 10, 12, 15–19] has indicated that nozzles with larger divergence half angles have better performance for Reynolds numbers below 1000, which are of interest to this research. The cause of the sub-par performance of low divergence angle nozzles are the relatively thick viscous subsonic boundary layers. These boundary layers reduce the effective expansion ratio available for supersonic flow expansion and acceleration,

thus reducing performance. By using a larger divergence angle one expands the nozzle faster removing a subtancial part of the surface area of the boundary layer to grow on. This results in an effective expansion ratio that is closer to the design value. However, increasing the divergence half angle does come with an increase in geometric losses as the thrust vector at the nozzle exit has a larger non-axial component. In conclusion, a lower throat Reynolds number results in a thicker boundary layer, warranting the use of larger divergence angles, and an optimal divergence half angle exists for each Reynolds number.

The remaining parameters such as R_a, R_t, θ_{in} were determined based on typical values applied in macro nozzles as presented in [20, 24, 25] or were set by the requirements. These values can be seen in Table 2.2.

Table 2.2: Linear nozzle design parameters

Parameter	Value
Convergence half angle (θ_{in})	45°
Divergence half angle (θ_{out})	15°, 30°, 45°
Throat width (W_t)	45 µm
Throat curvature ratio ($\frac{2 \cdot R_t}{W_t}$)	1
Convergence curvature ratio ($\frac{R_a}{W_{in}}$)	0.05
Inlet width (W_{in})	3000 µm
Nozzle length (L_{nozzle})	2893.04, 2177.4, 1917.63 µm
Area ratio (ε)	16.971
Truncation percentage $\%_{trunc}$	N/A

2.4. Aerospike nozzle geometries

As described in Section 2.2 the aerospike nozzles will be designed with very similar parameters as the linear nozzle. However, an aerospike is not a conventional nozzle and this does not follow the same design methodology of linear nozzles. For the design of the aerospike profiles the approximate method of Angelino was applied [26].

This method defines the central body of the aerospike through a distance l and an angle α from the throat lip which can be seen in Fig. 2.3. These two variables are calculated for a Mach number that ranges from one (the throat Mach number) to the exit Mach number M_e, which can be calculated through Eq. (2.4). The exit plane of an aerospike nozzle is difficult to unambiguously identify. However, generally the plane at the tip of the center body of the aerospike that spans the entire base of the aerospike, r_e in Fig. 2.3, is considered the exit plane [27].

$$M_e = \sqrt{\frac{2}{\gamma - 1}\left(\left(\frac{p_c}{p_e}\right)^{\frac{\gamma - 1}{\gamma}} - 1\right)} \tag{2.4}$$

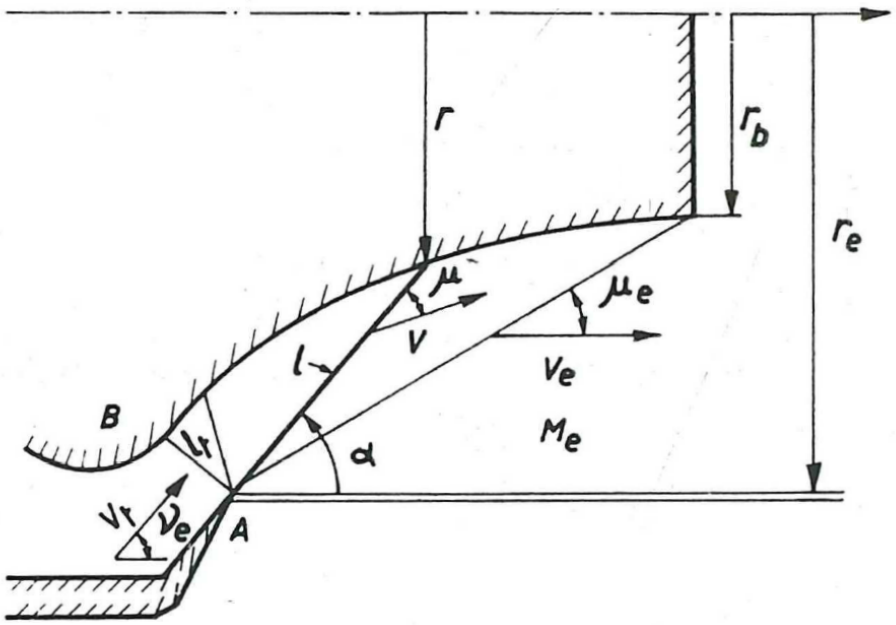

Figure 2.3: Spike definition through angelino method [26]

The equations defining length l and angle α are Eqs. (2.5) and (2.6). Where ν_e is the Prandtl-Meyer angle based on the exit Mach number, ν is the Prandtl-Meyer angle based on the local Mach number, μ is the Mach angle, M is the Mach number, W_t is the throat width and ε is the area ratio. The area ratio in this equation can be written as a function of the Mach number through Eq. (2.7). By doing this l and α are both a function of the Mach number or a constant and the entire spike geometry can be calculated.

$$\alpha = \nu_e - \nu(M) + \mu(M) \tag{2.5}$$

$$\frac{l}{W_t} = \varepsilon M \tag{2.6}$$

$$\varepsilon = \frac{1}{M}\left(\frac{2}{\gamma+1}\left(1+\frac{\gamma-1}{2}M^2\right)\right)^{\frac{\gamma+1}{2(\gamma-1)}} \tag{2.7}$$

The tip of the aerospike nozzle cannot be made too thin as the nozzles need to be produced and handled for experimental testing. This means that an ideal spike contour which ends in an infinitesimally thin tip, as defined by the equations described above, is not feasible. To reduce the fragility of the spike center body a truncation is applied at certain percentage of the total spike length.

This truncation will allow for a wider stronger base of the spike. However, truncating the center body influences the performance characteristics of the nozzle. In [9] it was found that a more truncated nozzle leads to similar thrust output but a reduced specific impulse. However, the numerical simulations performed in [9] were 2D simulation and 3D simulations of truncated micro aerospikes nozzles have not yet been performed to the knowledge of the writer. As such it was decided to investigate the effect of the truncation percentage on the nozzle performance.

From initial estimations it became clear that an aerospike nozzle truncated at 60% of a full spike would be the limit of what would be rigid enough for experimental testing. Further truncated nozzles would be truncated at 40 and 20 percent.

The center body geometry ,upstream from the throat, has been approximated by a wedge shape. In the literature there are two typical upstream shapes an ellipsoidal shape [7, 9] and a wedge shape [27, 28]. Due to the more steady pressure gradient that a wedge shape is expected to deliver it is selected for this study. However, this longer wedge shape also provides more surface area for a viscous boundary layer to grow on, possibly resulting in a more restricted throat.

Lastly, one can see the summary of all the design parameters in Table 2.3. Note that values for the throat are only for a single throat, two of which are present in the entire nozzle.

Table 2.3: Aerospike nozzle design parameters

Parameter	Value
Convergence half angle (θ_{in})	45°
Divergence half angle (θ_{out})	N/A
Throat width (W_t)	45 µm
Throat curvature ratio ($\frac{2 \cdot R_t}{W_t}$)	10
Convergence curvature ratio ($\frac{R_a}{W_{in}}$)	0.05
Inlet width (W_{in})	3000 µm
Nozzle length (L_{nozzle})	4479.76, 5163.04, 5846.19 µm
Area ratio (ε)	16.971
Truncation percentage $\%_{trunc}$	20%, 40%, 60%

3

Numerical Setup and Methodology

Numerical simulations are performed to acquire simulation results for the selected geometries, which will be validated through experimental testing. The numerical simulations are set up such that they will approximate the experimental tests as close as possible. As a result all numerical simulations will be 3D simulations in contrast to a significant portion of past research efforts [5, 7, 9, 18, 29–32]. In this chapter the underlying theory, the solver selection, and the numerical setup are treated.

3.1. Solver types

Numerical simulations on microscale flows can have difficulties to achieve accurate results due to flow rarefaction effects. To be sure that flow rarefaction will not cause any issues the appropriate type of solver needs to be selected fitting the degree of rarefaction of a flow. The rarefaction of a flow is indicated by the Knudsen number, with higher Knudsen numbers relating to higher degrees of rarefaction and vice versa, it is defined by Eq. (3.1) [18].

$$Kn = \frac{\lambda}{L} = \sqrt{\frac{\gamma\pi}{2}}\frac{M}{Re} = \frac{\mu}{\rho L}\sqrt{\frac{\pi m}{2k_B T}} \tag{3.1}$$

In this equation λ is the molecular mean free path, which is the average distance traveled by a molecule between collisions with other molecules and walls. L is the characteristic length of the flow, which for micronozzle studies is often set equal to the throat width. Furthermore, γ is the specific heat ratio, M is the Mach number, Re is the Reynolds number, μ is the dynamic viscosity, ρ is the density, k_B is the Boltzman constant, T is the temperature, and m is the mass of a single molecule of the flow. Using the Knudsen number one can separate a flow into four distinct flow regimes. In increasing degree of rarefaction these are:

- Continuum regime
- Slip flow regime
- Transitional regime
- Free molecular regime

The exact threshold where one flow regime stops and the next one starts has been an ongoing discussion within the academic world. But the most commonly accepted thresholds are as followed:

- **Continuum regime**: It is accepted that the continuum regime is valid within $Kn < 0.01$ [16, 18, 19, 33–38].
- **Slip flow regime**: The slip flow regime it is typically defined by a Knudsen number that is bounded by $0.01 < Kn < 0.1$ [18, 19, 37, 38].
- **Transitional regime**: The transitional regime is characterized by $0.1 < Kn < 10$ [18, 19, 37, 38].
- **Free molecular regime**: Once $Kn > 10$ the flow is defined by the free molecular regime [18, 19, 37].

One needs to select an appropriate solver and boundary conditions based on the degree of rarefaction. For flow inside the continuum regime conventional solvers based on the Navier Stokes equations are most frequently applied due to their low computational requirements. However, for flows with higher Knudsen numbers inaccuracies start to occur in the results of these solvers. It has been shown that the applicability of the Navier Stokes based solvers can be extended to the slip flow regime by applying slip flow wall boundary conditions [10, 18, 19, 39].

At higher degrees of rarefaction one has to use a non-continuum approach, for micronozzle purposes the most commonly applied of these is the Direct Simulation Monte Carlo (DSMC) method of Bird [38]. Previous research has shown that DSMC based solvers are able to present an accurate representation of the flowfield across all Knudsen numbers [40]. Contrary to most solvers, DSMC is a discrete Lagrangian method and thus models a flow by modeling the behavior of particles which each represents a group of molecules of the to be modeled medium. This means that in regions of higher density, thus lower Knudsen number, more computational particles and inter-particle collisions need to be modeled leading to an exponential growth in computational resources required.

A solution that has been suggested to get both the accuracy of DSMC and the computational efficiency of Navier Stokes based solves is to apply a hybrid method. These hybrid methods apply continuum solvers in the regions of low rarefaction and DSMC in the regions of high rarefaction. Past attempts have shown accurate results with a computational cost decrease of 75% [19].

For this research a Navier Stokes based solver using both no-slip and slip boundary conditions was selected. This was decided based on the fact that DSMC simulations would take too long to be viable within the time constraints of a MSc thesis. A hybrid DSMC Navier Stokes method was briefly considered as such a solver was already successfully developed at the faculty of Applied Physics of the TU Delft by la Torre [19]. However, the solver in question was not available for use as the development was done in cooperation with an external party which owns the rights to the solver.

As a solver based on continuum methods was selected, the bounds wherein its results are still accurate has to be determined. Various efforts by the academic world have been made to identify these bounds and will be briefly treated.
Alexeenko et al. [41], performed simulations using both a Navier-Stokes and DSMC solver on nozzles with a throat Knudsen number of 0.005. The resulting flow fields showed differences near the nozzle lip but the thrust and massflow predictions were in good agreement with each other.
Liu et al. [42] compared Navier Stokes simulations using slip flow wall boundary conditions with DSMC results. This comparison resulted in the recommendation to switch to non continuum methods if the local Knudsen number exceeded 0.045. Xie [43] determined that the results from DSMC

and Navier Stokes using slip conditions are in good agreement for an average Knudsen number below 0.01.
Lastly, la Torre [19] compared the results of DSMC and Navier Stokes with slip conditions for micronozzles with throat Knudsen numbers ranging from 0.008-0.125. He found that continuum methods produce large errors in the simulated flow field if the throat Knudsen number is larger than 0.01. Moreover, La Torre [19] also observed that the results for the integrated properties such as thrust, massflow, and specific impulse would be within 3% of a DSMC solution across the entire range of investigated Knudsen numbers. However, it was found that applying a continuum flow model in regions with higher degrees of rarefaction led to an over-estimation of the nozzle outlet pressure and an under-prediction of the the nozzle outlet velocity [16, 19]. The two effects almost perfectly canceled each other out to get the 3% error mentioned. Similar behavior where the integrated properties such as mass flow, specific impulse, and thrust are valid for higher Knudsen ranges than the flowfield results has been reported by the other sources as well [42, 43].

It can be seen that various metrics ($Kn_t, Kn_{local}, Kn_{avg}$) have been used to define whether a continuum method is still valid for the simulation at hand. Moreover, the method with which the local or average Knudsen number is calculated in these studies is often not clarified and can lead to further differences in the validity bounds. Lastly, for the average Knudsen number validity bounds it is not defined over what volume one should take the average.

For the simulations in this research it was decided to apply the validity bounds as suggested by La Torre [19]. This selection was made based on the fact that La Torre's was validity bounds are unambiguous and can be easily calculated a-priori using Eq. (3.1).

3.2. Governing equations

The numerical simulations in this study are done using a solver based on the compressible Navier Stokes equations. These equations are modeled according to the system of equations presented in Eqs. (3.2) to (3.7). In this system of equations the conservations of mass, moment and energy are modeled according to Eqs. (3.2) to (3.4) respectively. Furthermore, a Newtonian viscous model is used to model the viscous stress tensor $\boldsymbol{\tau}$ in Eq. (3.6). This entire model is closed out using the ideal gas relation in Eq. (3.7).

$$\frac{\partial \rho}{\partial t} + \nabla \cdot (\rho \mathbf{U}) = 0 \tag{3.2}$$

$$\frac{\partial}{\partial t}(\rho \mathbf{U}) + \nabla \cdot (\rho \mathbf{U}\mathbf{U}) = -\nabla p + \nabla \cdot \boldsymbol{\tau} + \rho g_0 \tag{3.3}$$

$$\frac{\partial}{\partial t}(\rho E) + \nabla \cdot (\rho E \mathbf{U}) = -\nabla \cdot (k \nabla T + (\boldsymbol{\tau} \cdot \mathbf{U})) \tag{3.4}$$

$$E = e + \frac{|\mathbf{U}|^2}{2} \tag{3.5}$$

$$\boldsymbol{\tau} = \mu \left(\left(\nabla \mathbf{U} + \nabla \mathbf{U}^T \right) - \frac{2}{3} (\nabla \cdot \mathbf{U}) \mathbf{I} \right) \tag{3.6}$$

$$p = \rho R T \tag{3.7}$$

In these equations ρ is the density, $\mathbf{U}$ the velocity vector, p the pressure, T the temperature, E the internal energy, k the thermal diffusion, μ the dynamic viscosity, $\mathbf{I}$ the identity matrix, e the specific internal energy, and R the specific gas constant.

3.3. OpenFOAM

Open source Field Operation And Manipulation better known as OpenFOAM is a C++ toolbox of Computational Fluid Dynamics (CFD) solvers. Within OpenFOAM there is a wide variety of solvers available from DSMC solvers to multiphase flow solvers. For this study the most recent version of OpenFOAM is used, OpenFOAM v5.0. Below the selection process of the solver is described followed by the numerical schemes, thermophysical models, turbulence models, and the boundary conditions used.

3.3.1. Solver selection

The decision was made to apply a solver based on the compressible Navier Stokes equations. Within OpenFOAM there are various solvers that are based on these equations: rhoCentralFoam, sonicFoam, rhoSimpleFoam and rhoPimpleFoam. Of these four solvers only rhoCentralFoam is a density based solver, with the other three being a pressure based solvers. This indicates that rhoCentralFoam could provide better results for flows with shock waves. Furthermore, of the four solvers only the capabilities of rhoCentralFoam and sonicFoam have been extensively researched for micronozzle purposes. Additionally, Marcantoni et al. [44] found that to get comparable results, sonicFoam needed three times more cells than rhoCentralFoam. Resulting from the higher efficiency, and the abundance of research done with the solver validating its accuracy, rhoCentralFoam was selected to be used for the numerical simulations in this research.

Next to the solver one also has to define the way the linear system of equations within the solver is to be solved. In this study a preconditioned conjugate gradient (PCG) solver is used with a diagonal preconditioner. Values of $1 \cdot 10^{-9}$ and $1 \cdot 10^{-4}$ are set for the absolute and relative tolerances. This combination was found to provide accurate results and quick convergence [10].

3.3.2. Numerical schemes

Within OpenFOAM all the numerical schemes are inputted through the *fvSchemes* document. The selection of these models will have a large impact on the convergence and accuracy of the solver. rhoCentralFoam has shown to be very sensitive to the selection of the discretization methods applied, leading to divergent behavior for some typically used schemes. Below an overview of the applied schemes is provided in Table 3.1, followed by a short description of the most important and non-conventional schemes used in this study.

Table 3.1: Numerical schemes applied in the numerical simulations

Scheme	Discretization method
Flux scheme	*Kurganov*
Time scheme	*localEuler*
Gradient scheme	*cellLimited leastSquares 1.0*
Divergent scheme	*Gauss linear*
Laplacian scheme	*Gauss linear corrected*
Interpolation scheme	*vanLeer*
Surface normal scheme	*corrected*

For the selection of the fluxscheme one has two options for rhoCentralFoam. One can use the central upwind scheme of Kurganov and Tadmore [45] or that of Kurganov, Noelle and Petrova [46]. The difference lies in the fact that the latter is not a pure central scheme but adjusts its weighting based

on the local propagation speed. According to Greenshields [47] the scheme by Kurganov Noelle and Petrova produces much more accurate results over the Kurganov Tadmore scheme, and is therefore chosen as the flux scheme in this research.

Within OpenFOAM the default scheme for interpolation is the linear scheme and it is considered highly unusual to deviate from this standard [48]. However, past work has shown that rhoCentralFoam delivers better results with a Total Variation Diminishing (TVD) schemes such as the vanLeer or vanAlbeda scheme [44]. The scheme which produces the best results is still a topic of research some claim that vanAlbeda is better than vanLeer and others even suggest that a Gamma differencing scheme would provide more accurate and stable results [49, 50]. However, it is generally accepted that the vanLeer scheme already produces very satisfactory results which behave predictable. For this reason it is one of the most applied, and thus very well understood, schemes for rhoCentralFoam. Therefore, the vanLeer TVD method was implemented as the interpolation scheme in the numerical simulations.

The last scheme that will be treated in depth is the time discretization scheme that is applied. As rhoCentralFoam is a transient solver one has to let the solver run a sufficient amount of time to reach steady state. As transient behavior is of no interest in this study it was decided to use the *localEuler* model which is a local time stepping (LTS) method. This means that the convergence of the results towards the steady state will accelerated. Consequently the intermittent solutions do not physically represent reality anymore and only the final steady state solution is representable of reality.

3.3.3. Thermophysical models

The models that define how a numerical solver approaches problems concerning energy, heat and physical properties of the fluid are called the thermophysical models. Within OpenFOAM one has to define what models and inputs should be used for these thermophysical models. The models and their inputs, that were selected for the numerical simulations will be briefly outlined below. An overview of the used thermophysical models can be seen below in Table 3.2 followed by a reasoning and explanation of the selected models.

Table 3.2: Thermophysical models applied in the numerical simulations

Thermophysical entry	Model
Class	*hePsiThermo*
Mixture	*pureMixture*
Transport	*Sutherland*
Thermodynamics	*JANAF*
Equation of state	*perfectGas*
Energy	*sensibleInternalEnergy*

One has to define the class of thermophysical model that will be used by the solver within OpenFOAM. Most solvers limit the choice of model classes as the solvers have specific needs. In the case of rhoCentralFoam one is limited to compressibility based thermophysical classes. This leaves three options: *psiThermo*, *psiReactionThermo* and *hePsiThermo*. All of these models are based on the compressibility [48] as defined in Eq. (3.8).

$$\psi = \left(\frac{\partial \rho}{\partial p}\right)_T = (RT)^{-1} \tag{3.8}$$

The difference between *psiThermo* and *psiReactionThermo* lies in the fact that *psiThermo* assumes a fluid of a fixed composition and *psiReactionThermo* is a model for reacting mixtures. The *hePsiThermo* model, which is the model used in this study, combines these two models and based on the user defined mixture input it picks the most fitting one for the simulation at hand. In the case of this study the mixture was set to *pureMixture* as all the numerical and experimental research will be done with pure nitrogen.

OpenFOAM models the dynamic viscosity μ, thermal conductivity κ and thermal diffusivity α according to the user defined transport model. In this study the Sutherland transport model was selected and within OpenFOAM it is defined by Eq. (3.9) [48]. This differs from the typically published formula from Sutherland which is defined by Eq. (3.10) [51].

$$\mu = \frac{A_s \sqrt{T}}{1 + T_s / T} \tag{3.9}$$

$$\mu = \mu_0 \frac{T_0 + T_s}{T + T_s} \left(\frac{T}{T_0} \right)^{3/2} \tag{3.10}$$

In these equations is μ the dynamic viscosity, T the temperature, μ_0 the dynamic viscosity at reference temperature, T_0 the Sutherland reference temperature, A_s and T_s are the Sutherland constant and Sutherland temperature which are gas dependent constants. The reasons for selecting this model are its well documented constants for nitrogen and its accuracy which it has proven throughout history. The coefficients for nitrogen to be used in Eq. (3.9), and the coefficients for Eq. (3.10) which they were calculated from, are listed in Table 3.3. Next to the values for the Sutherland model one also has to define the Prandtl number if one wants to use slip flow boundary conditions. As OpenFOAM only allows a single Prandtl number to be entered the most suitable value, which is valid for the widest temperature range present in the simulations, is selected. From [52] the Prandtl number was selected to be 0.71.

Table 3.3: Coeffients for Sutherland model

Coefficient	Value
T_s	111 K
T_0	300.55 K
μ_0	$17.81 \cdot 10^{-6}\ Pa\,s$
A_s	$1.4067 \cdot 10^{-6}\ Pa\,sK^{-1}$

The next model is the thermodynamics model which is concerned with calculating the specific heat c_p, specific enthalpy h and the specific entropy s from other fluid properties. One of the most used thermodynamics model inside of OpenFOAM is the JANAF model. The JANAF model defines these three properties through relations that all share the same gas dependent coefficients which are defined in the tables of the Joint Army Navy NASA Air Force (JANAF) interagency propulsion committee. The equations that define c_p, h and s are shown in Eq. (3.11) where $\Re$ is the universal gas constant, T is the temperature and $a_\#$ are the gas dependent coefficients [53]. Each gas has two sets of coefficients, each covering a range above or below a common threshold temperature, which is 1000 K in the case of nitrogen.

$$c_p = \Re\left(a_1 + a_2 T + a_3 T^2 + a_4 T^3 + a_5 T^4\right) \tag{3.11a}$$

$$h = \Re\left(a_1 T + \frac{a_2 T^2}{2} + \frac{a_3 T^3}{3} + \frac{a_4 T^4}{/4} + \frac{a_5 T^5}{5} + a_6\right) \tag{3.11b}$$

$$s = \Re\left(a_1 ln(T) + a_2 T + \frac{a_3 T^2}{2} + \frac{a_4 T^3}{3} + \frac{a_5 T^4}{4} + a_7\right) \tag{3.11c}$$

Initially the JANAF model was the preferred method for the numerical simulations. However, the coefficients for nitrogen from the JANAF tables are only valid above 200 K. During the experiments the nitrogen will be unheated as it enters the nozzle and can thus be assumed to be at room temperature (293 K). Based on this assumption one can calculate, using isentropic relations, that the temperature of the gas will decrease below the 200 K validity threshold. As a result the JANAF values are not a feasible method in this research.

Span et al. [54] presents an empirical relation to model the thermodynamic properties for nitrogen between 20 and 5000 K, which was adjusted to be used in the simulations, and is modeled using Eq. (3.12). They compared this relation to literature and found that the relationship deviated at most 0.01% from other relationships and could thus be deemed accurate.

$$\frac{c_p}{\Re} = a_1 + a_2 T + a_3 T^2 + a_4 T^3 + a_5 \frac{u^2 e^u}{(e^u - 1)^2} \tag{3.12a}$$

$$u = 3364.011 K / T \tag{3.12b}$$

To implement the relationship of Span et al. in OpenFOAM it needed to be rewritten to a JANAF format. As the temperature range that is of interest in the numerical simulation is far below the common threshold temperature of 1000 K only the JANAF coefficients for the lower temperature range have to be replaced. A fourth order polynomial was fitted to the data from the study of [54] to find all the coefficients necessary for the specific heat. The coefficients a_6 and a_7 were calculated based on the offset the JANAF fitted Span et al. model had from the JANAF values at temperatures where these are valid. The resulting coefficients can be found in Table 3.4 and were used to plot the unitless specific heat, specific enthalpy and specific entropy for comparison. The plots used for comparing the various models can be found in Figs. 3.1 to 3.3.

Table 3.4: Coefficients of thermodynamics models

Coefficient	JANAF [55] ($200 \leq T \leq 1000$)	JANAF [55] ($1000 \leq T \leq 6000$)	Span et al. [54]	Span et al. JANAF fitted
a_1	3.531	2.953	3.5	3.497
a_2	$-1.237 \cdot 10^{-4}$	$1.397 \cdot 10^{-3}$	$3.066 \cdot 10^{-6}$	$1.365 \cdot 10^{-4}$
a_3	$-5.030 \cdot 10^{-8}$	$-4.926 \cdot 10^{-7}$	$4.701 \cdot 10^{-9}$	$-1.232 \cdot 10^{-6}$
a_4	$2.435 \cdot 10^{-9}$	$7.860 \cdot 10^{-11}$	$-3.988 \cdot 10^{-13}$	$3.315 \cdot 10^{-9}$
a_5	$-1.409 \cdot 10^{-12}$	$-4.608 \cdot 10^{-15}$	1.013	$-1.792 \cdot 10^{-12}$
a_6	$-1.047 \cdot 10^{3}$	$-9.239 \cdot 10^{2}$	N/A	$-1.044 \cdot 10^{3}$
a_7	2.967	5.872	N/A	3.107

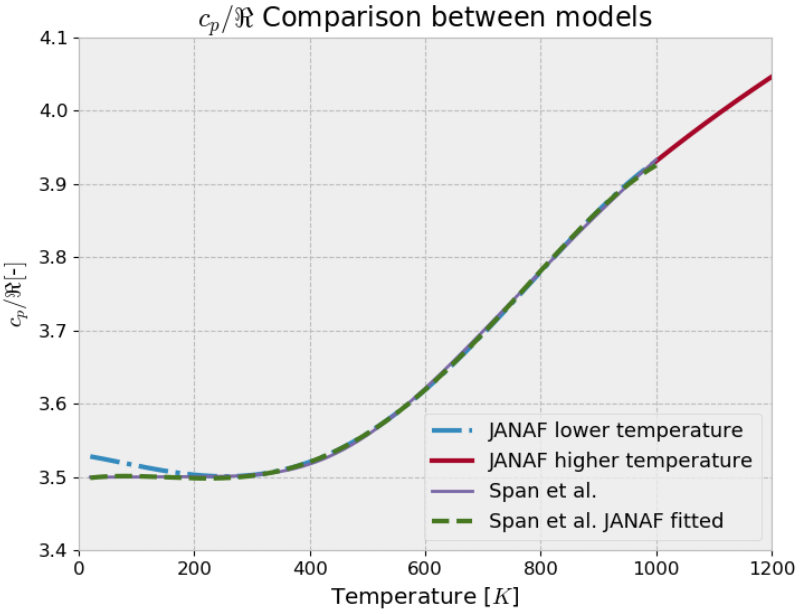

Figure 3.1: Comparison of the different models for $c_p/\Re$

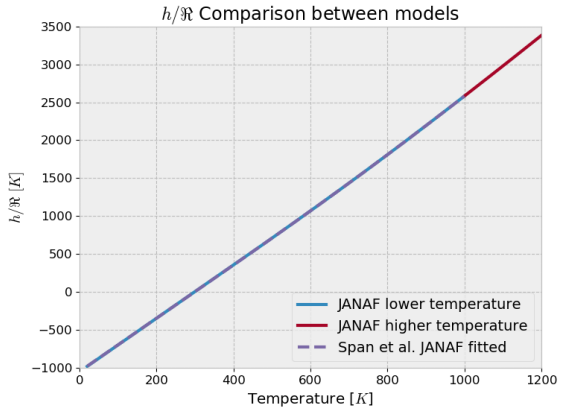

Figure 3.2: Comparison of the different models for $h/\Re$

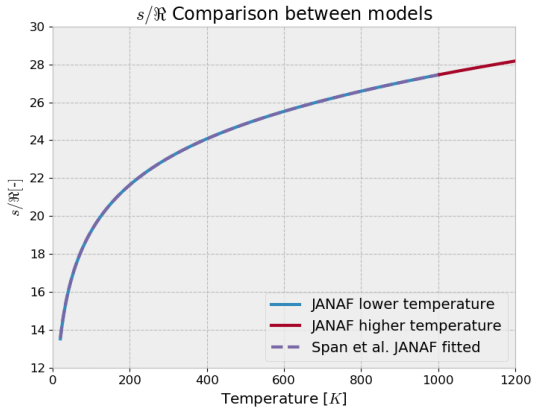

Figure 3.3: Comparison of the different models for $s/\Re$

From these graphs it becomes clear that the Span et al. model fitted to the JANAF format provides very good results. The only place where the models deviate from each other is for the specific heat at temperatures below 200K, which was expected due to the JANAF model not being valid at these temperatures. As such the JANAF fitted Span et al. model was used for the numerical simulations.

Finally, the last parameters that have to be input are the molar mass of the fluid one wants to model, the equation of state one wants to use, and the selection of the energy variable. The molar mass for nitrogen is set to 28.01348 g/mol, the equation of state is set to *perfectGas* and the energy variable is set to *sensibleInternalEnergy*. Commonly within OpenFOAM sensible energy variables are chosen over the absolute energy methods as sensible energy methods allow for easier calculations in reacting mixtures [48]. As in the case of the numerical simulations at hand the selection of the variable should not make a difference the standard of *sensibleInternalEnergy* is chosen.

3.3.4. Turbulence models

In previous research it has been stated that the implementation of a turbulence model to micronozzle simulations have a negligible influence with reported differences being less than 1.5 % [19]. Despite this, it was decided to run the numerical simulations with a turbulence model. This decision was made based on the fact that the extra accuracy was deemed to be worth it with the computational overhead being minimal.

The k-ω SST model [56] was selected as it can be used as a low Reynolds number turbulence model without extra damping functions, while still providing accurate results for both internal and external flows [57]. This accurate modeling of internal and external flows is of key importance in the current numerical simulations due to the presence of the aerospike nozzles where the internal flow transitions into an external flow.

This turbulence model is a two equation eddy-viscosity model based on the turbulence kinetic energy k and the specific dissipation rate ω. These variables are defined by Eqs. (3.13) and (3.14) [58].

$$k = \frac{3}{2}(UI)^2 \tag{3.13}$$

$$\omega = \frac{\sqrt{k}}{l} \tag{3.14}$$

Where U is the mean flow velocity, I is the turbulence intensity, and l is the turbulence length scale. In the present simulations the mean flow velocity is approximated by using the ideal rocket theory equation for massflow, which is treated more in depth later in Section 4.1, from which the inlet velocity can be calculated. The turbulence intensity is set equal to 5% which is equal to a medium to high turbulence case [58]. Lastly, the turbulence length scale is approximated as 0.038 of the hydraulic diameter, which is a value valid for fully developed pipe flow [59].

For the numerical simulations the turbulence kinetic energy and specific dissipation rate only need to be calculated at the inlet. At the other boundaries in the computational domain the turbulence model will calculate these variables through wall functions. As such possible errors in the initial values, which occur due to them being approximated by ideal rocket theory, will not have an influence on the results of the simulation if the inlet of the computational domain is defined far enough upstream.

3.3.5. Boundary conditions

To setup the solver the properly boundary conditions need to be applied. As a density based solver with a low Reynolds k-ω SST turbulence model is applied, boundary conditions for the following variables need to be defined:

- Pressure (p)
- Velocity (U)
- Temperature (T)
- Turbulence kinetic energy (k)
- Specific rate of dissipation (ω)

To visualize the boundaries on which the boundary conditions are defined a course overview of the computational domain is given. In Fig. 3.4 a sketch can be found of the computational domain for one of the linear nozzles.

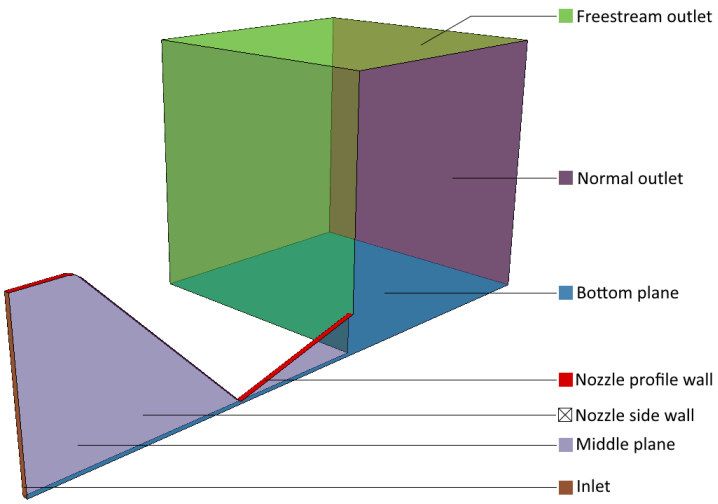

Figure 3.4: Computational domain for linear nozzles

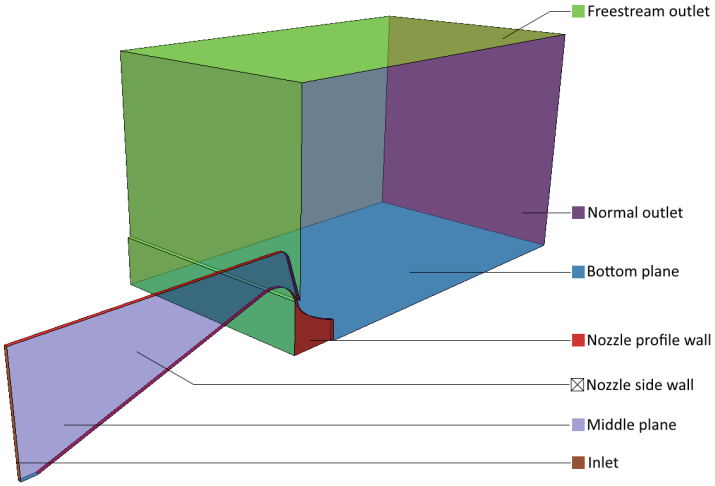

Figure 3.5: Computational domain for aerospike nozzles

As one can see only a quarter of the nozzle is simulated, reducing the computational cost to 25% of a complete nozzle simulation. The results for the full geometry can be obtained by using symmetry conditions, over which the results of this domain are extrapolated to the full geometry. In the figure each plane is color coded except for the nozzle sidewall, which is not visible as it directly behind the middle plane. The same naming scheme is used for the aerospike nozzle which can be seen in Fig. 3.5. With the computational domains defined an overview of the applied boundary conditions is given in Table 3.5, followed by a detailed look into the various boundary conditions.

Table 3.5: Boundary conditions applied in the numerical simulations

Boundary	Pressure	Velocity	Temperature	Turbulence kinetic energy	Specific rate of dissipation
Inlet	*totalPressure*	*zeroGradient*	*totalTemperature*	*fixedValue*	*fixedValue*
Freestream Outlet	*waveTransmissive*	*inletoutlet*	*waveTransmissive*	*zeroGradient*	*zeroGradient*
Normal Outlet	*waveTransmissive*	*inletoutlet*	*waveTransmissive*	*zeroGradient*	*zeroGradient*
Bottom plane	*symmetryPlane*	*symmetryPlane*	*symmetryPlane*	*symmetryPlane*	*symmetryPlane*
Middle plane	*symmetryPlane*	*symmetryPlane*	*symmetryPlane*	*symmetryPlane*	*symmetryPlane*
Nozzle side wall	*zeroGradient*	*noSlip OR maxwellSlipU*	*fixedValue OR smoluchowskiJumpT*	*kLowReWallFunction*	*omegaWallFunction*
Nozzle profile wall	*zeroGradient*	*noSlip OR maxwellSlipU*	*fixedValue OR smoluchowskiJumpT*	*kLowReWallFunction*	*omegaWallFunction*

Pressure
Considering that the nozzle flow is pressure driven, properly defining the pressure boundary conditions is of key importance. This starts at the inlet where the total pressure is defined. This total pressure is varied for the simulations to achieve throat Reynolds numbers over a wide range. The inlet pressures applied in the numerical simulations, and their corresponding Reynolds and Knudsen numbers, as calculated using 1D isentropic relations, are listed in Table 3.6. No simulations at inlet pressures lower than 0.2 bar were done as the throat Knudsen number would become higher than 0.01, which is beyond the validity bounds as determined by La Torre [19].

Table 3.6: Simulation inlet pressures and corresponding throat Reynolds numbers

p_{inlet} [bar]	Re_t	Kn_t
0.2	191	$7.78 \cdot 10^{-3}$
0.4	382	$3.89 \cdot 10^{-3}$
0.6	572	$2.59 \cdot 10^{-3}$
0.8	763	$1.94 \cdot 10^{-3}$
1.0	953	$1.55 \cdot 10^{-3}$
2.0	1908	$7.77 \cdot 10^{-4}$
3.0	2861	$5.18 \cdot 10^{-4}$

The outlets, both freestream and normal, are modeled with a wavetransmissive boundary condition. This boundary condition models the boundary such that the value of a parameter goes to the predefined freestream value after a certain distance. This freestream value is set to be 30 Pa in the simulations, as this will be the pressure of the vacuum chamber during the experimental testing of the nozzles.

The bottom and mid plane are modeled as symmetry planes. This is done to reduce the computational cost as mentioned before. All other variables will also be modeled using a symmetry plane at these boundaries. As such these boundaries will not be discussed in the sections treating the other variables.

Both the sidewall and the nozzle profile wall do not need any values to be imposed for the pressure. As a result both of these boundaries are modeled using a *zeroGradient* boundary condition.

Velocity
As the simulations are pressure driven systems no values need to be defined for the velocity at the inlet. As such a *zeroGradient* boundary condition was used.

Just as with the inlet no values need to be defined at the outlets as it is a pressure driven case. However, instead of applying a *zeroGradient* condition it was decided to apply an *inletOutlet* condition. This condition allows the flow to only flow outside of the domain and not return inside, thus removing any vortices that would appear close to the boundary. This was done to improve the speed of convergence and stability of the system.

The walls of the nozzle are modeled using two different methods. The first method that is used is the *noSlip* boundary condition and is the conventional boundary condition that is applied when the continuum flow assumption is still valid. This boundary condition assumes a zero velocity at the walls.

However, with increasing rarefaction of the flow, slip effect have shown to appear near walls. By applying slip flow boundary conditions at the wall it has been shown that Navier Stokes based solvers can still produce accurate results, extending the usable range of these solvers. To investigate the

differences between the simulation results with and without slip flow conditions all the cases are run with both wall boundary conditions.

The velocity slip in these numerical simulations is modeled using the first order velocity slip model from Maxwell [60]. This Maxwell velocity slip model is defined by Eq. (3.15).

$$\mathbf{U}_g - \mathbf{U}_w = \frac{2-\sigma_v}{\sigma_v}\lambda\left(\frac{\partial \mathbf{U}}{\partial y}\right)_w + \frac{3}{4}\frac{\mu}{\rho T}\left(\frac{\partial T}{\partial x}\right)_w \tag{3.15}$$

Where $\mathbf{U}$ is the velocity vector, subscripts g and w stand for the gas and the wall. Furthermore, λ is the molecular mean free path and μ, ρ and T are the dynamic viscosity, density and temperature of the medium respectively, and σ_v is a so-called Tangential Momentum Accommodation Coefficient (TMAC) which is defined by Eq. (3.16).

$$\sigma_v = \frac{V_i - V_r}{V_i - V_w} \tag{3.16}$$

Here V is the tangential velocity to the wall, subscript i refers to the incident tangential velocity of the flow upstream of a wall collision, and r refers to reflected tangential velocity (downstream of wall collision). Lastly, subscript w refers to the tangential velocity of the wall itself, in case a moving wall is present.

This TMAC value is set to 0.8, which is an experimental value found by Arkilic, [61] for polished silicon, which is the production material of the micronozzles.

Temperature
At the inlet boundary the temperature is set by a total temperature boundary condition. This condition maintains a user defined total temperature, in case of this research that temperature was 293 K. This temperature was selected as during the experimental tests nitrogen would enter the nozzle unheated and can thus be assumed to be at room temperature.

The temperature at the outlets is modeled by a wavetransmissive boundary condition similar to the condition set for the pressure. The temperature of the freestream in the wave transmissive condition is set at 293K, which is the expected temperature inside of the vacuum chamber during the experimental tests.

Similar to the velocity, the temperature near the walls is modeled using two methods. The first method is applied in the simulation cases where no-slip boundary conditions are imposed for the velocity. In these no-slip cases the temperature at the walls is fixed at 293K. One might note that it is more common in micronozzle research to model nozzle walls as adiabatic as micronozzles typically only fire for short pulses leading to insufficient time for noticeable heat transfer to take place. However, the presented numerical simulations are set up to represent the experimental tests, where thruster firing times are long enough, and the heat capacity of the silicon substrate in which the nozzle is etched is orders of magnitude larger than that of the nitrogen. As such, in agreement with the study of La Torre et al. [15], it is determined that modeling the wall with a fixed temperature is, in this case, more representable of reality.

The other method of modeling the temperature at the walls is by using slip flow boundary conditions. For the temperature the first order temperature slip model from Von Smoluchowski [62] is used. The expression of this boundary condition can be seen below:

$$T_g - T_w = \frac{2-\sigma_T}{\sigma_T}\left(\frac{2\gamma}{\gamma+1}\right)\frac{\lambda}{Pr}\left(\frac{\partial T}{\partial y}\right)_w \tag{3.17}$$

In this equation the subscripts g and w stand for the gas and the wall. In the formula λ is the molecular mean free path, Pr is the Prandtl number and σ_T is a so-called accommodation coefficient. This accommodation coefficient defines how the temperature propagates in direction tangential to the wall for the flow near the wall.

$$\sigma_T = \frac{T_i - T_r}{T_i - T_w} \tag{3.18}$$

Here T is the Temperature near the wall, subscript i and r refer to the incident, before the flow hits the wall and reflected temperature after wall interaction. Subscript w refers to the temperature of the wall.

In the simulations of this research the temperature accommodation coefficient is set to 0.85. This value was experimentally found to be a good approximate value for nitrogen in [63]. The Prandtl number was already defined in the thermophysical model to be 0.71.

Turbulence kinetic energy
As was mentioned in Section 3.3.4 one only needs to define the value for the turbulence kinetic energy at the inlet. As such at the inlet a fixed value boundary condition is imposed. Here the value is set that was calculated using Eq. (3.13).

The outlets of the computational domain were modeled using a *zeroGradient* boundary condition as no values need to be imposed on the outlet for the turbulence model.

It is important to select the appropriate wall functions for the simulation as the variables used by the turbulence model will be calculated through these. Based on the low Reynolds number of the flow, the selection was made to use the *kLowReWallFunction* boundary condition. Resulting from the small dimensions of the computational domain the y+ values will be tiny leading to negligible impact of the wall functions as the boundary layer is already fully resolved.

Specific dissipation rate
Similar to the turbulence kinetic energy the specific dissipation rate is modeled by imposing a fixed value at the inlet, where the value is calculated through Eq. (3.14).

Furthermore, the outlets are modeled by a *zeroGradient* boundary condition and the walls modeled through a wall function. However, while there is a low Reynolds number wall function for the turbulence kinetic energy no such wall function is available for the dissipation rate. As a result the wall function used is the *omegaWallFunction* boundary condition. However, as mentioned before the impact of the wall functions is negligible as the y+ values are much smaller than one.

3.4. Model verification

To make sure that the rhoCentralFoam solver is installed and working properly a simple verification case is run. In this verification case an inviscid, adiabatic, axisymmetric, converging diverging nozzle is simulated and compared to analytical data.

The analytical data, provided by the National Aeronautics and Space Administration (NASA), consists of the axial distribution of pressure and Mach number for three different pressure ratios [64]. The pressure ratios correspond to a subsonic, supersonic with normal shock, and fully supersonic case. These three cases give a good representation of the capabilities of rhoCentralFoam as few solvers in OpenFOAM are able to solve for such a wide range of Mach numbers. The case was setup using the files as provided by [65], keeping the boundary conditions and the mesh files constant while changing the numerical schemes to those as described in the sections above.

The results of this verification study can be seen on the next page in Figs. 3.6 to 3.8. Here one can observe that the results almost perfectly represent the analytical solution. The only noticeable difference can be found in the case with the shock. Here some diffusivity is present in the simulation, resulting in a slightly smeared out shock. Based on these results the numerical setup can be considered accurate and usable for the numerical simulations.

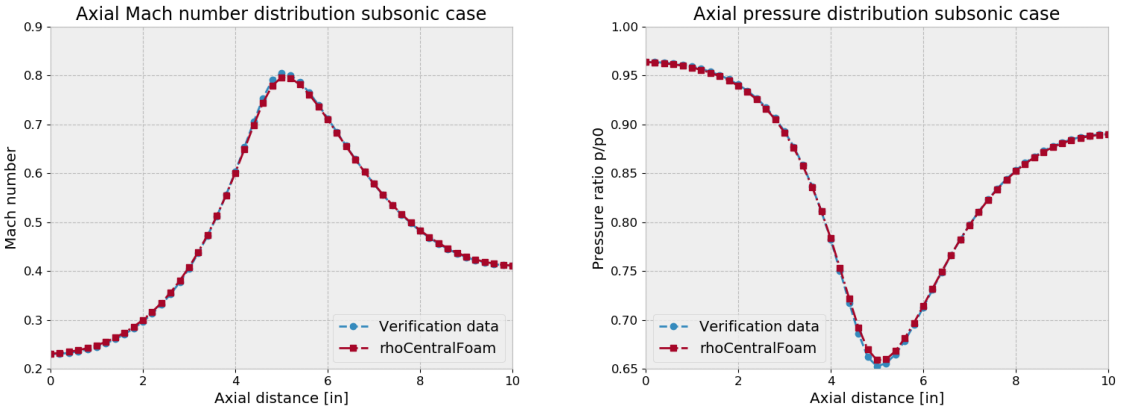

(a) Axial Mach number distribution

(b) Axial pressure distribution

Figure 3.6: Verification results in the subsonic case

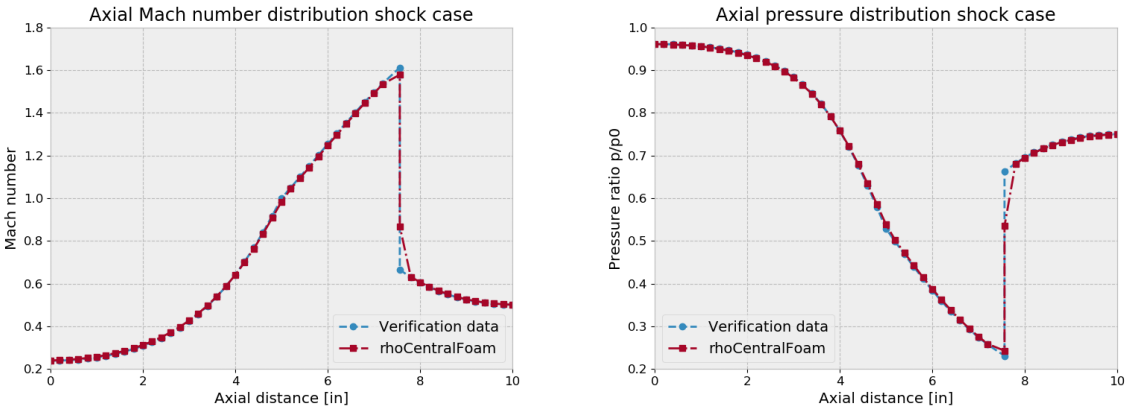

(a) Axial Mach number distribution

(b) Axial pressure distribution

Figure 3.7: Verification results in the shock case

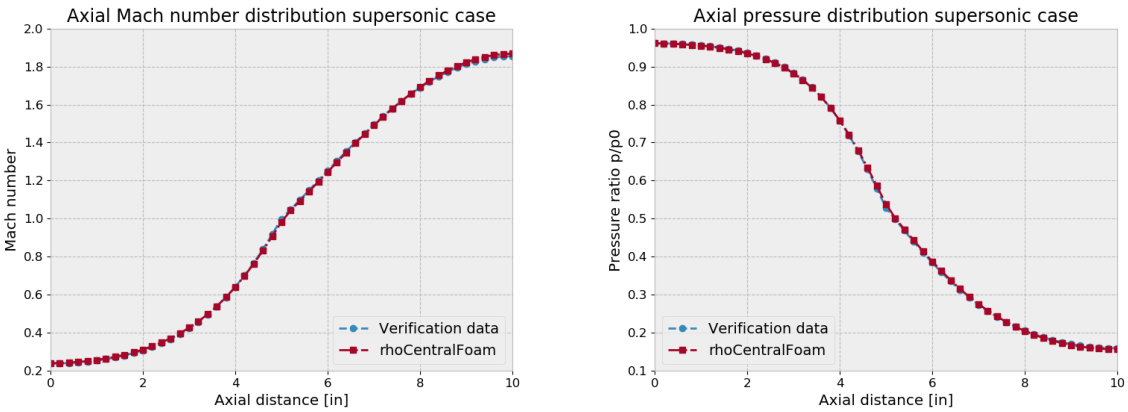

(a) Axial Mach number distribution

(b) Axial pressure distribution

Figure 3.8: Verification results in the supersonic case

3.5. Computational mesh

For CFD simulations one needs to generate a mesh and make sure that its quality and density are high enough for accurate results. As the general architecture of the meshes were already described before, here the methodology of generating the mesh and mesh convergence studies are presented.

3.5.1. Mesh generation

Two different methodologies were applied to generate the mesh for the simulations. For the linear nozzles OpenFOAM's built in blockmesh tool was used. Blockmesh is a text based input generating simple block based structured meshes. To be able to use blockmesh the outputs of a python script were written to a blockmesh file which was then used to generate te mesh. Such a mesh for the linear nozzle with a divergence angle of 15° can be seen in Fig. 3.9.

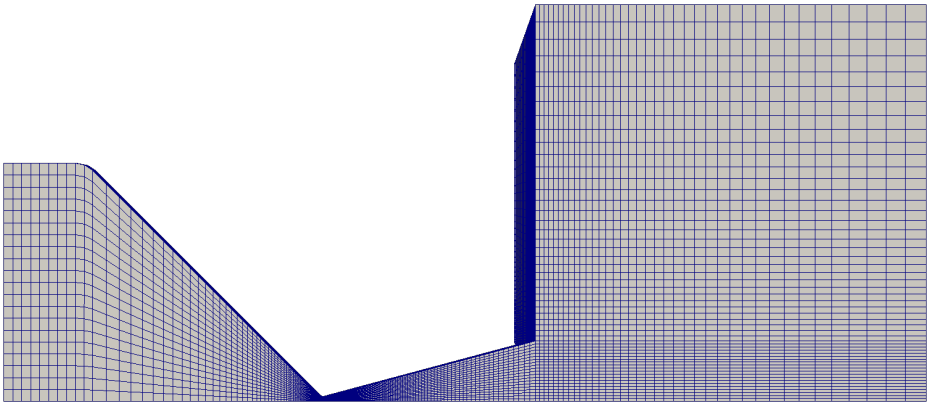

Figure 3.9: Mesh for the linear nozzle with $\theta_{out} = 15°$

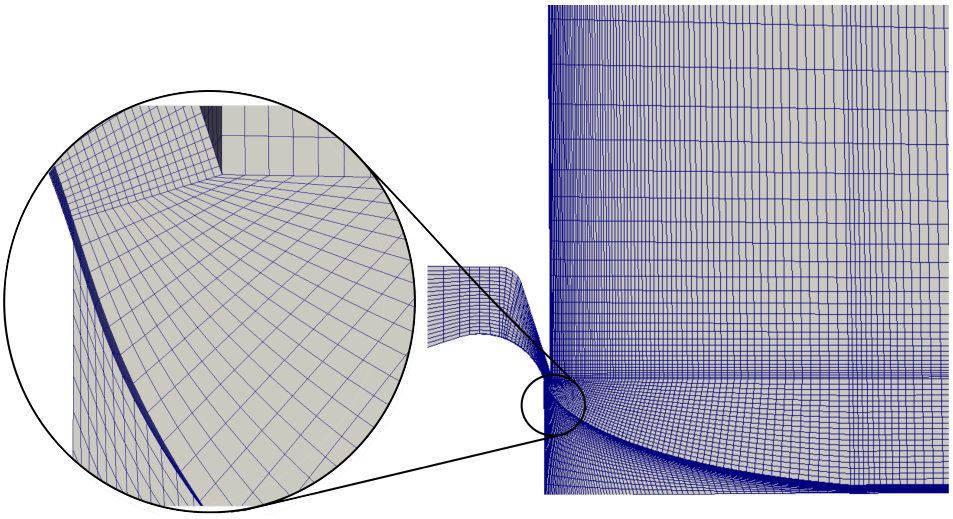

Figure 3.10: Mesh for the aerospike nozzle created with blockmesh tool

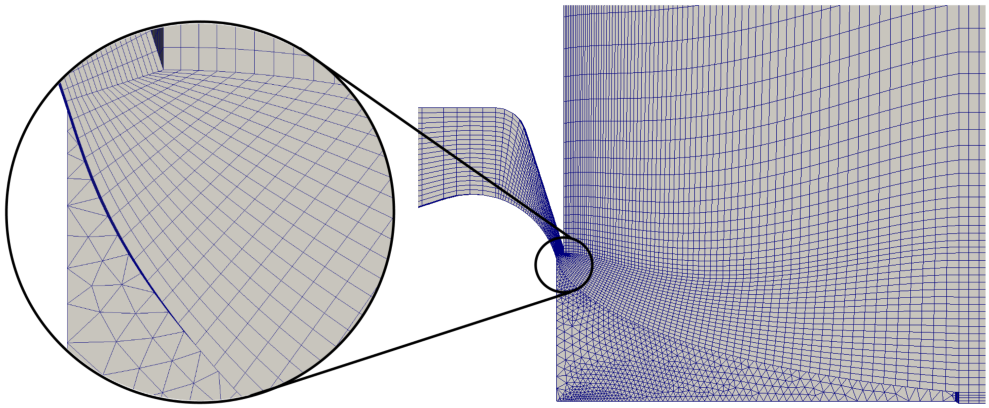

Figure 3.11: Mesh for the 60% truncated aerospike nozzle

For the aerospike nozzles the blockmesh tool did not suffice anymore. This has to do with the fact that the hexahedral cells near the nozzle throat of the aerospike would be extremely skewed as can be seen in Fig. 3.10. These skewed cells caused divergent behavior in the rhoCentralFoam solver. To solve this issue a hybrid mesh was generated, where the block representing the freestream behind the center body of the aerospike was turned into an unstructured mesh. As OpenFOAM does not provide a meshing tool to generate hybrid meshes, Ansys' ICEM meshing tool was used. The mesh which it generated was then imported into OpenFOAM using the *fluentMeshToFoam* command. This hybrid mesh can be seen in Fig. 3.11 and did result in convergent solver behavior.

3.5.2. Convergence study

One needs to be certain that the mesh density is appropriate to get physically accurate results. To test if the mesh is dense enough a mesh convergence study needs to be performed. This mesh convergence study was done for all the nozzle geometries using the no-slip case with a chamber pressure of three bars. During the convergence study the same simulation was run on various meshes increasing in mesh density.

The initial runs for all the convergence studies were performed on a mesh that approached 25,000 cells. This was followed by a rerun of the same simulation on a mesh after doubling of the amount of cells. To do this in a time efficient manner the *mapFields* command of OpenFOAM was used to map the results of the courser mesh, onto the refined one as the initial conditions.

A mesh was deemed converged if the relevant output parameters changed less than 0.1% after a doubling of the total amount of cells. In the case of this research the relevant parameters are the thrust, mass flow, and specific impulse.

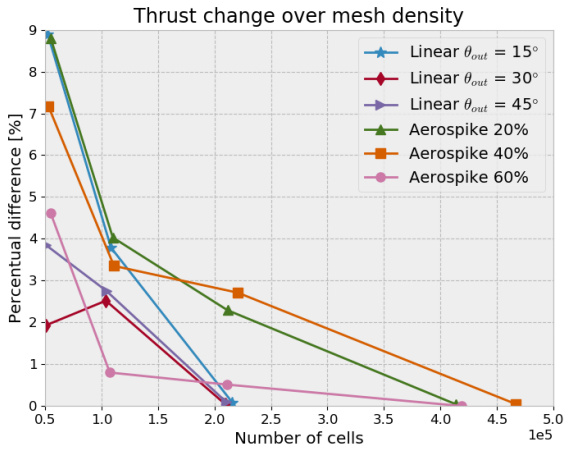

(a) Thrust convergence

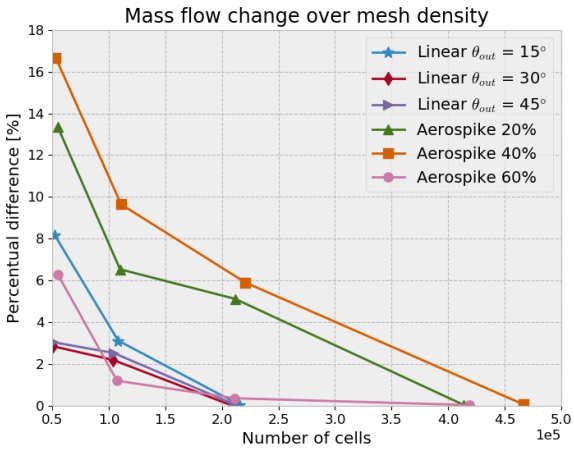

(b) Mass flow convergence

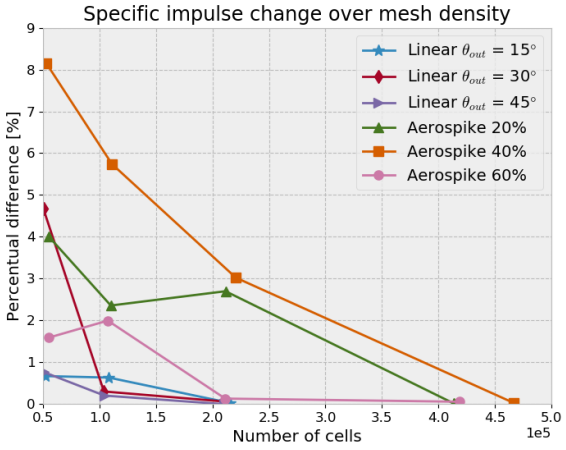

(c) Specific impulse convergence

Figure 3.12: Mesh convergence studies results

The results of the mesh convergence studies can be found in Fig. 3.12 where the percentual difference of a mesh, with respect to the one step courser mesh, is plotted. From these figures one can see that the last refinement of the meshes has approximately 200,000 and 400,000 cells for the linear and aerospike geometries respectively. As the last refinement step, which led to these mesh densities, resulted in less than a 0.1% difference, one can consider the mesh before the last refinement converged. This results in the final mesh for the linear nozzle configuration containing approximately 100,000 cells and those for the aerospike approximately 200,000 cells.

3.6. Simulation strategy

In this section the steps that were undertaken to run the numerical simulation will be described. Starting with the steps necessary to start the calculations, followed by the multistep process that was used during the calculation phase of the simulations, and ending with the solver postprocessing functions.

The simulations using rhoCentralFoam were run on a 8 core AMD Ryzen R7 1700 processor. To utilize all 8 cores of the computation processor the mesh needs to be decomposed and distributed over the various cores, which was done with the *decomposePar* command using the *scotch* decomposition method.

Following decomposition the solver can be started. However, the rhoCentralFoam solver turned out to be extremely sensitive to high pressure gradients, resulting in divergent solver behavior. As the cases were setup with an ambient pressure of 30 Pa and an inlet pressure which is at least 20000 Pa the pressure gradient near the inlet caused divergent behavior in rhoCentralFoam. To ensure convergence a three step process was followed which is described below:

step1: ambient pressure initialization
To make sure that the pressure gradients are low enough for convergent behavior, the simulations are not initialized with the wavetransmissive boundary condition for the pressure outlets, as stated in Section 3.3.5, but with a total pressure boundary condition. This is done because the total pressure boundary condition can easily be defined with a time dependent value. By using this time dependent value the ambient pressure can, slowly over many solver iterations, be reduced to the desired ambient pressure of 30 Pa. Furthermore, instead of a local time stepping method a regular upwind Euler time discretization is applied. This is done to prevent an unequal change of the ambient pressure for different cell sizes.

The rate of change of the ambient pressure, for which rhoCentralFoam exhibits convergent behavior, was experimentally determined. It was found that for the highest pressure ratio (pressure ratio of 10,000) a linear decrease of the ambient pressure over 5e-5 seconds, with a Courant Friedrichs Lewy (CFL) number of 0.5, consistently showed convergent behavior.

step2: boundary condition adjustment
After the ambient pressure has been gradually reduced, the desired boundary conditions can be reapplied. One can reapply the wave-transmissive boundary condition and the local time stepping methods by altering the last intermediate results file that OpenFOAM outputs at user defined time intervals. As the results are decomposed at this point, often over many computing nodes, it is very tedious and time consuming work to manually change the boundary conditions for each compute node. One could reconstruct the information of the various nodes to a single data file using the *reconstructPar* command, and change the boundary conditions in these files. While this would seem to be faster, it turned out that due to a bug in OpenFOAM reconstructing data of cases which applied slip flow boundary conditions could occasionally lead to corrupted data. Therefore, it was decided to change the boundary conditions without reconstructing the data from the various nodes to avoid any chance of corruptions. To make this process faster and less tedious this step was automated through a python script.

step3: temporal refinement
After running the solver with the preferred boundary conditions until the residuals are stable, constant, and have converged below $1 \cdot 10^{-6}$ the solver is considered to be converged. However, it was noticed that in some cases the CFL number was low enough for convergence but too high resulting in temporal oscillations in the results. To resolve these temporal oscillations the maximum CFL number was lowered to 0.1 and the cases were simulated for additional timesteps with this lower CFL number.

After the temporal refinement, additional postprocessing functions were run to get additional variable fields. The variables obtained through postprocessing functions were: the Mach number, dynamic viscosity, and deviatoric stress tensor. The necessity of these variables will be made clear in Section 4.1.

4

Numerical Results

With the methodology and setup of the numerical simulations explained the solvers were run. The results and analysis of said simulations are presented in this chapter. However, before one can analyze results the various performance metrics have to be defined, which is done in Section 4.1. This is followed by the results for the linear nozzles in Section 4.2.1 and the aerospike nozzles in Section 4.2.2. Lastly, based on the lessons drawn from these sections a new geometry is designed and numerically investigated, the results of this can be found in Section 4.2.3.

4.1. Performance metrics

To compare the performance of various nozzle geometries over a range of Reynolds numbers different unitless metrics are used. These metrics are the thrust efficiency η_F, the discharge coefficient C_D, and the specific impulse efficiency $\eta_{I_{sp}}$, which are defined by Eqs. (4.1) to (4.3). In these formulas F is the thrust, $\dot{m}$ is the massflow and I_{sp} is the specific impulse, the subscript $meas$ stands for the measured values from either numerical or experimental tests, and the subscript $1D$ stands for the values calculated through the ideal rocket theory equations.

$$\eta_F = \frac{F_{meas}}{F_{1D}} \tag{4.1}$$

$$C_D = \frac{\dot{m}_{meas}}{\dot{m}_{1D}} \tag{4.2}$$

$$\eta_{I_{sp}} = \frac{I_{sp_{meas}}}{I_{sp_{1D}}} \tag{4.3}$$

The measured values of these three metrics have to be calculated from the numerically simulated flowfield. In the case of the linear nozzles this is done by applying Eqs. (4.4) to (4.6) at the nozzle exit plane A_e. In these equations ρ is the density, $\boldsymbol{U}$ is the flow velocity vector, $\boldsymbol{n}$ is the normal vector of the exit plane, p is the pressure, p_∞ is the freestream pressure, $\boldsymbol{\tau}$ is the deviatoric stress tensor and g_0 is the gravitational constant.

$$\boldsymbol{F}_{meas} = \iint_{A_e} \rho \boldsymbol{U} \left(\boldsymbol{U} \cdot \boldsymbol{n}\right) dA_e + \iint_{A_e} \left(p - p_\infty\right) \boldsymbol{n}\, dA_e - \iint_{A_e} \left(\boldsymbol{\tau} \cdot \boldsymbol{n}\right) dA_e \tag{4.4}$$

$$\dot{m}_{meas} = \iint_{A_e} \rho \left(\boldsymbol{U} \cdot \boldsymbol{n}\right) dA_e \tag{4.5}$$

$$I_{sp_{meas}} = \frac{F_{meas}}{\dot{m}_{meas} \cdot g_0} \tag{4.6}$$

Note that the result of Eq. (4.4) is a vector, but for the calculations of the efficiency one is only interested in the thrust generated in the thrust direction. As such this directional component needs to be extracted from the vector.

Furthermore, one might notice that the thrust equation has an additional third term which is normally not taken into account. This third term defines the thrust caused by the stress state of the fluid at the exit plane. For higher Reynolds numbers this term is negligibly small, however, at lower Reynolds numbers the omission of this term can lead to a misrepresentation of the thrust of 50% [35]. As a result it is important to take this term into account during the calculations.

Another noteworthy observation is that the specific impulse efficiency is directly related to the thrust efficiency and the discharge coefficient, due to the definition of the specific impulse. Thus an error in one of them would lead to an error in the specific impulse efficiency.

As mentioned earlier this method of calculation of the measured/simulated data is only for the linear nozzles. As the aerospike is an atypical nozzle, the methodology used for extracting the performance from the simulation data differs from the linear nozzles. The thrust function for an aerospike not only has the three terms as described in Eq. (4.4) but also has an additional pressure thrust term over the surface of the spike.

Lastly, as an aerospike nozzles does not have a physical exit plane similar to that in conventional nozzle geometries, the moment thrust and a part of pressure thrust are generated at the nozzle throat. As a result these terms are integrated over the nozzle throat in the simulation thrust calculations instead of over the nozzle exit plane area. This leads to an updated formula for the thrust as seen in Eq. (4.7). The method of determining the massflow and specific impulse stays the same with the exception that the massflow is now taken at the throat.

$$\begin{aligned}\boldsymbol{F}_{meas,aerospike} = \iint_{A_t} \rho \boldsymbol{U} \left(\boldsymbol{U} \cdot \boldsymbol{n}\right) dA_t + \iint_{A_t} \left(p - p_\infty\right) \boldsymbol{n}\, dA_t + \iint_{A_{spike}} \left(p - p_\infty\right) \boldsymbol{n}\, dA_{spike} \\ - \iint_{A_{spike}} \left(\boldsymbol{\tau} \cdot \boldsymbol{n}\right) dA_{spike}\end{aligned} \tag{4.7}$$

These extracted values have to be compared against the 1D nozzle characteristics which are calculated through the ideal rocket theory. Thus the 1D thrust and massflow are defined by Eqs. (4.8) and (4.9) [20], the specific impulse is calculated through Eq. (4.6), substituting the measured values for the 1D values. Within these equations C_F is the thrust constant, c^* is the characteristic velocity and R is the specific gas constant.

$$F_{1D} = C_F p_c A_t = p_c A_t \sqrt{\frac{2\gamma^2}{\gamma-1}\left(\frac{2}{\gamma+1}\right)^{\frac{\gamma+1}{\gamma-1}}\left(1-\left(\frac{p_e}{p_c}\right)^{\frac{\gamma-1}{\gamma}}\right)} + A_e\left(p_e - p_\infty\right) \tag{4.8}$$

$$\dot{m}_{1D} = \frac{p_c A_t}{c^*} = \frac{\sqrt{\gamma}\left(\frac{2}{\gamma+1}\right)^{\frac{\gamma+1}{2(\gamma-1)}} p_c A_t}{\sqrt{RT_c}} \tag{4.9}$$

In contrast to the numerical calculations the 1D calculations for the aerospike can be made with the exact same equations. This is due to the fact that the sum of the surfaces, which are able to result in a force in the thrust direction, considered in Eq. (4.7), equal the nozzle area expansion ratio multiplied with the throat area. This can be mathematically summarized with Eq. (4.10), where n_{thrust} is the component of the surface normal vector $\boldsymbol{n}$ in the thrust direction. This is also the reason why it is convention, as mentioned before in Section 2.4, to consider the plane stretching between the two throat lips as the exit plane in an aerospike nozzle.

$$\iint_{A_t} n_{thrust}\, dA_t + \iint_{A_{spike}} n_{thrust}\, dA_{spike} = \varepsilon A_t = A_e \tag{4.10}$$

4.2. Results

From the numerical simulations the performance of the nozzles can be extracted and represented through the use of efficiency curves and contour plots.

To ensure that the numerical and experimental results are comparable over a range of Reynolds numbers the results for both of these should be represented using the Reynolds number as calculated by the isentropic flow relations. This is done as the actual Reynolds number during the experimental and numerical tests can vary from the ideal value due to differences in the effective throat area, mass flow, and hydraulic diameter caused by the growth of a viscous boundary layer.

The simulation results for the linear nozzles will be presented followed by those of the aerospike nozzles and the various double depth aerospike designs. However, before the various numerical results are treated, first an overview of the performance as expected through 1D calculations is provided, the results of which are summarized in Table 4.1.

Table 4.1: Thrust, mass flow, and specific impulse as calculated through 1D relations

	Linear			Aerospike		
Re_t	thrust [mN]	$\dot{m}$ [mg/s]	I_{sp} [s]	thrust [mN]	$\dot{m}$ [mg/s]	I_{sp} [s]
191	0.149	0.209	72.705	0.298	0.418	72.705
382	0.300	0.418	73.264	0.601	0.836	73.264
572	0.452	0.627	73.450	0.903	1.254	73.450
763	0.603	0.836	73.543	1.206	1.672	73.543
953	0.754	1.045	73.600	1.508	2.090	73.600
1908	1.511	2.090	73.711	3.021	4.180	73.711
2861	2.267	3.135	73.748	4.534	6.269	73.748

4.2.1. Linear nozzle results

The results that are treated first are those for the linear nozzles. Linear nozzles are the most commonly used nozzle geometry in the micronozzle industry. As such one should treat these results as the baseline performance currently possible for micronozzles.

On the next page, in Fig. 4.1, one can see Mach number contour plots for the linear nozzle with a 15° divergence half angle over the full range of throat Reynolds numbers investigated. In these contour plots the top half of the nozzle are the results as simulated using the no-slip boundary conditions and the bottom half as simulated using slip wall conditions. Furthermore, in the plots the solid black line indicates the $M = 1$ contour.

The contour plots for the linear nozzles with divergence half angles of 30° and 45° can be found in Fig. 4.2 and Fig. 4.3 respectively. Here only the results for $Re_t = 191$ and $Re_t = 2861$ are presented for legibility, the results over the full range of Reynolds numbers can be found in Appendix A.

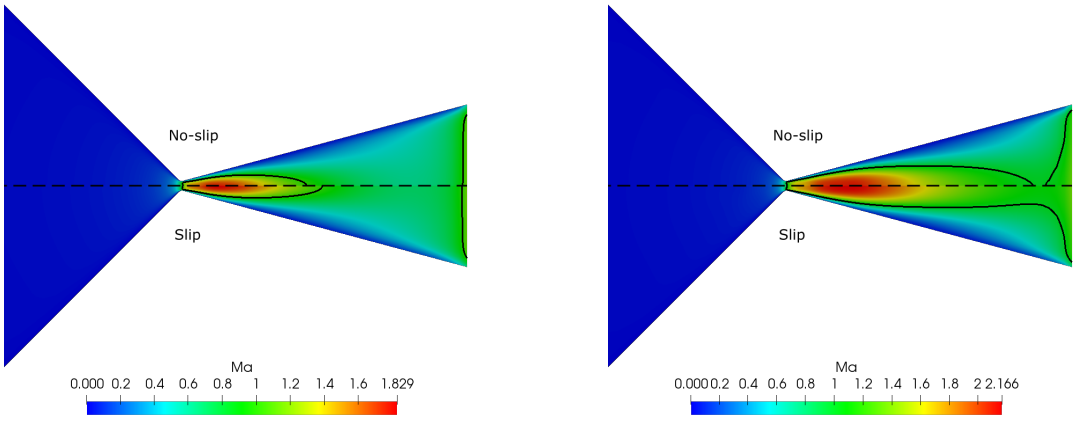

(a) $Re_t = 191$

(b) $Re_t = 382$

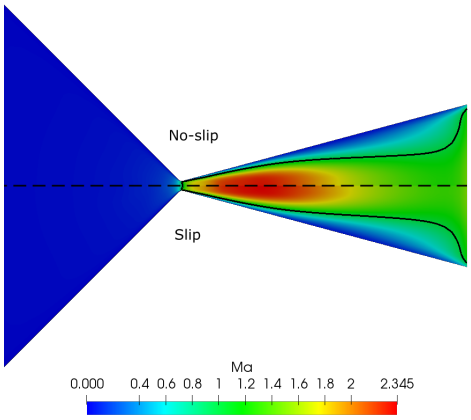

(c) $Re_t = 572$

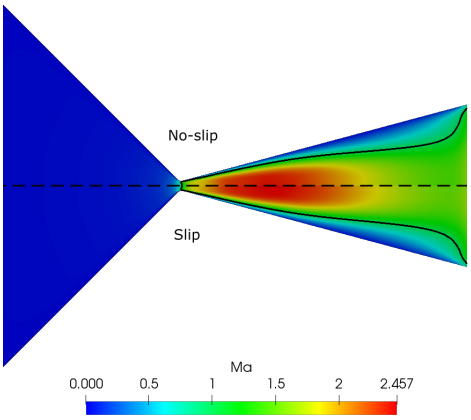

(d) $Re_t = 763$

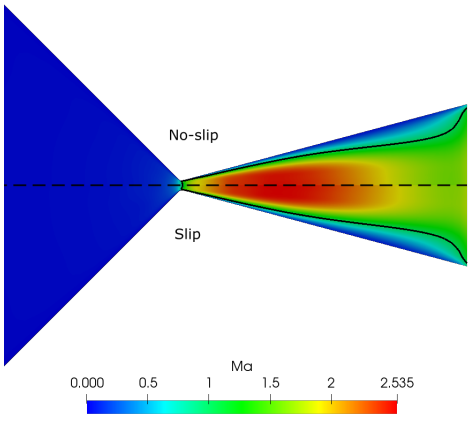

(e) $Re_t = 953$

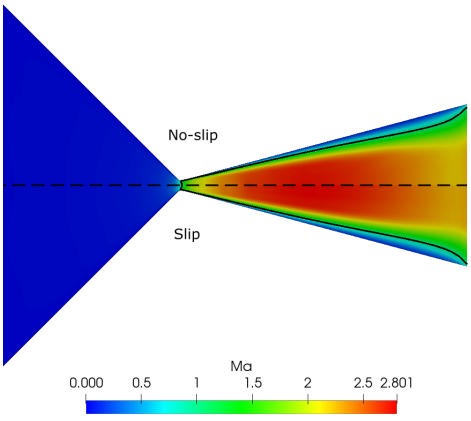

(f) $Re_t = 1908$

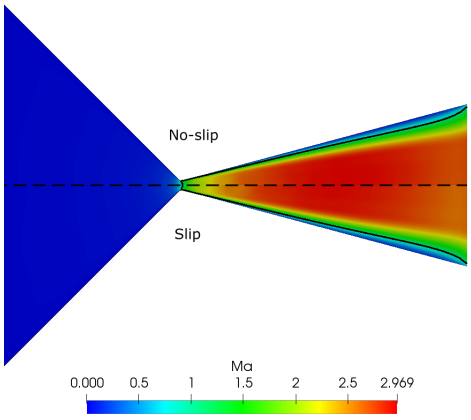

(g) $Re_t = 2861$

Figure 4.1: Mach contours for the linear nozzle with $\theta_{out} = 15°$ for $Re_t = 191 - 2861$

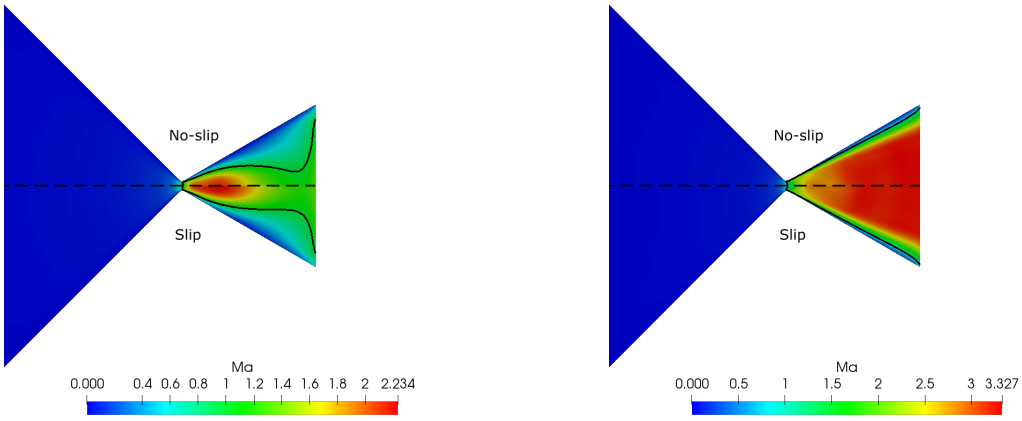

(a) $Re_t = 191$ (b) $Re_t = 2861$

Figure 4.2: Mach contours for the linear nozzle with $\theta_{out} = 30°$ for $Re_t = 191$ and $Re_t = 2861$

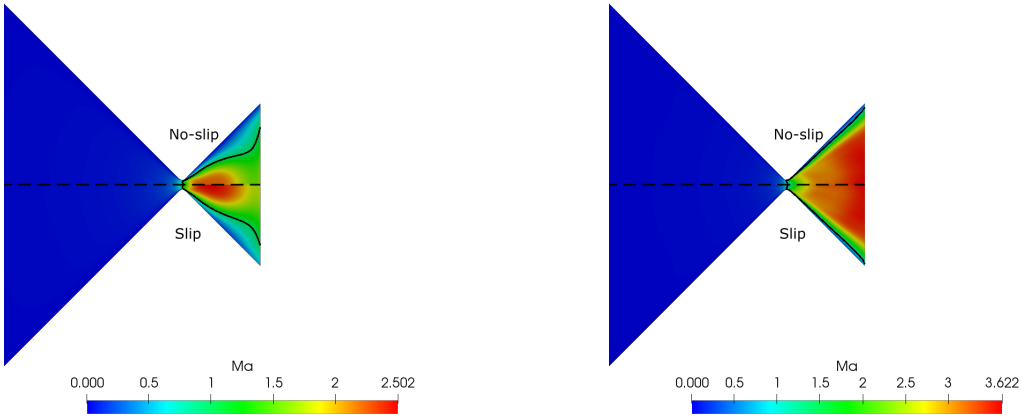

(a) $Re_t = 191$ (b) $Re_t = 2861$

Figure 4.3: Mach contours for the linear nozzle with $\theta_{out} = 45°$ for $Re_t = 191$ and $Re_t = 2861$

From the contour plots it can be seen that, as expected, the Mach number of the bulk flow decreases with the Reynolds number. Furthermore, it can be observed that the Mach number in the no-slip cases is lower than in the slip cases, with the difference increasing at lower Reynolds numbers.

Fig. 4.1 shows that for the nozzle with $\theta_{out} = 15°$ the viscous boundary layer grows to such proportions that at lower Reynolds numbers (382 for the no-slip conditions and 191 for the slip conditions) the flow becomes fully subsonic in the divergent of the nozzle. However, it is noteworthy that in these cases the flow returns to the supersonic regime near the nozzle exit. For the nozzles with the divergence half angles of 30° and 45° the core of the flow remains supersonic over the entire range of investigated Reynolds numbers. Similar flowfields have been predicted by Cheah et al. through numerical simulation in [33]. The nozzles under investigation by Cheah use the same nozzle depth but a larger throat width (100 µm) as those under investigation in this study. Based on their simulations it can be predicted that the flow would remain in the subsonic regime, even at the nozzle exit, would the Reynolds number drop even further. Based on the contour plots presented above one is able to describe the observed flow as heavily dominated by viscous effects and clearly shows why the observed nozzle performances have been so low in the past.

From the flow fields as calculated the various performance metrics can be calculated and plotted. The resulting plots for $\eta_F, C_D,$ and, $\eta_{I_{sp}}$ can be seen in Figs. 4.4 to 4.6 respectively.

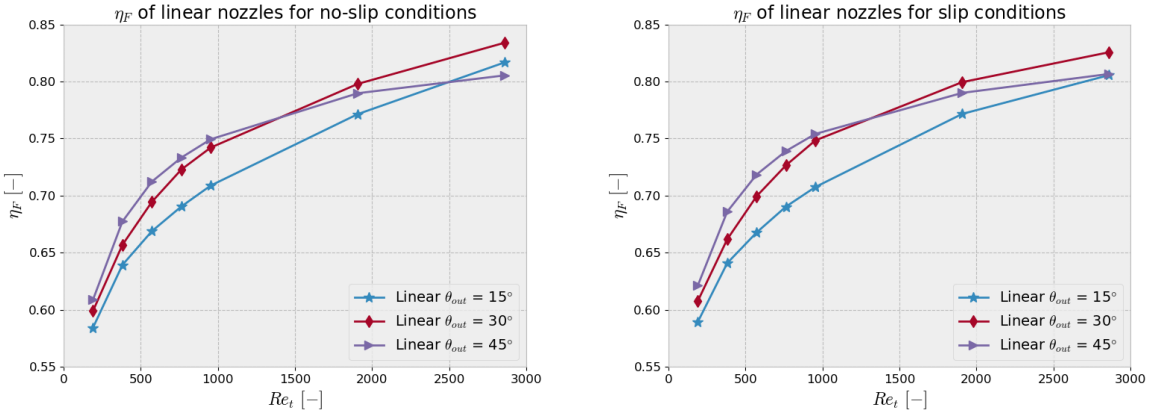

(a) No-slip conditions

(b) Slip conditions

Figure 4.4: Thrust efficiency of the linear nozzles for no-slip and slip conditions

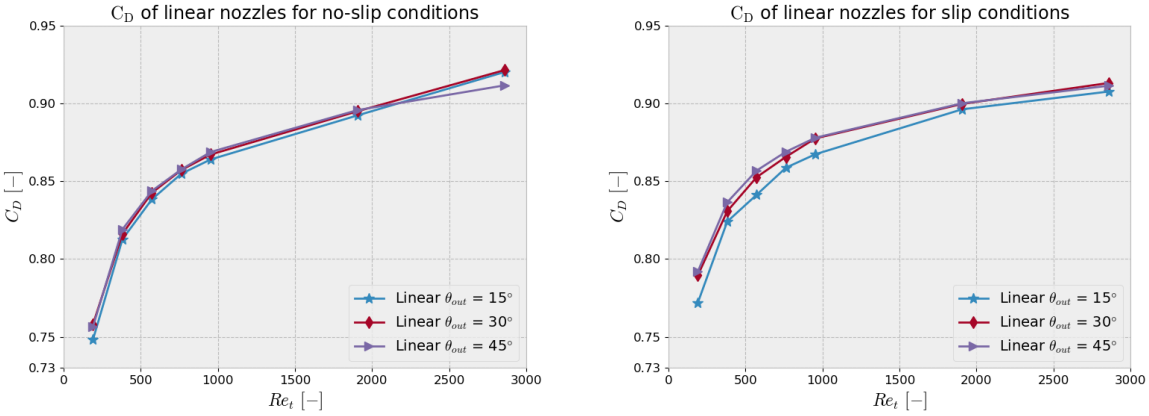

(a) No-slip conditions

(b) Slip conditions

Figure 4.5: Discharge coefficient of the linear nozzles for no-slip and slip conditions

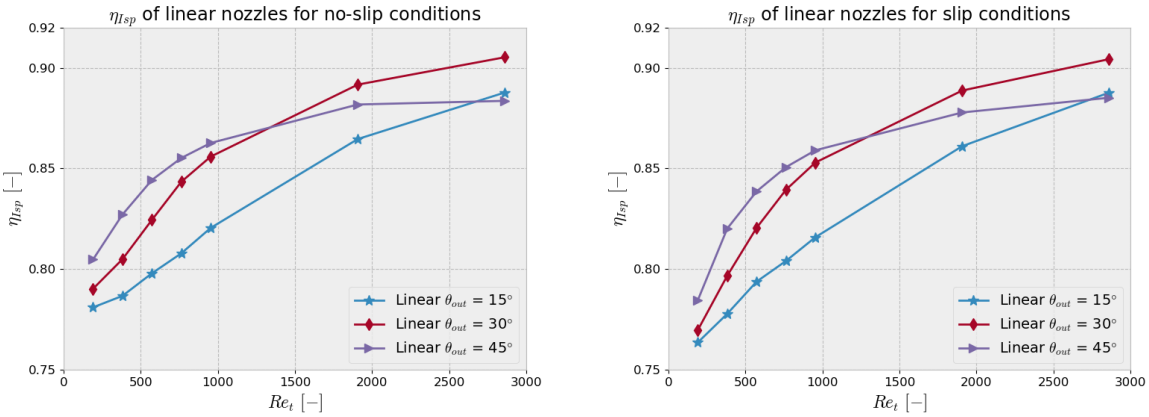

(a) No-slip conditions

(b) Slip conditions

Figure 4.6: Specific impulse efficiency of the linear nozzles for no-slip and slip conditions

From the graphs one can see that similar behavior to the literature can be observed, where a decrease in throat Reynolds numbers is accompanied by a decrease in performance. Furthermore, the characteristic collapse of performance can also be seen for Reynolds numbers below 1000.

The trend of this characteristic collapse is fairly similar in behavior for the various divergence angles. This is remarkable as the Mach contour plots indicated that, at low Reynolds numbers, the characteristics of the flow for the various angles are completely different. While the flow for the $\theta_{out} = 15°$ nozzle is almost completely subsonic, the $\theta_{out} = 30°$ and $\theta_{out} = 45°$ nozzles remain supersonic. Resulting from this one would expect a larger performance difference between the nozzles. The lack of this larger difference can partly be attributed to larger divergence losses encountered in the nozzles with larger divergence angles. Additionally, the $\theta_{out} = 15°$ nozzle has a higher pressure at the nozzle outlet due to the slower flow velocity. This higher pressure leads to a larger pressure thrust which partially compensates for the smaller momentum thrust. This combined effect explains why the difference between the various divergence angles is not larger with such different flow characteristics.

The contour plots indicated that higher divergence angles allow for better expansion of the flow when thicker boundary layers are present, e.g. at lower Reynolds numbers. These higher divergence angles come at the cost of increased divergence losses caused by a significant non-axial portion in the exiting flow. Based on this it is expected that nozzles with lower divergence angles will perform better at high Reynolds numbers and vice versa. This expectation is in line with the literature from [4, 10, 18, 22] where this behavior is observed.

The results for the thrust efficiency, which can be seen in Fig. 4.4, generally fall in line with the expectation, as at $Re_t < 1200$ the nozzle with $\theta_{out} = 45°$ is more efficient than the nozzles with smaller divergence half angles. For $Re_t > 1200$ the nozzle with $\theta_{out} = 45°$ starts outperforming the other linear nozzles.
Based on the minimal boundary layer thicknesses at high Reynolds numbers and the small divergence losses it was expected that the nozzle with $\theta_{out} = 15°$ would be the best performing linear nozzle at the higher Reynolds numbers. An expectation which was supported by the results presented by Bayt in [4]. However, the simulation results show a contrasting image where the $\theta_{out} = 15°$ nozzle has a worse thrust efficiency at all but one data point, where it still does not perform better than the nozzle with $\theta_{out} = 30°$.

A lower discharge coefficient could explain the lower than expected thrust efficiency. Looking at the results in Fig. 4.5 one can see that, in the slip cases, the $\theta_{out} = 15°$ nozzle does have a slightly lower discharge coefficient than the other two nozzles. On the other hand, in the no-slip cases the $\theta_{out} = 15°$ nozzle has near identical discharge coefficients to the other two nozzle. Following these observations one can conclude that the lower discharge coefficient in the slip cases could have contributed to the difference in thrust efficiency between the no-slip and slip cases for the $\theta_{out} = 15°$ nozzle. However, it could not have caused the overall sub-par performance of the $\theta_{out} = 15°$ nozzle, and can thus be ruled out as the underlying cause for this low performance.

This trend of under-performance continues for the specific impulse efficiency. Furthermore, at Reynolds numbers of 191, it can be observed that in the no-slip cases the rate of decrease in efficiency is reducing at lower Reynolds numbers. This is the opposite of the expected behavior based on past results from the literature, where an increase in the rate at which the efficiency decreases is observed [4, 8, 10, 18, 22, 33]. For the slip cases such tendencies cannot be observed, however, the rate at which the efficiency decreases is much larger for $\theta_{out} = 30°$ than for $\theta_{out} = 15°$. Extrapolating the results would lead to the $\theta_{out} = 15°$ nozzle outperforming the $\theta_{out} = 30°$ nozzle at $Re_t \approx 170$, the opposite of the expected outcome.

These peculiarities could have originated from various causes.
Firstly, the studies performed in [10, 18, 22] repeatedly used the same NASA GSFC linear nozzle geometry. This nozzle has an expansion ratio of 6.22 which is significantly smaller than the 16.971 which is used for the nozzles in this study. This smaller expansion ratio result in shorter nozzles for similar divergence half angles. The shorter nozzle will inherently have less surface area for the viscous boundary layer to grow on. With a thinner boundary layer the nozzle would immediately show increased efficiencies as one takes away a large portion of the viscous losses. However, as a result of the way nozzle efficiencies are defined in Eqs. (4.1) to (4.3), an increase in efficiency with a smaller expansion ratio will not lead to an absolute improvement in performance, as the 1D theoretical values for thrust and specific impulse are dependent on the expansion ratio. Thus, the smaller expansion ratio could be the possible cause of the low efficiency of the $\theta_{out} = 15°$ nozzle at high Reynolds numbers, while still providing better absolute performance.

The second possible cause for the peculiarities is the depth of the nozzles in the presented simulations. In [22] Louisos and Hitt presented results for nozzles with varying divergence half angles at $Re = 800$ for nozzle depths between 0-400 µm. It was shown that for these nozzle depths the nozzle with $\theta_{out} = 15°$ never performs the best and its performance will decrease the fastest with a decrease in nozzle depth. Despite the findings of Louisos and Hitt, the $\theta_{out} = 15°$ nozzle was still expected to perform the best in this study at higher Reynolds numbers ($Re_t > 1500$), which were not considered in the study of Louisos and Hitt, based on the results from Bayt.

Louisos and Hitt showed that the nozzle performance is dependent on the combination of nozzle depth and divergence angle which have shown interdependent behavior.
This interdependency is explained by the fact that the viscous boundary layer from the walls in the etch direction merge with the nozzle profile walls leading to an increased boundary layer thickness in the corners. The absolute increase in subsonic area on any given nozzle cross-section, assuming equal boundary layer thickness, is similar independent of nozzle depth. However, as the nozzle becomes more shallow the fraction of the nozzle cross-section that is occupied by this corner merging increases. Thus, a more shallow nozzle will amplify the impact of the corner merging. Similar phenomena were already hypothesized by Bayt, who found that based on the aspect ratio of an arbitrary nozzle cross-section the effective area for expansion can change, due to boundary layer growth [4].
Additionally, a small divergence angle further amplifies the impact of the corner boundary layer merging. This is due to the fact, that for any given nozzle area expansion ratio, the nozzles with smaller divergence angle will have to be longer, leading to a more surface area preceding the cross-section of said expansion ratio. This surface area will allow for the boundary layers to grow thicker in nozzles with smaller divergence angles. Resulting from the fact that the boundary layers that merge in the corner are already thicker, the thickness increase caused by the merging will also be of larger magnitude for nozzles with small divergence angles.
Based, on this it would be expected that the percentage of the flow that is subsonic, of a nozzle cross-section correlating to a specific area ratio, would increase with a decrease in nozzle divergence angle.

This expectation is confirmed by the numerical results presented in Fig. 4.7. In this figure cross-sections at 25, 50, 75, and 100% of the nozzle length together with the percentage of the area that is occupied by subsonic flow for the linear nozzles are shown for $Re_t = 191$. Only the subsonic area are visualized with supersonic areas being transparent.

From the figure one can observe that due to the shallow nature of the nozzles in this research the thicker boundary layer in the corner merges with the thick boundary layer in the nearest neighboring corner. This results in the pronounced thicker boundary layer on the top and bottom wall com-

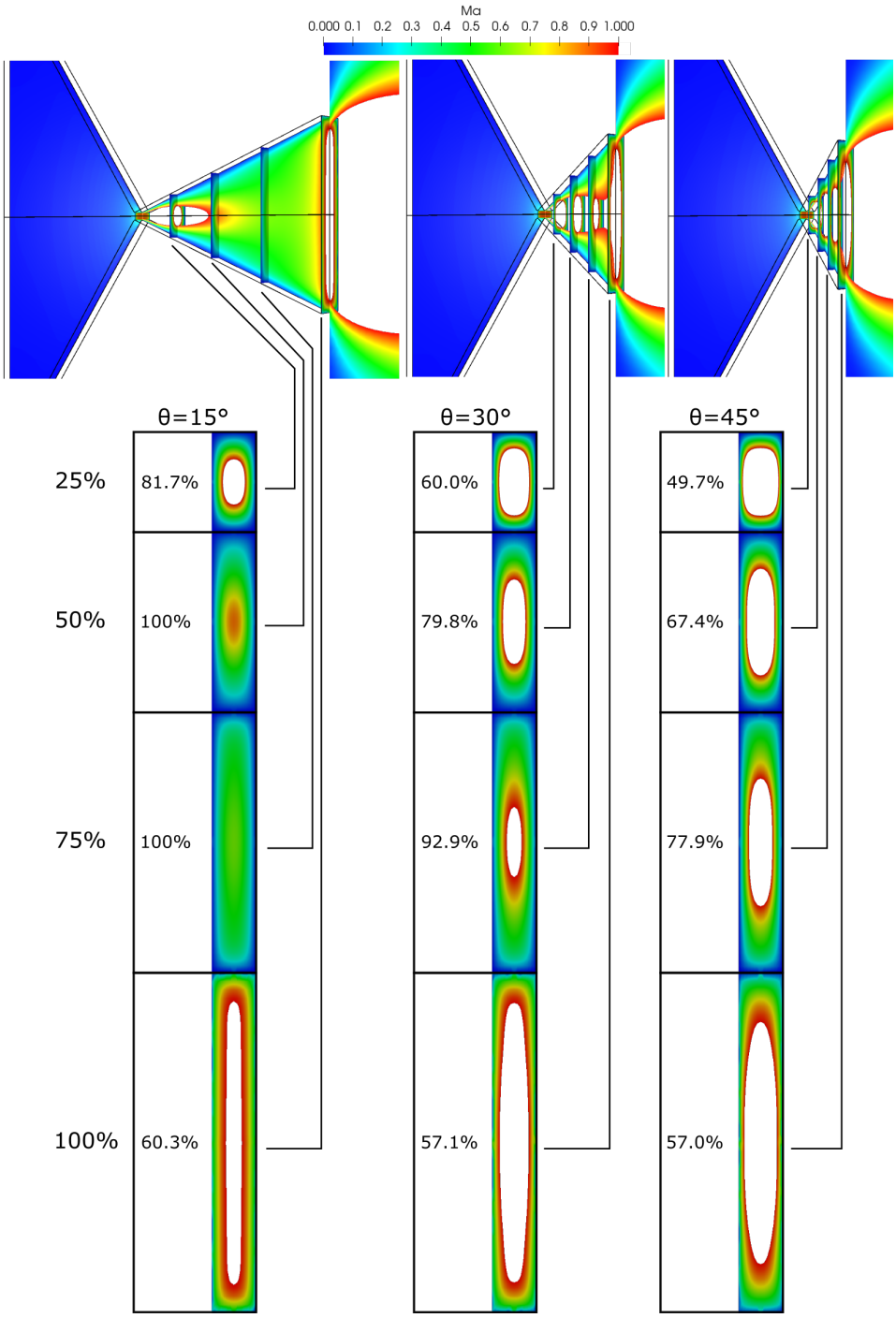

Figure 4.7: Boundary layer fraction of linear nozzles at $Re_t = 191$

pared to the side walls. Thus, this further increase in boundary layer thickness completely alters the effective nozzle profile raising the need of the higher divergence angles. This effect of nozzle depth on the optimal divergence angle is the interdependency for which indications were found in [22]. Through this effect the underperformance of the linear nozzle with $\theta_{out} = 15°$ can be explained. If the micronozzle would be sufficiently deep enough it is plausible that the nozzle with $\theta_{out} = 15°$ starts outperforming the other linear nozzles at high Reynolds numbers.

Additionally, a noteworthy observation from Fig. 4.7 is that the area occupied by the boundary layer,

at the exit plane, does not significantly decrease for divergence angles higher than 30°. This could indicate that for this nozzle depth, further increases in the divergence angle do not increase the area of supersonic flow. Further investigation into the exact interdependence of the nozzle depth, divergence angle and boundary layer should be performed to fully characterize the phenomenon.

These causes would together be able to explain the unexpected under-performance of the $\theta_{out} = 15°$ nozzle at high Reynolds number, but not the peculiarities observed at low Reynolds numbers. These are likely the result from the selection of the La Torre validity bounds for the continuum model in Section 3.1. The La Torre validity bounds state that, for the continuum models to remain valid with the application of slip boundary conditions, the throat Knudsen number cannot exceed 0.01. These validity bounds were tested a-priori, using the Reynolds number calculated with the 1D isentropic flow relations to calculate the Knudsen number. As the throat Reynolds number in the simulations deviates from 1D calculations, so will the Knudsen number.

The throat Knudsen numbers calculated, using the simulation results, of the linear nozzles can be found in Table 4.2. From this table it becomes clear that the simulated Knudsen number is consistently higher than that predicted using the 1D isentropic relations. Furthermore, with the Knudsen number from the simulations one can notice that the cases with $Re_t = 191$ are violating the validity threshold as imposed by La Torre. As a result one should treat the results at $Re_t = 191$ with suspicion and significant inaccuracies can be expected. Quantifying the inaccuracies should be done by running the same situation using DSMC, as it is able to produce accurate results for this range of Knudsen numbers. However, running such a simulation is beyond the scope of this research.

Table 4.2: Knudsen number in the throat for all simulated cases using the linear nozzle

Re_t	Kn 1D	Kn $\theta_{out} = 15°$		Kn $\theta_{out} = 30°$		Kn $\theta_{out} = 45°$	
		no-slip	slip	no-slip	slip	no-slip	slip
191	$7.78 \cdot 10^{-3}$	$1.10 \cdot 10^{-2}$	$1.12 \cdot 10^{-2}$	$1.10 \cdot 10^{-2}$	$1.11 \cdot 10^{-2}$	$1.13 \cdot 10^{-2}$	$1.15 \cdot 10^{-2}$
382	$3.89 \cdot 10^{-3}$	$5.56 \cdot 10^{-3}$	$5.60 \cdot 10^{-3}$	$5.48 \cdot 10^{-3}$	$5.51 \cdot 10^{-3}$	$5.63 \cdot 10^{-3}$	$5.66 \cdot 10^{-3}$
572	$2.59 \cdot 10^{-3}$	$3.72 \cdot 10^{-3}$	$3.73 \cdot 10^{-3}$	$3.65 \cdot 10^{-3}$	$3.66 \cdot 10^{-3}$	$3.75 \cdot 10^{-3}$	$3.76 \cdot 10^{-3}$
763	$1.94 \cdot 10^{-3}$	$2.79 \cdot 10^{-3}$	$2.80 \cdot 10^{-3}$	$2.73 \cdot 10^{-3}$	$2.74 \cdot 10^{-3}$	$2.81 \cdot 10^{-3}$	$2.81 \cdot 10^{-3}$
953	$1.55 \cdot 10^{-3}$	$2.23 \cdot 10^{-3}$	$2.24 \cdot 10^{-3}$	$2.18 \cdot 10^{-3}$	$2.18 \cdot 10^{-3}$	$2.24 \cdot 10^{-3}$	$2.24 \cdot 10^{-3}$
1908	$7.77 \cdot 10^{-4}$	$1.11 \cdot 10^{-3}$	$1.11 \cdot 10^{-3}$	$1.17 \cdot 10^{-3}$	$1.23 \cdot 10^{-3}$	$1.11 \cdot 10^{-3}$	$1.11 \cdot 10^{-3}$
2861	$5.18 \cdot 10^{-4}$	$7.28 \cdot 10^{-4}$	$7.37 \cdot 10^{-4}$	$7.12 \cdot 10^{-4}$	$9.30 \cdot 10^{-4}$	$7.17 \cdot 10^{-4}$	$7.38 \cdot 10^{-4}$

Furthermore, it is also plausible that the validity threshhold of La Torre is too lenient allowing continuum simulations to take place in a flow that is far too rarefied. In Figs. 4.8 to 4.10 one can see the Knudsen contours for the linear nozzles for the three divergence half angles at the two extremes of the investigated Reynolds number range. While for the majority of the cases the La Torre validity criterium is satisfied, from these figures one can observe that the threshold value as suggested by Liu et al. ($Kn_{local} < 0.045$) in [42] is not even satisfied for the highest Reynolds number, and the threshold recommended by Xie ($Kn_{avg} < 0.01$) in [43] is only satisfied in the $Re_t = 2861$ cases. Furthermore, comparing the maximum encountered Knudsen number in the $Re_t = 191$ cases with the literature it can be seen that a maximum Knudsen number between 0.65 and 1.5 at the nozzle lip is high. This leads to the conclusion that it is likely that the results of the cases ran with $Re_t = 191$ are deviating from the realistic values. The high Knudsen number in these simulations is the result of fixing the ambient pressure to 30 Pa, compared to the 1000 Pa applied in the literature. This 1000 Pa ambient pressure is normally selected to ensure that the ambient flow always remains in the continuum regime with at most minor rarefaction effects. In this study the decision was made to fix the ambient pressure at 30 Pa as this would be representable of the pressure inside the vacuum chamber during experimental testing of the nozzles. Furthermore, it was expected that due to the

selection of this low ambient pressure the nozzle plume would be highly rarefied and the numerical results of it would be unusable. However, as the plume was of lesser interest compared to the flow properties at the nozzle exit it was deemed that a more accurate representation of the results at the exit would warrant the lower ambient pressure.

Based on this Knudsen number analysis it can be said that future use of the results presented in this chapter should mainly focus on the results as generated with the slip flow boundary conditions. This recommendation is made as the difference between the results for slip and no-slip are negligible at the upper limit of investigated Reynolds numbers in this study. Additionally for the lower Reynolds numbers it is highly likely that rarefaction effects are abundantly present and thus slip boundary conditions give a better representation of the flow. Therefore, future numerical comparisons of performance will be based on the results acquired from the slip cases.

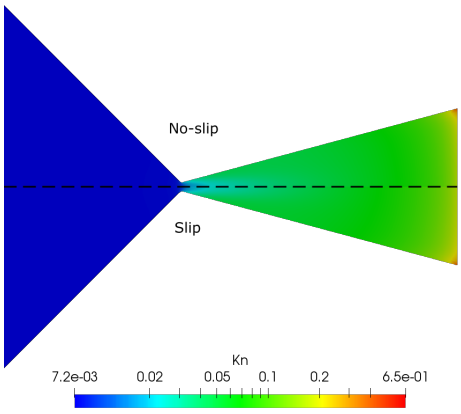

(a) $Re_t = 191$

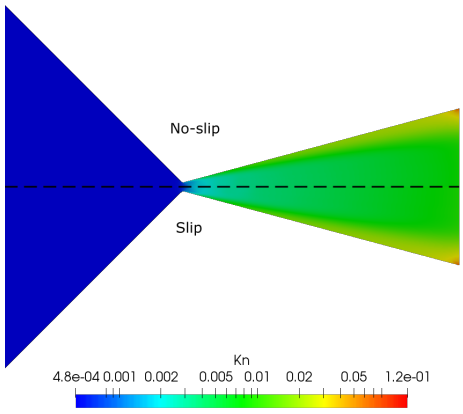

(b) $Re_t = 2861$

Figure 4.8: Knudsen contours of the linear nozzle with $\theta_{out} = 15°$ for $Re_t = 191$ and $Re_t = 2861$

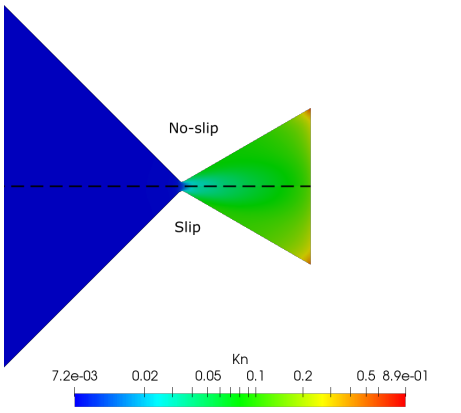

(a) $Re_t = 191$

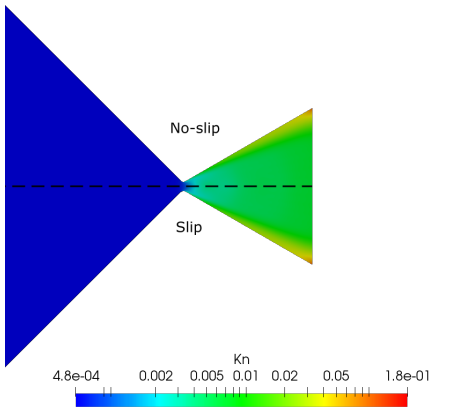

(b) $Re_t = 2861$

Figure 4.9: Knudsen contours of the linear nozzle with $\theta_{out} = 30°$ for $Re_t = 191$ and $Re_t = 2861$

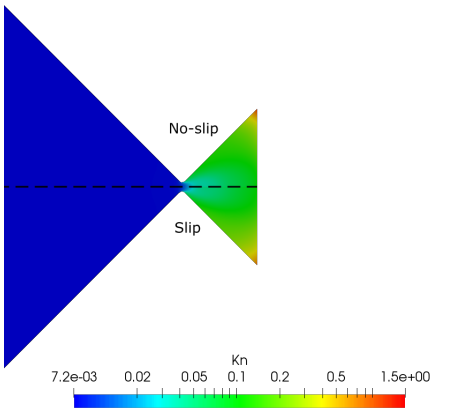

(a) $Re_t = 191$

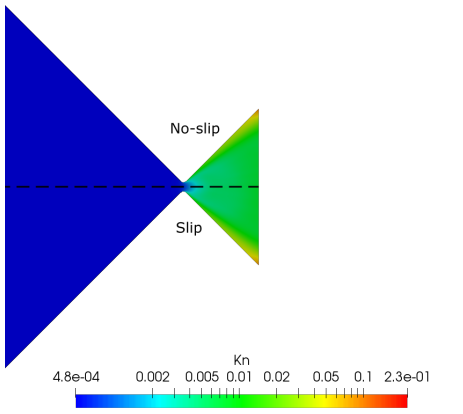

(b) $Re_t = 2861$

Figure 4.10: Knudsen contours of the linear nozzle with $\theta_{out} = 45°$ for $Re_t = 191$ and $Re_t = 2861$

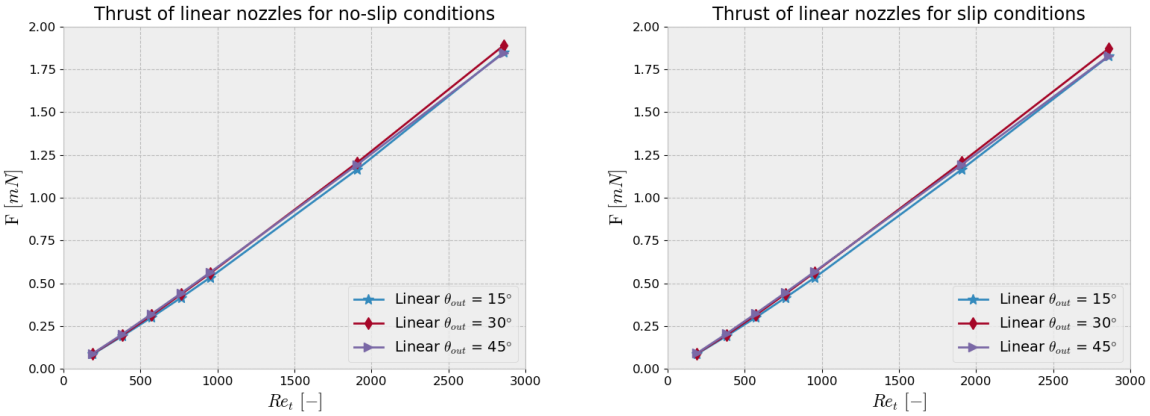

(a) No-slip conditions (b) Slip conditions

Figure 4.11: Thrust of the linear nozzles for no-slip and slip conditions

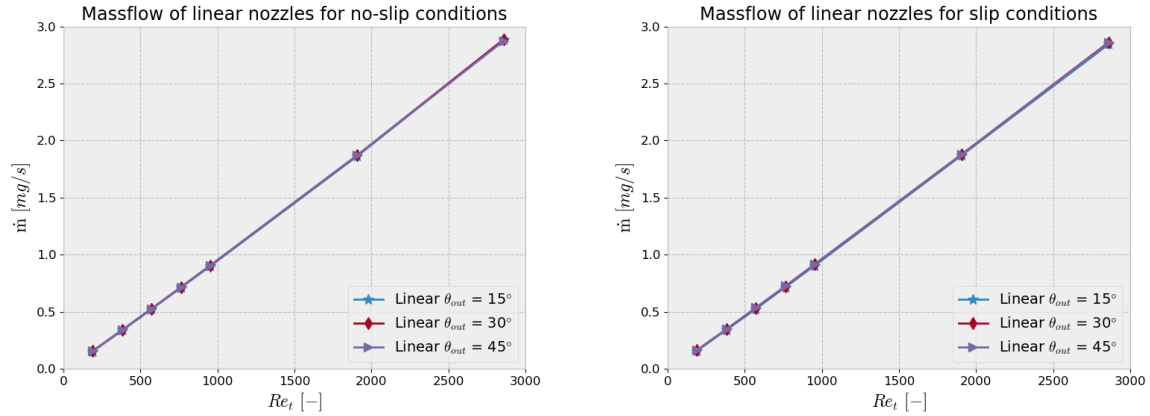

(a) No-slip conditions (b) Slip conditions

Figure 4.12: Massflow of the linear nozzles for no-slip and slip conditions

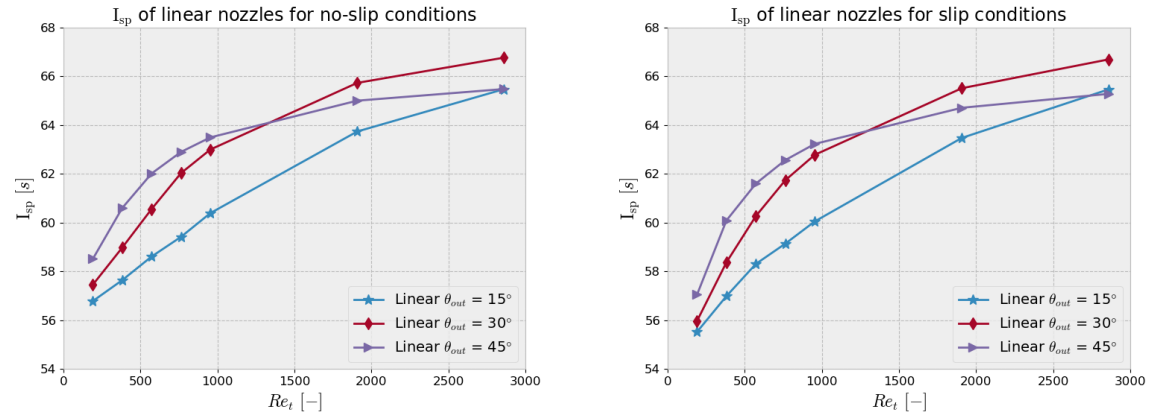

(a) No-slip conditions (b) Slip conditions

Figure 4.13: Specific impulse of the linear nozzles for no-slip and slip conditions

Within this study the various nozzles are being compared to each other using the performance metrics. This is a valid approach as the characteristic dimensions do not change between the nozzles and as such they will have the same ideal performance. However, for comparison to outside literature sources it is advantageous to look at the absolute performance. As such, to complete the picture of the nozzle performance, Figs. 4.11 to 4.13 present the absolute performance of the linear nozzles. In these figures it can be seen that over the full range of Reynolds the difference in absolute thrust between the nozzles, compared to the differences in thrust efficiency observed in Fig. 4.4, appears to be minimal. This can be explained by the large range of the y-axis in the plot which makes the differences in thrust appear much smaller. Most of the other noteworthy observations have already been made based on Figs. 4.4 to 4.6 and will not be repeated here. A more accurate overview of the performance numbers is provided in the tables of Appendix B.

4.2.2. Aerospike nozzle results

On the next page, in Fig. 4.14, one can see Mach number contour plots for the 60% truncated aerospike nozzle over the full range of throat Reynolds number investigated. In these contour plots the upper half represents the results using the no-slip boundary conditions and the lower half the slip boundary conditions. Furthermore, in the plots the solid black line indicates the $M = 1$ contour.

The contour plots for the 40% and 20% truncated aerospike nozzles are found in Fig. 4.15 and Fig. 4.16 respectively. Here only the results for $Re_t = 2861$ and $Re_t = 191$ are presented for legibility, for the results over the full range of Reynolds numbers see Appendix A

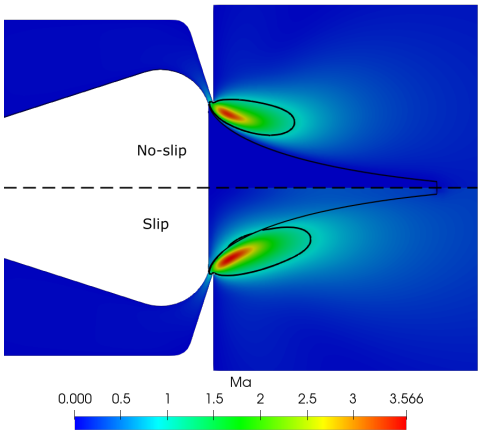

(a) $Re_t = 191$

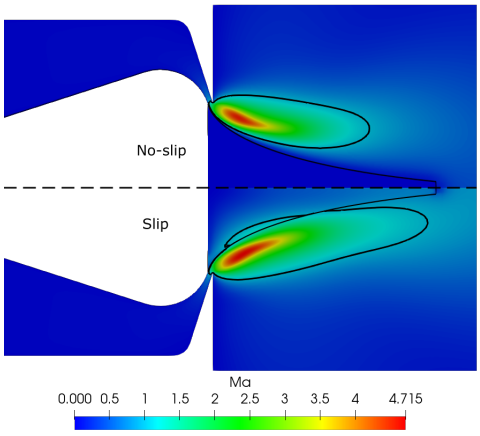

(b) $Re_t = 382$

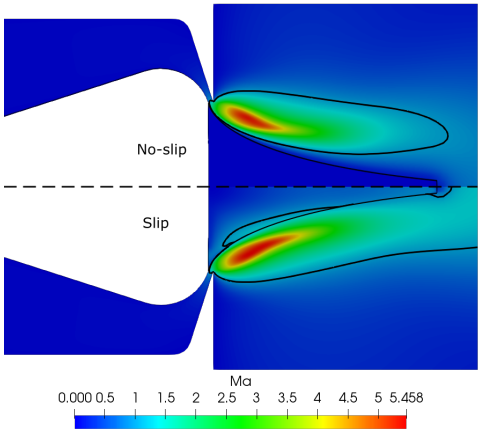

(c) $Re_t = 572$

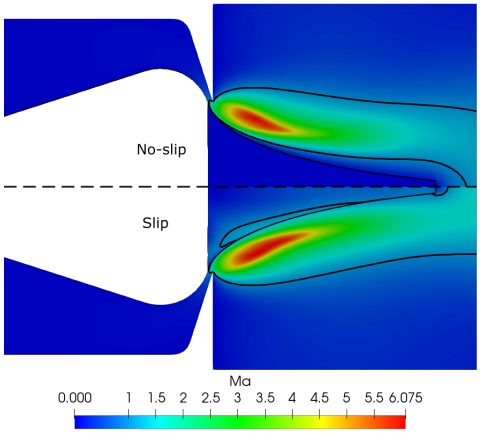

(d) $Re_t = 763$

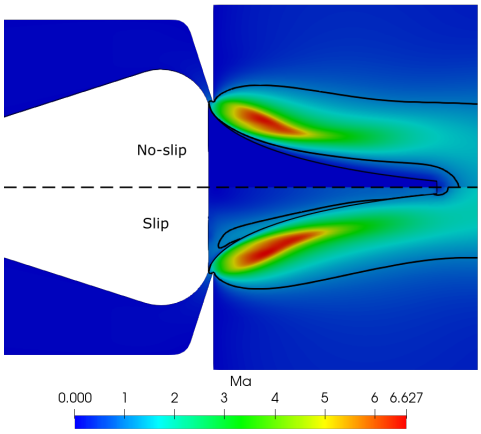

(e) $Re_t = 953$

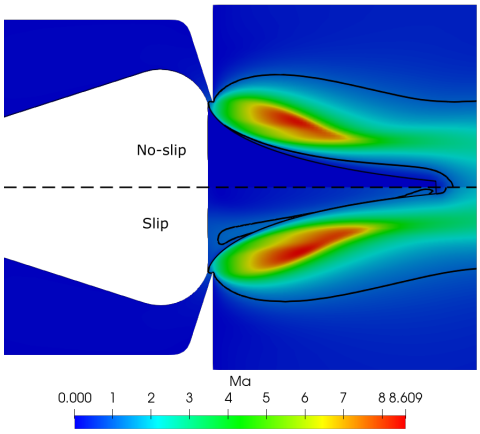

(f) $Re_t = 1908$

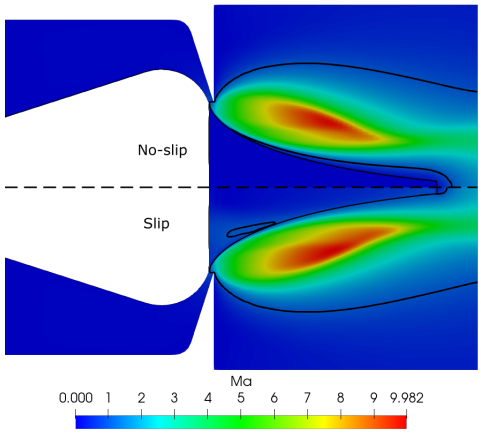

(g) $Re_t = 2861$

Figure 4.14: Mach contours of the 60% truncated aerospike nozzle for $Re_t = 191 - 2861$

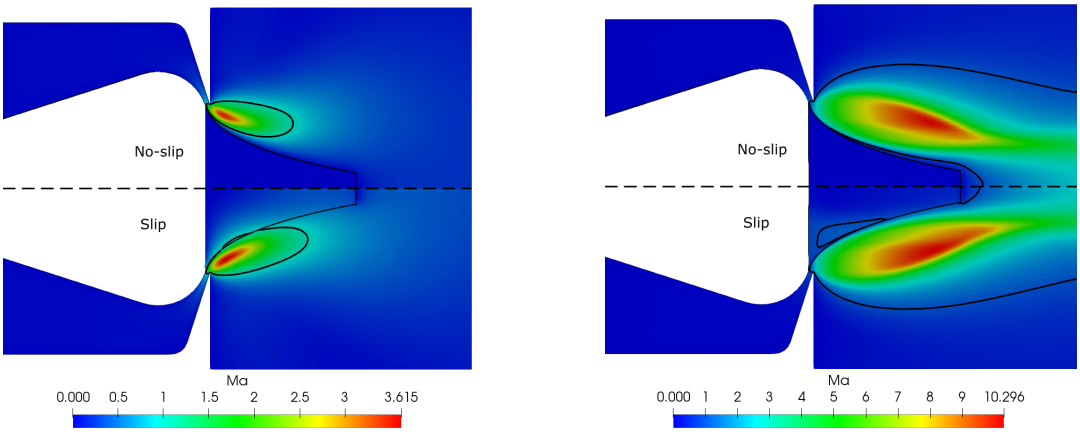

(a) $Re_t = 191$ (b) $Re_t = 2861$

Figure 4.15: Mach contours of the 40% truncated aerospike nozzle for $Re_t = 191$ and $Re_t = 2861$

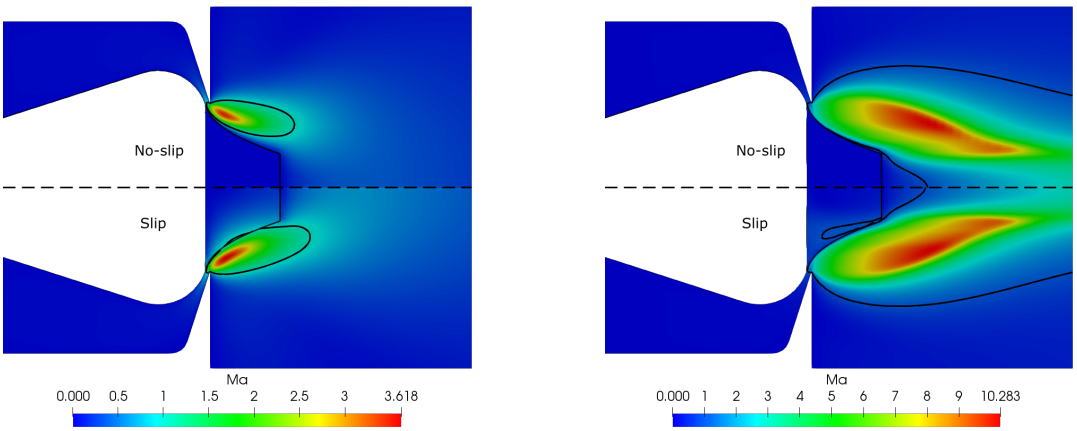

(a) $Re_t = 191$ (b) $Re_t = 2861$

Figure 4.16: Mach contours of the 20% truncated aerospike nozzle for $Re_t = 191$ and $Re_t = 2861$

From the figures one can observe that, similar to the linear nozzles, the cases using slip boundary conditions have a larger supersonic region, this is especially visible in Figs. 4.14b and 4.14c. Furthermore, it can be seen that a thick viscous boundary layer is present, which causes the supersonic flow to follow an effective spike contour that deviates from the optimal angelino contour. This is especially visible in the no-slip cases near the tip of the spike body, where the boundary layer can be as thick as the aerospike is wide.

Comparing the Mach contour plots of the various truncations for $Re_t = 2861$, an interesting observation can be made. At the end of the spike for the 20% truncated nozzle the flow expands into the location where the spike would have been. In contrast the flow of the less truncated nozzles expand away from the spike tip. Comparing the behavior of the 20% truncated nozzle to the Schlieren images presented in [66] it can be seen that this inward expansion behavior can also be found for macro aerospikes of various truncations. It is hypothesized that the absence of the inward expansion, in the less truncated nozzles, is due to the presence of a much thicker boundary layer. This thicker boundary layer forms a barrier, by means of a region of higher pressure.

Furthermore, one can compare the flowfields presented in this study with the theoretical flowfield that is expected for a macro aerospike. This theoretical flowfield is vizualized in Fig. 4.17. The Mach contour plots clearly show the presence of the envelope shock and the jet boundary. The inner shear layer is also clearly visible in the contour plots of the 20% and 40% truncated nozzles. For the 60% truncated nozzle the shear layer is also present but is harder to distinguish as a large part

falls outside the imaging area. The trailing shock is not visible in the images and also if one extends the image area it is difficult to identify this trailing shock wave. From this overall agreement in the flowfields one can conclude that the micro aerospike are much more similar to their macro scale counterparts, this cannot be said for the linear nozzles. This closer similarity could indicate a flow which is much less dominated by viscous forces, as was hypothesized, which could result in higher nozzle efficiencies, that are characteristic for macro nozzles.

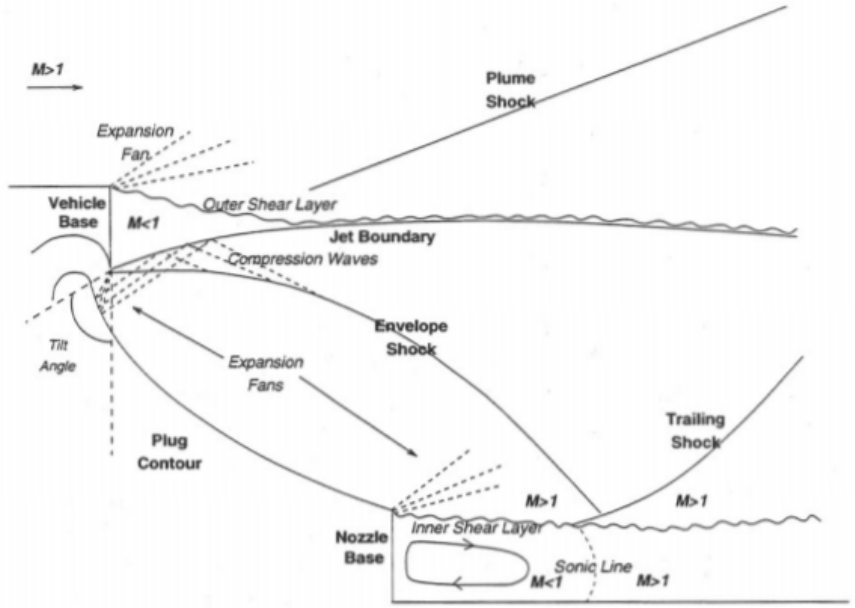

Figure 4.17: Theoretical flow field of a truncated aerospike nozzle with co-flow [67]

Lastly, in all of the slip cases one can see the $M = 1$ contour line behind the spike center body. Resulting from the fact that downstream of the throat the flow is not bounded by a wall in the etch direction, it can expand in this direction. This expansion leads to a portion of the flow to expand past and over the edge of the center body. Any flow that expands over the edge of the aerospike can essentially be seen as lost performance as it is not able to exert any force on the spike body in the axial direction.

From the flow fields as calculated the various performance metrics can be calculated and plotted. The resulting plots for $\eta_F, C_D,$ and, $\eta_{I_{sp}}$ can be seen in Figs. 4.18 to 4.20 respectively.

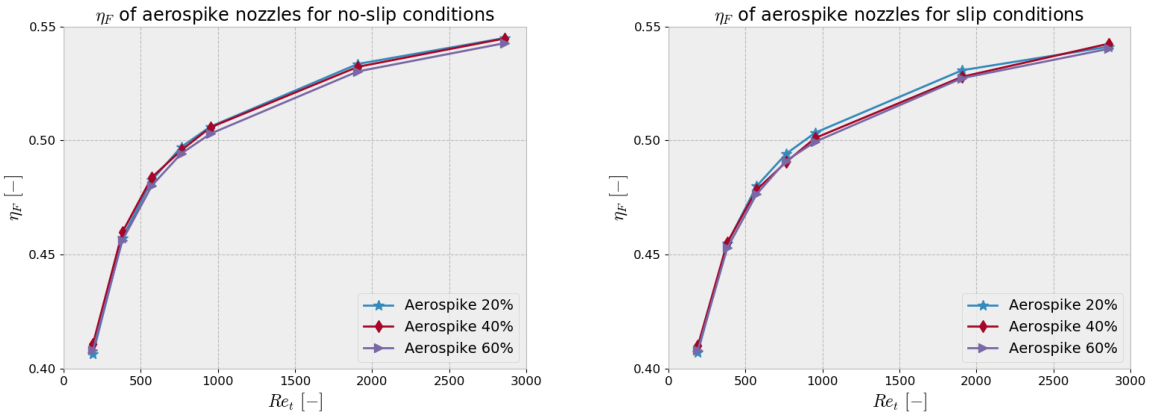

(a) No-slip conditions

(b) Slip conditions

Figure 4.18: Thrust efficiency of the aerospike nozzles for no-slip and slip conditions

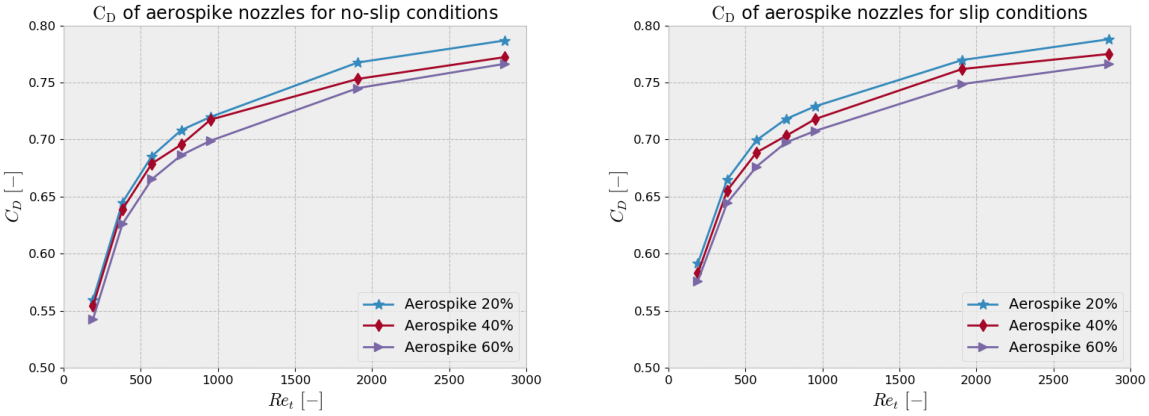

(a) No-slip conditions

(b) Slip conditions

Figure 4.19: Discharge coefficient of the aerospike nozzles for no-slip and slip conditions

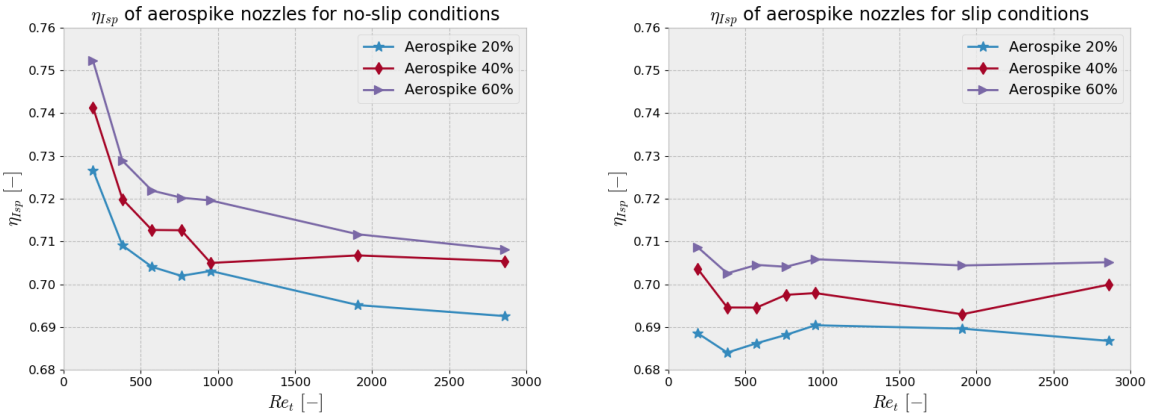

(a) No-slip conditions

(b) Slip conditions

Figure 4.20: Specific impulse efficiency of the aerospike nozzles for no-slip and slip conditions

From the results in Fig. 4.18 one can see that the thrust efficiency seems to be independent of the aerospike truncation. This is a well known phenomenon seen on macro aerospikes where the majority of the thrust is generated in the first 25% of the spike [68]. This can be explained by the higher pressures and larger axial component of normal vector **n** near the base of the aerospike center body. This results in the pressure thrust generated near the base of the center body being orders of magnitude larger than that at the tip.

In the case of the simulated micro aerospikes this demeanor can be can be observed in Fig. 4.21. Here the pressure distribution is shown over the center body of the 20% and 60% truncated nozzle at $Re_t = 2861$. From these figures it can be seen that the pressure near the tip is orders of magnitude smaller, and thus such heavily truncated center bodies will still be able to generate near to the same center body thrust.

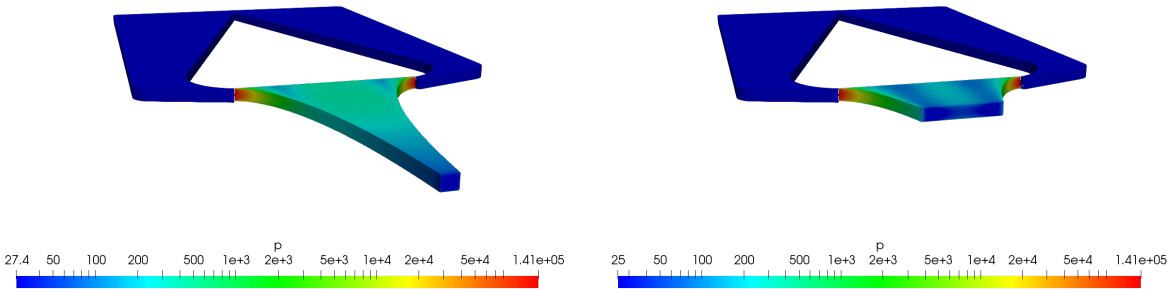

(a) 60% truncated (b) 20% truncated

Figure 4.21: Center body pressure distribution of 20% and 60% truncated aerospike at $Re_t = 2861$

Additionally, from Fig. 4.18 one can also notice that the thrust efficiency of the aerospike nozzles is significantly lower than that of the linear nozzles, with linear nozzles having between 21.1% and 28.3% higher thrust efficiency. This results in an average lower performance, over the entire range of investigated Reynolds numbers, of 24.7% when comparing the best aerospike nozzzle with the best linear nozzle in slip conditions. This lower performance contradicts all past studies performed. In [9] Zilic et al. performed a 2D numerical study on micro aerospikes for $Re_t = 50 - 625$. Here a thrust per unit depth for a 40% truncated aerospike of 24.2 µN was found at $Re_t = 625$. As the throat area considered by Zilic is twice as large, one can safely assume that this predicted thrust should be halved to be comparable. However, even when halved the 12.1 µN is still significantly higher than the 5.98 µN of thrust per unit depth found for the 40% truncated nozzle, at similar Reynolds number, in this study. This indicates that due to the 3D nature of the simulations some form of losses occur that significantly reduce the nozzle performance.

Looking at the discharge coefficient in Fig. 4.19 one can see that there is a trend that more truncated nozzles have a higher discharge coefficient. A possible explanation for this can be that less truncated nozzles have more surface area for a boundary layer to grow on. Leading to an effective spike contour which deviates further from the Angelino contour and as such restricts the optimal flow expansion and thus massflow.

Furthermore, comparing the results for the discharge coefficient with those from the linear nozzles shows a discharge coefficient which is between 12.5% and 20.0% lower for the aerospike nozzles. This results in a lower performance on average of 15.5%, when one compares the best aerospike nozzle to the best performing linear nozzle. This is a logical result from the usage of a dual throat which leads to a higher throat perimeter to throat area ratio, assuming equal aspect ratio and total

throat area. Subsequently, the ratio of boundary layer to core flow is larger which results in the lower discharge coefficients observed.

As a result from the truncation independent thrust efficiency, combined with the higher discharge coefficient for more truncated nozzles, it arises that nozzles that are less truncated will have a higher specific impulse efficiency. This is exactly what can be seen in Fig. 4.20, and is in line with the results as presented by Zilic in [9]. However, the specific impulse efficiency is still 14.4% lower on average compared to the best performing linear nozzle.

In Fig. 4.20 there are indications that the specific impulse efficiency would increase with a decreasing Reynolds number. This in contradiction with most of the published numerical micronozzle research, only Zilic [9] reports slightly comparable behavior. Similarly to the linear nozzles this behavior can be explained by extremely high Knudsen numbers. In Figs. 4.22 to 4.24 one can see the contour plots for the Knudsen number of the aerospike nozzles. One can observe that the regions of supersonic flow are still within acceptable limits for the Knudsen number. However, especially at the tip of the center body there is a region where the Knudsen number can locally exceed values far beyond 10. With Knudsen numbers exceeding the threshold value for free molecular flow one can assume that locally the simulation results are inaccurate. However, as the regions most critical for the simulation of the thrust, massflow, and specific impulse of the aerospikes are within acceptable Knudsen numbers, and the flow field results are in line with past numerical efforts in the literature, one can assume that the results are still quantitatively useful but that there will be minor discrepancies with respect to reality. To quantify the inaccuracies a full scale DSMC simulation would have to be done which is beyond the scope of this study.
Furthermore, similar to the linear nozzle simulations the validity threshold of La Torre is not satisfied in the cases of $Re_t = 191$ and therefore these cases have to be treated with additional scrutiny.

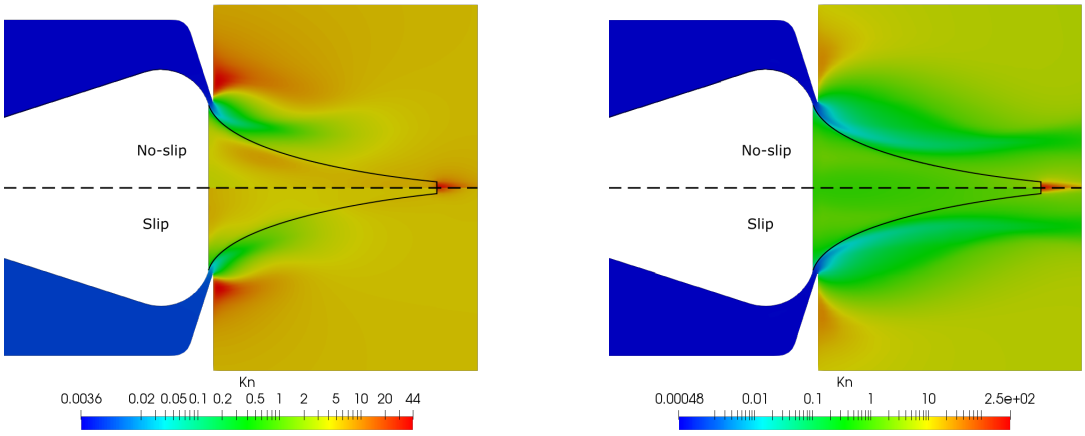

(a) $Re_t = 191$ (b) $Re_t = 2861$

Figure 4.22: Knudsen contours of the 60% truncated aerospike nozzle for $Re_t = 191$ and $Re_t = 2861$

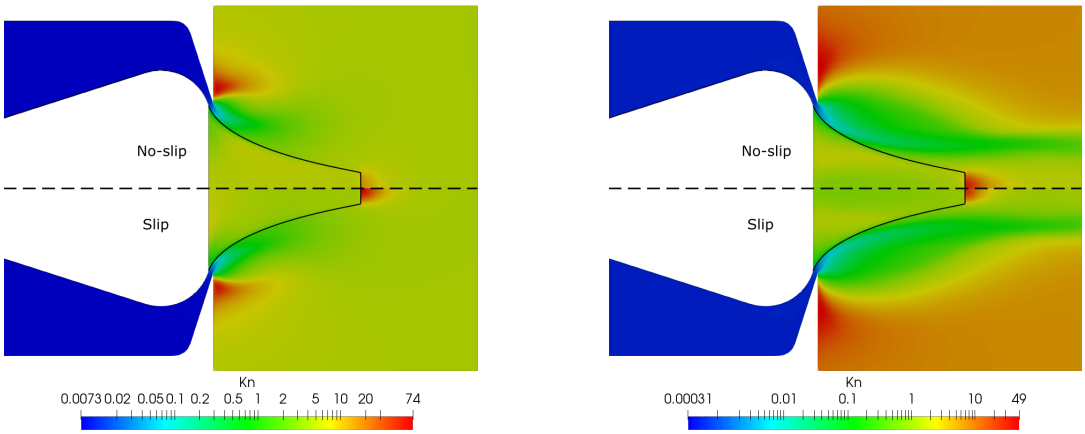

(a) $Re_t = 191$ (b) $Re_t = 2861$

Figure 4.23: Knudsen contours of the 40% truncated aerospike nozzle for $Re_t = 191$ and $Re_t = 2861$

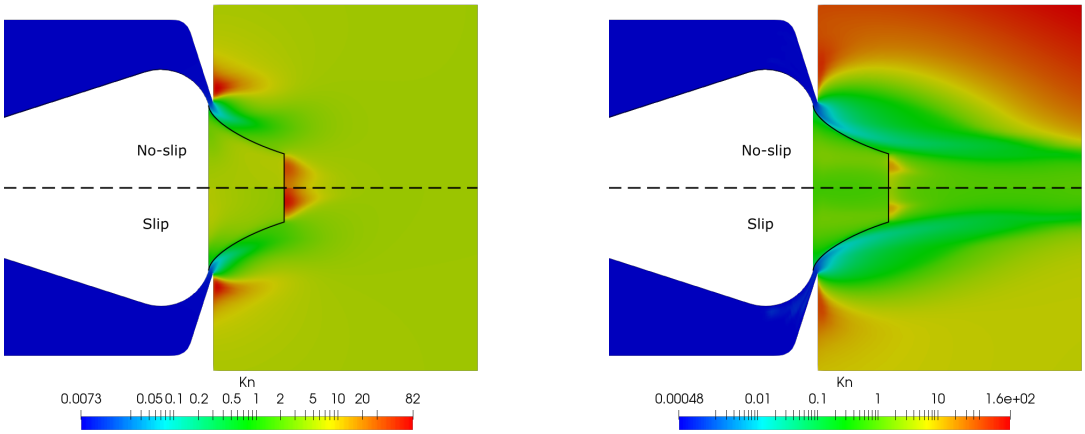

(a) $Re_t = 191$ (b) $Re_t = 2861$

Figure 4.24: Knudsen contours of the 20% truncated aerospike nozzle for $Re_t = 191$ and $Re_t = 2861$

Overall these results indicate that aerospike nozzles would provide significantly lower performance than their respective linear nozzle counterparts, which is not in line with past results from [7–10]. The meager performance of the aerospikes in this study can mainly be attributed to excessive losses by the over edge expansion of the flow. The first indications of these losses were seen in the contour plots for the slip cases. Moreover, in Figs. 4.25 and 4.26 $M = 1$ isovolume plots of the aerospike nozzles are presented which illustrates the magnitude of the flow which expands over the edge.

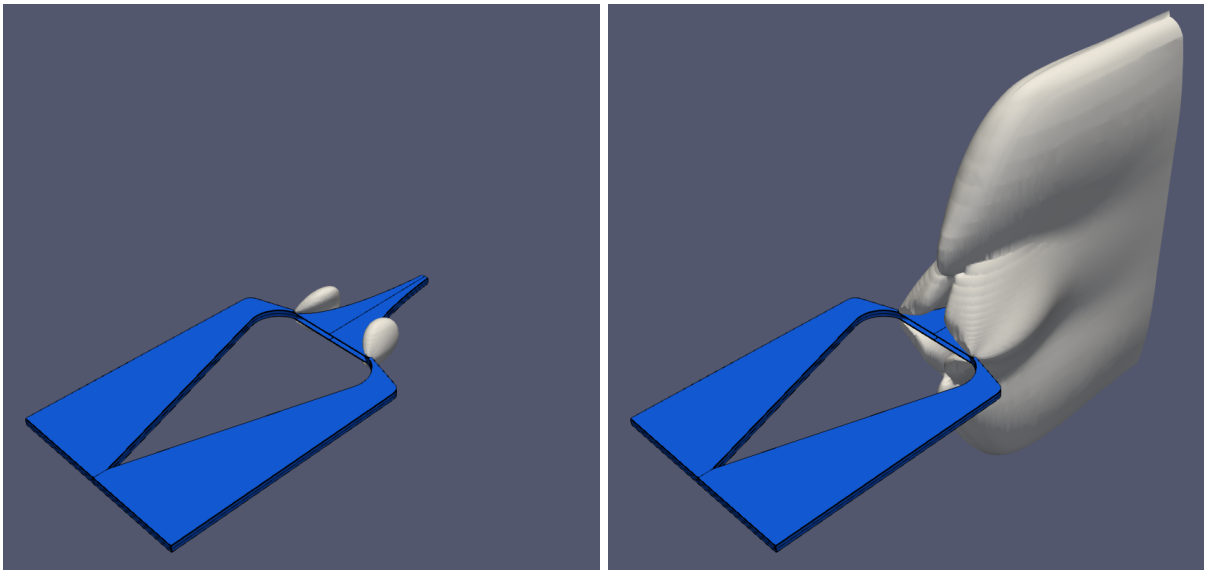

(a) $Re_t = 191$ (b) $Re_t = 2861$

Figure 4.25: Mach 1 isovolume plot for 60% truncated aerospike at $Re_t = 191$ and $Re_t = 2861$

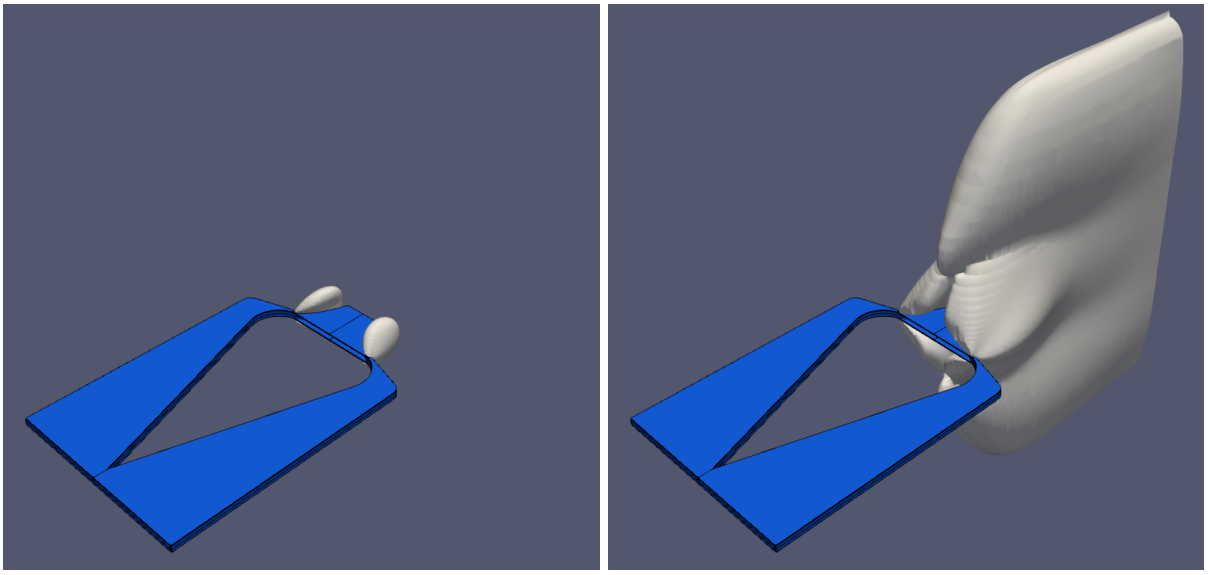

(a) $Re_t = 191$ (b) $Re_t = 2861$

Figure 4.26: Mach 1 isovolume plot for 20% truncated aerospike at $Re_t = 191$ and $Re_t = 2861$

This specific loss can be quantified by Eq. (4.11) which calculates the percentage of the thrust which is not in the desired axial direction. It is calculated based on the simulation results of just a quarter of the nozzle, as the off-axis thrust compensates itself with an equal but opposite oriented thrust in the other quarters. The results for L_{align} of both the linear and aerospike nozzle can be found

in Fig. 4.27. In these graphs it can be seen that the aerospike nozzles generate between 17 and 20 percent of the thrust of-axis, which explains the meager performance of the aerospike nozzles. Another possible cause for reduced performance is the suboptimal effective spike contour due to the presence of the thick boundary layer.

$$L_{align} = (1 - \frac{F_{axial}}{\|\boldsymbol{F}\|} * 100) \tag{4.11}$$

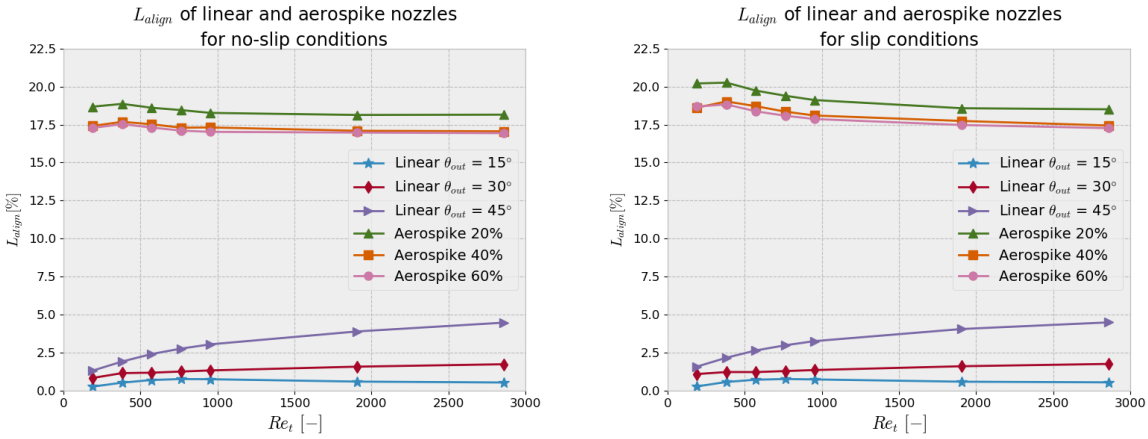

(a) No-slip conditions

(b) Slip conditions

Figure 4.27: Of-axis thrust fraction of the linear and aerospike nozzles for no-slip and slip conditions

Similar to the linear nozzles the absolute performance figures of the aerospike nozzles are provided below in Figs. 4.28 to 4.30 for completeness. Here the same behavior as in Figs. 4.18 to 4.20 can be seen. Lastly, exact performance numbers of these nozzles can be found in Appendix B.

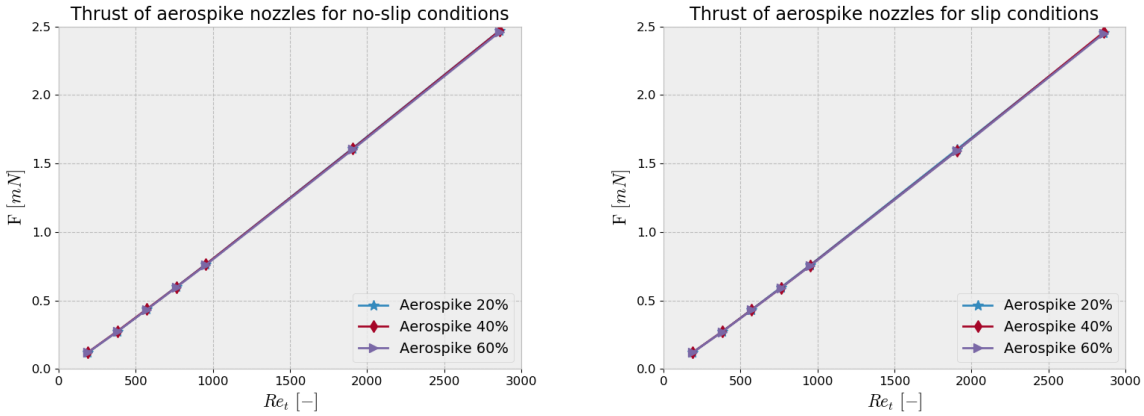

(a) No-slip conditions

(b) Slip conditions

Figure 4.28: Thrust of the aerospike nozzles for no-slip and slip conditions

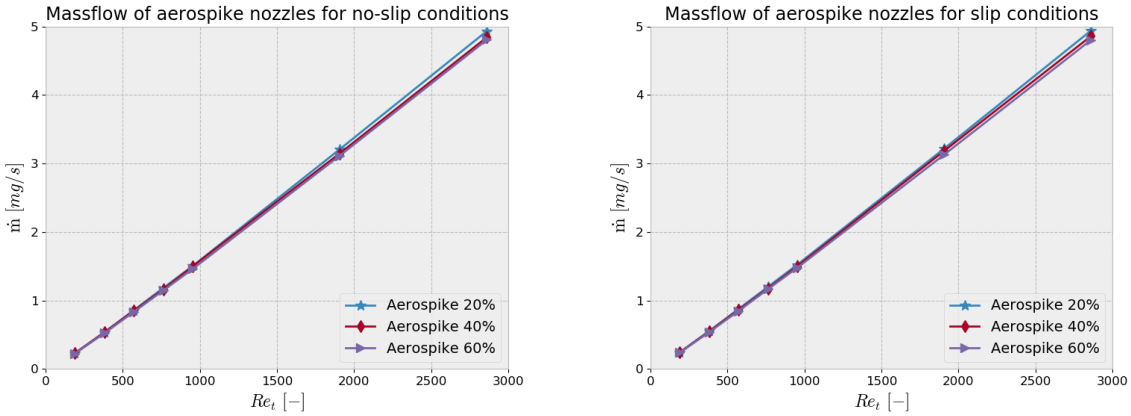

(a) No-slip conditions

(b) Slip conditions

Figure 4.29: Massflow of the aerospike nozzles for no-slip and slip conditions

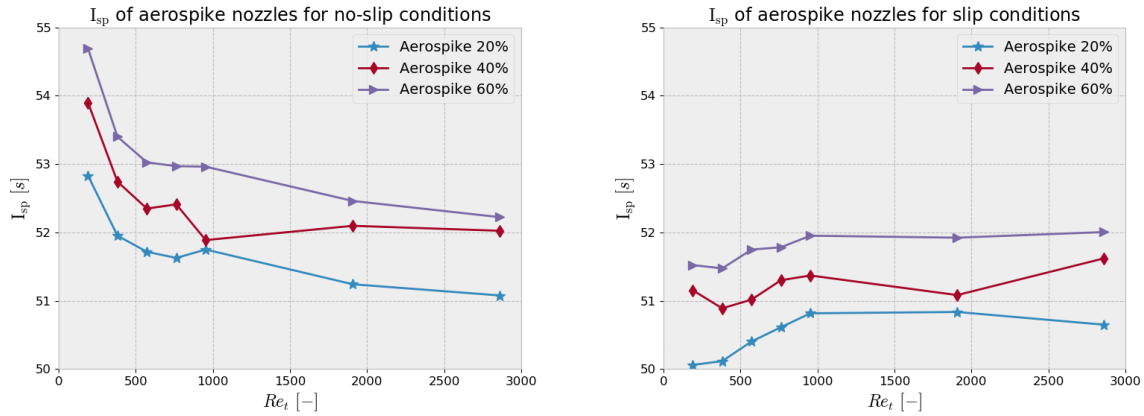

(a) No-slip conditions

(b) Slip conditions

Figure 4.30: Specific impulse of the aerospike nozzles for no-slip and slip conditions

4.2.3. Double depth aerospike nozzle results

Louisos and Hitt found that the over edge expansion losses would become less prevalent if the entirety of the nozzle is deeper [8]. However, this is not an option for the aerospike nozzles in this study, as the requirements dictated a nozzle depth of 100 µm for compatibility reasons.
Whereas deepening the entire nozzle beyond 100 µm is prohibited by requirements, just deepening the center body downstream of the throat is an option as it does not compromise the compatibility with past work. By deepening the center body it is expected that the performance of the aerospike nozzles is increased as one forces the flow to expand over a spike contour, where it is able to generate thrust, instead of expanding over the edge. Thus it was decided to investigate the performance of such a "double depth" aerospike nozzle, the results of which are presented in this section. Moreover, an aerospike nozzle using a spike depth of 100 µm would prove unfeasible during the manufacturing of the nozzles because of structural concerns. This resulted in the produced aerospike nozzles having a convergent depth of 100 µm combined with a spike depth of 600 µm. More detailed information on the production process can be found in Chapter 5.

For the investigation in the double depth aerospike only the 60% truncated nozzles were considered. This level of truncation was selected because even though the thrust seems to be independent of the truncation the specific impulse shows a clear improvement for less truncated nozzles. The spike depth of this 60% truncated aerospike nozzle was varied over a range of 200-1000 µm. This range was selected as depths larger than 1000 µm would likely raise problems during the fabrication as etching straight walls becomes increasingly more problematic the deeper one has to etch. Finally, the methodology applied in the simulations of the double depth aerospike nozzles is the same as that described in Chapter 3.

In Fig. 4.31 one can see $M = 1$ isovolume plots for the double depth aerospike nozzle with a spike depth, h_{spike}, of 600 µm. The nozzle using a depth of 600 µm is of extra interest as the produced nozzles will use this depth. From these isovolume plots it becomes immediately clear that by increasing the depth of the spike body the amount of flow that expands over the edge is reduced. Furthermore, one can see that due to the increase in spike depth there is also a little trailing edge shock present in the $Re_t = 2861$ case, which was previously invisible for the single depth aerospikes.

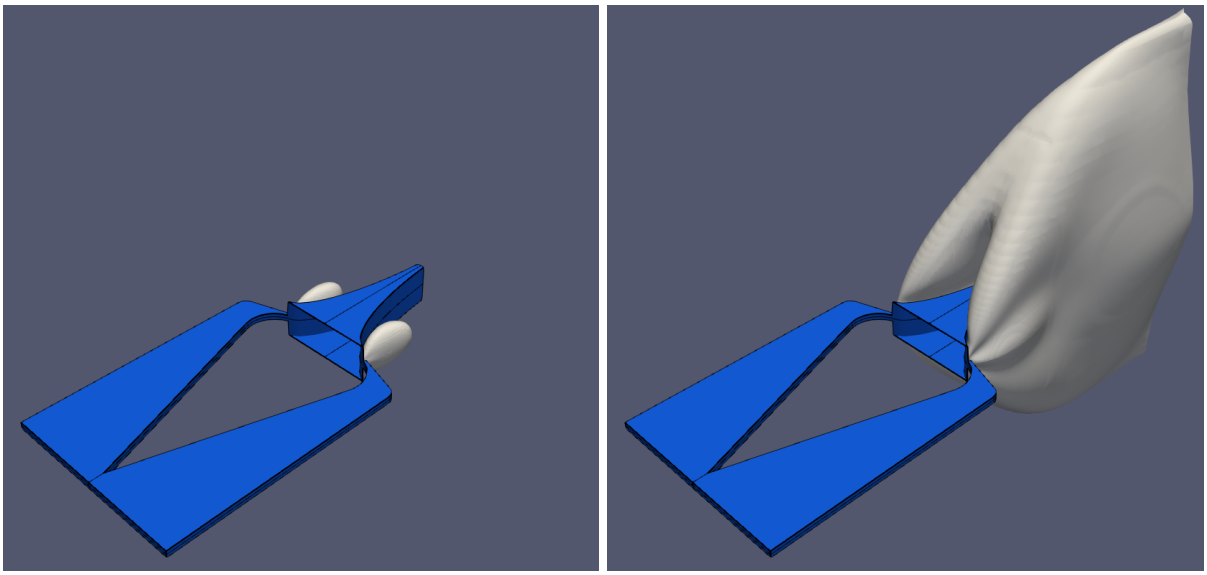

(a) $Re_t = 191$ (b) $Re_t = 2861$

Figure 4.31: Mach 1 isovolume plot for double depth aerospike with a spike depth of 600 µm at $Re_t = 191$ and $Re_t = 2861$

Starting from the cases with $Re_t = 572$ and upwards various interesting observations can be made in the Mach contour plots. The contour plots for this Reynolds number can be found in Fig. 4.32. Here one can observe that with increasing spike depth the area of supersonic flow increases in size. This is a result from the fact that a larger portion of the flow is forced to expand over a nozzle profile, instead of freely expanding in all directions. The $M = 1$ isolines behind the spike body, in the Mach contour plots of the single depth aerospike nozzles provided the initial indications that over the edge expansion was present. In Fig. 4.32 these same $M = 1$ isolines can be found for spike depths below 600 µm. For depths of 600 µm and above no supersonic flow behind the spike body is observed. This suggests, that for this Reynolds number, spike depths larger than 600 µm do not yield significant performance improvements. Furthermore, one can also notice that the increasing spike depth brings a thicker boundary layer near the spike tip. As a result the supersonic flow deviates farther from the optimal spike profile and in certain cases, such as the no-slip cases with $h_{spike} \geq 600$ µm, even looks to fully separate from the spike.

For the double depth aerospike the Mach contour plots over Reynolds number are very similar, as the same spike profile of the single depth aerospike nozzles was used. As such the Mach contour plots of the double depth aerospike nozzles over the complete range of Reynolds numbers will not be shown here, but can be found in Appendix A.

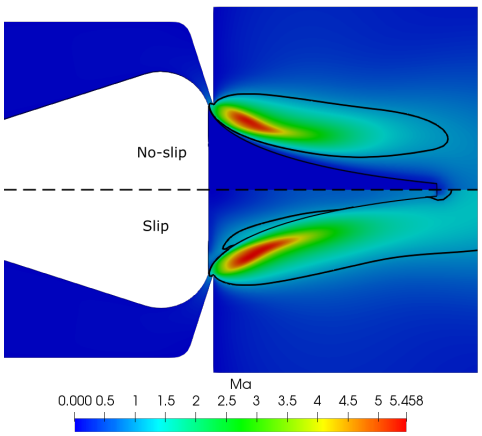

(a) $h_{spike} = 100\,\mu m$

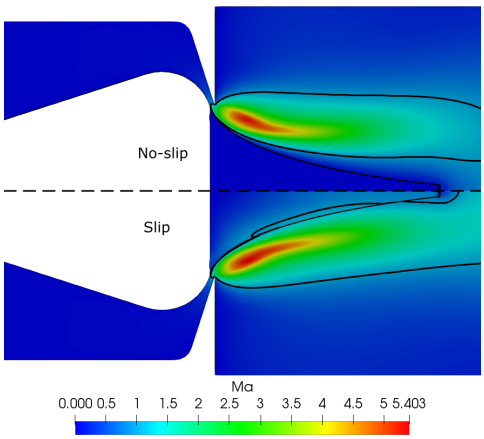

(b) $h_{spike} = 200\,\mu m$

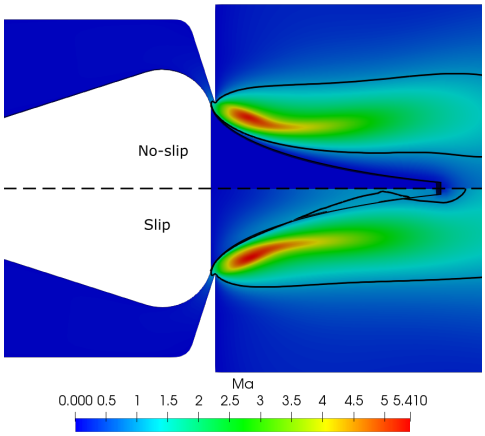

(c) $h_{spike} = 400\,\mu m$

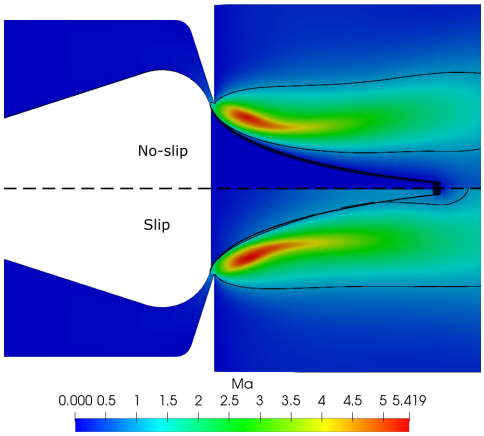

(d) $h_{spike} = 600\,\mu m$

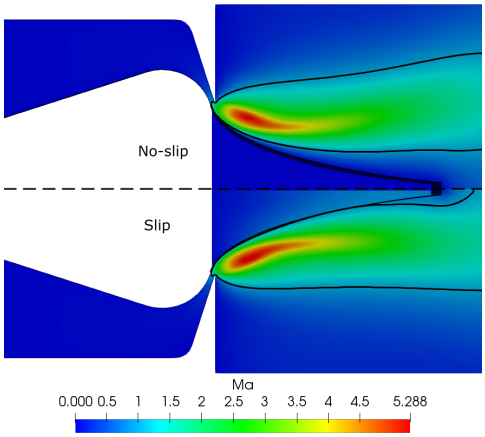

(e) $h_{spike} = 800\,\mu m$

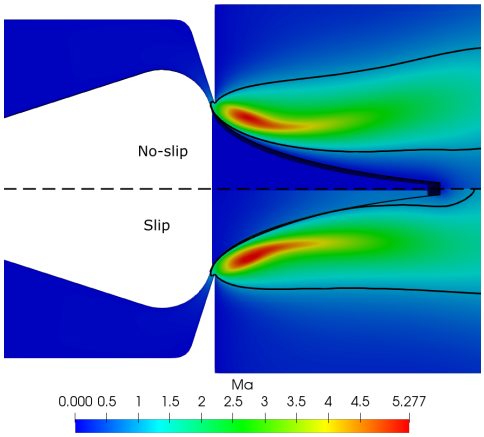

(f) $h_{spike} = 1000\,\mu m$

Figure 4.32: Mach contours of the double depth aerospike nozzle at $Re_t = 572$ for $h_{spike} = 100 - 100\,\mu m$

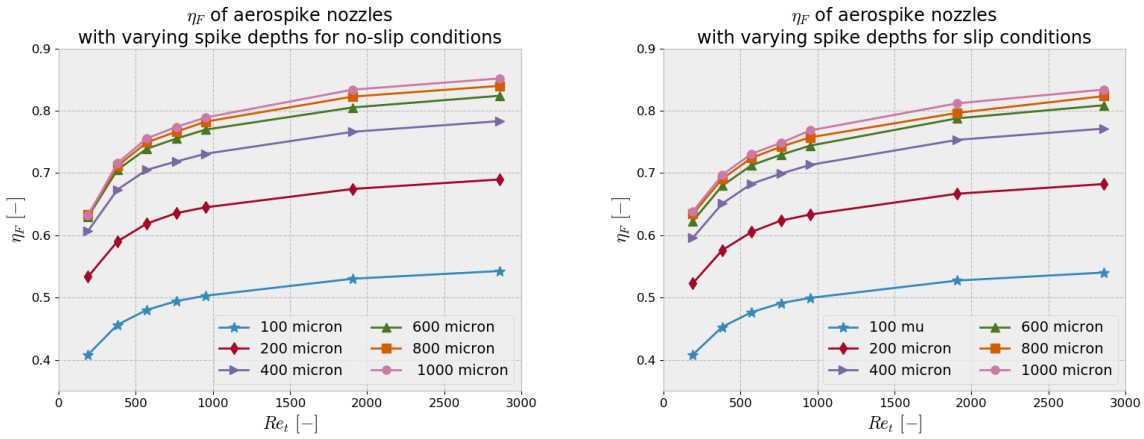

(a) No-slip conditions

(b) Slip conditions

Figure 4.33: Thrust efficiency of the double depth aerospike nozzles for no-slip and slip conditions

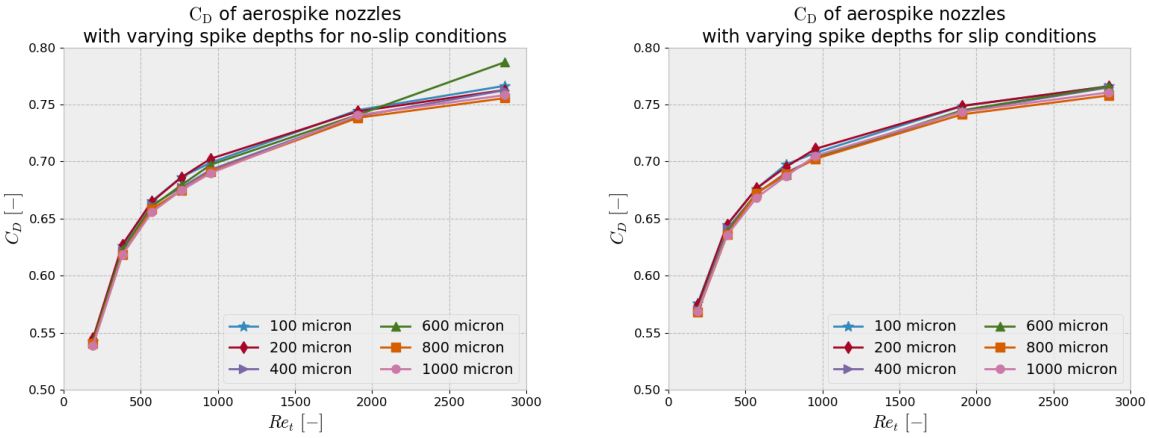

(a) No-slip conditions

(b) Slip conditions

Figure 4.34: Discharge coefficient of the double depth aerospike nozzles for no-slip and slip conditions

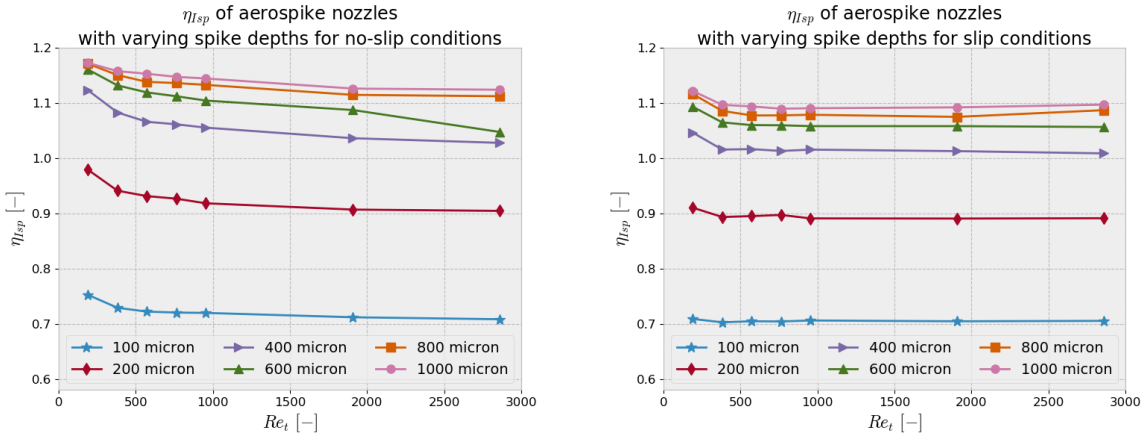

(a) No-slip conditions

(b) Slip conditions

Figure 4.35: Specific impulse efficiency of the double depth aerospike nozzles for no-slip and slip conditions

From the simulation data the performance metrics are extracted and plotted, which can be seen in Figs. 4.33 to 4.35. Due to the ambiguous definition of the exit plane of an aerospike nozzle, and the fact that the conventional 1D equations are not easily adapted for such a peculiar geometry, it was decided to keep the definition of the exit plane as was used for the single depth aerospike nozzles. As a result efficiencies higher than one can be observed, and are the logical consequence of the larger surface area over which the spike thrust is integrated in. As such considering the graphs with the performance metrics as efficiencies is not valid anymore in the case of the double depth aerospikes. Nevertheless, the graphs provide very valuable information on the performance of the double depth aerospikes relative to that of the linear and single depth aerospike nozzles.

From Fig. 4.33 it becomes immediately clear that the thrust efficiency produced by the double depth aerospike increases significantly with increasing depth. With the best performing double depth aerospike nozzle on average having a 1.2% higher η_F with respect to the best performing linear nozzle, and a 25.9% higher η_F compared to the best performing single depth aerospike nozzle. Despite the performance increases with larger spike depths, a point of diminishing returns is observed with only modest increases in thrust efficiency for spike depths larger than 600 µm. Furthermore, it can be noticed that the amount of thrust efficiency gained by increasing the depth is reduced at smaller Reynolds numbers. This can especially be noticed in Fig. 4.33a where for Reynolds numbers below 500 an increase in spike depth beyond 600 µm does not yield any benefit. This outcome is coherent with the expected behavior as the expansion of the flow in the etch direction in low Reynolds cases is significantly smaller compared to high Reynolds cases. Consequently, an increase in spike depth beyond a certain depth is useless as the flow has already fully expanded in the etch direction.

Following from the fact that upstream propagation of information is not possible in supersonic flow, and no changes were made upstream of the throat, no changes are expected in the discharge coefficient. This hypothesis is confirmed with the results in Fig. 4.34, here the discharge coefficient for the aerospike nozzles for all spike depths are near the same. This results in the best performing double depth nozzle having, on average, a 17.5% lower C_D with respect to the best performing linear nozzle, and a 2.0% lower C_D compared to the best performing single depth aerospike nozzle.
One can notice that there is a difference for the nozzle with a spike depth of 600 µm at $Re_t = 2861$ this is most likely an outlier caused by an error somewhere in the numerical simulation process.

Even though the differences in the discharge coefficient are minimal they are present nonetheless. Furthermore, after closer examination it can be seen that a trend is present where the nozzles with larger spike depths have slightly lower coefficients. It is likely that this demeanor is caused by the slight increase in boundary layer thickness, that resulted from the increase in spike depth. The effective profile deviates further from the ideal due to this thickness increase, caused by increasing spike depth. This effect could have resulted in suboptimal expansion and thus lower discharge coefficients.

Looking at Fig. 4.35 it can be observed that the increase in spike depths has tremendously positive effects on the specific impulse efficiency. With performance increases up to 41.2% with respect to the best performing single depth aerospike nozzle. On average the best double depth nozzle has a 24.7% higher $\eta_{I_{sp}}$ compared to the best performing linear nozzle and a 39.2% higher $\eta_{I_{sp}}$ compared to the best performing single depth aerospike. This tremendous increase in specific impulse efficiency results in double depth aerospikes using spike depths larger than 400 µm outperforming the theoretically possible performance of the single depth aerospike and linear nozzle. Here again the effect of diminishing returns can be noticed for spike depths beyond 600 µm.

Lastly, in Fig. 4.36 the results for the off-axis thrust percentage, L_{align}, are presented. From this it becomes clear that by utilizing the double depth design the majority if not all of the over the edge

expansion losses are mitigated by forcing the flow to expand over a spike contour. Furthermore, these graphs show that with a spike depth of 600 µm there is almost no more off-axis thrust component to mitigate. Thus, further confirming the other results which state that increasing the spike depth beyond 600 µm is not sensible, for the nozzle conditions considered in this study.

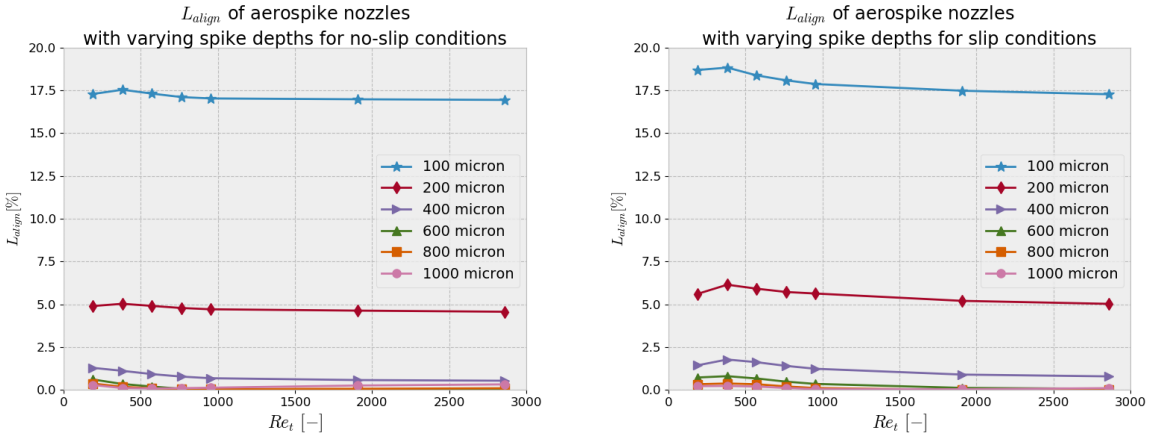

(a) No-slip conditions

(b) Slip conditions

Figure 4.36: Of-axis thrust fraction of the double depth aerospike nozzles for no-slip and slip conditions

Similar to the linear and the single depth aerospike nozzles the absolute performance is necessary to provide the complete picture of the nozzle performance. Thus, this performance is plotted and can be found on the next page in Figs. 4.37 to 4.39. Additionally, the exact performance numbers can be found tabulated in Appendix B. From the figures, it can be observed that the increase in thrust caused by the increased spike depth is very significant, especially for the higher Reynolds numbers. Additionally, very respectable specific impulse figures are obtained with specific impulses of above 80 seconds for cold gas thrusters.

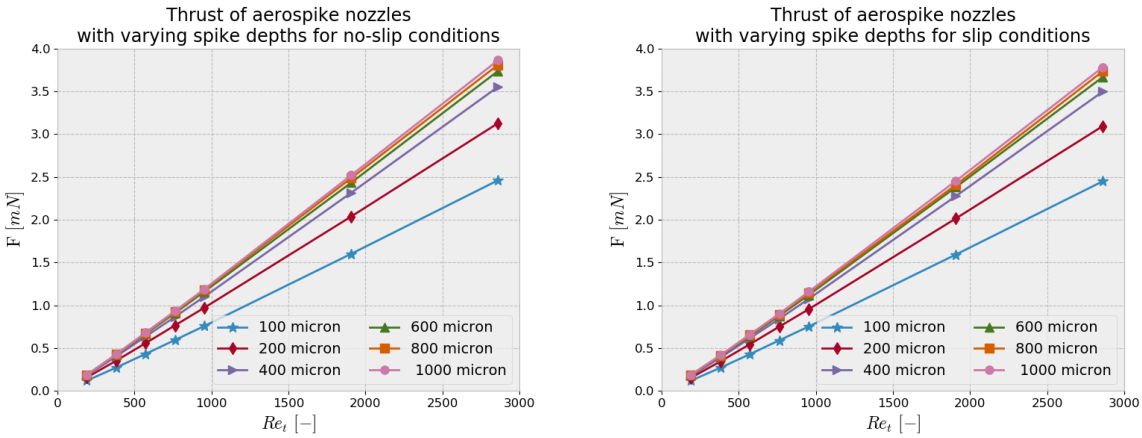

(a) No-slip conditions

(b) Slip conditions

Figure 4.37: Thrust of the double depth aerospike nozzles for no-slip and slip conditions

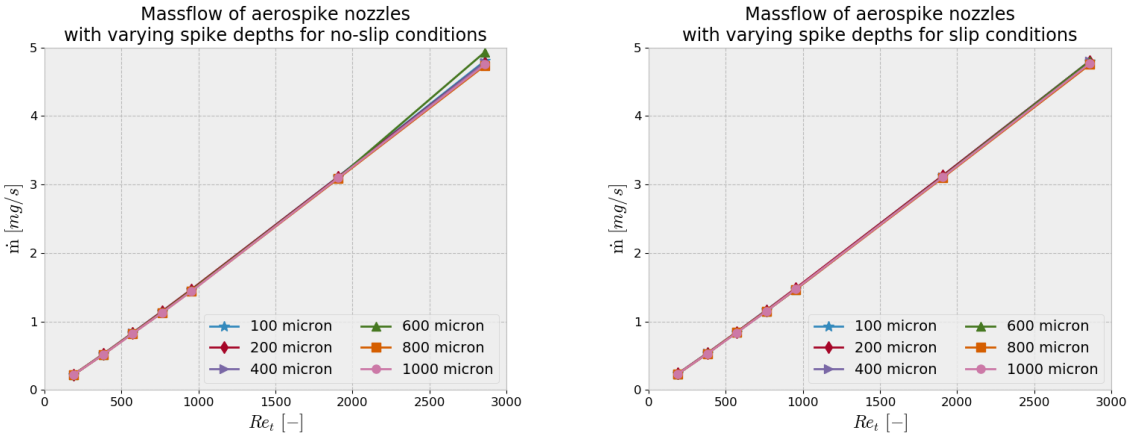

(a) No-slip conditions

(b) Slip conditions

Figure 4.38: Massflow of the double depth aerospike nozzles for no-slip and slip conditions

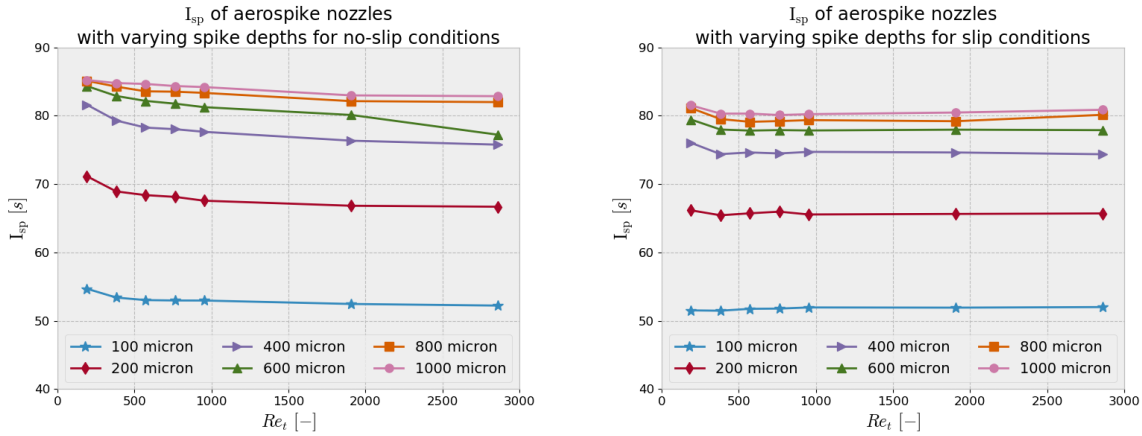

(a) No-slip conditions

(b) Slip conditions

Figure 4.39: Specific impulse of the double depth aerospike nozzles for no-slip and slip conditions

4.3. Chapter summary

Within this chapter the numerical results for the various nozzle geometries were presented and analyzed. The findings of this analysis are summarized in this section.

The results of the various nozzle geometries were visualized through Mach contour plots and graphs depicting the performance metrics. From the contour plots of the linear nozzles it was found that, with decreasing Reynolds number the supersonic portion of the flow shrunk in size. This effect was more pronounced for smaller divergence angles, with the flow in the $\theta_{out} = 15°$ nozzle becoming fully subsonic at low Reynolds numbers. In contrast the flow in the nozzles with higher divergence angles did remain supersonic.

The performance metric graphs of the linear nozzles were in line with the results of past research. Namely a slow decline in performance with decreasing Reynolds at higher Reynolds numbers ($Re_t = 1000 - 3000$), followed by a steep decrease in performance after the Reynolds number drops below 1000.

These graphs showed that for $Re_t > 1200$ the $\theta_{out} = 30°$ nozzle is providing the best thrust efficiency. For $Re_t < 1200$ the $\theta_{out} = 45°$ nozzle started outperforming the other two linear nozzles. The $\theta_{out} = 15°$ nozzle was the worst performing nozzle for all but one case considered. This low performance of the $\theta_{out} = 15°$ nozzle was unexpected as, at the higher Reynolds numbers, the lower divergence losses were expected to result in superior perfomance compared to the higher divergence angle nozzles. This underperformance of the $\theta_{out} = 15°$ was attributed to the combination of small divergence angles and a shallow nozzle depth. This combination leads to excessive boundary layer corner merging which results in significantly lower effective nozzle expansion ratios, and thus lower overall performance.

Furthermore, it was found that the discharge coefficient for the various linear nozzles were fairly similar. Due to this similar discharge coefficient the findings for the specific impulse efficiency are similar to that of the thrust efficiency. Thus for $Re_t > 1200$ the $\theta_{out} = 30°$ nozzle is providing the best specific impulse efficiency and for $Re_t < 1200$ the $\theta_{out} = 45°$ nozzle is the best linear nozzle.

The specific impulse efficiency did show peculiar results at the lower Reynolds numbers. Here the rate of efficiency decrease, decreased at low Reynolds numbers. Extrapolating these results would lead to the $\theta_{out} = 15°$ nozzle outperforming the other nozzles at low Reynolds numbers. These peculiar results were explained by the fact that the simulations were done in a flow too rarefied for continuum methods. It was found that the throat Knudsen number for the $Re_t = 191$ cases exceeded the validity thresholds of La Torre. As such it was determined that one should treat the results at this Reynolds number with some suspicion.

The Mach contour plots of the aerospike nozzles showed that the flowfields of these micronozzles were much more in line with the flowfield of its macro scale counterpart. This indicated a flow less influenced by viscous losses. The graphs of the performance metrics showed that the aerospike nozzles have a truncation independent thrust. This was explained as the majority of the thrust is generated on the first portion of the spike.

In contrast the discharge coefficient was found to be truncation dependent, with less truncated nozzles having a lower discharge coefficient. This truncation dependent discharge coefficient was explained by the larger surface area present in less truncated nozzles. This larger surface area led to thicker boundary layers which resulted in a more restricted flow.

Furthermore, it was found that the specific impulse efficiency for the aerospike is fairly constant over the entire range of investigated Reynolds numbers in the slip cases. However, for the no-slip cases an increase in specific impulse efficiency was found with decreasing Reynolds numbers. This peculiar result was attributed to very large Knudsen numbers encountered in the aerospike simulations. Therefore, similar to the linear nozzle simulations, the results at low Reynolds numbers of the aerospikes have to be treated with scrutiny.

From the performance metrics it was found that on average the best aerospike nozzle performed 24.7%, 15.5%, and 14.4% worse than the best linear nozzle for η_F, C_D, and $\eta_{I_{sp}}$ respectively. Investigation of this performance deficit showed that, due to excessive over-the-edge expansion of the flow, a significant portion of the potential performance was lost. Based on these findings the double depth aerospike geometry was designed and numerically investigated.

For these double depth nozzles it was found that the majority of the over the edge expansion can be prevented by increasing the spike center body depth. This resulted in major improvements in the thrust and specific impulse efficiencies, with the discharge coefficient staying mostly constant. Any minor deviations in the discharge coefficient were caused by the thicker boundary layers, which resulted from the enlarged surface area of the deepened spike center body. Specific impulse efficiencies increased by as much as 41.2% making the double depth aerospike nozzle the best performing nozzle geometry over the entire range of investigated Reynolds numbers. However, while increasing the depth did improve the performance, a point of diminishing returns is observed. For the conditions considered in this study no significant improvements in performance were observed for spike depths larger than 600 µm.

Thus, based on the results found from the numerical simulations one can conclude that the double depth aerospike nozzle is the best nozzle geometry at the conditions investigated. This is followed by the performance of the various linear nozzles, with the single depth aerospike nozzle grossly underperforming.

5

Micronozzle Production

For this study a variety of micronozzles need to be experimentally tested. For the experimental part of this study the nozzles of interest need to be produced. Within the TU Delft production of linear nozzles with integrated heaters were previously performed by Silva [11]. Nevertheless a new production process would have to be designed due to the presence of the atypical aerospike geometries. The design of this new production plan will be described below, followed by the issues encountered during production, and recommendations for the future optimization of the production process.

5.1. Production nozzle design

Earlier in Chapter 2 the nozzle profiles were defined that will be produced. With the aim of experimentally testing the produced nozzles come the requirements that the nozzles have to be compatible with the experimental setup, and have to be strong enough to withstand handling. Furthermore, certain nozzle profiles might prove problematic during the production and need slight alterations to be manufacturable. Therefore, the complete nozzle design and its deviations from the defined nozzle profile in Chapter 2 are presented below.

5.1.1. Linear nozzle

In the past similar linear nozzles have been manufactured and experimentally tested by Silva [11]. During these experimental tests the linear nozzles held up well, even under repeated handling. As a result manufacturability and structural rigidity do not impose any limitations for the linear nozzles and thus the dimensions are unchanged to those presented in Chapter 2.

However, to be compatible with the interface of the experimental setup the silicon substrate in which the nozzle profile is etched, needs to be 11 by 7 mm in size. Furthermore, there needs to be an inlet hole with a diameter of 0.5 mm at a distance of 2.55 mm from the base of the substrate. This results in a final design which is presented in Fig. 5.1 and is vizualized in Fig. 5.2.

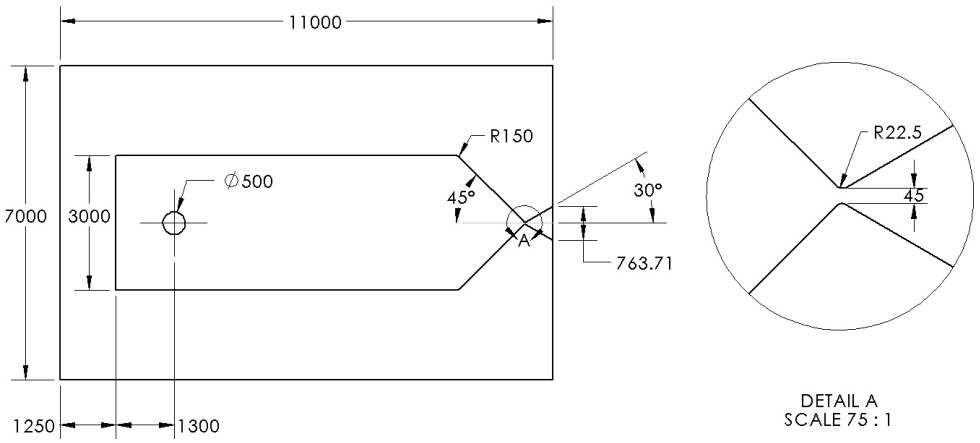

Figure 5.1: Technical drawing in µm of the linear nozzle with $\theta_{out} = 30°$

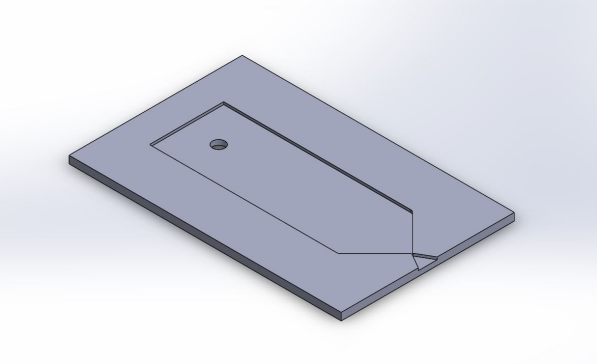

Figure 5.2: Silicon substrate of linear nozzle with $\theta_{out} = 30°$

5.1.2. Aerospike nozzle

The design of the aerospike used for production had to differ from that defined in Chapter 2 due to manufacturability limitations, experimental setup interface requirements, and structural rigidness concerns.
As the aerospike nozzles have to fit in the same interface as the linear nozzles the size requirements for the silicon substrate are similar to those for the linear nozzle. However, as the spike of the aerospike is freehanging, the dimension of 11 mm is taken from the base of the silicon substrate to the nozzle lip, see Fig. 5.3. This results in the flow around the spike not being restricted due to the testing interface.

In Chapter 2 all the designs were nozzle profiles which would be turned into a 3D planar nozzle by etching it 100 µm deep perpendicular to the nozzle profile. However, if one would only etch 100 microns deep in the case of the aerospike nozzles, the resulting spike would also be 100 µm thick. This leaves a thin fragile spike which would be prone to breaking during handling. As such it was decided that the fabricated aerospike design would not have a depth equal to the convergence depth,

but rather equal to 600 µm. This thickness was selected as it is equal to the thickness of the two silicon wafers necessary for the production of the nozzles. Two wafers are necessary, one in which the fluidic channel is etched, and the other to seal the channel by bonding it on top. This results in a nozzle that is the double depth aerospike nozzle with a spike depth of 600 µm as described in Chapter 4, which can be seen in Fig. 5.4.

Lastly, the designed nozzle lip of the aerospike has an infinitesimally thin edge. This sharp edge would be rounded in production leading to a nozzle throat which could be significantly larger than the designed dimension. To mitigate this the nozzle lip was widened to a width of 20 µm.

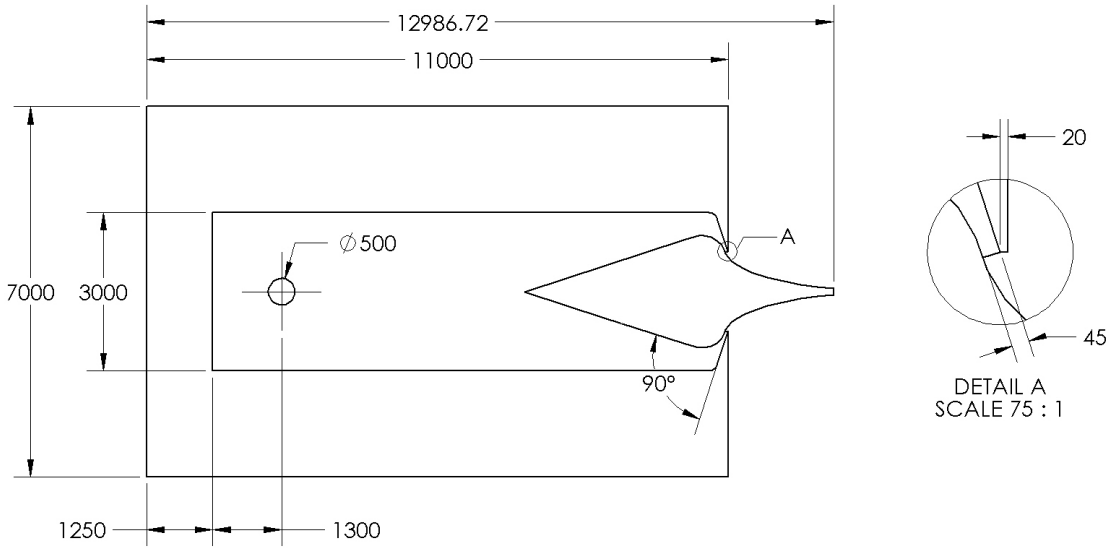

Figure 5.3: Technical drawing in µm of the aerospike nozzle truncated at 60% spike length

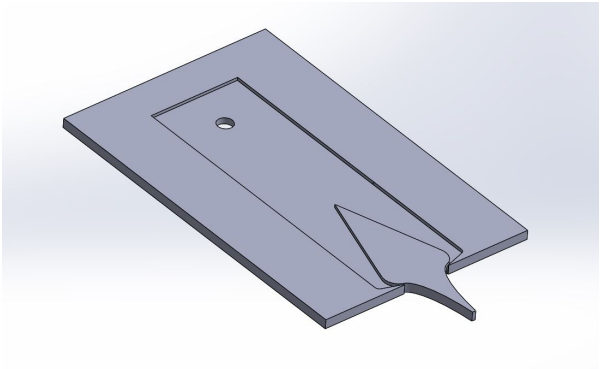

Figure 5.4: Silicon substrate of aerospike nozzle truncated at 60% spike length without the bonded silicon wafer

5.2. Production environment

The TU Delft has the fortunate position where it possesses its own highly advanced Integrated Circuit (IC) processing lab called the Else Kooi Laboratory (EKL) . Within EKL there are multiple processing labs with the most advanced being the class 100 (ISO5) cleanroom, which is used for production purposes in this study. This class 100 cleanroom, here-on abbreviated with CR100 , has the

Deep Reactive Ion Etching (DRIE) etchers necessary for producing the planar nozzles of this study. These DRIE etchers are necessary as they are able to anisotropically etch silicon to large depths. In comparison regular Reactive Ion Etching (RIE) etchers are not able to etch to the depths necessary for these nozzles, and wet chemical etching results in isotropic etches which would result in major deviations from the designed profile.

5.3. Production methodology

Below the production steps as they were initially designed will be treated. The linear and aerospike nozzles have a lot of production steps in common. For this reason all steps described are applicable to both profiles unless otherwise mentioned. Furthermore, all steps described are visualized in Fig. 5.5, where a simplified lengthwise cross-section is shown. The necessary cleaning and inspection steps, which are critical for reliable and accurate fabrication, will be omitted in the description below for the sake of legibility. The full production flowchart can be found in Appendix C.

Step 1
The nozzle production was performed with 4" silicon double side polished wafers (DSP) of 300 µm thick. For the aerospike nozzles the thickness of two wafers needs to be completely etched away locally. As etching deeper can lead to larger inaccuracies it was decided to use the 300 µm wafers instead of the more common 500 µm wafers. DSP wafers are necessary as processing needs to take place at both sides of the wafer. Alignment markers are etched on the top surface of the wafer, these are not visible in Fig. 5.5 due to their negligible depth. These alignment markers provide a reference frame on the wafer such that the ASML PAS5500/80 wafer-stepper, which is used to expose the to be etched patterns, to align the various patterns extremely accurately.

Step 2
Following the etching of the alignment markers both sides of the wafer are deposited with silicon dioxide SiO^2 through a Plasma Enhanced Chemical Vapor Deposition (PECVD) process. This oxide will function as the hard mask for the various patterns during the etching of the silicon.

Step 3
The oxide layer that was deposited on the bottom of the wafer in the previous step is etched with a RIE etcher, opening holes in the shape of the to be etched fluidic channel. The opening of specific shapes in the oxide layer is done by covering the oxide with a protective photo-resist layer. This photo-resist layer is exposed with an uv-light, which is shined through a photomask, on which only the user-defined patterns are transparent. The exposure with uv-light makes the exposed photo-resist soluble, allowing the protective photo-resist to be removed on the to be etched areas. This process of applying photo-resist and exposing is called patterning and has to be done every time a hard mask has to be etched in oxide. For legibility reasons this has been left out in the remaining steps. The layout of the mask used during the production can be found in Appendix D.

Step 4
On the topside of the wafer the hard mask for the center body of the aerospike downstream of the throat is etched into the silicon dioxide. This geometry will in the following explanation be called the spike geometry. However, instead of fully etching away the PECVD oxide layer it is only partly etched away. This decision resulted from a multitude of interrelated limitations which will be concisely described:

Firstly, one has to perform the DRIE etch of the spike geometry, which will locally completely etch away all silicon, after bonding the two wafers together, which is performed in step 8. As etching the

geometry before bonding would leave enormous holes in the wafer resulting in production equipment refusing to handle the wafer.
Furthermore, during the DRIE etch of the spike geometry the throat geometries, etched in step 6, have to be protected by an additional oxide layer. Failure to do so could lead to the unwanted etching of the throat geometry altering critical dimensions of the nozzle.
However, applying the oxide on the throat before bonding is not an option, as the bottom side of the wafer needs to be completely clean for the wafer bonding. Additionally, one cannot deposit a PECVD oxide layer on the throat geometries post bonding as the bonded wafer will block of the access to the throat. Therefore, a thermal oxide needs to be used, moreover, to get the necessary oxide thickness a wet thermal oxide is required. For such a wet thermal oxide it is necessary that the surfaces, on which the oxides need to be grown, are exposed to the atmosphere of the furnace in which the oxide is grown.
This means that to grow the wet thermal oxide, on the nozzle throat, the inlet hole has to be etched first. If one would have fully opened the hard mask of the spike geometry in this production step, the spike center body could have been etched fully away, while the inlet hole is etched. Lastly, it is highly preferred to do the majority of the patterning of the wafers before bonding. As during bonding one has to manually align the wafers resulting in a slight offset between the two wafers. This offset can lead to issues during post-bonding alignment and exposure.

By partially etching the hard mask one removes the need for post bonding patterning of the spike geometry. Furthermore, one can etch the entirety of the top wafer while still maintaining a thick enough oxide hard mask due to the difference in thickness caused by the partial etch. Note that this step is only necessary for the aerospike nozzles.

Step 5
The hard mask for the inlet hole is etched in the oxide layer on the topside of the wafer. A thick photo-resist is applied to ensure that the partially etched mask of the aerospike nozzles is protected.

Step 6
Using the DRIE etcher the fluid channels on the bottom side of the wafer are etched 100 microns deep. As important nozzle dimensions are not measurable after the production is finished they get immediately measured after the DRIE etch step. This is done using a Keyence VK-X250 scanning laser microscope. More on the measurements of the nozzle can be found in Section 5.4.

Step 7
To prepare the wafer for bonding the PECVD silicon dioxide needs to be stripped from the bottom, which is done in a BHF solution. To ensure that the hard mask on the top side of the wafer is not etched as well a thick layer of photo-resist is applied on the top acting as a protective layer.

Step 8
In this step the wafer that was processed in the previous steps is bonded to another 300 µm thick silicon DSP wafer, resulting in closed of fluidic channels. The bonder at EKL is considered to be a contaminated tool and processing steps are necessary after bonding. Therefore, to prevent cross-contamination between fabrication equipment contamination mitigation strategies need to be applied. One of which is the fact that instead of bonding the wafers under an elevated temperature, the bonding is performed without any addition of heat. However, this does bring the requirement of an additional annealing step in the furnaces to ensure a strong wafer bond.

Step 9
To be able to accurately dice (cutting wafers into the final test sample dimensions using a thin blade) the nozzles out of the wafers special shallow cutting lines have to be etched into the silicon, which

is done on the backside using a RIE etch. This is not visible in Fig. 5.5 due to the negligible thickness of the lines.

Step 10
Using the DRIE etcher the inlet hole is etched into the silicon, opening the channels. At this point all the features are etched in the linear nozzles. Thus all following steps, except step 16, are only relevant for the aerospike nozzles.

Step 11
A wet thermal oxide is grown to protect the throat of the aerospike nozzles during the spike etching step.

Step 12
After the thermal oxide has been grown a PECVD oxide layer is deposited on the bottom side. This oxide is necessary because it was decided to etch the silicon surrounding the spike body away from two sides, this leads to better etch quality. Thus the PECVD oxide deposited in this step will act as an hard mask with the same geometry as the mask which was partially etched in step 4.

Step 13
The hard mask on the bottom and the top are completely opened using RIE etches.

Step 14
A DRIE etch is performed on the bottom side of the wafer, etching away 300 µm.

Step 15
The spike geometry on the top side of the wafer is now etched 200 µm deep by means of a DRIE etch. This results in a fully open spike body.

Step 16
In this step the wafer gets stripped of all its oxides by means of a vapor HF strip. This step is done for both the linear and aerospike nozzles. After this step the nozzles are ready to be diced out of the wafers.

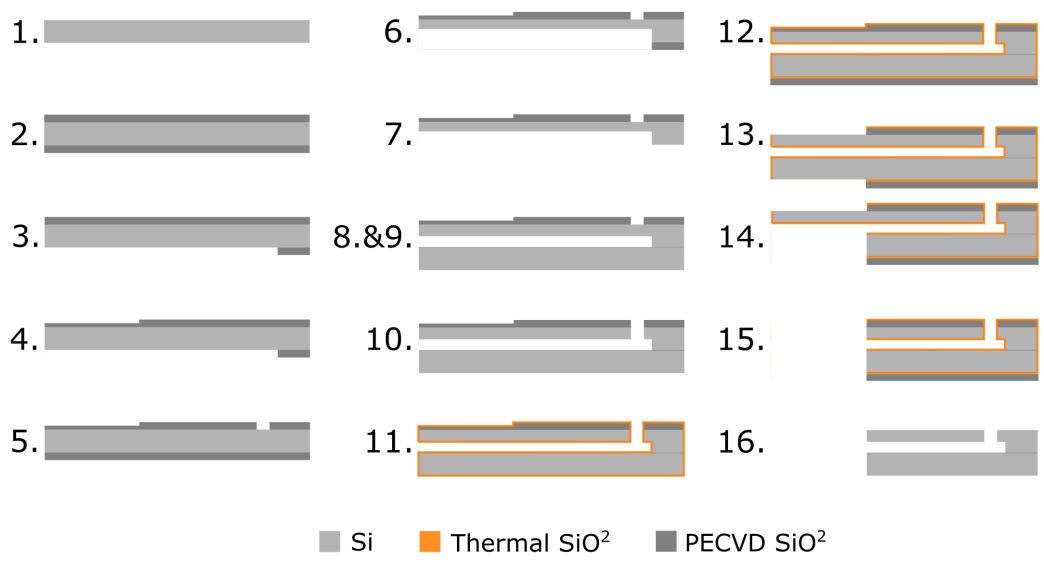

Figure 5.5: Production steps for the aerospike nozzle simplified

5.4. Naming and measurement

In the past various linear micronozzles were produced by Silva and a number of characteristic dimensions for the nozzles were measured. The measurements of Silva showed that there were significant deviations in critical design dimensions, such as the throat width. As such it is of the utmost importance that all the nozzles are measured and the dimensions accurately characterized before one does experimental tests with said nozzle. During the production this was done by measuring every nozzle using the Keyence VK-X250 microscope. An overview of the mean and standard deviation of various nozzle dimensions can be found in Table 5.1. From these measurements it is clear that the production methodology is much more controlled as all the dimensions were very close to the design variables. One might notice that while the throat width and depth are both very close to te designed value the throat area is still quite far off. By means of the 3D measurement capabilities of the Keyence microscope the profile of the throat can be measured, one example of the output can be found in Fig. 5.6. From the figure one can see that the throat area is smaller than designed due to the nozzle profile walls not being perfectly perpendicular to the wafer surface. Additionally the corners exhibit small indications of rounding instead of being a perfect 90 degree corner. The entirety of the nozzle measurements and the wafer layout can be found in Appendix E.

Table 5.1: Mean and standard deviation of measured nozzle dimensions

Nozzle type	W_t [µm]	h_t [µm]	A_t [µm^2]	W_e [µm]	h_e [µm]
Linear	45 ± 0.4 (45)	104.4 ± 2.1 (100)	3826.6 ± 109.7 (4500)	756 ± 0.7 (763.7)	109.7 ± 2.4 (100)
Aerospike	45 ± 0.5 (45)	97.0 ± 3.4 (100)	3721.2 ± 152.9 (4500)	N/A	N/A

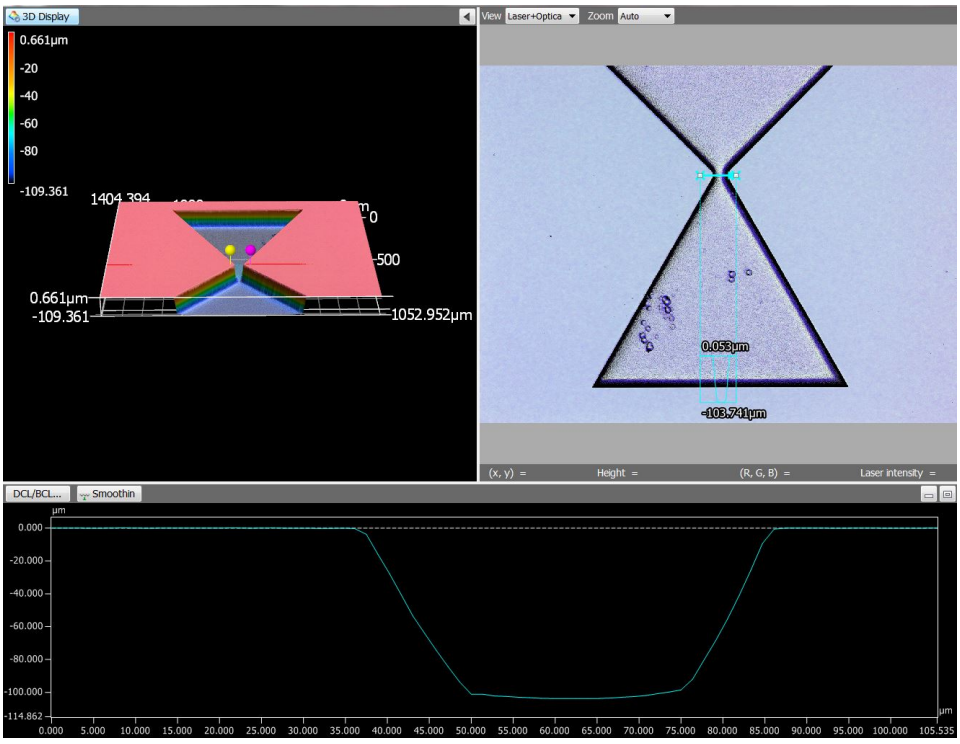

Figure 5.6: Profile measurement of nozzle throat

To be able to link the measured dimensions to a specific nozzle, on a production wafer, a naming scheme was set up, to identify the nozzles after dicing. In the name the nozzle type (aerospike or linear nozzle), the nozzle variable (θ_{out} or $\%_{trunc}$), location on the wafer, and on which wafer the nozzle is located are defined. The wafers were named by means of a letter-number combination

which indicates the type of nozzle that was etched on the wafer, and a number indicating the specific wafer in a production run. A clarifying image of the naming structure can be found in Fig. 5.7.

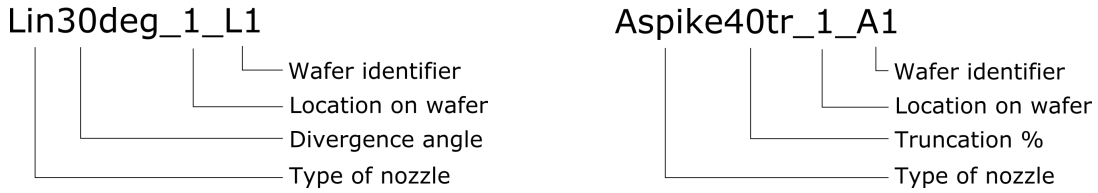

(a) Linear nozzle

(b) Aerospike nozzle

Figure 5.7: Naming scheme for the nozzles

5.5. Production challenges

During the production a multitude of issues were encountered, the causes of which can and have to be changed for future production runs. In this section the various issues and their work-arounds are treated.

The first issue was encountered during the patterning of the wafers. As double side processing is necessary for the production, patterns have to symmetric over the same axis over which the production machines flip the wafers. The convention is that one flips a wafer over the axis going through the large flat of the wafer, which is located at the bottom of a wafer. However, on the photo-mask all the nozzle geometries are oriented towards the right. As a result the wafer stepper needed to be programmed to rotate the wafer 90 degrees before exposure. Consequently the alignment markers also have to be etched with a rotation of 90 degrees.

The second issue was encountered during step 3 in the production process and was a result from the rotated alignment markers. The ASML waferstepper uses interference to find the alignment markers. To generate this interference the alignment markers have a specific orientation. This orientation allows for alignment markers on one side of the wafer to be used for both top and bottom side alignment of patterns. For the exposure of the fluidic channels the wafer needed to be both flipped and rotated, which resulted in an incorrect orientation of the alignment markers. Consequently, the wafer stepper was not able to locate the alignment markers even though it was looking right at them. This problem was solved by first exposing alignment markers with a rotated orientation in the photoresist on the backside. These alignment markers were exposed using the frontside alignment markers to ensure a consistent alignment throughout the production. Then the wafer-stepper was programmed to look for alignment markers on the frontside of the wafer while the wafer was loaded with the backside up. This allowed the the various patterns to be exposed. A consequence of this mitigation strategy is that because the alignment markers were exposed in the photo-resist they will also be etched. For future production runs it is recommended that if one would re-use the photo-mask, an additional set of alignment markers with adjusted orientation is exposed on the front side, such that regular backside alignment can be performed.

The third and last issue was encountered during the post bonding annealing. During the annealing step a thick layer of PECVD oxide was present on the top wafer. This resulted in the occurrence of a large amount of debonding and warping in the wafer, which was caused by the difference in thermal expansion between the PECVD oxide and the silicon wafer. The middle part of the wafers remained bonded but led to a significantly stressed wafer with slip induced crystal lattice defects visible to the naked eye. This can be seen in Fig. 5.8, where the images are sharpened in post-processing to make the defect lines more visible. Note that all the lines visible on these wafers are the result of the annealing as wafers generally are perfectly smooth.

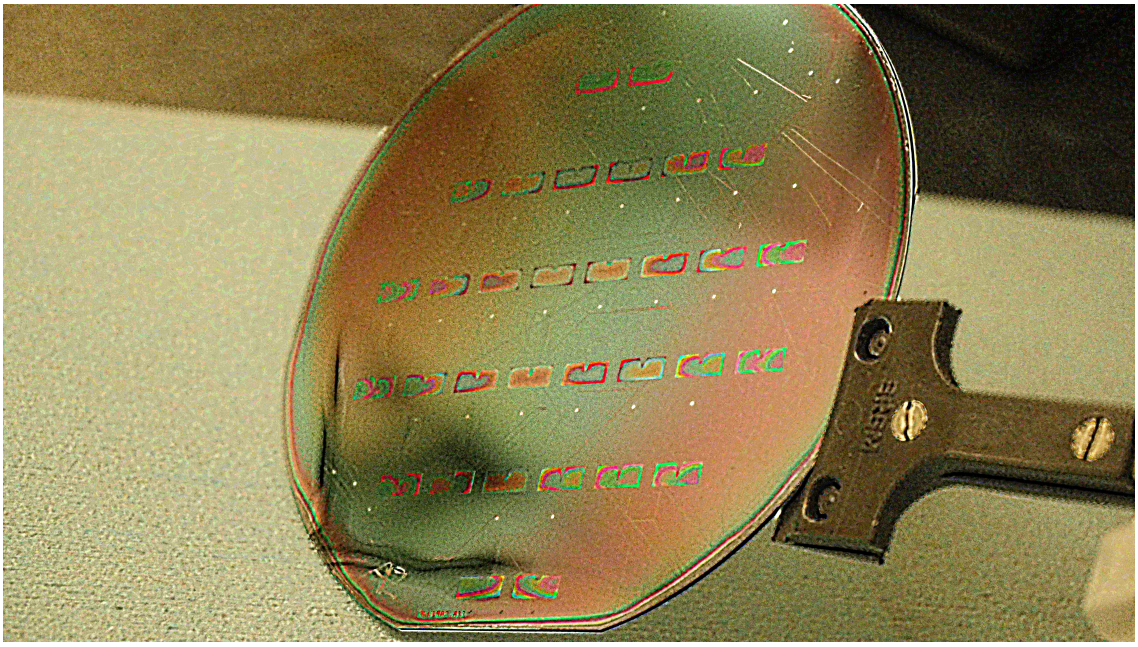

(a) Right side of the A2 wafer

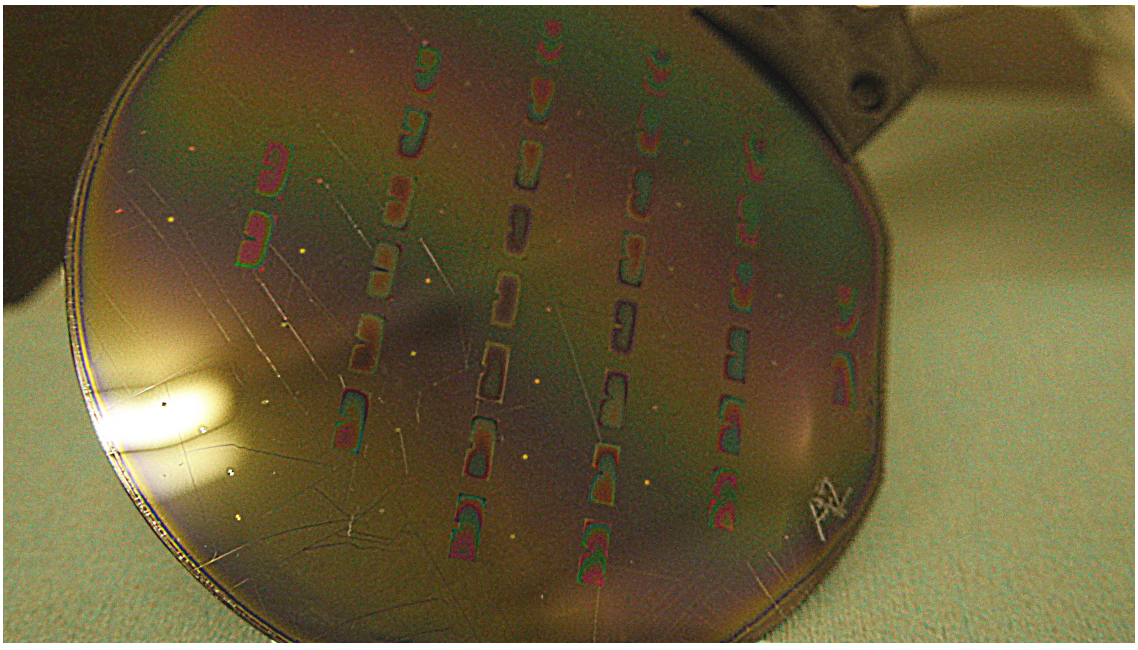

(b) Left side of the A2 wafer

Figure 5.8: Slip induced effects on the A2 wafer on the right and left side of the wafer

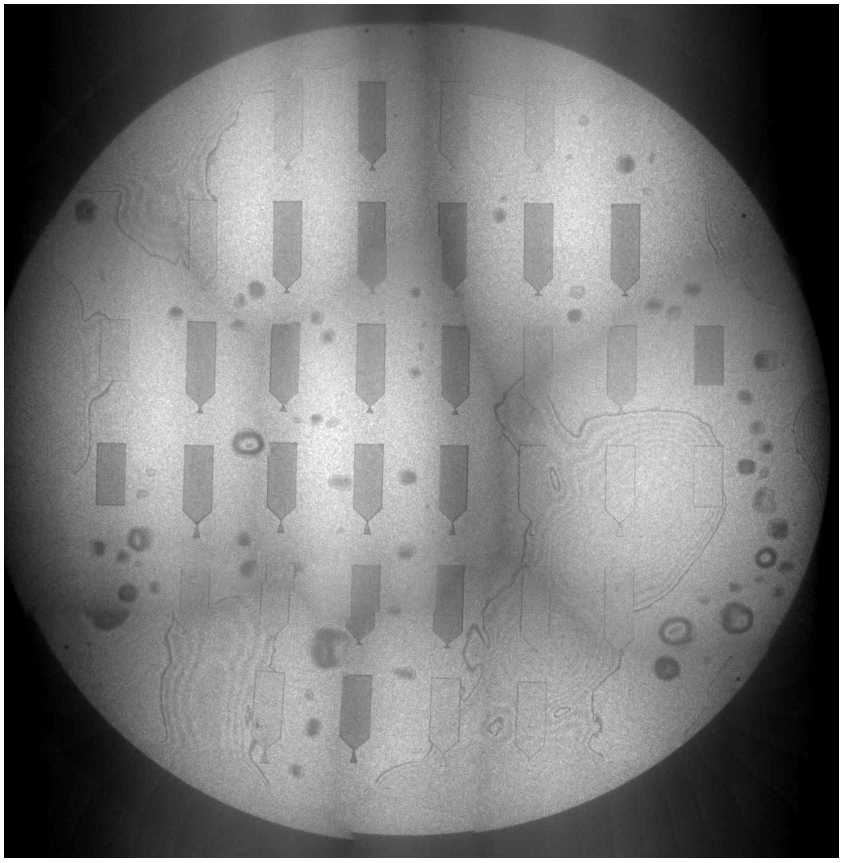

(a) Wafer with linear nozzles

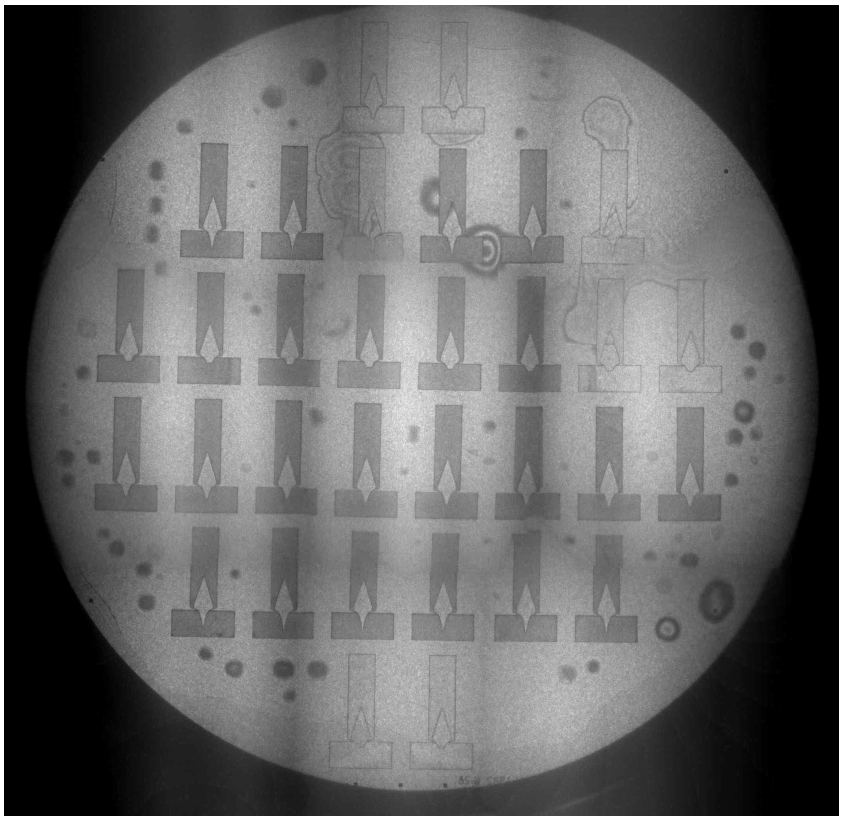

(b) Wafer with aerospike nozzles

Figure 5.9: Infrared images of wafers used for linear and aerospike nozzle production

After the annealing, infrared images were made to investigate the amount of debonded area, and identify the usable nozzles, these images can be seen in Fig. 5.9. As the images are composited of multiple smaller images, artifacts, such as streaks of unequal illumination and minor shifts in the image, can be seen. Within the image debonded areas can be identified by the slightly darker gray areas, which start at the border of the wafer. As one can observe, a significant amount of wafer area did debond and as a result the nozzles in these debonded areas are unusable. Unusable nozzles can be identified by the nozzle profile being a light gray instead of a deep dark gray. Furthermore, one can observe a lot of dark gray spots on the wafers, this is caused by particles which were present on the wafer during bonding. This unusually high amount of particles indicates that something is wrong with the RCA clean used to prepare the silicon wafers before bonding.

Due to the highly stressed wafers the top wafer was visibly curved upwards near the edges, which can be seen in Fig. 5.10. However, it is likely that due to the high stress present in the wafers the bottom wafer also had a minor curvature which was not visible to the naked eye. This curvature resulted in the refusal of production equipment to handle the wafers. Thus, unfortunately a solution that would save the wafers produced with the production flow presented in Section 5.3 could not be found.

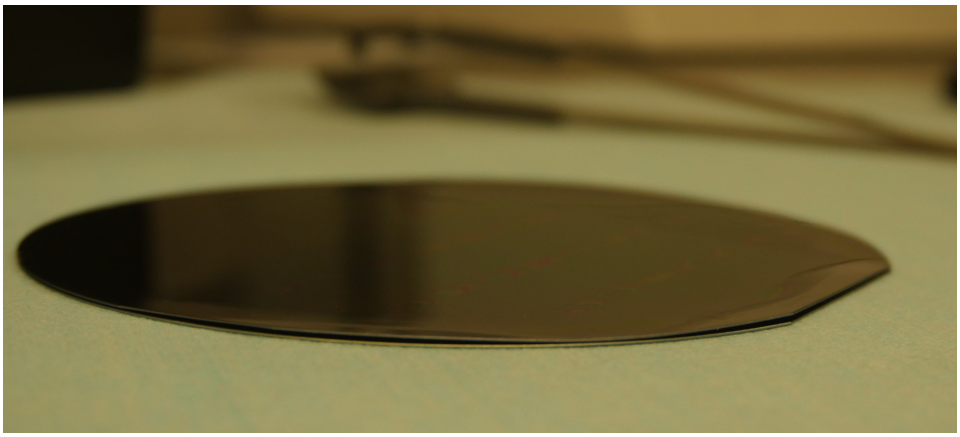

Figure 5.10: Debonding of the wafer

However, by redesigning the production flow one can still produce the designed nozzles. It is possible to replace the SiO^2 hard mask with a photo-resist layer during the DRIE etching. This is only possible if the photo-resist has a high enough selectivity for the specific DRIE etch recipe. Using a small experiment it was determined that the selectivity of a chemically enhanced photo-resist would be around 1:100 for the etch recipe applied in this fabrication process. Taking into account the various uncertainties in this selectivity one needs to apply a safety factor of about 1.5 to 2 on the required photo-resist thickness. As a result, etching a depth of 300 µm, which is the required depth in this study, would require a photo-resist layer thinner than 10 µm. Therefore, one is able to replace the oxide hard mask, that caused the largest complication during fabrication, with a photo-resist mask.

Removing the oxide layers from the production process did not only solve the issues encountered, but also significantly shortened the production time and with it the cost. This reduction in production time and cost is realized by being able to completely skip the deposition, patterning, etching, cleaning and inspection steps involved with the oxide layer. Adjusting the production flow as presented in Section 5.3 with this new methodology would allow one to skip step 2, 3, 4, 5, 7, 12, and 13 making future fabrication much more attainable.

5.6. Modular design

The research presented in this thesis solely focuses on the impact of the nozzle. However, as was mentioned in Chapter 2 these nozzles are also meant to increase the performance of the VLM of the TU Delft. This VLM uses resistive heaters upstream of the nozzle to vaporize the propellant, usually water in the case of the VLM. Thus, to make the designed fabrication process usable for the VLM it needs to be able to accommodate the future addition of heaters.

Previous production processes, such as that described in [11], illuminated the entire micro-thruster in one exposure step. To accommodate the future addition of heaters to the designed nozzle geometries the decision was made to make so called modules. These modules would be exposed individually and would each describe a certain part of the micro-thruster, i.e. the nozzle, the inlet or the heaters.

During the production process one can "stitch" the various modules together by perfectly aligning them for the exposure step. This process does require a high level of alignment accuracy which in this study was achieved by using the ASML PAS5500/80 wafer-stepper.

The implementation of this modular method not only allows for easy implementation of the heater geometry for the final production of the VLM, but also allows for easy production of a wide variety of nozzle-heater combinations aiding in future research efforts. A. Kurmanbay, is currently investigating various heater geometries attempting to optimize the heat transfer. As the dimensions and the production methodology of Kurmanbay's heaters are compatible with the nozzle modules from this study one can easily combine the two. This utilization of modular production design will allow a quick and therefore cheap production of a wide variety microthrusters aiding in future research. Furthermore, possible future commercialization of similar microthrusters will benefit from the modular design, as a produced thruster can be easily adjusted to customer needs.

6

Experimental Setup and Methodology

Due to the various complications experienced during the fabrication of the micronozzles no experimental test could be performed within the schedule of this thesis. As a result this chapter will only describe the test setup and methodology as prepared for the experimental tests, such that future research efforts will be able to reproduce and use this test setup for experimental studies.

6.1. Experimental setup

In this section the entire setup is described that was prepared for the experimental tests. The experimental setup needs to deliver measurements for the massflow and thrust of the nozzles such that the performance metrics defined in Section 4.1 can be calculated. The setup will be described in detail and will allow for the measurements of these variables and more with a good accuracy.

6.1.1. Nitrogen feed system

The experimental tests were designed to be performed with nitrogen as the propellant. Nitrogen was selected as it removes any difficulties of vaporizing water, and simplifies the numerical simulations. The nitrogen feed system is responsible for feeding the nitrogen from its 10 liter storage bottle, where nitrogen is stored at 200 bar, to the micronozzle where pressures ranging from 0.2 to 3 bars are required for this research.
The feed system that is used in the experimental setup is the same feed system as used by [69, 70]. This system and its components can be seen in Fig. 6.1.

The nitrogen bottle has an integrated valve which leads to an in-line rotary valve at the bottom of the feed system board, see Fig. 6.1. This rotary valve feeds the nitrogen past a manometer into a pressure regulator, which steps the pressure down to a user defined value. Precise control of this user defined value proved difficult, as this regulator is manually controlled by a spring loaded wingnut. Therefore, the exact pressures during the experimental tests will differ from the nozzle inlet pressures used in the numerical simulations. From this pressure regulator the feed system continues to the main shut-off valve. Between, the pressure regulator and the shut-off valve Jansen [69] detected a leak. Attempts to fix this leakage were made by [70] but proved unfruitful as the exact location of this leak could not be localized. As a result it is of utmost importance that either the rotary valve or the valve of the nitrogen bottle is closed when the system is not in use to avoid depressurization of the nitrogen bottle.

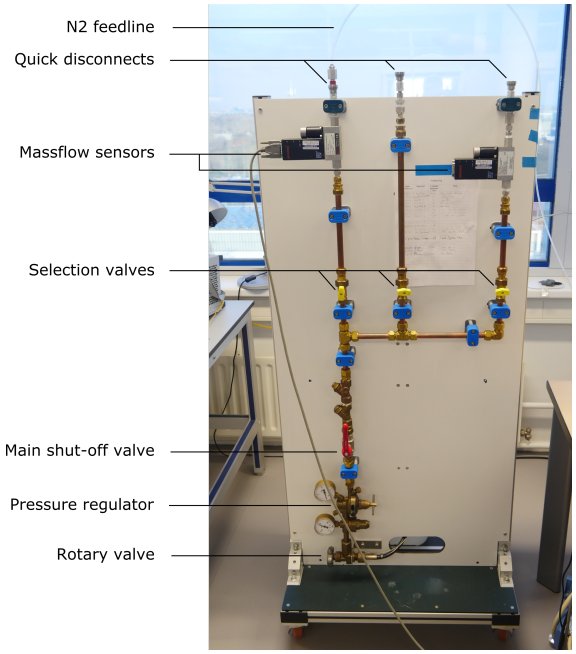

Figure 6.1: Nitrogen feed system board

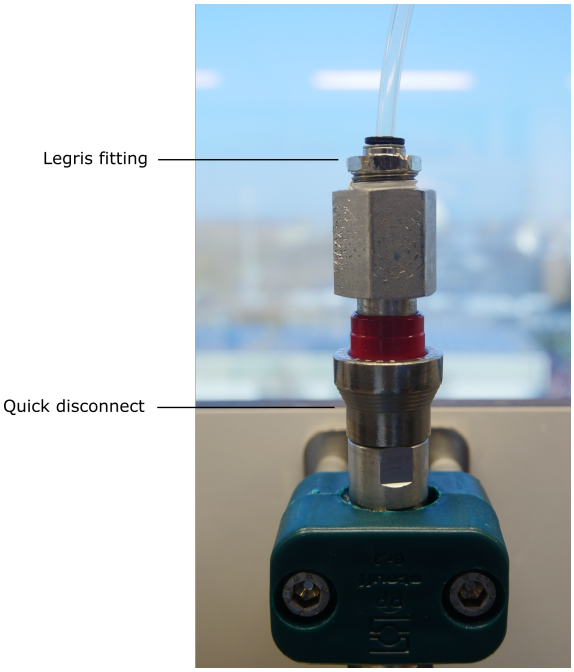

Figure 6.2: Quick disconnect and Legris fitting

From the main shut-off valve the feed system splits up into three branches each with its own dedicated selection-valve to close unused branches. At the point of writing only the left and right branch are in use and have a massflow sensor attached to them. As such further description of the system will be limited to these branches. These massflow sensors, are used to measure the massflow going through the nozzles. Therefore, it is key that any leakage between the nozzles and the massflow sensors is eliminated to ensure the accuracy of the experimental results.

After the massflow sensors, on which more detailed information will be given in Section 6.1.2, the nitrogen flows through a quick disconnect into a Legris push fitting visible in Fig. 6.2. This fitting clamps down a flexible tube with an outer diameter of 4 mm that leads towards the vacuum chamber wherein the experiments will take place. This Legris fitting has shown to be a possible location where leakage can start to occur. This is caused by the deterioration of the material surface of the clamped tube. Once such a leakage is detected it can be fixed by removing the tube, cutting 2 cm of tubing off, and placing it back into the fitting.

This tube leads to a pressure temperature sensor, which was not used in this study, followed by the vacuum chamber feedthrough, as can be seen in Fig. 6.3. One might notice that the in-line pressure temperature sensor is connected to the tube by means of more Legris fittings. The fittings at these locations have shown to be less prone to leakage as they are rarely handled, in contrast to the fitting at the feed system board. However, it is highly recommended to test for leakage at this location before one starts a large scale test campaign.

From the feedthrough, which leads the nitrogen to the inside of the vacuum chamber, the nitrogen flows through a series of Swagelok adapters (SS-QC4-D-400, SS-QC4-B-400, SS-400-R-1). These adapters are glued to a polytetrafluorethylene (PTFE) tube with an inner diameter of 1.5 mm. The other end of this tube is glued using epoxy (Loctite EA 3421) to a LFA tubing adapter from the Lee Company 062 MINSTAC family, this assembly can be seen in Fig. 6.4.

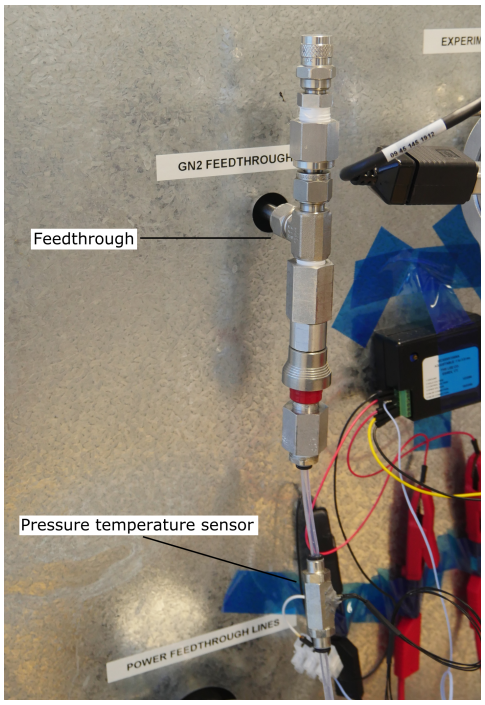

Figure 6.3: Vacuum chamber feedthrough and inline pressure temperature sensor

Figure 6.4: Swagelok to LFA tubign adapter assembly

This LFA tubing adapter connects to a micro solenoid valve, model VHS-M/M-24V, from the same company. The other end of the solenoid valve is connected to a 0.062" PTFE tube from the lee company, this tube then leads to the nozzle interface, which will be described in more detail in Section 6.1.4. This nozzle interface is connected to the thrust pendulum, which is used to measure the nozzle thrust during the experiments, more information on this pendulum will follow in Section 6.1.5. To ensure good long term behavior of this thrust pendulum the 0.062" PTFE tube has to be taped down in a certain orientation. Makhan [70] found that the best results are achieved by taping the tube to the side support pillar of the thrust pendulum, followed by a single loop in the air, subsequently taping it to the pendulum cross beam, and winding the tube down the pendulum arm. Lastly the tube is connected to the nozzle interface through a MINSTAC 062 to 125/156 adapter from the lee company.

6.1.2. Massflow sensors

On the top of the feed system board there are two massflow sensors, one of which was selected to be used for the experimental tests. Note that these massflow sensors are actually massflow controllers with a massflow sensing mode. However, as was noted by [70] the massflow controller mode did not provide stable massflow values and as such the controllers were only used in sensing mode.

These massflow sensors are both of the Brooks 5850S model but are calibrated for different flowrates. To distinguish the two sensors from each other they are called the left and right sensor based on their location on the feed system board as viewed from the from of the board. These sensors are calibrated to measure the nitrogen flow rate, Q, in ml/min under normal conditions ($T = 273.15K$, $p = 1\ atm$). This means that to get massflow in the conventional units of kg/s one has to multiply all the output data with the density of nitrogen at normal conditions, which is 1.2504 kg/m^3 and has to be divided by 60. The detailed characteristics of the two mass flow sensors can be found in

Table 6.1, where F.S. stands for full scale of the measurement range. In the case one uses the sensor in controller mode the set point (S.P.) errors are of interest.

Table 6.1: Massflow sensor characteristics

	Left	Right
Model number	Brooks 5850S-BC1KA1BA0BA1B1	Brooks 5850S-BC1KA1AA0BB1B1
Range & accuracy	0-144 mln/min ±0.2% of F.S. ±0.7% of S.P.	0-2000 mln/min ±0.2% of F.S. ±0.7% of S.P.
Measurement signal	1-5 V or 4-20mA	0-5 V or 0-20 mA
Warm up time	45 min to reach specified accuracy	45 min to reach specified accuracy
Drift	< ±0.5% S.P. per year	< ±0.5% S.P. per year

The mass flow sensors are connected electronically through a 15 pin D-type connection with a custom made printed circuit board (PCB), which can be seen in Fig. 6.5. This PCB receives power from an external powersupply, this power is then fed to the massflow sensors through this PCB. Additionally, it returns the data produced by the massflow sensors to the measurement computer that collects all the data. Lastly, there is a switch on the PCB that determines the mode (massflow controlling or sensing) that the sensors are working in.

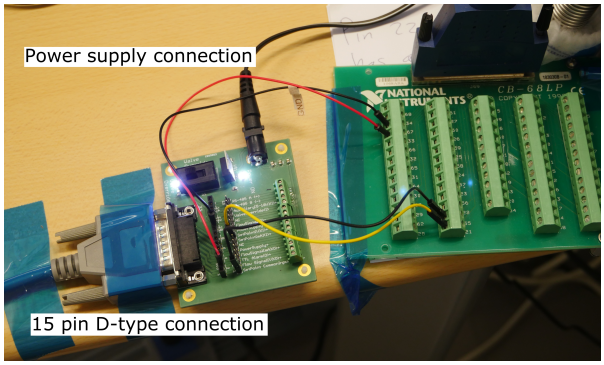

Figure 6.5: Custom PCB for the massflow sensors

The sensors have an uncertainty which is defined as a percentage of the maximum measured value. As a result the uncertainties will be larger, relative to the measurements, at the lower end of the sensors measurement range. This study focuses on very low Reynolds numbers which will result in small massflows. Therefore, choosing the mass flow sensor with the smaller measurement range will result in the most accurate data for the experimental tests. This massflow sensor is able to measure the massflow over the entire range of Reynolds numbers for the linear nozzles. However, the aerospike nozzles have twice the throat area of the linear nozzle, and as a result the expected massflow based on numerical simulations at $Re_t \gtrapprox 1500$ will be beyond the measurement range of this sensor. As such it is decided that for the measurements at said Reynolds numbers will be done with the larger range sensor. To be able to do this, the measurement difference, if present, between the two massflow sensors needs to be identified. The procedure used for identifying this relationship will be explained further in Section 6.2.

6.1.3. Vacuum chamber

All the experimental testing was done in a vacuum chamber, which was pumped down to 30 Pa. The vacuum chamber in question is actually a vacuum oven as it has the ability to heat the inside environment. As this function is not needed for the experimental setup it will be called a vacuum chamber from here on. The vacuum chamber used in the experimental tests is a Heraeus Vacutherm vacuum oven which can be seen in Fig. 6.6.

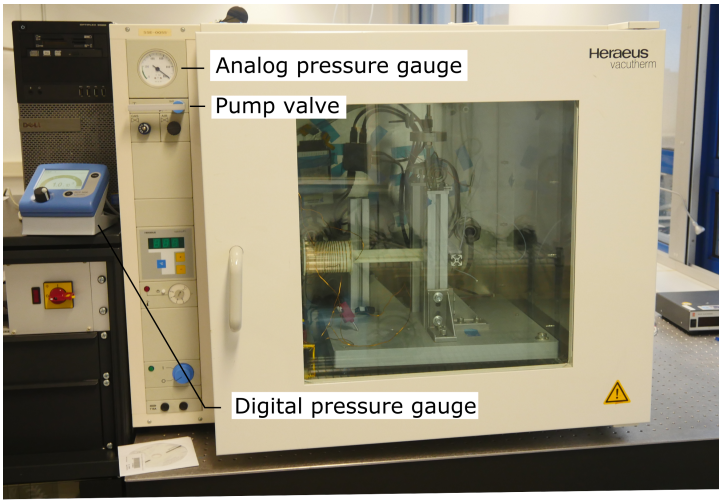

Figure 6.6: Heraeus vacuum oven

The vacuum chamber is pumped down using a Vacuubrand RZ 6 rotary vane vacuum pump. This pump can only be turned off and on and thus only coarse control over the vacuum chamber pressure is possible. Future implementation of a pressure regulator system could improve consistency in vacuum chamber pressures during the experimental tests. However, one can achieve pressure regulation with a very coarse accuracy by manually turning the pump off and on. If such manual control is needed it is of critical importance that special measures are used to prevent reverse flow in the vacuumpump. Thus, if the vacuumpump has to be turned off while a vacuum is present, one first has to close the valve to the chamber, visible in the top left of Fig. 6.6 before shutting off the pump. Secondly, if one then wants to re-engage the pump, one first has to turn on the pump, followed by opening the valve. Fortunately, shutting off the pump during testing is of no interest for the experimental tests in this study.

The pressure of the inside environment of the vacuum chamber is continuously measured by both an analog gauge, which can be seen in in the top left of Fig. 6.6, and by a Vacuubrand DCP+VSP3000 combination digital gauge display combination. This digital gauge was connected to the Data Acquisition (DAQ) system which continuously logs the pressure. Furthermore, due to the digital display it is much easier to accurately read the vacuum chamber pressure compared to reading it of the analogue gauge.

6.1.4. Nozzle interface

In Section 6.1.1 the feedsystem was explained up to the nozzle interface. Here the exact details of the nozzle interface will be explained. The interface is a milled block of PTFE with a size of 22 by 25 mm. This block houses the nozzles by having a milled out notch in the shape of the nozzles. In this notch a cut to size silicon seal is laid, followed by the nozzle itself. To ensure a leaktight seal between the nozzle and the nozzle interface a glass plate is used to firmly press the nozzle in place. Pressure

is applied on this glass plate by means of aluminium brackets which are tightened using screws. A glass plate is used for the interface as it ensures a flat pressing surface. Furthermore, previous research required one to observe inside the evaporation chamber of the VLM. An exploded view of the interface can be seen in Figs. 6.7 and 6.8.

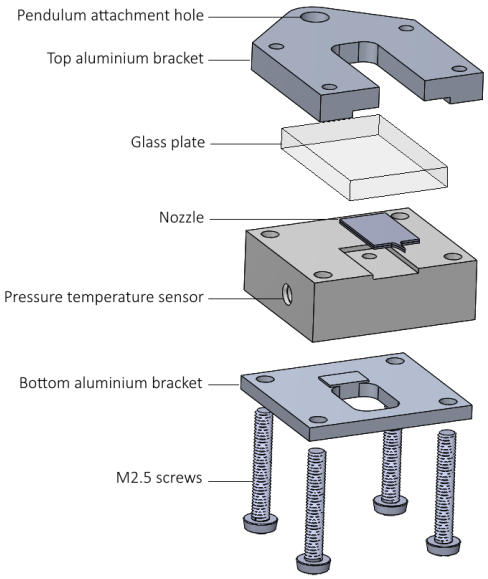

Figure 6.7: left side exploded view of nozzle interface

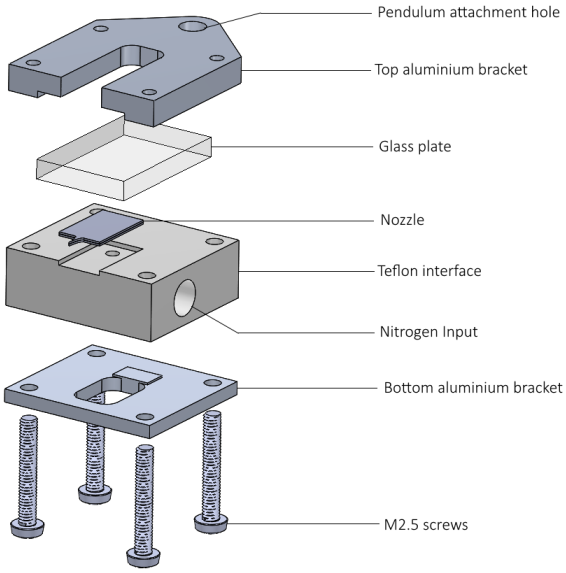

Figure 6.8: Right side exploded view of nozzle interface

In the nozzle shaped notch a large hole is present which feeds the nitrogen to the inlet hole of the nozzles. The hole inside the PTFE block splits up into two holes, one on either side of the interface, see Figs. 6.7 and 6.8. One of these holes is connected to the nitrogen feed system by means of the MINSTAC 062 to 125/156 adapter, described in Section 6.1.1. In the other hole a combined pressure-temperature sensor is glued, which provides the measurements for pressure and temperature at the nozzle inlet. The sensor used in question is a MS5837-30BA sensor by sensor solutions.

6.1.5. Thrust pendulum

Measuring the thrust generated by microthrusters is not a trivial task. Load cells used in the thrust measurement of macro thrusters do not have the measurement accuracy necessary for microthrusters. To still be able to get accurate and reliable results from the experimental tests the AE-TB-5m thrust bench is used. This thrust bench was designed in [71] and improved in [69].

This thrust bench which can be seen in Fig. 6.9, is a pendulum with a mass at the top, a rotational spring at the hinge-point, and at the bottom of the pendulum the nozzle interface is attached. Due to the steady thrust produced by the nozzle the pendulum will rotate slightly to a new resting position. The distance between the original (no thrust) and new resting position is measured, using a CS2 displacement sensors, and compared to the displacement measured under a well characterized calibration force. Performing this comparison allows for the determination of the thrust generated by the microthruster with a good accuracy.

The spring at hinge point of the pendulum allows for a greater thrust measurement range as it provides a counterforce to reduce the rotation caused by the nozzle thrust. With this larger thrust mea-

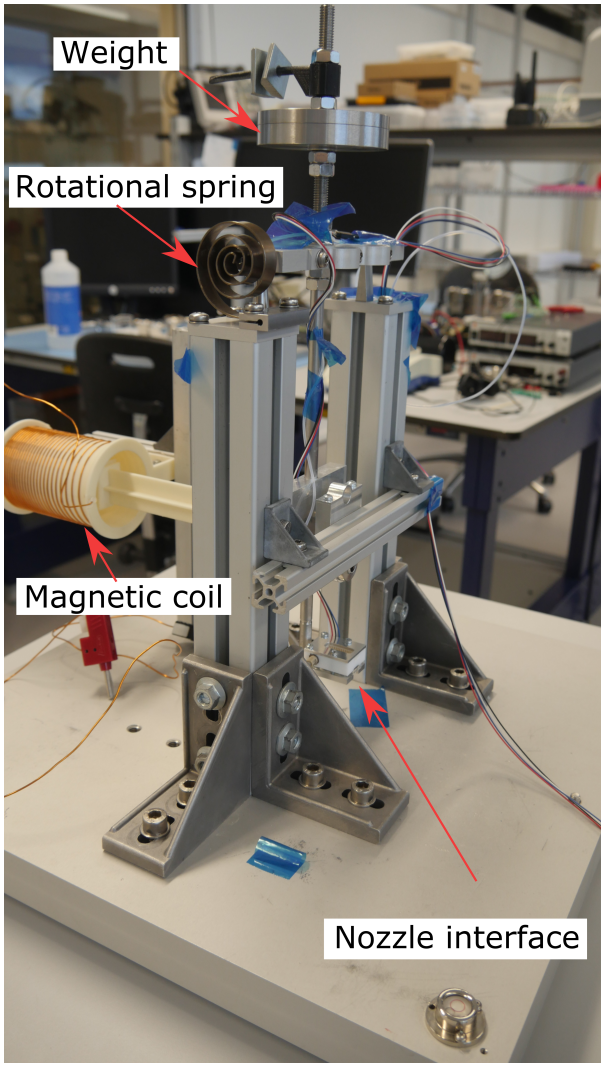

Figure 6.9: AE-TB-5m thrust pendulum

surement range also comes a reduced accuracy, due to the measurement resolution of the CS2 sensor. From the numerical study steady state thrusts between 87 µN and 3.73 mN were predicted. The thrust bench without the spring is not able to measure thrust ranges above 2 mN. As a result it is recommended that some of the cases, especially those at low Reynolds numbers, are performed both with and without the spring and the rest only with the spring. By measuring the lower Reynolds cases with and without the spring one can make sure that the measurements are consistent with each other.

The thrust pendulum is designed to allow for consistent measurements of thrust even if the pendulum is modified between tests. This is the result of the automated calibration procedure as developed by [69]. The pendulum is calibrated using a current loop causing a magnetic field whose properties are extremely well defined, this can be seen in Fig. 6.9. The relation between the magnetic force caused by the current loop and the current itself was determined by both [69, 71] and differed slightly from each other. The relationship as determined in [69] was used for this study as it was determined more recent and in the time between [71] and [69] the pendulum was deconstructed and reconstructed by [69]. As a result of this, the force-current relationship that is used can be seen in Eq. (6.1).

$$F[mN] = 0.827 \cdot I[A] \pm 13.1 \cdot 10^{-3} \tag{6.1}$$

This pendulum was placed sideways into the vacuum chamber as it was found that the natural oscillations of the building would introduce the least amount of noise into the measurements using this orientation.

6.1.6. Electrical and data connections

In the experimental setup there are many devices that generate measurements which need to be collected into a single location and stored for analysis. Furthermore, there are also devices that need be controlled remotely as access is restricted when the system is in the vacuum chamber for testing. This all is done by the cleanroom computer in combination with National Instruments (NI) DAQs.

Most devices were not connected directly to the cleanroom computer but through DAQs. Five devices were directly connected to the computer, these devices were: The NI PCI-6229 DAQ which is an internal add in card for the computer, an USB hub, the DT6220/DL6230 DAQ which is connected through a CAT-5E ethernet cable, the DCP+VSP3000 vacuum chamber pressure sensor, and a RedBearLab Blend Micro control board connected through usb.

The NI PCI-6229 DAQ is connected to two NI CB-68LP breakout boards through a 136 to 2x68 pin cable. One of these boards is connected to the Delta Elektronika SM7020 and SM7020-D power supplies, visible in Fig. 6.10. These power supplies provide the power to the magnetic coil on the thrust pendulum with which it is calibrated. The signal that defines what current the power supplies send to the coil is forwarded through the NI CB-68LP breakout board. It is important to note that to control the power supplies through the LabVIEW code, which is used to collect all data and control devices remotely, the switches on the back of the power supply have to be set to "program" for current and "manual" for the voltage. The other NI-CB-68LP breakout board provides the connections from the computer to the custom PCB of the massflow sensors.

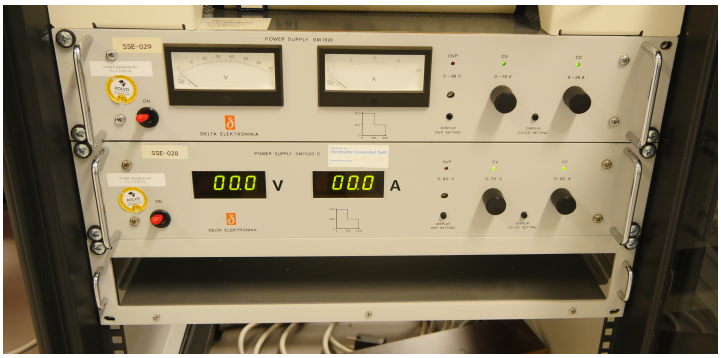

Figure 6.10: Delta Elektronika SM7020 and SM7020-D power supplies used for thrust pendulum calibration

The USB hub splits the signals to and from the computer to three NI DAQs: A NI USB-6008, a NI USB-8451, and a NI USB-9162+NI9211. The NI USB-6008 and the NI USB-8451 are both connected to a breadboard which can be seen in Fig. 6.11. This breadboard is connected to the pressure temperature sensor inside of the nozzle interface. Furthermore, this breadboard can also be connected to a liquid massflow sensor if any thrusters need to be tested with a liquid propellant such as water. The pressure-temperature sensor is connected to the breadboard with a 4-pin header at the top left corner of the breadboard with the blue wire oriented to the top, see Fig. 6.12.

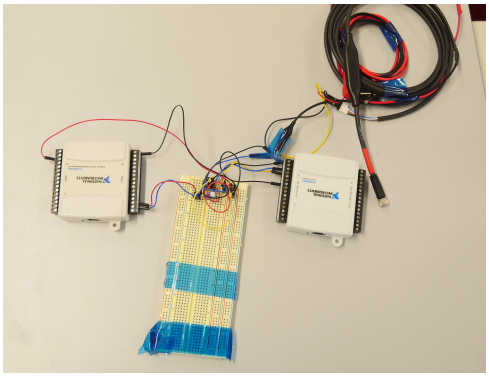

Figure 6.11: Breadboard connected to the NI USB-6008 and NI USB-8451 DAQs

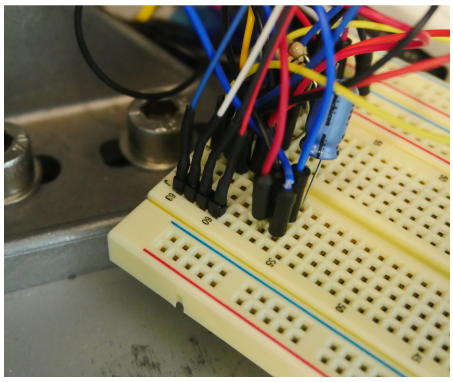

Figure 6.12: Orientation of pressure-temperature connection

The NI USB-9162+NI9211 is actually a DAQ (NI9211) inside of a DAQ to usb adapter (NI-USB9162), as can bee seen in Fig. 6.13, and allows for the measuring of temperatures through thermocouples. Thermocouples were not used in this research however, as the LabVIEW code is programmed around the use of thermocouples it is looking for this DAQ. As a result running the LabView code without the NI USB-9162+NI9211 DAQ will lead to an error and failed measurement collection.

Figure 6.13: NI USB-9162+NI9211 DAQ combination

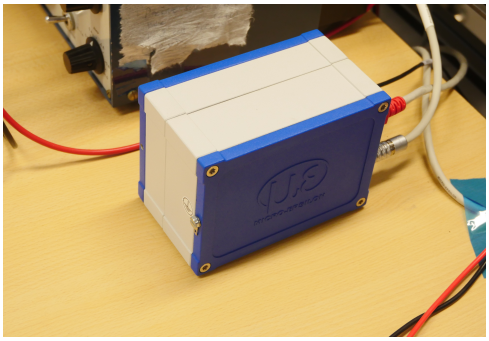

Figure 6.14: DT6220/DL6230 DAQ for the CS2 displacement sensor

The DT6220/DL6230 DAQ is a DAQ designed solely to interface with the CS2 displacement sensor. The DAQ is placed outside of the vacuumchamber, see Fig. 6.14, and is connected to the CS2 sensor through one of the many feedthroughs in the vacuum chamber.

The DCP+VSP3000 vacuum chamber pressure sensor is connected directly to the cleanroom computer through the use of a RS-232C serial cable. Through the use of LabVIEW the measurements made by the pressure sensor will be combined with the data of the NI DAQs

Lastly, the RedBearLab Blend Micro control board is used to control the solenoid valve of the nitrogen feed system remotely. This solenoid valve needs a continuous 3.2 Volt and a peak voltage of 24 Volt for 0.35-2[ms] during actuation. For this reason two power supplies are used, one for the peak and one for the continuous power. The power supplies used for peak and continuous are the Delta Elektronika E030-1 and D030-1 respectively, visible in Fig. 6.15, which in their turn are connected to the RedBearLab Blend Micro control board. Inside the vacuum chamber the power supplies are

connected to the solenoid valve through an RS232C connector which ends in three strands, two of which end in two power connections, see Fig. 6.16. The connection that is not labeled with the white tape has to be used if one uses only a single solenoid valve.

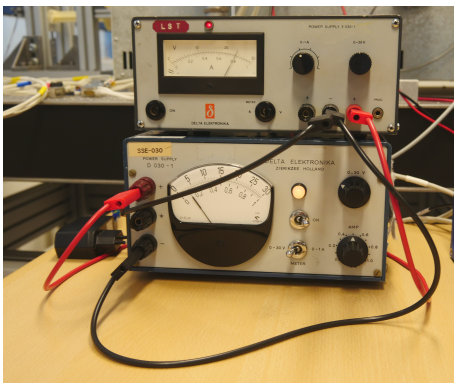

Figure 6.15: Delta Elektronica E030-1 and D030-1 providing power to the solenoid valve

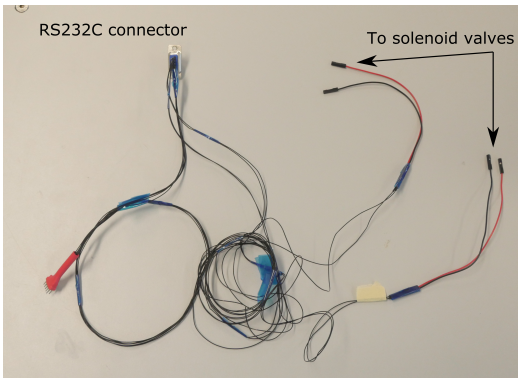

Figure 6.16: Wiring to power the solenoid valve

All these different connections to the computer are combined into one through the use of a LabVIEW code. This code not only gathers the data from all sources and logs them into one file but it also acts as a user interface trough which the entire system can be monitored and controlled.

6.2. Preliminary tests

Before a large scale test campaign can be undertaken various smaller tests have to be performed to ensure the proper functioning of the system. These various tests will be described, and if they were performed their results be treated.

6.2.1. Mass flow sensor relation identification

As was described before the decision was made to use the left mass flow sensor (small measurement range) for the majority of the experimental tests. It is expected that the experiments on the aerospike nozzles at higher Reynolds numbers will exceed this sensors measurement range. Thus for these experiments at higher Reynolds the right sensor will be used. However, the results obtained with the right sensor need to be consistent with the left sensor. To ensure that this is the case the relation between the results of the left and right sensor has to be identified.

This relationship is identified by comparing flowrate-(inlet)pressure curves of the two massflow sensors for the same nozzle. The relationship is defined such that the curve of the right sensor is closely fitted to the curve of the left sensor, which was selected as the main massflow sensor in this study. It is of critical importance that the flowrate-pressure curves cover the transition point where one switches from the left to the right sensor. This transition point is logically near the upper limit of the left sensor.
Failure to measure near the transition point would lead to an exaggerated influence of the errors of the right sensor on the relationship.

In this report the relationship could not be defined as no nozzles were available that would provide flowrates at the transition point at reasonable pressures. However, to see if the concept would work the test was performed with an old nozzle fabricated by Silva [11], which was also tested by Makhan [70].

The setup of this relationship identification is the exact same as described in the sections above. The test consisted of two runs varying the used massflow sensor between the two. In each of the runs the nozzle inlet pressure was set at 2.5 bars, using the pressure regulator, and slowly decreased over time by closing the main shut-off valve and opening the nozzle solenoid valve. During this time the flow rate and the pressure at the nozzle interface were continuously measured. In Fig. 6.17 one can see the flowrate-pressure curve.

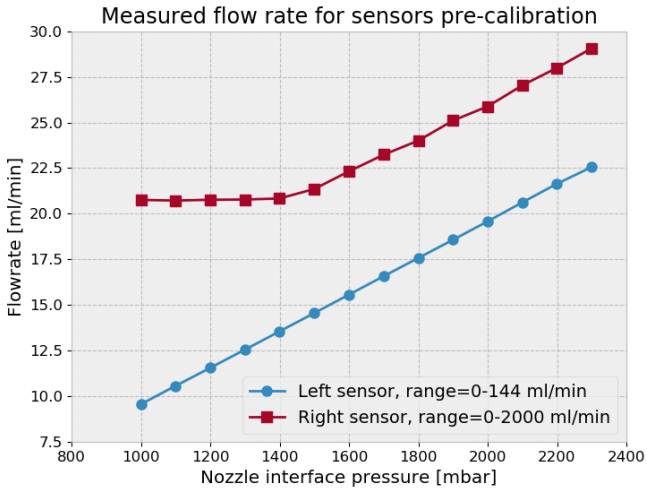

Figure 6.17: Measured flow rate for the mass flow sensors before calibration

From this graph it becomes apparent that there are some issues with these results. A difference between the two sensors is to be expected due to internal differences and errors due to the accuracy of the sensors. Generally the curve should describe a linear relation for nozzles, as was seen in the figures describing the absolute massflow over Reynolds numbers in Chapter 4. Therefore, the flattening of the results for the right sensor in Fig. 6.17 are cause for concern. As the sensors were not calibrated in the last 10 years it was decided to send them both for calibration. After calibration the same experiment was run again, the results of which can be seen in Figs. 6.18 and 6.19. One can see that the calibration resulted in results that are more in line with expectations.

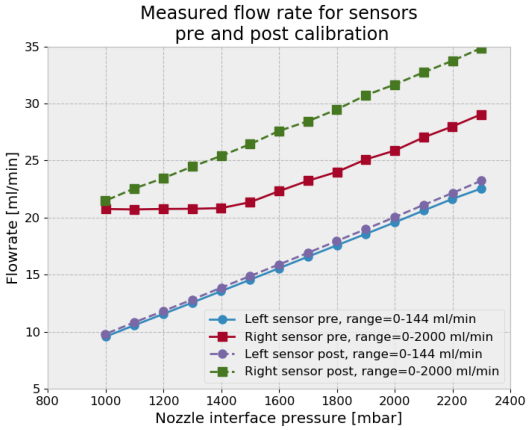

Figure 6.18: Measured flow rate for the mass flow sensors before and after calibration

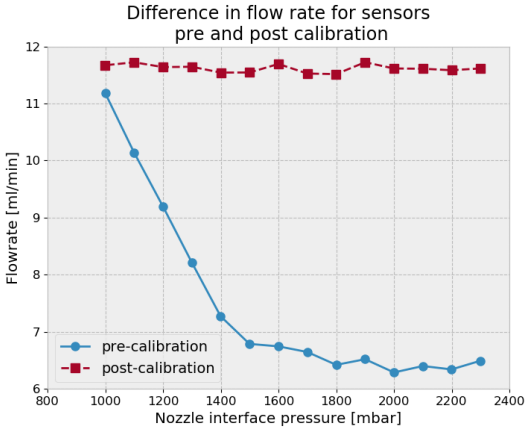

Figure 6.19: Difference in measured flow rate before and after calibration

It can be noticed that after calibration there is an offset, which is fairly constant, in the measured curves. This offset can be explained by the fact that the curves were measured over very low flowrates.

At these flowrates the error of the right sensor is relatively large and could result in the offset observed. For this reason it is of key importance that this relationship determination is done near the upper limit of the left sensor, once the aerospike nozzles are available, which will have massflows outside the measurement range of the left sensor.

Thus for experimental testing in the future it is of key importance that this test is repeated near the transition point. After which the two curves are compared and the relationship between the curves can be determined and applied to the results to get consistent results.

6.2.2. Leakage test

In addition to the massflow sensor relation one also needs to make sure that no leakage is present between the exit of the massflow sensor and the nozzle inlet. This is of importance as any leakage in that section of the feed system would result in a higher measured massflow than truly is present in the nozzle.

For this reason four nozzles which were intentionally produced with a blocked nozzle were present on each of the wafers containing the linear nozzles. This was done by completely removing the nozzle module during production and only using the inlet module.

Using these blocked nozzles one can experimentally determine if any leakage is present. This is done by pressurizing the system using the blocked nozzle in the interface. A leak is present if the massflow sensor will measure any non-zero massflow. Using this procedure one can firstly investigate if a leak is present, if a leak is present one can investigate its origins and fix the leak. The suggested method of investigating the origins of a leak differs depending on the magnitude of the leakage. In the case of a large leak one can apply soapy water to all the connections in the pressurized feedsystem and look for bubbles, which will form at the leakage location. In case a leak is too small to locate using soapy water a helium sniffer is suggested.
Lastly, if the leak cannot be located one can at least characterize the leak, by measuring massflow rate for various pressures, which can be subtracted from the measured massflow to acquire the real massflow.
Unfortunately due to the complications in production this experiment could not be performed as the blocked nozzles were not present.

6.3. Test procedure

In this section a step by step checklist is presented which was designed to be used during the experimental testing. Through the use of a checklist one can ensure that the steps followed are the same for each test, minimizing the chance of human error.

Step	**Description**	**performed Y/N**
1	Safety checks:	
	1. Check if the vacuum chamber is empty and is cold.	
	2. Check if all valves of the nitrogen feed system are closed and that the system is at atmospheric pressure.	
2.	Physical setup:	
	1. Clean the surface of the nozzle that will be pressed against the seal using Isopropyl alcohol (IPA).	

	2. Insert the to be tested nozzle inside the nozzle interface and attach the interface to the pendulum.	
	3. Put the thrust pendulum in the vacuum chamber with the magnetic coil oriented to the left wall of the vacuum chamber.	
	4. Connect the quick disconnect inside the vacuum chamber.	
	5. Attach the solenoid valve to the 1.5 mm PTFE tube leading from the vacuum chamber wall. The power terminals should be on the side that is being attached in this step. NOTE: Hold the solenoid valve at the plastic ends when screwing in the tube.	
	6. Attach the solenoid valve to the 0.062" PTFE tube that leads towards the thrust pendulum. NOTE: Hold the solenoid valve at the plastic ends when screwing in the tube.	
	7. Attach the 0.062" PTFE tube to the nozzle interface and check that the connectors is screwed in tight.	
	8. Check that the nitrogen feed is connected to the to be used branch of the nitrogen feed system board.	
	9. Fully close the wingnut of the pressure regulator.	
	10. Open the nitrogen bottle valve.	
	11. Open the rotary valve and check if there is enough nitrogen for the test.	
3.	Electronical setup:	
	1. Connect the NI DAQs to the USB hub (NI USB-6008, NI USB-8451, and NI USB-9162+NI9211).	
	2. Connect the pressure temperature sensor of the nozzle interface to the breadboard.	
	3. Connect the CS2 displacement sensor to the DT6220 /DL6230 DAQ.	
	4. Connect the power lines of the magnetic coil to terminal 1 and 2 on the power brick in the vacuum chamber.	
	5. Attach the RS232C connector of the solenoid valve wiring on the left hand side of the vacuum chamber and connect the leads to the solenoid valve power terminals.	
	6. Attach the D-type cable to the correct mass flow sensor and custom mass flow sensor PCB.	
4.	Powering on systems and wait for warm-up time:	
	1. Turn on the Delta Elektronika E030-1 and D030-1, and check the voltages they output. These voltages should be 24V and 3.2V respectively. These power supplies have a 1 hour warm up time.	
	2. Turn on the Delta Elektronika SM7020 and SM7020-D, and check the position of the switches on the back. These have a 1 hour warm up time.	
	3. Connect the power supply of the massflow sensors to the PCB. Put the switch on the board to the left. A bright white LED should light up and an audible click from the massflow sensor should be heard. The mass flow sensor has a 45 minutes warm up time.	
	4. Turn on the DT6220/DL6230 DAQ. It has a 15 minute warm up time.	
	5. Power the USB hub that connects all the DAQs to the computer.	

5.	Checking the system	
	1. Open program "main_TEST_wDisplacementSensor.vi" to be found in "D:\Userdata\Chaggai\Chaggai_N2_TEST_Including _Displacement_Sensor\" and actuate the solenoid valve with the vacuum chamber door open, a click should be heard. If not heard inverse the polarity of the solenoid terminals and try again.	
	2. Using the same program as step 5.1 check that all data is properly being read.	
	3. Stop the program.	
	4. Start the DT6200 tool and look at the distance measured without any thrust by the CS2 sensor.	
	5. Move around the weights at the top of the thrust pendulum to get a measured distance, by the CS2 sensor, of the unexcited pendulum which is below 1000 μm.	
	6. Stop the program.	
6.	Testing	
	1. Close the vacuum chamber door and start pumping down. Wait till the vacuum chamber pressure gauges measure 30 Pa.	
	2. Start the DT6200 tool and click "Protocol" to log the displacement data for calibration.	
	3. Start LabVIEW program "Pendulum_Calibration_Required _Range_exploration.vi" from folder "D:\Userdata\Chaggai \Pendulum Calibration\" and run the code to start calibrating the thrust pendulum, this will take around 15 minutes. Once completed LabVIEW will provide a popup message that it is done. Note this popup message can be mistaken for a warning message.	
	4. Close the tools and save the calibration data to the nozzle sample test folder.	
	5. Slowly open the shut-off valve and the selector valve of the branch to be used on the feed system board.	
	6. Either open program "main_TEST_wDisplacementSensor.vi", if the right massflow sensor is used, or "main_TEST_wDisplacementSensor_andMFCdiff.vi" if the left massflow sensor is used. Both codes can be found in "D:\Userdata\Chaggai \Chaggai_N2_TEST_Including_Displacement_Sensor\". Before starting the code check that the save path does not override old data. After this start the program and open the solenoid valve. This is done to reduce the pressure in the feedsystem to below atmospheric minimum value attainable is around 0.3 bar this can take up to 1.5 hours. Once 0.3 bar is achieved close the solenoid valve and stop the program.	
	7. In this step the actual data is gathered. Thus, open the same code from the previous step, select the correct save path for the data, and run it. Let the pendulum reach a steady position (Noise amplitude less than 10-15 micron) before moving to the next step.	

	8. Open the manual pressure regulator very slowly, while watching the live data visualization, to the point where nitrogen just starts flowing (one should see a sudden spike in the massflow measured). This pressure will be the lowest possible regulated, and thus constant, pressure possible with the system.	
	9. Let the pendulum achieve a steady position and wait another 60 seconds.	
	10. Open the pressure regulator to the next nozzle chamber pressure of interest.	
	11. Repeat steps 6.8 to 6.10 until the entire range of nozzle chamber pressures has been tested.	
	12. Close solenoid valve, stop the LabVIEW program chosen in step 6.6, and store the data in the nozzle sample folder.	
	13. Perform a second pendulum calibration test (step 6.2-6.4).	
7.	Finalization:	
	1. Close the pressure regulator, shut-off valve, and selector valve.	
	2. Re-pressurize the vacuum chamber.	
	3. If another nozzle is to be immediately tested repeat step 2.1 to step 6.13, note that some steps can be skipped as the system is set up and warmed up. Otherwise if no other tests will be carried out shut off all tools, close all valves, and remove all devices from the vacuum chamber.	

6.4. Analysis methodology

The raw data that is gathered during the experimental tests needs to be processed further to be useful for analysis. These processes that are applied will be briefly described below.

The variables that are the most important are the thrust, massflow and specific impulse. As mentioned in the test setup the thrust pendulum does not measure the thrust produced but rather the distance. As a result of this it is necessary to convert the distance measured to a force, by applying the calibration procedure.

During the experimental tests two calibrations, one before the test and one after the thrust measurements, are done as it was noticed that there is a slight drift over the duration of a test. Using the data from these calibrations two displacement force curves are made. The average of these two relations is the force displacement curve used to analyze the test data.

The force that the magnetic coil applies on the pendulum during the calibration is not at the same distance from the pendulum pivot point as the thrust from the nozzle during testing. As a result the thrust calculated through the calibration curves needs to be multiplied with a constant which is determined by:

$$\varepsilon_F = \frac{l_{mag}}{l_{nozzle}} \tag{6.2}$$

where l_{mag} is the distance from the pendulum pivot point to the magnetic coil, and l_{nozzle} is the distance from the pivot point to the nozzle exit plane.

As the specific impulse can be calculated from the massflow and the thrust the only remaining measurement that is of key importance is the massflow. As mentioned before this can easily be acquired by converting the flow rate as measured by the massflow sensors. Using this, one can calculate the various performance metrics as defined in Section 4.1 and start the analysis of the nozzle performance.

7

Conclusions and Recommendations

In the previous chapters the reasoning, numerical simulation methodology, numerical simulation results, fabrication, and experimental setup for the micronozzle research were presented. This chapter will present the conclusions and recommendations based on the outcomes of this research effort. Starting with the conclusions in Section 7.1 followed by the recommendations in Section 7.2.

7.1. Conclusions

At the start of this thesis a research objective was formulated:

The research objective is to help improve the understanding of better performing micronozzle geometries and make recommendations for future improvements for the micronozzle performance, such that future microsatellites are enabled to perform more complicated missions, by identifying suitable ways to analyze the flowfield, analyzing the flowfield in alternative micronozzle geometries, and experimentally testing and validating the performance of said geometries.

To fulfill this research objective firstly the nozzle geometries of interest were indentified. These geometries were linear nozzles with three different divergence half angles (θ_{out} = 15°, 30°, 45°) and aerospike nozzles truncated at 20%, 40% and 60% of the full spike length. Numerical simulations were performed on these six nozzle geometries to determine their performance over a range of Reynolds numbers. For these numerical simulations a numerical solver was selected based on available resources such as time, cost, and availability. Based on these criteria it was decided that the numerical simulations would be performed using the rhoCentralFoam solver from the open source C++ CFD toolbox OpenFOAM. This selection was made as more accurate methods such as DSMC solvers would take weeks if not months to simulate a single nozzle. Thus this would be unfeasible within the time constraints of a Msc. thesis. Other options, such as hybrid DSMC-Navier-Stokes solvers, were considered however, no affordable and widely validated solvers were available. The rhoCentralFoam solver was specifically selected for it widespread validation and its computational efficiency in simulation cases covering a large range of Mach numbers.

Using rhoCentralFoam the six nozzle geometries were simulated for throat Reynolds numbers between $Re_t = 191-2861$, using both slip and no-slip wall conditions, for a total of 84 simulation cases. Comparing the nozzle performance was done by the using non-dimensional performance metrics η_F, C_D, and $\eta_{I_{sp}}$. For which pressure, density, velocity and dynamic viscosity need to be drawn from

the numerical simulation results. Furthermore, the addition of the temperature allows the calculation of the Mach number which provides very valuable information of the boundary layer thickness.

Contour plots were made based on the Mach number. The plots indicated that the flow in the linear nozzles locally becomes fully subsonic, which shows that the flow is heavily dominated by viscous effects. In comparison this is much less visible for the aerospike nozzles where the flowfield was very comparable to that predicted for macro scale aerospikes. This indicated that for aerospike nozzles viscous losses are of lesser concern compared to the linear nozzles.

Numerical simulation results showed that of all the nozzles the linear nozzle with $\theta_{out} = 30°$ provides the best η_F, C_D, and $\eta_{I_{sp}}$ for $Re_t > 1200$. Below this Reynolds number the $\theta_{out} = 45°$ nozzle is the optimal choice. Furthermore, it was found that the decrease in performance caused by the corner merging of the boundary layer is more pronounced for nozzles with smaller divergence angles. Additionally, it was hypothesized that a shallow nozzle depth even further amplifies the effect due to merging of the boundary layers from the various corners, that already were thicker due to the merging in their respective corner. It is hypothesized that this combined is the reason why, in these numerical simulations, the $\theta_{out} = 15°$ never outperforms the other linear nozzles.
In contrast to results from the literature it was found that compared to the best linear nozzle, the best aerospike nozzles on average performs lower by 24.7% for the thrust efficiency, 15.5% for the discharge coefficient, and 14.4% for the specific impulse efficiency. This was attributed to excessive loses caused by flow expansion in the etch direction, past and over the edge of the spike body. This resulted in an additional of axis loss of 20% compared to the linear nozzles. Additionally it was found that for the various aerospike nozzles the thrust was truncation independent, resulting in the same thrust efficiency for all the aerospike nozzles. This, combined with a lower discharge coefficient for the less truncated nozzles results in better specific impulse efficiencies for the less truncated nozzles. The difference in the discharge coefficient can be attributed to a larger deviation from the ideal spike contour, caused by the presence of a thicker boundary layer, which results in a sub-optimal expansion.

Based on the results, improvements in the nozzle geometries can be suggested. Specifically for the aerospike nozzles it is suggested that one replaces the aerospike nozzle geometry with a double depth design. In this new design the depth of only the spike center body is increased, while the section upstream of the throat remains at the 100 µm depth, imposed by the requirements. By applying this double depth approach one is able to prevent the majority, if not all, of the over the edge expansion. This new geometry was investigated with an additional 70 numerical simulations. Using these it was found that by employing a double depth aerospike design one is able to increase specific impulse efficiencies by up to 41.2% with respect to the single depth aerospikes. Comparing the best performing double depth aerospike nozzle to the baseline best performing linear nozzle, results on average in a 24.7% higher specific impulse efficiency.

Through this numerical study the nozzle geometries were investigated, and improvements to the nozzle geometry were suggested. However, the research objective also states the experimental testing and validation of the six initially selected nozzle geometries. For this reason a production flow was designed, according to which the nozzles were manufactured in the Else Kooi Laboratory. During the micronozzle production complications arose which resulted in the failure of the first production run. This failed production run led to a delay that made experimental testing of the nozzles impossible within the schedule of a Msc. thesis and as a result this was scrapped for this thesis. A new production flow was designed based on the learned lessons. By replacing the silicon dioxide layer, which is used as a hard mask during DRIE etching, with a thick photo-resist layer, one gets a functional, reliable, faster, and cheaper production process. During the production process it was also confirmed that due to maturation of various production processes within the Else Kooi Labo-

ratory the accuracy to which features can be etched is significantly better than the past production runs indicated [6, 11].

While not the entire research objective was fulfilled, it is clear that with this study massive steps forward have been made in the field of micronozzles, realizing specific impulse efficiency increases of 24.7% with respect to the industry standard linear nozzles, identifying various mechanisms causing the losses, and suggesting methods to improve future designs. It is believed that the new double depth aerospike nozzle could allow more efficient propulsion subsystems of nano- or picro satellite missions. These improvements can aid in future decreases in cost of accessing space and space exploration altogether.

Finally, in the beginning of this thesis various research questions were posed based on the research objective. Below answers on these questions will be treated briefly.

1. **Are the computational results in the literature in line with the experimental results and with what accuracy?** This research question can unfortunatelly not be answered due to the absence of experimental data.

   (a) **What are the flowfield characteristics of the selected geometries?** Through Mach contour plots it was found that the linear nozzles are heavily dominated by viscous forces, with locally the entire flow becoming subsonic. This behavior was not observed in the aerospike nozzles, where the flow behavior is much more reminiscent to that of a macro scale aerospike nozzle, due to the free boundary layer mechanism. Furthermore, in the case of the linear nozzles a mechanism called corner boundary layer merging was observed. This mechanism causes further reductions in nozzle performance through a effect dependent on both nozzle depth and nozzle divergence angle.

   (b) **What is the best way to analyze the flowfield, taking into account availability of resources such as time, cost and availability at the university?** The best way to numerically analyze the flow field is through the use of a continuum based solver from the OpenFOAM toolbox. Other options, were either too computationally demanding (DSMC) or were not freely available (hybrid solvers). Because of the proper validation, and the fact that no other limitations regarding licensing were present OpenFOAM was selected.

   (c) **What are the most valuable variables to look for in a flowfield to assess its performance?** To compare the various nozzles using the performance metrics, pressure, density, velocity and dynamic viscosity need to be known. Furthermore, the addition of temperature allows for the calculation of the Mach number. As a result these five variables are the most valuable.

2. **Can alterations to the nozzle geometry improve the performance, and if yes what alterations are recommended?** It is shown that alterations to the nozzle geometry have a large impact on the nozzle performance. Based on the findings of the numerical study it was found that by using a double depth aerospike design the performance of a micronozzle can be increased by up to 41.2% with respect to the single depth aerospike design. Other suggestions that could lead to improvements can be made based on the observations but have not been studied yet. Therefore, no conclusive answer can be provided if these suggestions would lead to improvements. An example of such a suggestion is increasing the linear nozzle depth with decreasing throat width to maintain equal throat area. Another possible suggestion could be to make alterations to the profile of the aerospike nozzle to accommodate for boundary layer growth.

(a) **Is there a relationship between the characteristics of the flowfield and the experimental performance of the micronozzles and how can this relation be used to improve future designs?** This research question can unfortunately not be answered due to the absence of experimental data.

(b) **How do the performances of the different geometries relate to each other?** During the numerical simulations it was found that of the initial six geometries the $\theta_{out} = 30°$ nozzle has the highers performance for all three performance metrics at $Re_t > 1200$. For lower Reynolds numbers the $\theta_{out} = 45°$ nozzle is the optimal choice. Single depth aerospikes proved inefficient with the best performing aerospike having on average a 24.7% lower thrust efficiency, 15.5% lower discharge coefficient, and 14.4% lower specific impulse efficiency compared to the best linear nozzle. Based on the results from Pearl et al. [8] it is hypothesized that this could be reduced by making the entire nozzle deeper. However, the conclusion still remains that, for the nozzle depth investigated, single depth aerospikes are not an attractive alternative to the industry standard linear nozzles. These finding led to the suggested geometry alterations such as the double depth aerospike which was treated in question 2.

7.2. Recommendations

During the research various points came up which could provide valuable information for future micronozzle or micro propulsion efforts. In this section each of these points will be treated with an argumentation of its beneficial nature for the future of micronozzle and micro propulsion.

DSMC simulations

In the numerical results of this research it was observed that areas of high Knudsen numbers exist for simulations at low Reynolds numbers. As the areas of interest still remained within acceptable ranges of Knudsen numbers it is assumed that the results are still quantitatively useful but that inaccuracies in the results exist. Quantifying these inaccuracies would allow for the development of better validity criterium for the continuum based numerical simulations. As such it is advised to perform DSMC simulations to quantify the errors present in the numerical study of this report. During the thesis research an attempt was made to simulate a single case using DSMC to quantify the errors. During this attempt it was observed that the amount of computational particles necessary to fulfill the quality requirements of DSMC would exceed 100 million particles. This resulted in computational times exceeding months for a single case on a high performance cluster using 48 cores. Therefore, it is recommended that for future research using DSMC simulations either the computational domain is reduced in size, or that one requests access through the surf sara programme to the Lisa or Cartesius supercomputer [72].

Multiphase flow simulations

The research presented in this report is partially aimed at aiding the development of the TU Delft VLM microthruster. This thruster will be using liquid water as its propellant, which it vaporizes in a heater chamber before the micronozzle. While efforts are made into making this heating highly efficient it is plausible that the water is not fully vaporized at the nozzle inlet. Liquid water has a viscosity that is orders of magnitude larger than gaseous water. As a result it is likely that the presence of some form of multiphase flow has consequences for the viscous losses and the underlying mechanisms at play inside the nozzle, and thus on the overall nozzle performance.

Temperature varying flow simulations

In this report the flow is simulated under cold gas conditions with a fixed wall temperature. However, if one of the nozzles from this study would be implemented in the VLM then the fluid at the inlet of the nozzle would be at an elevated temperature. Furthermore, heat generated by the heating elements used in the chamber of the VLM will also indirectly heat up the nozzle walls. As higher temperatures in steam correspond to higher viscosities one can assume that it might result in higher viscous losses. As such it might be of interest to investigate the effect of the temperature on the viscous losses.

Alternative aerospike contours

The Angelino method, as described in [26], was applied to design the contour used by the various aerospike nozzles. However, as was noted in Section 4.2.2, the discharge coeffient experienced by these nozzles were dependent on the truncation length of said nozzle. With higher truncations resulting in higher discharge coefficients. This tendency was attributed to the thicker boundary layer present in less truncated nozzles. Which by their presence changed the effective spike contour away from the ideal, and thus restricted the flow from expanding ideally. Thus, by altering the spike contour one can leave more space for the boundary layer, and let the effective spike contour approximate the ideal one. Similiar research, has already been performed in [7, 10] for 2D aerospike nozzles. As such it would be beneficial to see the effect of contour alteration methods on 3D aerospikes and possibly also on double depth aerospike nozzles.

Impact of nozzle convergent

The research in this report solely focused on the effects of nozzle geometry alterations downstream of the nozzle throat. All design parameters inside and upstream of the nozzle throat were kept equal between the designs to minimize the effect of these parameters on the results. As such it is very valuable to investigate the performance impact of alterations to the geometry upstream of the throat. For example, in this research the convergent of the aerospike nozzles was designed using a wedge shape instead of using an ellipsoidal shape. This selection was made based on the assumption that it would provide a more steady pressure distribution due to the more constant decrease in cross-sectional area. Validation, of this assumption, and optimization of this convergent shape could result in increases in nozzle performance. Other suggested design parameters open for investigation are the throat radius of curvature and the convergence half angle.

Transient nozzle behavior

All the numerical simulations from this report looked at the steady state performance of the nozzles. However, micro thrusters are often considered for the use in attitude control systems. As such the firing times of said thrusters will be rather short and transient effects will have an influence on the performance. Therefore, it would be valuable to identify any transient effects that could have an influence on the nozzle and its design.

Impact of surface roughness

The walls of the nozzles in this study were considered to be perfectly smooth. However, in reality surface roughness is present and plays an important role in the micronozzle performance. Especially as the nozzles are fabricated using DRIE etching which leaves scallops on the nozzle profile walls in the flow direction. Thus being able to model the surface roughness in the numerical simulations could prove very useful for the accurate prediction of nozzle performance.

Use real geometries in simulations

From the results obtained by the Keyence microscope it became clear that the nozzle throat does not have a perfect rectangular cross-section. As a result the thrust generated by the fabricated mi-

cronozzles might have an of-axis thrust. Characterizing this tendency can be done by loading the 3D model generated by the Keyence microscope into the CFD solver, and using it to generate the mesh for the numerical simulations. This might generate valuable lessons that can be applied to improve the production process or the nozzle design.

Experimental validation of the numerical results

Due to the unfortunate complications during the fabrication of the micronozzles no experimental testing could be performed. However, the experimental setup is ready and at the time of writing the micronozzles are being fabricated with the improved production methodology. As such it would be very valuable to experimentally test the micronozzles, such that the numerical results can be validated. Furthermore, using the experimental data one could possibly form a correlative relation between the numerical and experimental results, such that numerical results can be adjusted to better predict experimental performance.

Schlieren or particle image velocimetry investigations

With the experimental tests one can validate the performance of the nozzles by comparing the integrated flowfield properties to measured values. However, schlieren images and particle image velocimetry (PIV) are able to provide information on the base flowfield characteristics. Especially PIV imagery could be very valuable as it is able to experimentally determine the velocity flowfield of the nozzles. This is achieved by inserting microscopic particles upstream in the flow and taking two photos rapidly after each other. By comparing the two photos one is able to measure the distance a certain particle has traveled in the time that passed between the two photos. From this one can calculate the velocity of said particle and construct a velocity flowfield by combining the velocities of various particles. While schlieren and/or PIV imagery would provide invaluable information on the accuracy of the actual flowfield various challenges exist. Firstly, both methodologies require camera's to observe the to be measured flow. As a result only the plume of the linear nozzles and the divergent section of the aerospike would be able to be studied. Furthermore, inserting the appropriate amount of particles, for the PIV method, at such a small scale has various challenges, and would require a complete redesign of the nozzle feedsystem.

Bibliography

[1] M.F. Osborn, T.D. Holman, D.A. Rosenberg, and S.G. Tuttle. Overcoming low nozzle efficiency: A test-correlated numerical investigation of low reynolds number micro-nozzle flow. *51 AIAA/SAE/ASEE Joint Propulsion Conference*, 2015.

[2] D Rothe. Electron-beam studies of viscous flowing supersonic nozzles. *AIAA Journal*, 9(5):804–810, 1971.

[3] M. V. Whalen. Low reynolds number nozzle flow study. *Nasa Techincal Memorandum*, 1987.

[4] R. L. Bayt. *Analysis, Fabrication and Testing of a MEMS-based Micropropulsion System*. PhD thesis, Massachusetts Institute of Technology, 1999.

[5] W. F. Louisos and D. L. Hitt. Numerical studies of supersonic flow in bell-shaped micronozzles. *Journal of Spacecraft and Rockets*, 51(2):491–500, 2014.

[6] M.A.C Silva. *MEMS Micropropulsio Design, Modeling and Control of Vaporizing Liquid Microthrusters*. PhD thesis, Delft University of Technology, 2018.

[7] J.M. Pearl, W.F. Louisos, and D.L. Hitt. Viscous effects on performance of linear plug micronozzles. *Proceedings of the ASME 2014 International Mechanical Engineering Congress and Exposition*, 2014.

[8] J.M. Pearl, W.F. Louisos, and D.L. Hitt. Three-dimensional numerical study of linear plug micronozzles. *53rd AIAA Aerospace Sciences Meeting*, 2015.

[9] A. Zilic, D. L. Hitt, and A. A. Alexeenko. Numerical simulations of supersonic flow in a linear aerospike micronozzle. *37th AIAA Fluid Dynamics Conference and Exibit*, 2007.

[10] J.M. Pearl. Two-dimensional numerical study of micronozzle geometry. Master's thesis, University of Vermont, 2016.

[11] M.A.C. Silva, D.C. Guerrieri, H. Van Zeijl, A. Cervone, and E. Gill. Vaporizing liquid microthrusters with integrated heaters and temperature measurement. *Sensors and Actuators*, 265, 2017.

[12] X. Xiangming, L. Xingchen, Z. Jian, Z. Baojun, X. Dingbang, H. Yiyong, and W. Xuezhong. Numerical and experimental analysis of cold gas microthruster geometric parameters by univariate and orthogonal method. *Microsystem Technologies*, 23(10):5003–5016, Oct 2017.

[13] R.A. Ellis and R.B. Keller. Solid rocket motor nozzles. *NASA-SP-8115*, 1975.

[14] NASA. Liquid Rocket Engine Nozzles. NASA SP-8120. *NASA Special Publication*, 8120, 1976.

[15] W. F. Louisos and D. L. Hitt. Influence of wall heat transfer on supersonic micronozzle performance. *Journal of Spacecraft and Rockets*, 49(3):450–460, 2012.

[16] F. La Torre, S. Kenjeres, J. L. Moerel, and C. R. Kleijn. Hybrid simulations of rarefied supersonic gas flows in micro-nozzles. *Computers and Fluids*, 49(1):312–322, 2011.

[17] W. F. Louisos and D. L. Hitt. Viscous effects on performance of two-dimensional supersonic linear micronozzles. *Journal of Spacecraft and Rockets*, 45(4):706–715, 2008.

[18] W. F. Louisos, A. A. Alexeenko, D. L. Hitt, and A Zilic. Design considerations for supersonic micronozzles. *International Journal of Manufacturing Research*, 3(1):80–113, 2008.

[19] F. La Torre. *Gas Flow in Miniturized Nozzles For Micro-Thrusters*. PhD thesis, Delft University of Technology, 2011.

[20] B.T.C. Zandbergen. Thermal rocket propulsion (version 2.07). *TUDelft Reader*, 2018.

[21] A. D. Ketsdever, M. T. Clabough, S. F. Gimelshein, and A. Alexeenko. Experimental and numerical determination of micropropulsion device efficiencies at low reynolds numbers. *Aiaa Journal*, 43(3):633–641, 2005.

[22] W. F. Louisos and D. L. Hitt. Viscous effects on performance of three-dimensional supersonic micronozzles. *Journal of Spacecraft and Rockets*, 49(1):51–58, 2012.

[23] W. F. Louisos and D. L. Hitt. Performance characteristics of 3d supersonic micronozzles. *38th Fluid Dynamics Conference and exhibit*, 2008.

[24] J.R. Wertz, D.F. Everett, and J.J. Puschell. *Space Mission Engineering: The New SMAD*. Space Technology Library. Microcosm Press, 2011.

[25] R.W. Humble, G.N. Henry, and W.J. Larson. *Space propulsion analysis and design*. McGraw-Hill, 1995.

[26] G. Angelino. Approximate method for plug nozzle design. *AIAA Journal*, 2(10), 1964.

[27] G. Angelino and E. Sacchi. Experimental investigation on annular and throttleable plug nozzles. *Technical note von karman institute for fluid dynamics*, 1964.

[28] J. Dennis, F. Hernandez, S. Shark, and J. Villarreal. Design of a n20/htpb hybrid rocket motor utilizing a toroidal aerospike nozzle, 01 2010.

[29] I. B. Sebastiao and W.F.N. Santos. Numerical simulation of heat transfer and pressure distributions in micronozzles with surface discontinuities on the divergent contour. *Computers and Fluids*, 92:125–137, 2014.

[30] W. F. Louisos and D. L. Hitt. Analysis of transient flow in supersonic micronozzles. *Journal of Spacecraft and Rockets*, 48(2):303–311, 2011.

[31] V. Lijo, T. Setoguchi, and H.D. Kim. Analysis of supersonic micronozzle flows. *Journal of Propulsion and Power*, 31(2):754–757, 2015.

[32] R. Hameed, A.H.and Kafafy, W. Asrar, and M. Idres. Improving the efficiency of micronozzle by heated sidewalls. *The 4th International Meeting of Advances in thermofluids*, 2011.

[33] K. H. Cheah and J. K. Chin. Performance improvement on mems micropropulsion system through a novel two-depth micronozzle design. *Acta Astronautica*, 69(1-2):59–70, 2011.

[34] J. Gomez and R. Groll. Pressure drop and thrust predictions for transonic micronozzle flows. *Physics of Fluids*, 28(2), 2016.

[35] J. M. Pearl, W. F. Louisos, and D. L. Hitt. Thrust calculation for low-reynolds-number micronozzles. *Journal of Spacecraft and Rockets*, 54(1):287–298, 2017.

[36] D.S. Watvisave, U.V. Bhandarkar, and B.P. Puranik. Investigation of wall effects on flow characteristics of a high knudsen number nozzle. *Nanoscale and Microscale Thermophyisical Engineering*, 17(2):124–140, 2013.

[37] C Shen. *Rarefied Gas Dynamics*. Heat and mass Transfer. Springer, 2005. Translated from Chinese.

[38] G.A. Bird. *Molecular Gas Dynamics and the Direct Simulation of Gas Flows*. Number 42 in Oxford Engineering Science Series. Oxford Science Publications, 1994.

[39] M. S. Ivanov and S. F. Gimelshein. Current status and prospects of the dsmc modeling of near-continuum flows of non-reacting and reacting gases. *AIP Conference Proceedings*, 663(1):339–348, 2003.

[40] M. S. Ivanov, G. N. Markelov, A. D. Ketsdever, and D. C. Wadsworth. Numerical study of cold gas micronozzle flows. *AIAA*, 37th Aerospace Sciences Meeting and Exhibit, 1999.

[41] A.A. Alexeenko, D.A. Levin, S.F. Gimelshein, R.J. Collins, and B.D. Reed. Numerical modeling of axisymmetric and three-dimensional flows in microelectromechanical systems nozzles. *AIAA Journal*, 40(5):897–904, 2002.

[42] M. H. Liu, X. F. Zhang, G. X. Zhang, and Y. L. Chen. Study on micronozzle flow and propulsion performance using dsmc and continuum methods. *Acta Mechanica Sinica*, 22(5):409–416, 2006.

[43] C. Xie. Characteristics of micronozzle gas flows. *Physics of Fluids*, 19(3):037102, 2007.

[44] L.F.G. Maracantoni, J.P. Tamago, and S.A. Elaskar. High speed flow simulation using openfoam. *Asociacion Aregentina de Mecanica Computacional*, 31:2939–2959, 2012.

[45] A. Kurganov and Tadmor. E. New high-resolution central schemes for nonlinear conservation laws and convection–diffusion equations. *Journal of Computational Physics*, 160(1):241 – 282, 2000.

[46] A. Kurganov, S. Noelle, and G. Petrova. Semidiscrete central-upwind schemes for hyperbolic conservation laws and hamilton–jacobi equations. *SIAM Journal on Scientific Computing*, 23(3):707–740, 2001.

[47] C.J. Greenshields, H.G. Weller, L. Gasparini, and J.M. Reese. Implementation of semi-discrete, non-staggered central schemes in a colocated, polyhedral, finite volume framework, for high-speed viscous flows. *International Journal for Numerical Methods in Fluids*, 63(1):1–21, 2010.

[48] The OpenFOAM Foundation. Openfoam v5 user guide. https://cfd.direct/openfoam/user-guide, 2017.

[49] H. Jasak. *Error Analysis and Estimation for the Finite Volume Method with Applications to Fluid Flows*. PhD thesis, Imperial College of Science, Technology and Medicine, 1996.

[50] CuriosityfluidsAdmin1. Shocktube – rhocentralfoam tvd schemes test. www.curiosityfluids.com/2016/07/18/shocktube-rhocentralfoam-tvd-schemes-test/, 2016.

[51] Z. Tan. *Air Pollution and Greenhouse Gases*. Green Energy and Technology. Springer, 2014.

[52] Engineering Toolbox. Nitrogen-prandtl number. www.engineeringtoolbox.com/nitrogen-N2-Prandtl-number-temperature-pressure-d_2102.html, 2018.

[53] The OpenFOAM Foundation. Contrib/janaf. www.openfoamwiki.net/index.php/Contrib/Janaf, 2012.

[54] R. Span, E.W. Lemmon, R.T. Jacobsen, W. Wagner, and A. Yokozeki. A reference equation of state for the thermodynamic properties of nitrogen for temperatures from 63.151 to 1000 k and pressures to 2200 mpa. *Journal of Physical and Chemical Reference Data*, 29(6):1361–1433, 2000.

[55] B.J. McBride, S. Gordon, and M.A. Reno. Coefficients for calculating thermodynamic and transport properties of individual species. *NASA Technical Memorandum 4513*, 1993.

[56] F.R. Menter. Two-equation eddy-viscosity turbulence models for engineering aplications. *AIAA journal*, 32(8), 1994.

[57] CFD online. Sst k-omega model. www.cfd-online.com/Wiki/SST_k-omega_model, 2011.

[58] CFD online. Turbulence free-stream boundary conditions. www.cfd-online.com/Wiki/Turbulence_free-stream_boundary_conditions, 2014.

[59] CFD online. Turbulence length scale. www.cfd-online.com/Wiki/Turbulent_length_scale, 2012.

[60] J.C. Maxwell. On stresses in rarified gases arising from inequalities of temperature. *Philosophical Transactions of the Royal Society of London*, 170:231–256, 1879.

[61] E.B. Arkilic. *Measurement of the Mass Flow and Tangential Momentum Accommodation Coefficient in Silicon Micromachined Channels*. PhD thesis, Massachusetts Institute of Technology, 1996.

[62] M. Smoluchowski von Smolan. Ueber wärmeleitung in verdünnten gasen. *Annalen der Physik*, 300(1):101–130, 1898.

[63] W.M. Trott, J.N. Casteñeda, J.R. Torczynski, M.A. Gallis, and D.J. Rader. An experimental assembly for precise measurement of thermal accommodation coefficients. *Review of Scientific Instruments*, 82, 2011.

[64] J.W. Slater. Nparc alliance cfd verification and validation archive. www.grc.nasa.gov/WWW/wind/valid/cdv/cdv.html, 2008.

[65] CuriosityfluidsAdmin1. Converging-diverging nozzle v2- rhocentralfoam. www.curiosityfluids.com/2016/07/14/converging-diverging-nozzle-v2-rhocentralfoam/#comments, 2016.

[66] M. Onofri, M. Calabro, G. Hagemann, H. Immich, P. Sacher, F. Nasuti, and P. Reijasse. Plug nozzles: Summary of flow features and engine performance. *AIAA*, 2002-0584, 2002.

[67] W.J. Bannink, E.M. Houtman, and M.M.J. Schoones. Preliminary study of a plug nozzle model. Memorandum M-844, 1998.

[68] T. Ito, K. Fujii, and A.K. Hayashi. Computations of axisymmetric plug-nozzle flowfields flow structures and thrust performance. *Journal of Propulsion and Power*, 18(2), 2002.

[69] E. H. W. Jansen. Improvement and validation of test stand performance for novel micropropulsion systems. Master's thesis, Delft University of Technology, 2016.

[70] R.A. Makhan. Performance of the mems vaporizing liquid microthruster using cold nitrogen gas as propellant. Master's thesis, Delft University of Technology, 2018.

[71] R.J.F. Bijster. Design, verification and validation of a micropropulsion thruststand. Master's thesis, Delft University of Technology, 2014.

[72] Surf Sara. Apply for computing time via the isaac system of nwo. www.userinfo.surfsara.nl/systems/shared/iris-ncf.

A

Full Range Mach Contour Plots

In this appendix the various Mach contour plots are provided for the full range of Reynolds numbers that were left out of the main text for legibility. The mach contour plots for the following nozzles can be found below:

- Linear nozzle with $\theta_{out} = 30°$
- Linear nozzle with $\theta_{out} = 45°$
- Aerospike nozzle 40% truncated
- Aerospike nozzle 20% truncated
- Double depth aerospike nozzle $h_{spike} = 200$ µm
- Double depth aerospike nozzle $h_{spike} = 400$ µm
- Double depth aerospike nozzle $h_{spike} = 600$ µm
- Double depth aerospike nozzle $h_{spike} = 800$ µm
- Double depth aerospike nozzle $h_{spike} = 1000$ µm

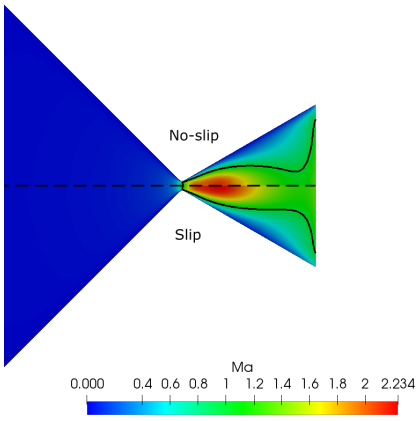

(a) $Re_t = 191$

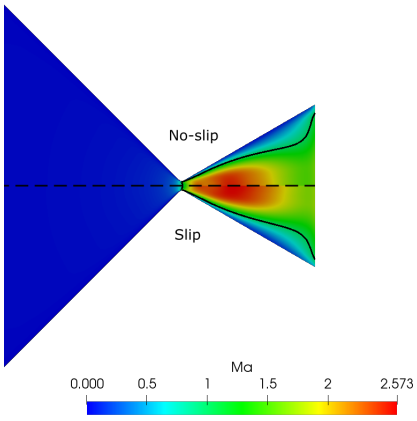

(b) $Re_t = 382$

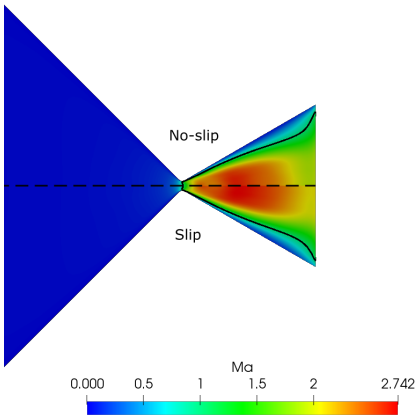

(c) $Re_t = 572$

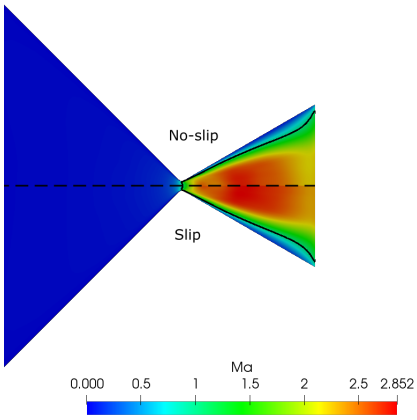

(d) $Re_t = 763$

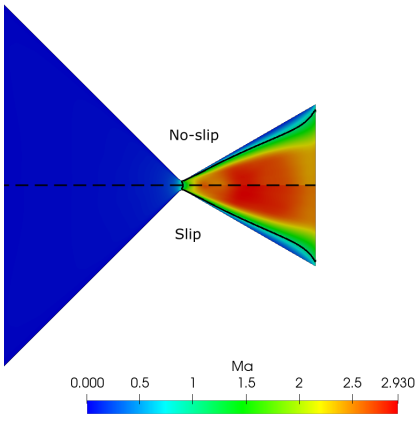

(e) $Re_t = 953$

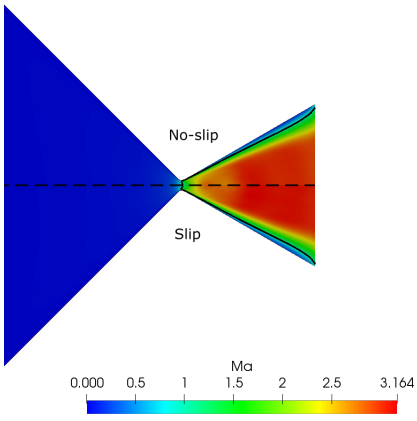

(f) $Re_t = 1908$

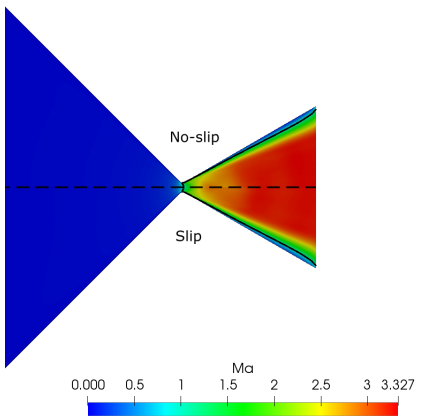

(g) $Re_t = 2861$

Figure A.1: Mach contours of the linear nozzle with $\theta_{out} = 30°$ for $Re_t = 191 - 2861$

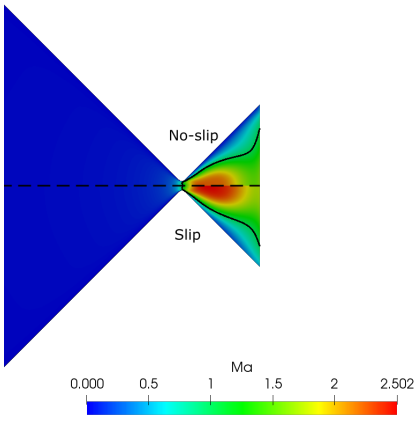

(a) $Re_t = 191$

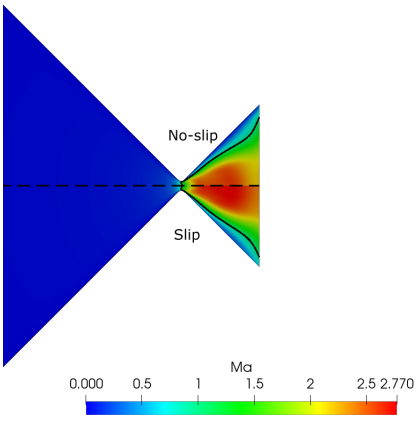

(b) $Re_t = 382$

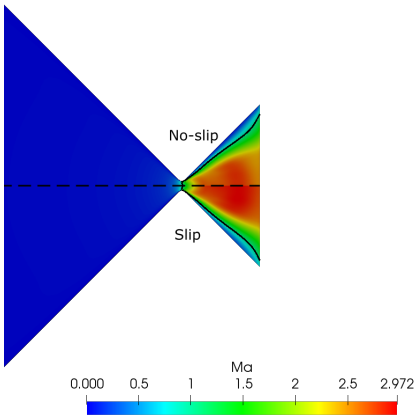

(c) $Re_t = 572$

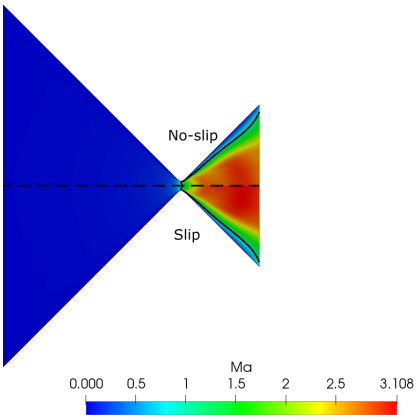

(d) $Re_t = 763$

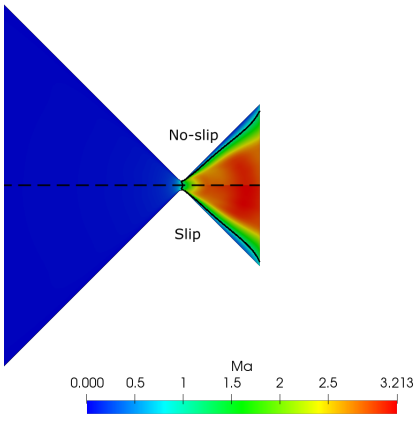

(e) $Re_t = 953$

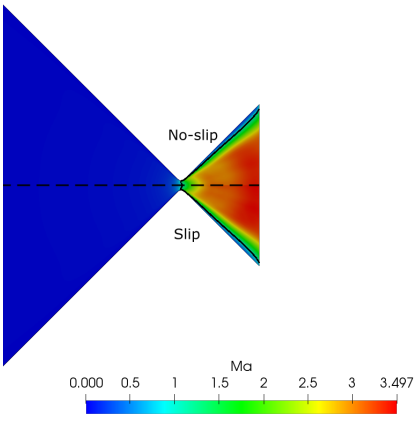

(f) $Re_t = 1908$

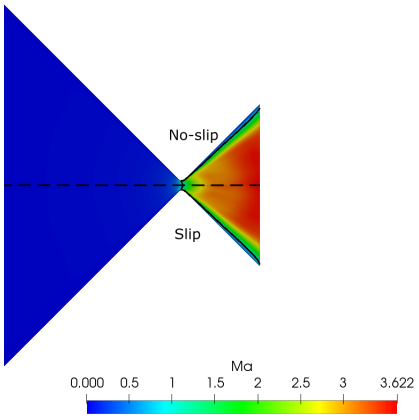

(g) $Re_t = 2861$

Figure A.2: Mach contours of the linear nozzle with $\theta_{out} = 45°$ for $Re_t = 191 - 2861$

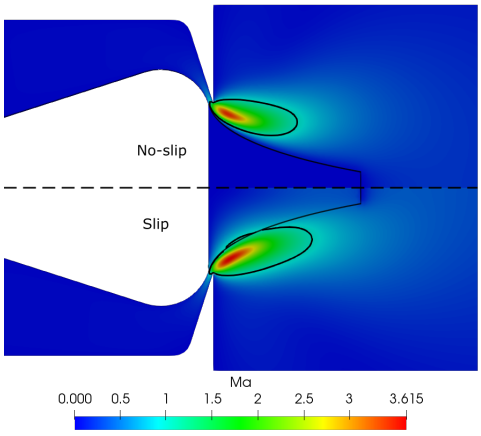

(a) $Re_t = 191$

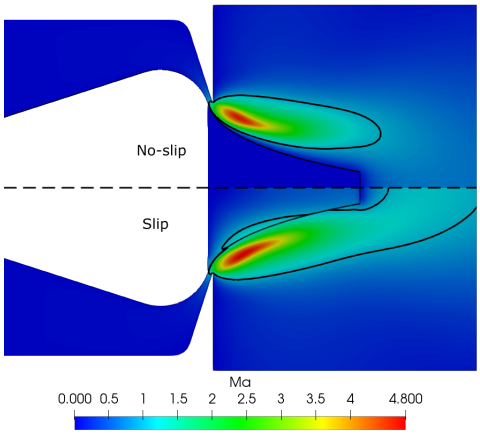

(b) $Re_t = 382$

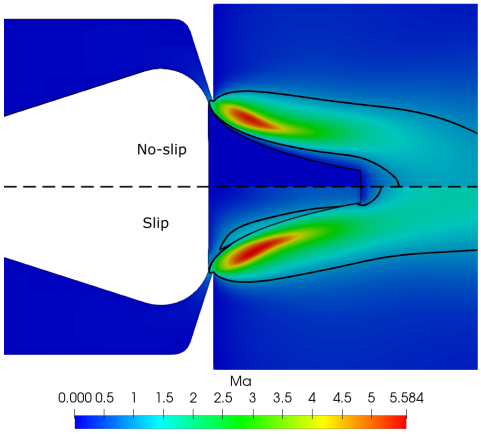

(c) $Re_t = 572$

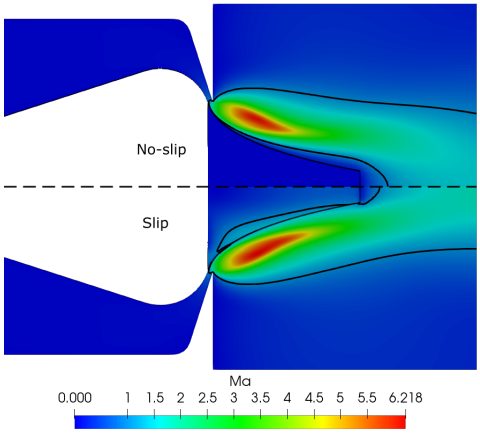

(d) $Re_t = 763$

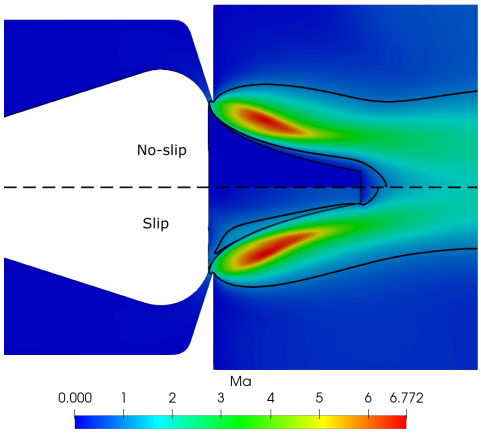

(e) $Re_t = 953$

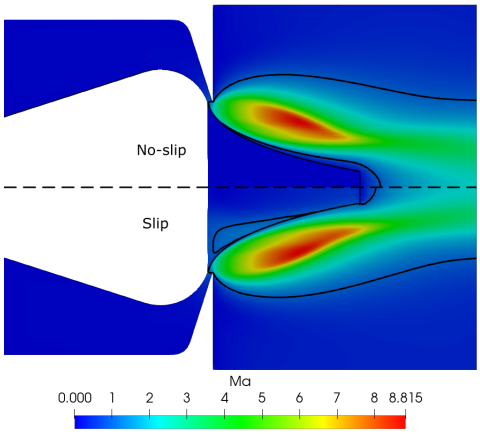

(f) $Re_t = 1908$

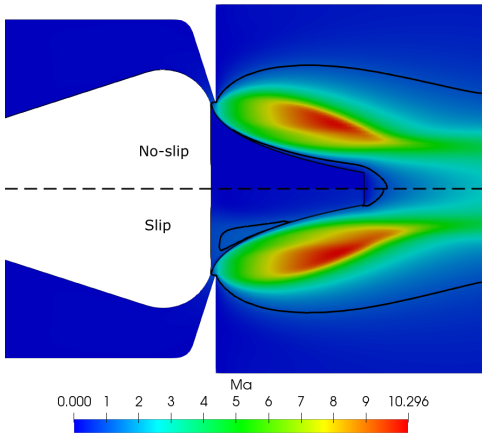

(g) $Re_t = 2861$

Figure A.3: Mach contours of the 40% truncated aerospike nozzle for $Re_t = 191 - 2861$

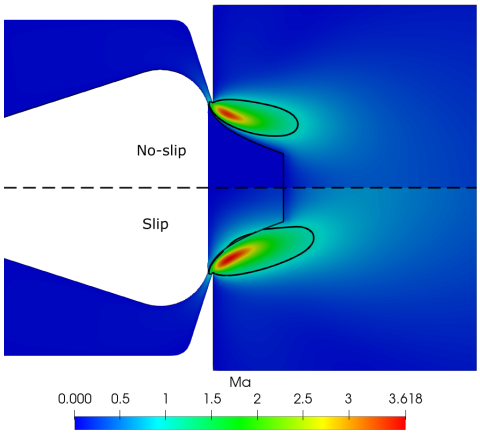

(a) $Re_t = 191$

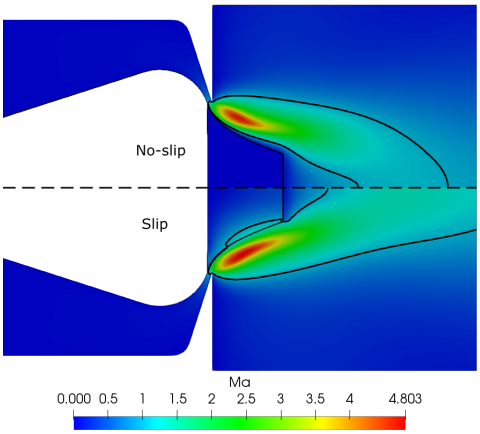

(b) $Re_t = 382$

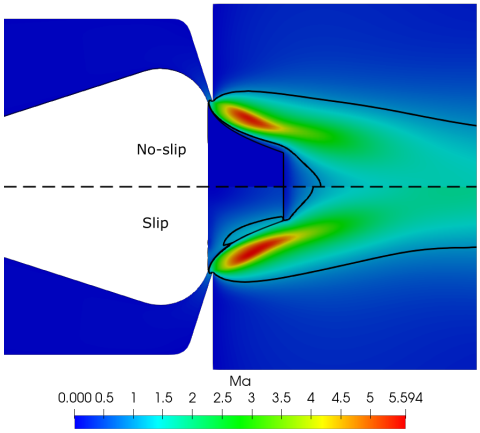

(c) $Re_t = 572$

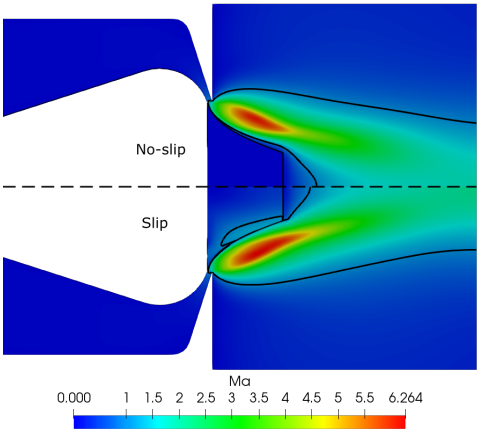

(d) $Re_t = 763$

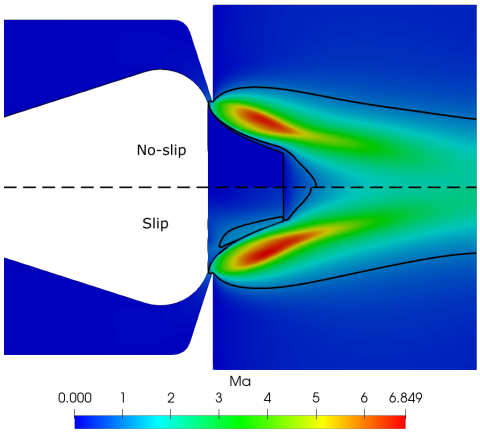

(e) $Re_t = 953$

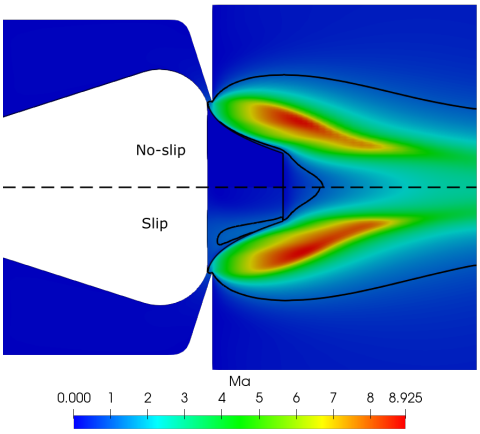

(f) $Re_t = 1908$

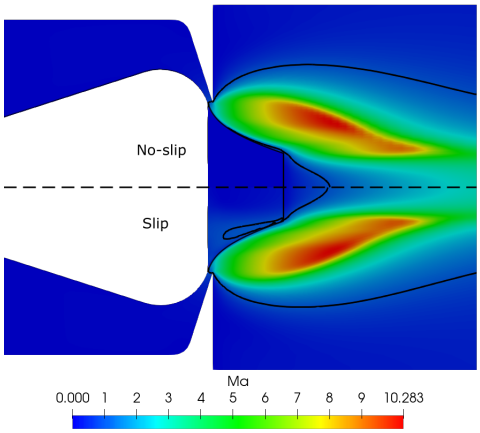

(g) $Re_t = 2861$

Figure A.4: Mach contours of the 20% truncated aerospike nozzle for $Re_t = 191 - 2861$

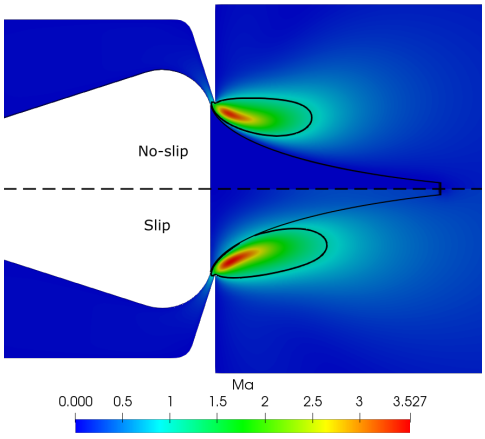

(a) $Re_t = 191$

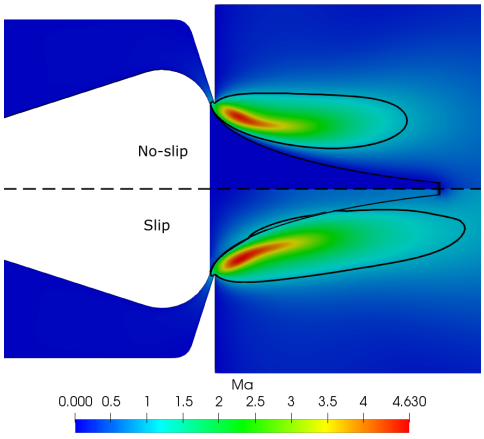

(b) $Re_t = 382$

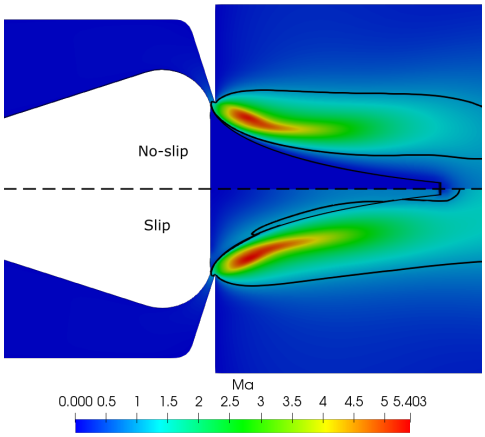

(c) $Re_t = 572$

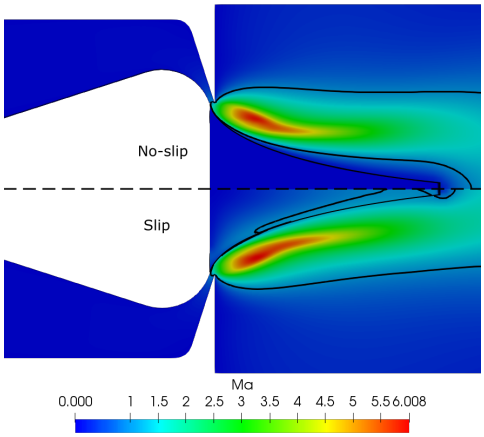

(d) $Re_t = 763$

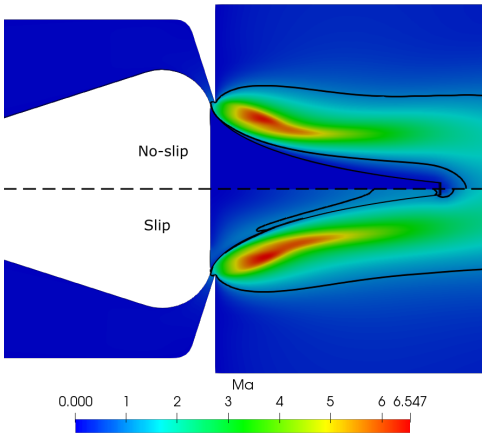

(e) $Re_t = 953$

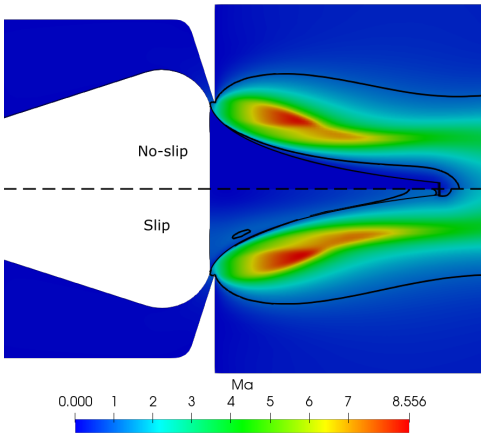

(f) $Re_t = 1908$

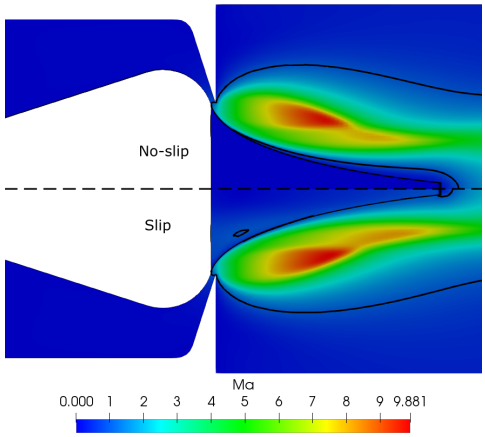

(g) $Re_t = 2861$

Figure A.5: Mach contours of the double depth aerospike nozzle with $h_{spike} = 200\ \mu m$ for Re_t=191-2861

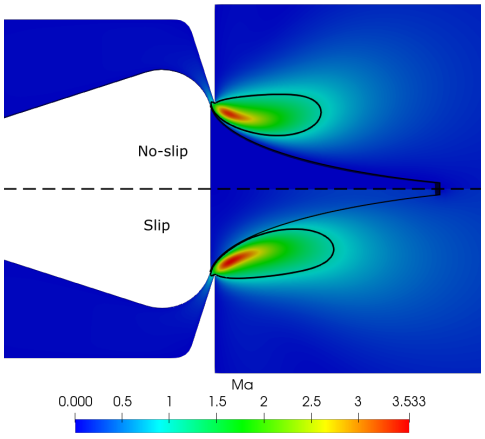

(a) $Re_t = 191$

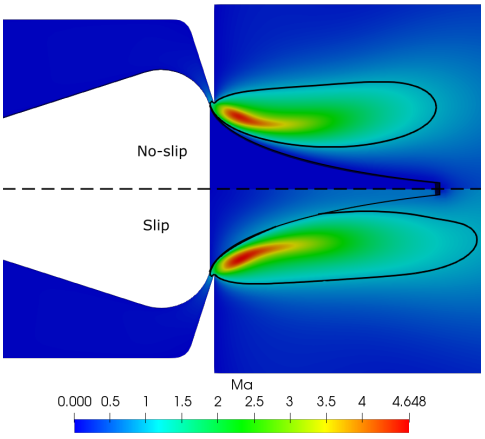

(b) $Re_t = 382$

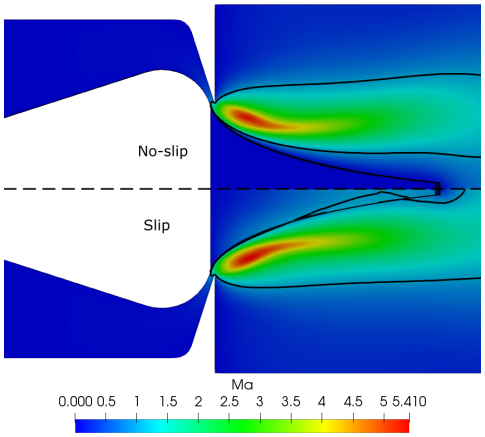

(c) $Re_t = 572$

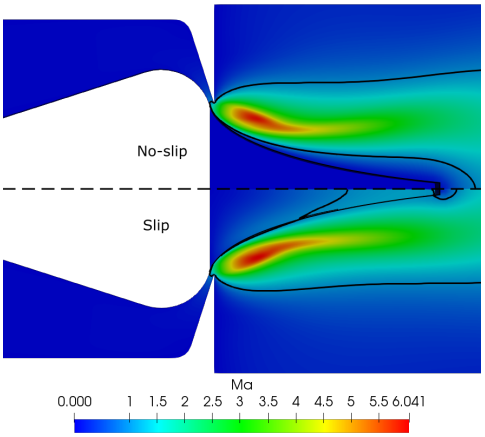

(d) $Re_t = 763$

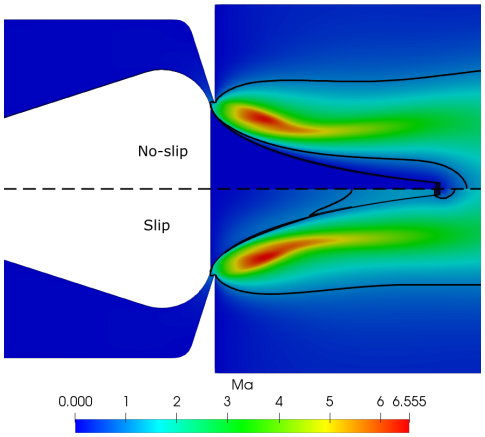

(e) $Re_t = 953$

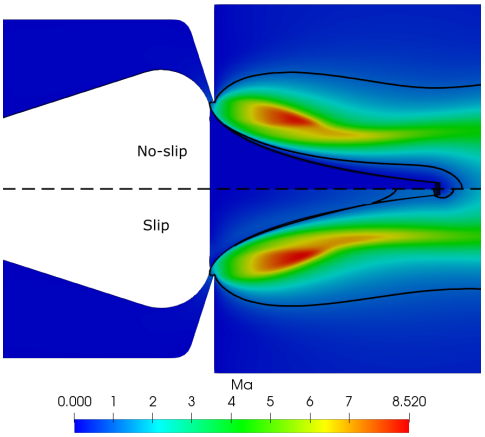

(f) $Re_t = 1908$

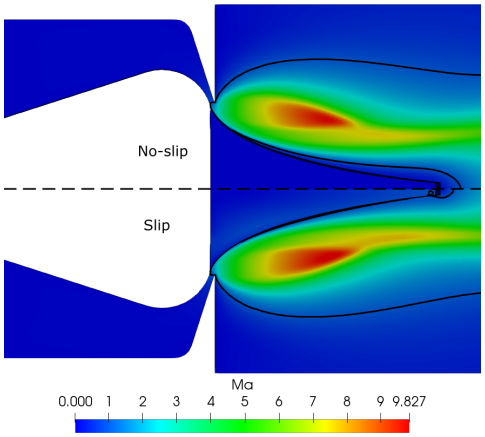

(g) $Re_t = 2861$

Figure A.6: Mach contours of the double depth aerospike nozzle with $h_{spike} = 400\ \mu m$ for Re_t=191-2861

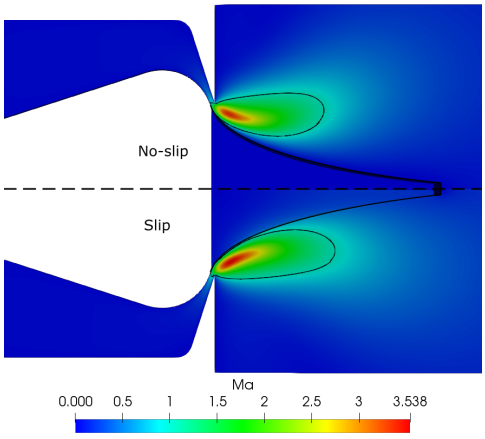

(a) $Re_t = 191$

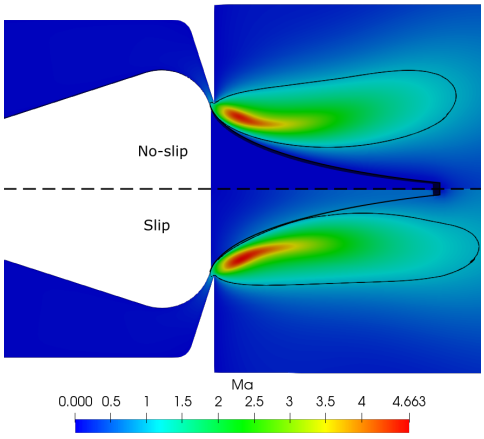

(b) $Re_t = 382$

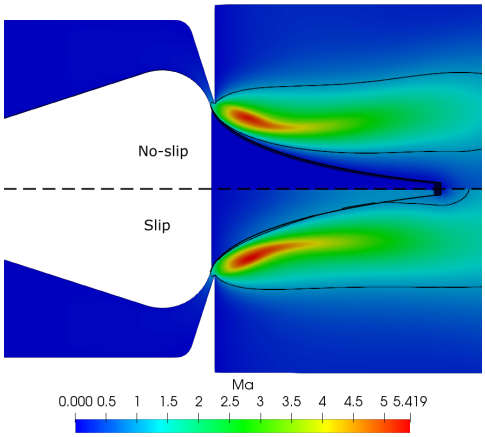

(c) $Re_t = 572$

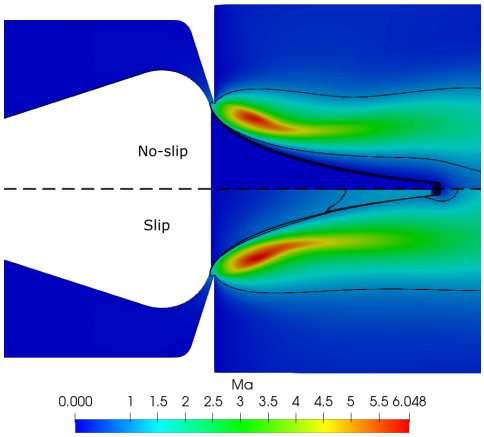

(d) $Re_t = 763$

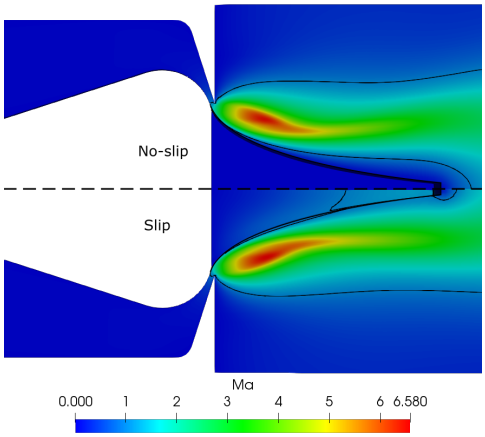

(e) $Re_t = 953$

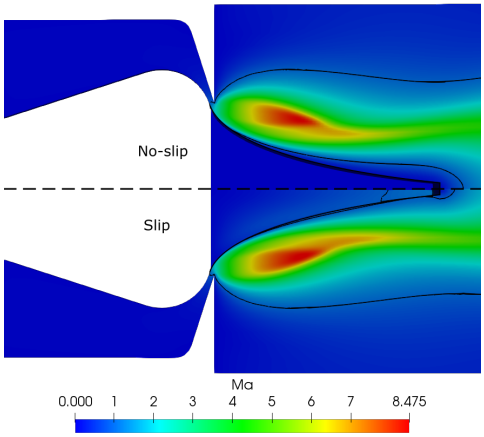

(f) $Re_t = 1908$

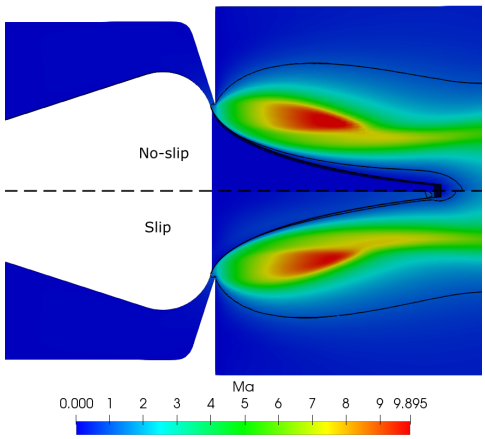

(g) $Re_t = 2861$

Figure A.7: Mach contours of the double depth aerospike nozzle with $h_{spike} = 600$ µm for Re_t=191-2861

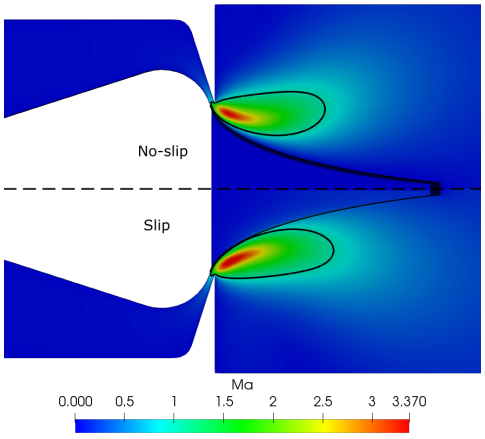

(a) $Re_t = 191$

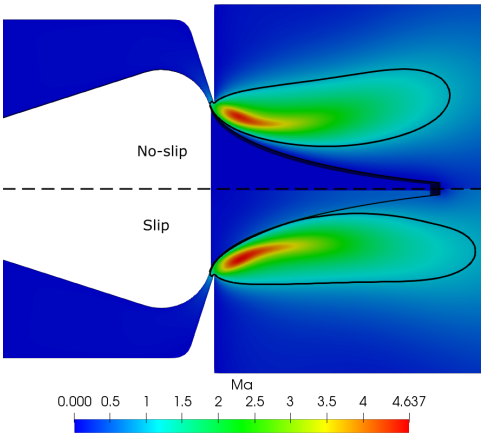

(b) $Re_t = 382$

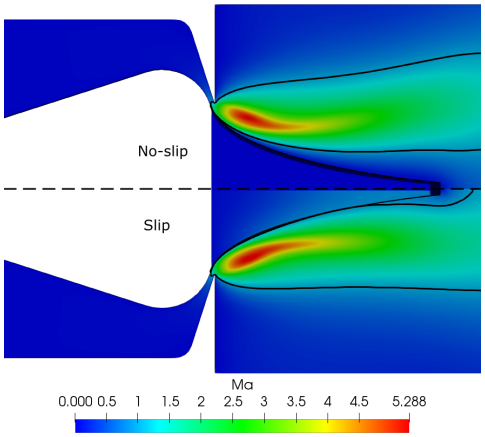

(c) $Re_t = 572$

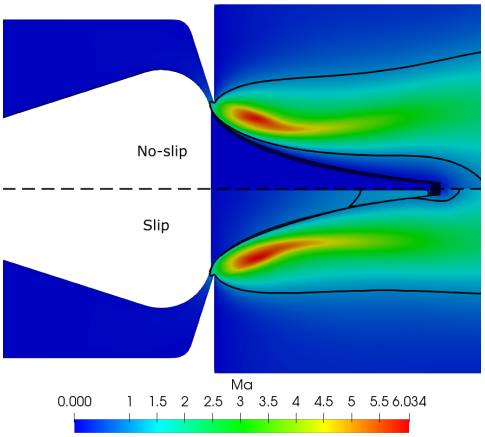

(d) $Re_t = 763$

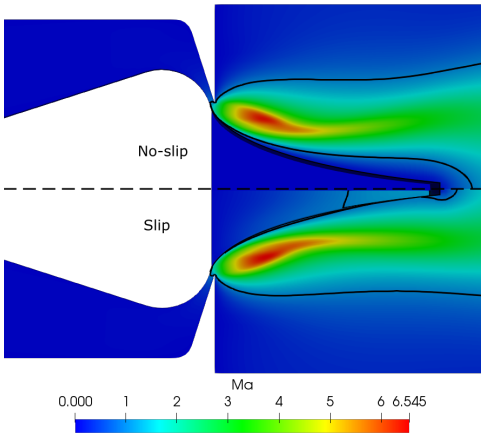

(e) $Re_t = 953$

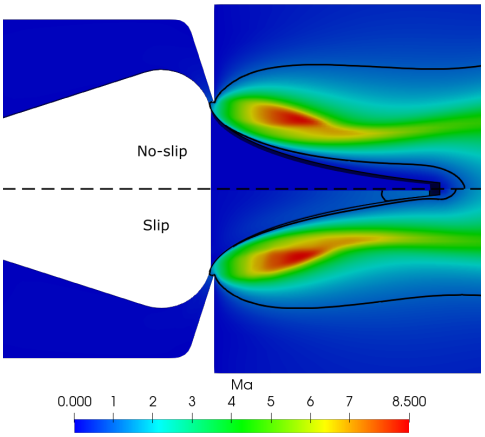

(f) $Re_t = 1908$

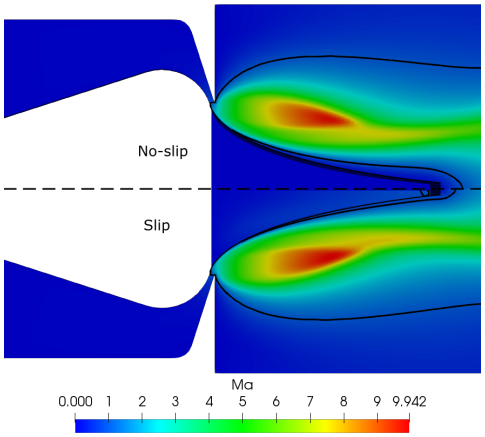

(g) $Re_t = 2861$

Figure A.8: Mach contours of the double depth aerospike nozzle with h_{spike} = 800 µm for Re_t=191-2861

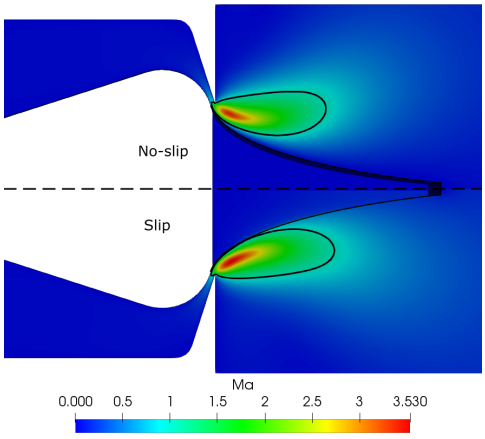

(a) $Re_t = 191$

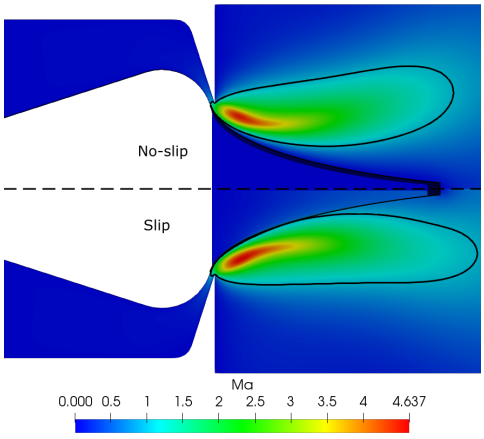

(b) $Re_t = 382$

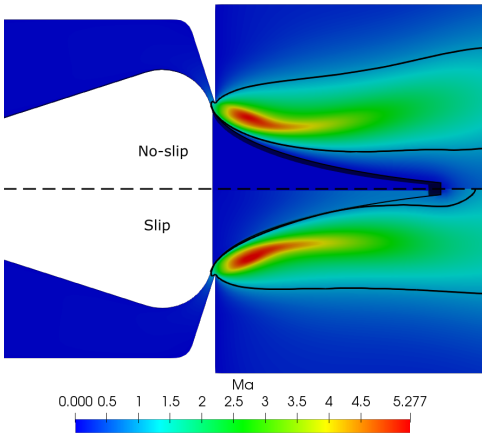

(c) $Re_t = 572$

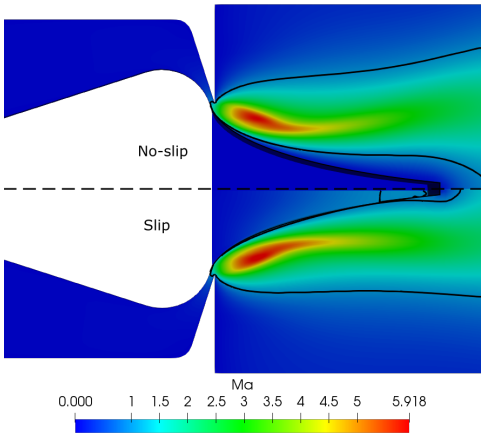

(d) $Re_t = 763$

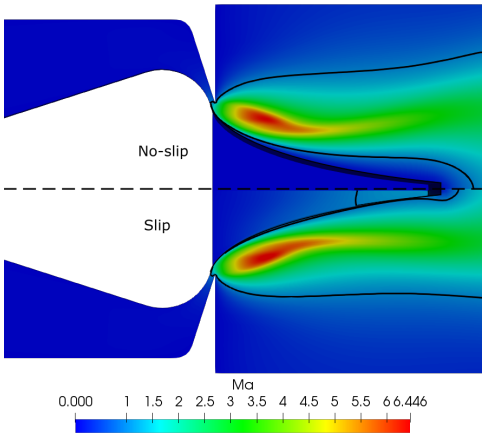

(e) $Re_t = 953$

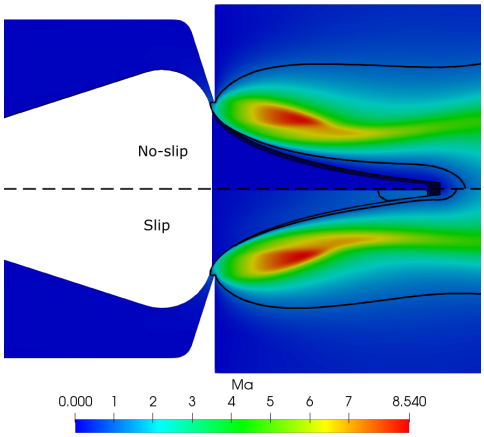

(f) $Re_t = 1908$

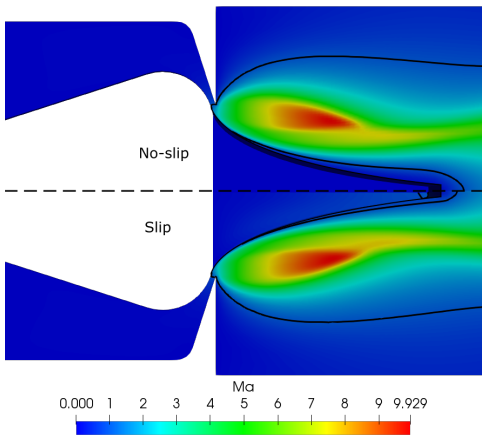

(g) $Re_t = 2861$

Figure A.9: Mach contours of the double depth aerospike nozzle with $h_{spike} = 1000\ \mu m$ for Re_t=191-2861

B

Absolute Numerical Performance Results

To aid future research efforts the exact values of produced thrust, massflow, and specific impulse of all the investigated nozzles are provided below.

Table B.1: Thrust of the linear nozzles in millinewton

		$\theta_{out} = 15°$		$\theta_{out} = 30°$		$\theta_{out} = 45°$	
Re_t	1D	no-slip	slip	no-slip	slip	no-slip	slip
191	0.149	0.087	0.088	0.089	0.091	0.091	0.093
382	0.300	0.192	0.192	0.197	0.199	0.203	0.206
572	0.452	0.302	0.302	0.314	0.316	0.322	0.324
763	0.603	0.416	0.416	0.436	0.438	0.442	0.446
953	0.754	0.535	0.534	0.560	0.564	0.565	0.569
1908	1.511	1.165	1.166	1.205	1.208	1.193	1.193
2861	2.267	1.852	1.826	1.891	1.872	1.846	1.829

Table B.2: Massflow of the linear nozzles in milligram per second

		$\theta_{out} = 15°$		$\theta_{out} = 30°$		$\theta_{out} = 45°$	
Re_t	1D	no-slip	slip	no-slip	slip	no-slip	slip
191	0.209	0.156	0.161	0.158	0.165	0.158	0.166
382	0.418	0.340	0.344	0.341	0.347	0.342	0.350
572	0.627	0.526	0.527	0.528	0.534	0.529	0.537
763	0.836	0.714	0.718	0.716	0.724	0.717	0.726
953	1.045	0.903	0.906	0.906	0.917	0.908	0.917
1908	2.090	1.865	1.873	1.870	1.880	1.872	1.881
2861	3.135	2.884	2.845	2.888	2.862	2.876	2.857

Table B.3: Specific impulse of the linear nozzles in seconds

		$\theta_{out} = 15°$		$\theta_{out} = 30°$		$\theta_{out} = 45°$	
Re_t	1D	no-slip	slip	no-slip	slip	no-slip	slip
191	72.705	56.789	55.527	57.460	55.974	58.516	57.053
382	73.264	57.644	56.992	58.977	58.376	60.599	60.091
572	73.450	58.612	58.309	60.557	60.271	62.013	61.599
763	73.543	59.416	59.139	62.026	61.736	62.894	62.561
953	73.600	60.390	60.048	62.994	62.776	63.491	63.223
1908	73.711	63.731	63.469	65.722	65.504	64.994	64.703
2861	73.748	65.467	65.461	66.757	66.687	65.471	65.275

Table B.4: Thrust of aerospike the nozzles in millinewton

		20% truncated		40% truncated		60% truncated	
Re_t	1D	no-slip	slip	no-slip	slip	no-slip	slip
191	0.298	0.121	0.121	0.122	0.122	0.122	0.122
382	0.601	0.275	0.273	0.276	0.273	0.274	0.272
572	0.903	0.436	0.434	0.437	0.432	0.434	0.430
763	1.206	0.600	0.596	0.598	0.592	0.596	0.592
953	1.508	0.764	0.759	0.763	0.756	0.759	0.753
1908	3.021	1.612	1.604	1.608	1.595	1.602	1.593
2861	4.534	2.471	2.454	2.470	2.460	2.461	2.449

Table B.5: Massflow of the aerospike nozzles in milligram per second

		20% truncated		40% truncated		60% truncated	
Re_t	1D	no-slip	slip	no-slip	slip	no-slip	slip
191	0.418	0.234	0.247	0.232	0.244	0.227	0.241
382	0.836	0.539	0.556	0.534	0.548	0.523	0.539
572	1.254	0.860	0.877	0.851	0.864	0.834	0.848
763	1.672	1.184	1.200	1.163	1.176	1.147	1.166
953	2.090	0.504	1.524	1.499	1.501	1.461	1.479
1908	4.180	3.208	3.217	3.148	3.184	3.114	3.129
2861	6.269	4.933	4.940	4.841	4.859	4.805	4.803

Table B.6: Specific impulse of the aerospike nozzles in seconds

		20% truncated		40% truncated		60% truncated	
Re_t	1D	no-slip	slip	no-slip	slip	no-slip	slip
191	72.705	52.831	50.062	53.897	51.153	54.687	51.522
382	73.264	51.952	50.118	52.742	50.890	53.399	51.474
572	73.450	51.717	50.406	52.349	51.018	53.025	51.749
763	73.543	51.627	50.613	52.410	51.301	52.969	51.783
953	73.600	51.750	50.817	51.888	51.370	52.961	51.952
1908	73.711	51.242	50.836	52.097	51.084	52.460	51.923
2861	73.748	51.078	50.650	52.024	51.621	52.223	52.005

Table B.7: Thrust of the double depth aerospike nozzles in millinewton

		h_{spike} = 100 µm		h_{spike} = 200 µm		h_{spike} = 400 µm		h_{spike} = 600 µm		h_{spike} = 800 µm		h_{spike} = 1000 µm	
Re_t	1D	no-slip	slip	no-slip	slip	no-slip	slip	no-slip	slip	no-slip	slip	no-slip	slip
191	0.298	0.122	0.122	0.159	0.156	0.181	0.178	0.188	0.186	0.189	0.189	0.188	0.190
382	0.601	0.274	0.272	0.354	0.346	0.404	0.391	0.424	0.408	0.427	0.415	0.430	0.419
572	0.903	0.434	0.430	0.559	0.547	0.637	0.617	0.667	0.644	0.677	0.654	0.683	0.660
763	1.206	0.596	0.592	0.766	0.752	0.866	0.843	0.911	0.879	0.924	0.895	0.933	0.902
953	1.508	0.759	0.753	0.923	0.955	1.102	1.076	1.161	1.122	1.180	1.142	1.190	1.159
1908	3.021	1.602	1.593	2.037	2.014	2.315	2.276	2.433	2.380	2.485	2.406	2.519	2.453
2861	4.534	2.461	2.449	3.127	3.094	3.552	3.497	3.736	3.667	3.808	3.734	3.862	3.781

Table B.8: Massflow of the double depth aerospike nozzles in milligram per second

		h_{spike} = 100 µm		h_{spike} = 200 µm		h_{spike} = 400 µm		h_{spike} = 600 µm		h_{spike} = 800 µm		h_{spike} = 1000 µm	
Re_t	1D	no-slip	slip	no-slip	slip	no-slip	slip	no-slip	slip	no-slip	slip	no-slip	slip
191	0.418	0.227	0.241	0.228	0.240	0.226	0.238	0.227	0.238	0.226	0.238	0.225	0.238
382	0.836	0.523	0.539	0.524	0.539	0.520	0.536	0.521	0.534	0.517	0.532	0.517	0.532
572	1.254	0.834	0.848	0.834	0.848	0.830	0.843	0.828	0.843	0.826	0.843	0.822	0.838
763	1.672	1.147	1.166	1.147	1.162	1.132	1.154	1.136	1.151	1.128	1.152	1.128	1.149
953	2.090	1.461	1.479	1.468	1.486	1.448	1.468	1.457	1.470	1.444	1.468	1.442	1.473
1908	4.180	3.114	3.129	3.109	3.130	3.092	3.110	3.097	3.113	3.086	3.099	3.096	3.108
2861	6.269	4.805	4.803	4.782	4.801	4.780	4.796	4.934	4.801	4.737	4.752	4.754	4.768

Table B.9: Specific impulse of the double depth aerospike nozzles in seconds

		h_{spike} = 100 µm		h_{spike} = 200 µm		h_{spike} = 400 µm		h_{spike} = 600 µm		h_{spike} = 800 µm		h_{spike} = 1000 µm	
Re_t	1D	no-slip	slip	no-slip	slip	no-slip	slip	no-slip	slip	no-slip	slip	no-slip	slip
191	72.705	54.687	51.522	71.143	66.153	81.601	76.027	84.330	79.433	85.094	81.101	85.206	81.509
382	73.264	53.399	51.474	68.919	65.432	79.286	74.373	82.879	77.972	84.248	79.501	84.767	80.299
572	73.450	53.025	51.749	68.377	65.719	78.252	74.623	82.156	77.815	83.558	79.098	84.637	80.301
763	73.543	52.969	51.783	68.121	65.958	78.020	74.472	81.753	77.889	83.506	79.208	84.332	80.091
953	73.600	52.961	51.952	67.560	65.550	77.634	74.705	81.239	77.833	83.329	79.348	84.180	80.217
1908	73.711	52.460	51.923	66.824	65.628	76.340	74.618	80.101	77.951	82.123	79.189	82.963	80.458
2861	73.748	52.223	52.005	66.681	65.702	75.759	74.357	77.210	77.879	81.982	80.124	82.849	80.859

C

Production Flowchart

*

Name: Micropropulsion Nozzles

Version: 3
Valid from: 20/11/18
Made by: Chaggai Ganani

Run number: LR2309
Process engineer: Chaggai Ganani
Mentor: Henk van Zeijl

Start date processing: 21/11/18

Contamination: NONE but contamination mitigation necessary in AML bonder

Labs: CR100

EKL(Else Kooi Laboratory)
DELFT UNIVERSITY OF TECHNOLOGY

Address	:	Feldmannweg 17, 2628 CT Delft, The Netherlands
P.O. Box	:	5053, 2600 GB Delft, The Netherlands
Phone	:	+31 - (0)15 - 2783868
Fax	:	+31 - (0)15 - 2622163
Website	:	http://ekl.tudelft.nl/EKL/Home.php

Micropropulsion

This page is left intentionally blank

Micropropulsion

GENERAL RULES

CLEANROOM BEHAVIOUR

Always follow the "Security and Behaviour" rules when working in the EKL laboratories.

Always handle wafers with care during processing. Use cleanroom gloves and work as clean as possible!!

Use cleanroom gloves when working with vacuum equipment. Do not touch the inside or carriers with bare hands.

Always check equipment and process conditions before starting a process. Do NOT make unauthorized changes!

Directly notify the responsible staff member(s) when there are problems with equipment (like malfunction or contamination). Put the system down in the Phoenix reservation system, and turn the equipment status sign from **UP** or **Usable** to **DOWN**.

DO NOT TRY TO REPAIR OR CLEAN EQUIPMENT YOURSELF, and **NEVER** try to refresh a contaminated etch or cleaning bath! Only authorized staff members are allowed to do this.

PCC RULES

All substrates, layers and chemicals which are not CMOS compatible are considered to be "NON-STANDARD" materials, and may be contaminating.

The use of "non-standard" materials for processing in the class100 and SAL cleanroom must **ALWAYS BE EVALUATED AND APPROVED** by your mentor and in agreement with the PCC document.

Wafers that are contaminated may **NEVER** be processed in any of the equipment without permission of the Equipment owner Special precautions may have to be taken, like the use of a special substrate holder or container.

Check the PCC "Rules & Instructions" - available on the "EKL intranet webpage" - for more details.

CLASS 100 RULES

CLEANING OF WAFERS

After several hours (4 hours max) of storage wafers must always be cleaned before performing a COATING, FURNACE, EPITAXY or DEPOSITION step.

Use the correct cleaning procedure:

Tepla stripper	for removal of implanted or plasma etched photoresist
Acetone	for removal of photoresist that is not implanted or plasma etched
HNO3 99% (Si)	for IC compatible wafers which do not need a HNO3 69.5% step
HNO3 99% (Al)	for wafers which are or have been in contact with one of the following metals: like Al, Al(1%Si), Ge, Ti, Zr
HNO3 99% (Si) + HNO3 69.5% (Si)	for all other IC compatible wafers

Note: The above described cleaning procedures are only valid for IC compatible wafers with "standard" materials on them. **In all other situations follow the PCC rules (Previously to be discussed with the mentor).**

Wafers do not have to be cleaned **after** a furnace, epitaxy or deposition step if the next process step will be performed immediately, unless the wafers are covered with particles.

FURNACE RESTRICTIONS

Wafers that are covered with photoresist or a metal layer may NEVER be processed in any of the furnaces. This also applies for wafers from which a metal layer has been removed by etching. Only alloying in tube C4 is allowed for wafers with an aluminium layer.

MEASUREMENTS

Always perform all the measurement and inspection steps, and write down the results in your journal and in the result tables that can be found at some of the equipment!! The results are used to check the condition of the processes and/or equipment.

It is possible to use the following Class 100 equipment to measure directly onto your (IC compatible) process wafers:

- The Leitz MPV-SP, the WOOLLAM and the SAGAX. These systems are used for thickness measurements of transparent layers. The measurements are non-destructive and without contact to the wafer surface.
- The Dektak 8 surface profilometer. This system is used for step height measurements. In this case a needle will physically scan over the wafer surface (contact measurement), which can be destructive for structures.
- The XL50 SEM. It can be used for inspection of your wafers and for width, depth or thickness measurements.

Note: **After certain measurements cleaning of your wafers may be required for further processing.**

An extra wafer must be processed when other measurement methods will be used (like sheet resistance and junction depth measurements). These wafers cannot be used for further processing.

Micropropulsion

STARTING MATERIAL

Use 8 DOUBLE SIDE polished with preprocessing on front and backside outside EKL with the following specifications:

Type:	DSP
Orientation:	<100>
Resistivity:	N/A
Thickness:	300 ± 15 μm
Diameter:	100 mm
Number of wafers:	4 (300) x 2

BACKGROUND

The goal of this project is to fabricate micronozzle devices which are to be tested to further research in the micronozzle efficiency field. 2 main type of nozzles will be manufactured: linear nozzles and aerospike nozzles. Both of the nozzle types follow a similar process with a few additional steps which have to be made for the aerospike nozzles.

The linear nozzles contain of an inlet section which consists of a single in plane hole and a nozzle section to accelerate the gas (nitrogen) during testing. See image below of an example.

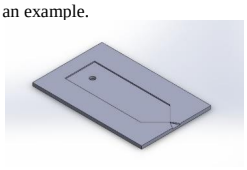

The aerospike nozzles again consist of a similar inlet section as the linear nozzles. This again is followed by a nozzle section. However the nozzle section in the aerospike nozzle is not an internal flow device such as the linear nozzles but an external flow device. This means that the so called spike (the centerbody) need to be free from the inlet section. See image below

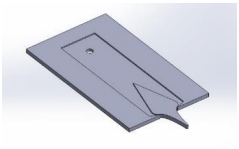

In this manufacturing series 4 wafers (2 for each nozzle type) containing multiple variations of the different nozzles will be produced. In the flowchart the steps pertaining to a specific wafer are indicated by the wafer letter: L for the wafer with the linear nozzles, and A for the wafer with aerospike nozzles

FRONT AND BACKSIDE DEFINITION

In this project processing will be done on both sides of a wafer and processing will be continued after 2 wafers are bonded. To avoid confusion the following definitions of front and back side are used.

BEFORE BONDING:
Front side is the side with the wafer number on it.
Back side is the side without the number.

AFTER BONDING:
Front side is the side with the number on it (this is equal to the frontside of the wafer before bonding)
Back side is the visible side of the wafer that was bonded to the numbered wafer.

MASK AND STEPPER PROGRAM

The mask used is called AIRSPIKENOZZLE and is in box 492 all PAS5500/80 programs are in folder:
SPECIAL/PROGRAMS2018/AEROSPIKE/

Micropropulsion

FLOWCHART

1. COATING FRONT SIDE (4x)

Use the coater station of the EVG120 system to coat the wafers with photoresist. The process consists of:
- a treatment with HMDS (hexamethyldisilazane) vapor, with nitrogen as a carrier gas
- spin coating of Shipley SPR3012 positive resist, dispensed by a pump
- a soft bake at 95 °C for 90 seconds
- an automatic edge bead removal with a solvent

Always check the relative humidity (48 ± 2 %) in the room before coating, and follow the instructions for this equipment.

Use program "1_**Co – ZERO LAYER**". There will be a larger edge bead removal.

Coat one additional test wafer for future use.

2. ALIGNMENT AND EXPOSURE

Processing will be performed on the ASM PAS 5500/80 automatic waferstepper.

Follow the operating instructions from the manual when using this machine.

Mask: **COMURK**
Use the correct litho job **SPECIAL/PROGRAMS2018/AEROSPIKE/ZEROLAYER** and the correct exposure energy (**150mj/cm**) Use layer ID **PM-1-T-14**.

3. DEVELOPMENT

Use the EVG 120 wafertrack to develop the wafers, and follow the instructions specified for this equipment.
The process consists of a post-exposure bake at 115 degC for 1 minute, followed by a development step using Shipley MF322 developer (single puddle process), and a hard bake at 100 degC for 1 minute.
Always check the temperature of the hotplates first.

Use development program **1Dev_SP**.

4. INSPECTION: LINEWIDTH AND OVERLAY

Visually inspect the wafers with a microscope, and check the linewidth and overlay. No resist residues are allowed.

5. PLASMA ETCHING OF ALIGNMENT MARKS

Use the Trikon Ωmega 201 plasma etcher.
Follow the operating instructions from the manual when using this machine.
It is **not** allowed to change the process conditions and times from the etch recipe!

Use sequence **URK_NPD** (with a platen temperature of **20 °C**) to etch **120** nm deep ASM URK's into the Si.

NOTE these markers are rotated 90 degrees to the normal

6. PHOTORESIST STRIPPING

Strip resist — Use the Tepla Plasma 300 system to remove the photoresist in an oxygen plasma.
Follow the instructions specified for the Tepla stripper, and use the quartz carrier.
Use **program 1**: 1000 watts power and automatic endpoint detection + 2 min. over etching.

7. MARK WAFERS

Use quartz scratcher to mark the 4 wafers using markings: A1, A2, L1, L2 where A corresponds to the wafers containing aerospike nozzles and L to the linear nozzle wafers. The number indicates the wafer number of that batch.

8. CLEANING PROCEDURE: HNO_3 100% and 69.5%

Cleaning	10 minutes in fuming nitric acid (HNO_3 99%) at ambient temperature. Use wet bench "HNO_3 (100%)" and the carrier with the white dot.
QDR	Rinse in the Quick Dump Rinser with the standard program until the resistivity is 5 MΩ.
Cleaning	10 minutes in concentrated nitric acid (HNO_3 69.5%) at 110 °C. Use wet bench "HNO_3 (69.5%)" and the carrier with the white dot.
QDR	Rinse in the Quick Dump Rinser with the standard program until the resistivity is 5 MΩ.
Drying	Use the Semitool "rinser/dryer" with the standard program, and the white carrier with a red dot.

End of zero layer

9. DEPOSITION OF SiO2 BACKSIDE: 2000nm

Use the Novellus PECVD reactor.
Follow the operating instructions from the manual when using this machine.
Enable the proper gases as indicated next to the machine.
The process conditions of the deposition program may not be changed!

Use program **.xxxSiOstd** to deposit a 2000 nm thick PECVD SiO2 layer. Check time in the logbook.
T= **XXX**s

10. DEPOSITION OF SiO2 FRONTSIDE: 5000nm

Use the Novellus PECVD reactor.
Follow the operating instructions from the manual when using this machine.
Enable the proper gases as indicated next to the machine.
The process conditions of the deposition program may not be changed!

Use program **.xxxSiOstd** to deposit a 5000nm thick PECVD SiO2 layer. Calculate the time using the logbook.
T= **XXX**s

11. INSPECTION BACKSIDE

Use the Leitz MPV-SP measurement system to measure the oxide thickness:

Program: Novellus lostr SiO2 > 50nm on Si 10x

Wafer	Point 1	Point 2	Point 3	Point 4	Point 5

12. INSPECTION FRONTSIDE

Use the Leitz MPV-SP measurement system to measure the oxide thickness:

Program: Novellus lostr SiO2 > 50nm on Si 10x

Wafer	Point 1	Point 2	Point 3	Point 4	Point 5

13. COATING BACKSIDE

Use the EVG 120 wafertrack to coat the wafers with resist, and follow the instructions specified for this equipment.
The process consists of a treatment with HMDS (hexamethyldisilazane) vapor with nitrogen as a carrier gas,
spin coating with Shipley SPR3027 positive photoresist, and a soft bake at 95degC for 1 minute.
Always check the temperature of the hotplate and the relative humidity (48 ± 2 %) in the room first.

Use program **1_Co - 3027 - 2.1µm-noEBR.**

14. ALIGNMENT AND EXPOSURE OF CHANNELS

Processing will be performed on the ASM PAS 5500/80 automatic waferstepper.

Follow the operating instructions from the manual when using this machine.

Use mask **AIRSPIKENOZZLE (**box 492**)**
Use the correct litho job:

for **A** wafers: **/AEROSPIKE** using layer ID: **ASPIKECHANNEL**
for **L** wafers: **/LINNOZZLE** using layer ID: **LINNOZCHANNEL**
Using the correct exposure energy: **260 mj/cm**

15. DEVELOPMENT (BACKSIDE)

Use the EVG 120 wafertrack to develop the wafers, and follow the instructions specified for this equipment.
The process consists of a post-exposure bake at 115 degC for 1 minute, followed by a development step using Shipley MF322 developer (single puddle process), and a hard bake at 100 degC for 1 minute.
Always check the temperature of the hotplates first.

Use development program **1 Dev SP**.

16. INSPECTION: LINEWIDTH AND OVERLAY

Visually inspect the wafers with a microscope, and check the linewidth and overlay. No resist residues are allowed.

17. ETCHING SiO2 BACKSIDE (HARDMASK CHANNELS)

Use the Drytek Triode 384T to etch the wafers, and follow the instructions specified for this equipment.
Delete one MAGWEG recipe and copy the **STDOXIDE** to MAGWEGCG. Alter MAGWEGCG to change the time of etching. The etchrate is around 10 nm/s
The etch time is: **240 s**
Set helium backside leakage to **45**.

18. INSPECTION

Use the Leitz MPV-SP measurement system to measure the oxide thickness in the channels.

Program: Novellus lostr SiO2 > 50nm on Si 10x

Note: the measurement should be 0.

19. PHOTORESIST STRIPPING

Strip resist	Use the Tepla Plasma 300 system to remove the photoresist in an oxygen plasma. Follow the instructions specified for the Tepla stripper, and use the quartz carrier. Use **program 1**: 1000 watts power and automatic endpoint detection + 2 min. over etching.

20. CLEANING PROCEDURE: HNO_3 100% and 69.5%

Cleaning	10 minutes in fuming nitric acid (HNO_3 99%) at ambient temperature. Use wet bench "HNO_3 (100%)" and the carrier with the white dot.
QDR	Rinse in the Quick Dump Rinser with the standard program until the resistivity is 5 MΩ.
Cleaning	10 minutes in concentrated nitric acid (HNO_3 69.5%) at 110 °C. Use wet bench "HNO_3 (69.5%)" and the carrier with the white dot.
QDR	Rinse in the Quick Dump Rinser with the standard program until the resistivity is 5 MΩ.
Drying	Use the Semitool "rinser/dryer" with the standard program, and the white carrier with a red dot.

21. COATING FRONTSIDE (ONLY A WAFERS)

Use the EVG 120 wafertrack to coat the wafers with resist, and follow the instructions specified for this equipment.
The process consists of a treatment with HMDS (hexamethyldisilazane) vapor with nitrogen as a carrier gas,
spin coating with Shipley SPR3027 positive photoresist, and a soft bake at 95degC for 1 minute.
Always check the temperature of the hotplate and the relative humidity (48 ± 2 %) in the room first.

Use program **1_Co - 3027 - 3.1µm-noEBR.**

22. ALIGNMENT AND EXPOSURE OF AEROSPIKE TOP (ONLY A WAFERS)

Processing will be performed on the ASM PAS 5500/80 automatic waferstepper.
Follow the operating instructions from the manual when using this machine.

Use mask **AIRSPIKENOZZLE (**box 492**)**
Use the correct litho job:

for **A** wafers: /**AEROSPIKE** using layer ID: **ASPIKEFREETOP**
Using the correct exposure energy: **430 mj/cm**
And adjust the focus: **-1 mu**

23. DEVELOPMENT (ONLY A WAFERS)

Use the EVG 120 wafertrack to develop the wafers, and follow the instructions specified for this equipment.
The process consists of a post-exposure bake at 115 degC for 1 minute, followed by a development step using
Shipley MF322 developer (single puddle process), and a hard bake at 100 degC for 1 minute.
Always check the temperature of the hotplates first.

Use development program **1 Dev SP**.

24. INSPECTION: LINEWIDTH AND OVERLAY (ONLY A WAFERS)

Visually inspect the wafers with a microscope, and check the linewidth and overlay. No resist residues are allowed.

25. ETCHING 4000nm SiO2 (HALF HARDMASK AEROSPIKE FREESTREAM) (ONLY A WAFERS)

Use the Drytek Triode 384T to etch the wafers, and follow the instructions specified for this equipment.
Delete one MAGWEG recipe and copy the **STDOXIDE** to MAGWEGCG. Alter MAGWEGCG to change the time of etching.
FIRST: etch for **360 sec**
Set helium backside leakage to **45**.

SECOND: measure remaining oxide in the half hardmasks. Calculate etchrate and determine remaining etch time to end up with around 1000 nm of oxide at the thinnest location

THIRD: etch for calculated remaining time

26. INSPECTION (ONLY A WAFERS)

Use the Leitz MPV-SP measurement system to measure the oxide thickness in the spike hard mask.

Program: Novellus lostr SiO2 > 50nm on Si 10x

Note: the measurement should be around **1000nm** at the thinnest location.

27. PHOTORESIST STRIPPING (ONLY A WAFERS)

Strip resist Use the Tepla Plasma 300 system to remove the photoresist in an oxygen plasma.
Follow the instructions specified for the Tepla stripper, and use the quartz carrier.
Use **program 1**: 1000 watts power and automatic endpoint detection + 2 min. over etching.

28. CLEANING PROCEDURE: HNO_3 100% and 69.5% (BOTH A&L WAFERS)

Cleaning	10 minutes in fuming nitric acid (HNO_3 99%) at ambient temperature. Use wet bench "HNO_3 (100%)" and the carrier with the white dot.
QDR	Rinse in the Quick Dump Rinser with the standard program until the resistivity is 5 MΩ.
Cleaning	10 minutes in concentrated nitric acid (HNO_3 69.5%) at 110 °C. Use wet bench "HNO_3 (69.5%)" and the carrier with the white dot.
QDR	Rinse in the Quick Dump Rinser with the standard program until the resistivity is 5 MΩ.
Drying	Use the Semitool "rinser/dryer" with the standard program, and the white carrier with a red dot.

29. COATING FRONTSIDE

Use the EVG 120 wafertrack to coat the wafers with resist, and follow the instructions specified for this equipment.
The process consists of a treatment with HMDS (hexamethyldisilazane) vapor with nitrogen as a carrier gas,
spin coating with Shipley SPR3027 positive photoresist, and a soft bake at 95degC for 1 minute.
Always check the temperature of the hotplate and the relative humidity (48 ± 2 %) in the room first.

Use program **CO_TOPO_3027_3.1µm_noEBR**
Followed by programme: **SPECO_TOPO_3027_3.1µm_noEBR_noHMDS**

LET RESIST REHYDRATE FOR 15 MINUTES AFTER COATING

ASK ENGINEER ON DUTY TO REMOVE SPLASH RINGS FIRST.

30. ALIGNMENT AND EXPOSURE OF INLETHOLE

Processing will be performed on the ASM PAS 5500/80 automatic waferstepper.
Follow the operating instructions from the manual when using this machine.

Use mask **AIRSPIKENOZZLE (**box 492**)**
Use the correct litho job:

for **A** wafers: **/AEROSPIKE** using layer ID: **FRONTINlETHOLE**
for **L** wafers: **/LINNOZZLE** using layer ID: **FRONTINlETHOLE**
Using the correct exposure energy: **800 mj/cm**
And adjust the focus: **-1 mu**
AFTER EXPOSURE LET RESIST REST FOR 15 MINUTES

31. DEVELOPMENT

Use the EVG 120 wafertrack to develop the wafers, and follow the instructions specified for this equipment.
The process consists of a post-exposure bake at 115 degC for 1 minute, followed by a development step using
Shipley MF322 developer (single puddle process), and a hard bake at 100 degC for 1 minute.
Always check the temperature of the hotplates first.

Use development program **1 Dev DP_4**.

32. ETCHING 5000nm SiO2 HARDMASK INLETHOLES

Use the Drytek Triode 384T to etch the wafers, and follow the instructions specified for this equipment.
Delete one MAGWEG recipe and copy the **STDOXIDE** to MAGWEGCG. Alter MAGWEGCG to change the time of
etching. To prevent excessive resist burning etch in multiple steps

FIRST: etch for **240 sec, s**et helium backside leakage to **45**.
SECOND: etch for **240 sec, s**et helium backside leakage to **45**.
THIRD: etch for **200 sec, s**et helium backside leakage to **45**.

33. INSPECTION

Use the Leitz MPV-SP measurement system to measure the oxide thickness in the opened inletholes hard masks:

Program Novellus lostr SiO2 > 50nm on Si 10x
The measured thickness should me 0 nm

34. PHOTORESIST STRIPPING

Strip resist — Use the Tepla Plasma 300 system to remove the photoresist in an oxygen plasma.
Follow the instructions specified for the Tepla stripper, and use the quartz carrier.
Use **program 1**: 1000 watts power and automatic endpoint detection + 2 min. over etching.

35. CLEANING PROCEDURE: HNO_3 100% and 69.5%

Cleaning — 10 minutes in fuming nitric acid (HNO_3 99%) at ambient temperature.
Use wet bench "HNO_3 (100%)" and the carrier with the white dot.

QDR — Rinse in the Quick Dump Rinser with the standard program until the resistivity is 5 MΩ.

Cleaning — 10 minutes in concentrated nitric acid (HNO_3 69.5%) at 110 °C.
Use wet bench "HNO_3 (69.5%)" and the carrier with the white dot.

QDR — Rinse in the Quick Dump Rinser with the standard program until the resistivity is 5 MΩ.

Drying — Use the Semitool "rinser/dryer" with the standard program, and the white carrier with a red dot.

36. DRIE ETCHING Si (FLUID CHANNELS) 100 MICRON BACKSIDE

Use Rapier Omega i2L, and follow the instructions specified for this equipment. Use program
0EKL_FLATBOTTOM_XXX
First use a test wafer to determine etch rate per loop from this calculate amount of loops necessary for 100 microns.
Amount of loops is: 45 for L wafers, 48 for A wafers

37. INSPECTION (depth measurement)

Use Keyenes microscope to measure the following dimensions on each channel:

- Throat width
- Throat depth
- Depth exit plane
- Width exit plane
- Depth along the axis of the nozzle

Do this for each channel and log it properly do this during module training
ALSO MAKE IMAGES OF THE WAFERS AT THIS STAGE

38. PASSIVATION STRIPPING

Use the TEPLA photoresist stripper.
Use **2xprogram 8 (2x15 minutes)**
Let wafers cool down they will be HOT

39. CLEANING PROCEDURE: HNO_3 100% and 69.5%

Cleaning — 10 minutes in fuming nitric acid (HNO_3 99%) at ambient temperature.
Use wet bench "HNO_3 (100%)" and the carrier with the white dot.

QDR — Rinse in the Quick Dump Rinser with the standard program until the resistivity is 5 MΩ.

Cleaning — 10 minutes in concentrated nitric acid (HNO_3 69.5%) at 110 °C.
Use wet bench "HNO_3 (69.5%)" and the carrier with the white dot.

QDR — Rinse in the Quick Dump Rinser with the standard program until the resistivity is 5 MΩ.

Drying — Use the Semitool "rinser/dryer" with the standard program, and the white carrier with a red dot.

40. COATING FRONTSIDE (BOTH A&L WAFERS)

Use the EVG 120 wafertrack to coat the wafers with resist, and follow the instructions specified for this equipment.
The process consists of a treatment with HMDS (hexamethyldisilazane) vapor with nitrogen as a carrier gas,
spin coating with Shipley SPR3012 positive photoresist, and a soft bake at 95degC for 1 minute.
Always check the temperature of the hotplate and the relative humidity (48 ± 2 %) in the room first.

Use program **1_CO _3012_1.4µm_noEBR**

41. RESIST BAKING (BOTH A&L WAFERS)

Use the MEMERT oven to bake the resist for 15 minutes.

42. SiO2 REMOVAL
Etching: Use (B)HF Si and blue stars handler
XXXmin to remove all the oxide from the backside of the wafers.

Note: when all SiO2 is etched away the wafer will become hydrophobic
Rinse: Rinse in water for 5 min.
Drying: Use the Semitool "rinser/dryer" with the standard program, and the white carrier with a blue dot.

End of Processing of top wafer

43. NATIVE SiO2 REMOVAL BOTH WAFERS (dip etch)
Etching: Use (B)HF green metals and blue stars handler
XXXmin to remove XXX nm.

Note: when all SiO2 is etched away the wafer will become hydrophobic
QDR: Rinse in water for 5 min.

Drying: Use the **MARANGONI** to dry

44. AML BONDING
Bond the 2 300 micron silicon wafer to eachother. With the AML waferbonder.
CONTAMINATION PREVENTION:
Put the to be bonded wafers between 2 nitride covered dummy wafers which have nitride on both sides to act as contamination prevention barriers.

45. INFRARED INSPECTION
Check the quality of the bonding through infrared microscope.

46. COATING BACKSIDE

Use the EVG 120 wafertrack to coat the wafers with resist, and follow the instructions specified for this equipment.
The process consists of a treatment with HMDS (hexamethyldisilazane) vapor with nitrogen as a carrier gas,
spin coating with Shipley SPR3012 positive photoresist, and a soft bake at 95degC for 1 minute.
Always check the temperature of the hotplate and the relative humidity (48 ± 2 %) in the room first.

Use program **1_CO _3012_1.4µm_noEBR**

47. ALIGNMENT AND EXPOSURE OF CUTTING LINES

Processing will be performed on the ASM PAS 5500/80 automatic waferstepper.
Follow the operating instructions from the manual when using this machine.

Use mask **AIRSPIKENOZZLE (**box 492**)**
Use the correct litho job:

for **A** wafers: **/AEROSPIKE** using layer ID: **CUTTINGLINES**
for **L** wafers: **/LINNOZZLE** using layer ID: **CUTTINGLINES**
Using the correct exposure energy: **150 mj/cm**

48. DEVELOPMENT BACKSIDE

Use the EVG 120 wafertrack to develop the wafers, and follow the instructions specified for this equipment.
The process consists of a post-exposure bake at 115 degC for 1 minute, followed by a development step using Shipley MF322 developer (single puddle process), and a hard bake at 100 degC for 1 minute.
Always check the temperature of the hotplates first.

Use development program **1 Dev SP**.

49. PLASMA ETCHING OF CUTTING LINES

Use the Trikon Ωmega 201 plasma etcher.
Follow the operating instructions from the manual when using this machine.
It is **not** allowed to change the process conditions and times from the etch recipe!

Use sequence **DEEP_SI with time 120sec** (with a platen temperature of **20 °C**) to etch **300** nm deep ASM URK's into the Si.

50. PHOTORESIST STRIPPING

Strip resist	Use the Tepla Plasma 300 system to remove the photoresist in an oxygen plasma. Follow the instructions specified for the Tepla stripper, and use the quartz carrier. Use **program 1**: 1000 watts power and automatic endpoint detection + 2 min. over etching.

51. CLEANING PROCEDURE: HNO_3 100% and 69.5%

Cleaning	10 minutes in fuming nitric acid (HNO_3 99%) at ambient temperature. Use wet bench "HNO_3 (100%)" and the carrier with the white dot.
QDR	Rinse in the Quick Dump Rinser with the standard program until the resistivity is 5 MΩ.
Cleaning	10 minutes in concentrated nitric acid (HNO_3 69.5%) at 110 °C. Use wet bench "HNO_3 (69.5%)" and the carrier with the white dot.
QDR	Rinse in the Quick Dump Rinser with the standard program until the resistivity is 5 MΩ.
Drying	Use the Semitool "rinser/dryer" with the standard program, and the white carrier with a red dot.

52. DRIE ETCHING Si FRONT SIDE (INLET HOLE) 200 MICRONS

Use Rapier Omega i2L, and follow the instructions specified for this equipment. Use program
0EKL_FLATBOTTOM_XXX
First use a test wafer to determine etch rate per loop from this calculate amount of loops necessary for 200 microns.
Amount of loops is: 93

53. INSPECTION (depth measurement)

Use the Dektak to check if the holes are open (should be about 300 micron deep)

54. PASSIVATION STRIPPING

Use the TEPLA photoresist stripper.
Use **2xprogram 8 (2x15 minutes)**
Let wafers cool down they will be HOT

FROM HERE L WAFERS ARE DONE AND CAN JUMP TO STEP 76 (VAPOR HF ETCH AND CUTTING) OTHER STEPS ARE ONLY FOR A WAFERS

NOTE STEPS 55-62 SHOULD ALL BE DONE IMMEDIATELY AFTER EACHOTHER TO PREVENT ADDITIONAL CLEANING AND THUS BAKEOUT STEPS

55. CLEANING PROCEDURE: HNO_3 100% and 69.5%

Cleaning	10 minutes in fuming nitric acid (HNO_3 99%) at ambient temperature. Use wet bench "HNO_3 (100%)" and the carrier with the white dot.
QDR	Rinse in the Quick Dump Rinser with the standard program until the resistivity is 5 MΩ.
Cleaning	10 minutes in concentrated nitric acid (HNO_3 69.5%) at 110 °C. Use wet bench "HNO_3 (69.5%)" and the carrier with the white dot.
QDR	Rinse in the Quick Dump Rinser with the standard program until the resistivity is 5 MΩ.
Drying	Use the Semitool "rinser/dryer" with the standard program, and the white carrier with a red dot.

56. BAKEOUT STEP MERMERT

Use the MERMERT oven to make sure that all the water is evaporated from the cavities before entering the furnaces.
use **program (15 minutes)**

AT THIS POINT THE WAFERS WITH THE LINEAR NOZZLES ARE READY FOR CUTTING JUMP TO STEP 74

57. FURNACE WET THERMAL OXIDE: 2000 nm

Use furnace to grow wet thermal oxide check the book for the time
time: XXX

58. DEPOSITION OF SiO2 BACKSIDE: 2500nm

Use the Novellus PECVD reactor.
Follow the operating instructions from the manual when using this machine.
Enable the proper gases as indicated next to the machine.
The process conditions of the deposition program may not be changed!

Use program **.xxxSiOstd** to deposit a 2500 nm thick PECVD SiO2 layer. Check time in the logbook.
T= **XXX**s

59. INSPECTION

Use the Leitz MPV-SP measurement system to measure the oxide thickness on the back side of the wafers:

Program: Novellus SiO2 > 50nm on Si 10x

Wafer	Point 1	Point 2	Point 3	Point 4	Point 5

60. COATING BACKSIDE

Use the EVG 120 wafertrack to coat the wafers with resist, and follow the instructions specified for this equipment.
The process consists of a treatment with HMDS (hexamethyldisilazane) vapor with nitrogen as a carrier gas,
spin coating with Shipley SPR3027 positive photoresist, and a soft bake at 95degC for 1 minute.
Always check the temperature of the hotplate and the relative humidity (48 ± 2 %) in the room first.

Use program **1_Co - 3027 - 2.1µm-noEBR.**

61. ALIGNMENT AND EXPOSURE OF BOTTOM SPIKE

Processing will be performed on the ASM PAS 5500/80 automatic waferstepper.
Follow the operating instructions from the manual when using this machine.

Use mask AIRSPIKENOZZLE **(**box 492**)**

AEROSPIKE using layer ID: **ASPIKEFREEBOTTOM**
Using the correct exposure energy: **260 mj/cm**

62. DEVELOPMENT BACKSIDE

Use the EVG 120 wafertrack to develop the wafers, and follow the instructions specified for this equipment.
The process consists of a post-exposure bake at 115 degC for 1 minute, followed by a development step using Shipley MF322 developer (single puddle process), and a hard bake at 100 degC for 1 minute.
Always check the temperature of the hotplates first.

Use development program **1 Dev SP**.

63. ETCHING SiO2 BACKSIDE (HARDMASK BOTTOM SPIKE)

Use the ALCATEL to etch the hardmask of the bottom spike

64. PHOTORESIST STRIPPING

Strip resist — Use the Tepla Plasma 300 system to remove the photoresist in an oxygen plasma.
Follow the instructions specified for the Tepla stripper, and use the quartz carrier.
Use **program 1**: 1000 watts power and automatic endpoint detection + 2 min. over etching.

65. CLEANING PROCEDURE: HNO_3 100% and 69.5%

Cleaning — 10 minutes in fuming nitric acid (HNO_3 99%) at ambient temperature.
Use wet bench "HNO_3 (100%)" and the carrier with the white dot.

QDR — Rinse in the Quick Dump Rinser with the standard program until the resistivity is 5 MΩ.

Cleaning — 10 minutes in concentrated nitric acid (HNO_3 69.5%) at 110 °C.
Use wet bench "HNO_3 (69.5%)" and the carrier with the white dot.

QDR — Rinse in the Quick Dump Rinser with the standard program until the resistivity is 5 MΩ.

Drying — Use the Semitool "rinser/dryer" with the standard program, and the white carrier with a red dot.

66. BAKEOUT STEP MERMERT
Use the MERMERT ovenr to make sure that all the water is evaporated from the cavities before entering the furnaces.
use **program (15 minutes)**

67. DRIE ETCHING Si (BOTTOM SPIKE) 300 MICRONS

Use Rapier Omega i2L, and follow the instructions specified for this equipment. Use program
0EKL_FLATBOTTOM_XXX
Amount of loops is: 139

68. INSPECTION (measurement)

Use KEYENS inspection to see if all the silicon is gone

69. PASSIVATION STRIPPING

Use the TEPLA photoresist stripper.
Use **2xprogram 8 (2x15 minutes)**
Let wafers cool down they will be HOT

D

Production Mask

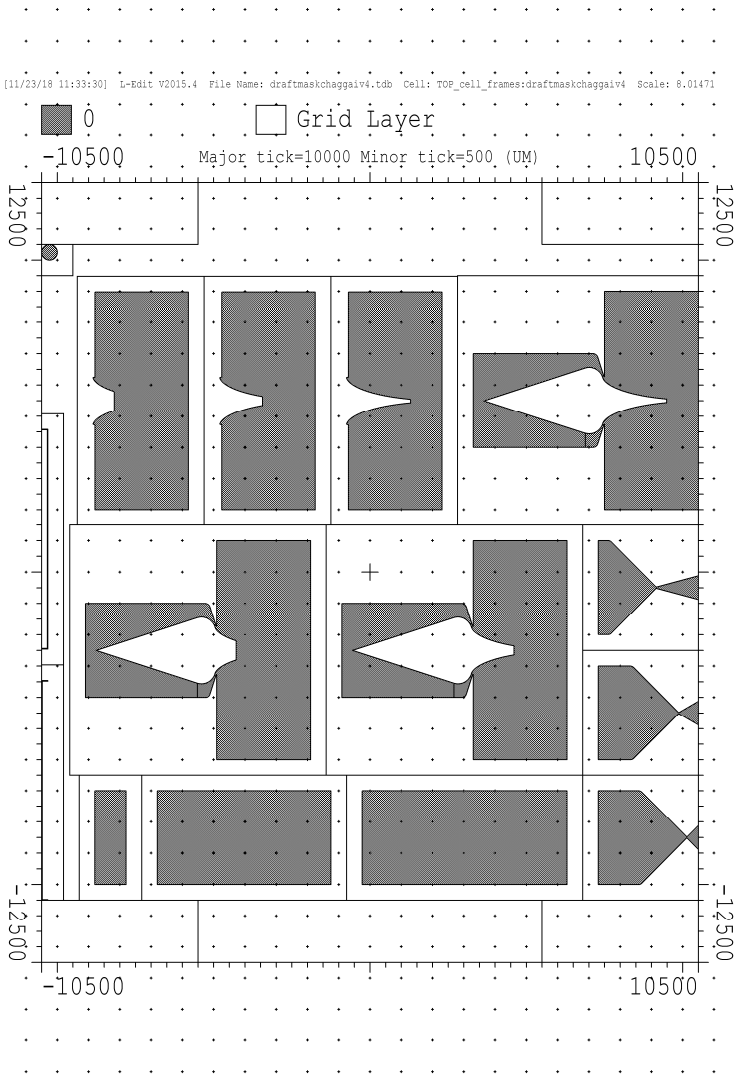

E

Wafer Layout and Measurements

In this appendix the wafer layout, including the nozzle names are provided for each wafer, followed by the measurements of the nozzles on said wafer as acquired using the Keyence VK-X250 microscope. Note that the locations of the nozzles on the wafer are made looking at the backside of the wafer before bonding. Thus the location map is valid if one looks at the back of the finalized production wafer.

In the tables with the measurements the width and depth measurements are the maximum values measured. The DRIE etching method does not provide perfectly perpendicular sidewalls. This also explains why the throat area is not equal to the throat width multiplied with the throat depth. At the end of each table the mean and standard deviation is given for each of the measured dimensions. This is done for the entirety of the wafer aswell as the specific designs on that wafer.

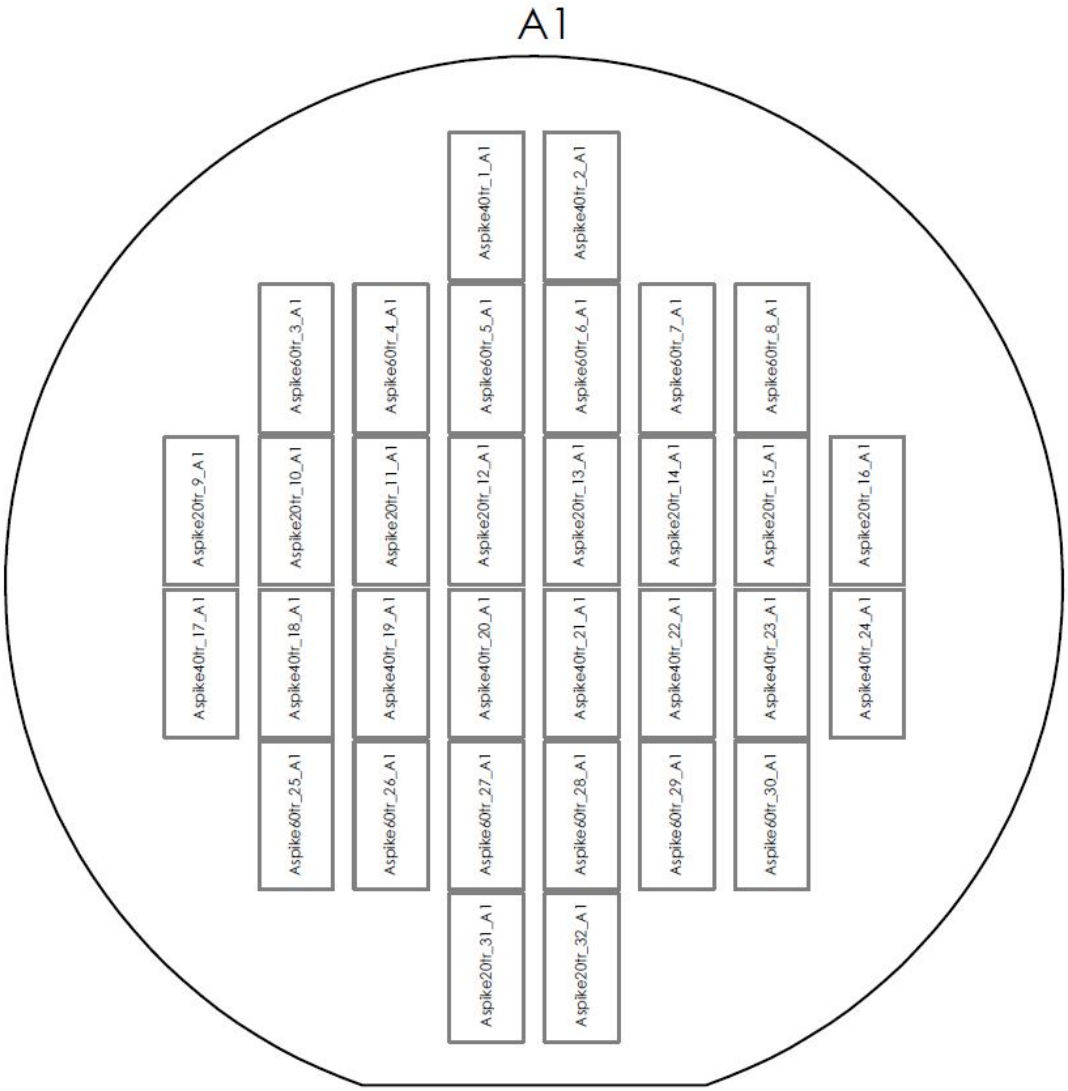

Figure E.1: Layout of A1 wafer

Table E.1: Measured dimensions of nozzles on A1 wafer

Name	throat width [µm]	throat depth [µm]	throat area [µm^2]	spike tip width [µm]	spike depth [µm]	inlet depth [µm]
Aspike40tr_1_A1	45.842	100.424	3885.658	284.694	101.219	104.907
Aspike40tr_2_A1	45.319	101.095	3818.225	284.358	101.304	106.216
Aspike60tr_3_A1	46.072	99.039	3785.089	111.209	101.095	104.712
Aspike60tr_4_A1	45.012	95.407	3710.129	110.685	97.584	101.217
Aspike60tr_5_A1	45.321	94.828	3789.699	110.970	96.325	100.228
Aspike60tr_6_A1	45.696	95.135	3748.832	110.081	96.373	100.369
Aspike60tr_7_A1	45.185	96.332	3758.355	111.578	97.576	101.760
Aspike60tr_8_A1	44.646	100.345	3792.729	110.157	100.706	106.609
Aspike20tr_9_A1	44.712	100.222	3910.706	602.079	103.189	105.363
Aspike20tr_10_A1	45.447	95.533	3724.053	603.251	98.215	100.829
Aspike20tr_11_A1	44.723	92.892	3648.526	601.968	96.296	98.900
Aspike20tr_12_A1	44.607	92.463	3542.530	603.230	95.795	98.680
Aspike20tr_13_A1	44.931	92.508	3506.984	603.031	95.903	98.671
Aspike20tr_14_A1	45.652	93.830	3715.190	603.238	95.994	99.156
Aspike20tr_15_A1	44.971	96.731	3739.105	602.092	98.172	101.663
Aspike20tr_16_A1	44.093	101.608	3642.067	602.696	102.726	107.646
Aspike40tr_17_A1	45.553	101.627	4019.238	283.967	105.720	106.951
Aspike40tr_18_A1	44.604	96.650	3760.782	282.977	99.533	101.907
Aspike40tr_19_A1	44.906	94.473	3610.052	282.382	97.092	99.926
Aspike40tr_20_A1	45.208	93.453	3752.337	283.417	96.638	99.809
Aspike40tr_21_A1	44.804	93.449	3571.960	283.832	97.155	99.562
Aspike40tr_22_A1	45.459	94.279	3744.638	283.078	97.135	100.149
Aspike40tr_23_A1	45.822	96.709	3715.095	283.402	99.466	102.966
Aspike40tr_24_A1	44.734	103.052	3778.997	283.862	105.563	109.050
Aspike60tr_25_A1	45.608	102.036	3980.752	108.998	108.022	107.298

Aspike60tr_26_A1	45.239	98.473	3866.694	110.347	104.610	104.200
Aspike60tr_27_A1	45.340	97.211	3811.400	110.212	101.197	103.197
Aspike60tr_28_A1	44.776	96.598	3659.288	110.264	101.205	103.190
Aspike60tr_29_A1	45.490	98.951	3750.997	110.978	104.136	104.949
Aspike60tr_30_A1	45.800	104.492	3986.179	109.956	108.082	109.720
Aspike20tr_31_A1	45.390	102.574	3847.878	603.076	105.636	107.537
Aspike20tr_32_A1	45.115	102.619	4037.617	603.025	105.518	108.852
$\boldsymbol{\mu}$	**45.190**	**97.657**	**3769.118**	**318.409**	**100.474**	**103.318**
$\boldsymbol{\sigma}$	**0.457**	**3.548**	**129.822**	**207.884**	**3.843**	**3.433**
$\boldsymbol{\mu_{20\%}}$	**44.964**	**97.098**	**3731.466**	**602.769**	**99.744**	**102.730**
$\boldsymbol{\sigma_{20\%}}$	**0.462**	**4.270**	**163.553**	**0.524**	**4.081**	**4.173**
$\boldsymbol{\mu_{40\%}}$	**45.225**	**97.521**	**3765.698**	**283.597**	**100.083**	**103.144**
$\boldsymbol{\sigma_{40\%}}$	**0.449**	**3.697**	**127.617**	**0.687**	**3.389**	**3.444**
$\boldsymbol{\mu_{60\%}}$	**45.349**	**98.237**	**3803.345**	**110.453**	**101.409**	**103.954**
$\boldsymbol{\sigma_{60\%}}$	**0.417**	**2.952**	**98.530**	**0.683**	**4.125**	**2.912**

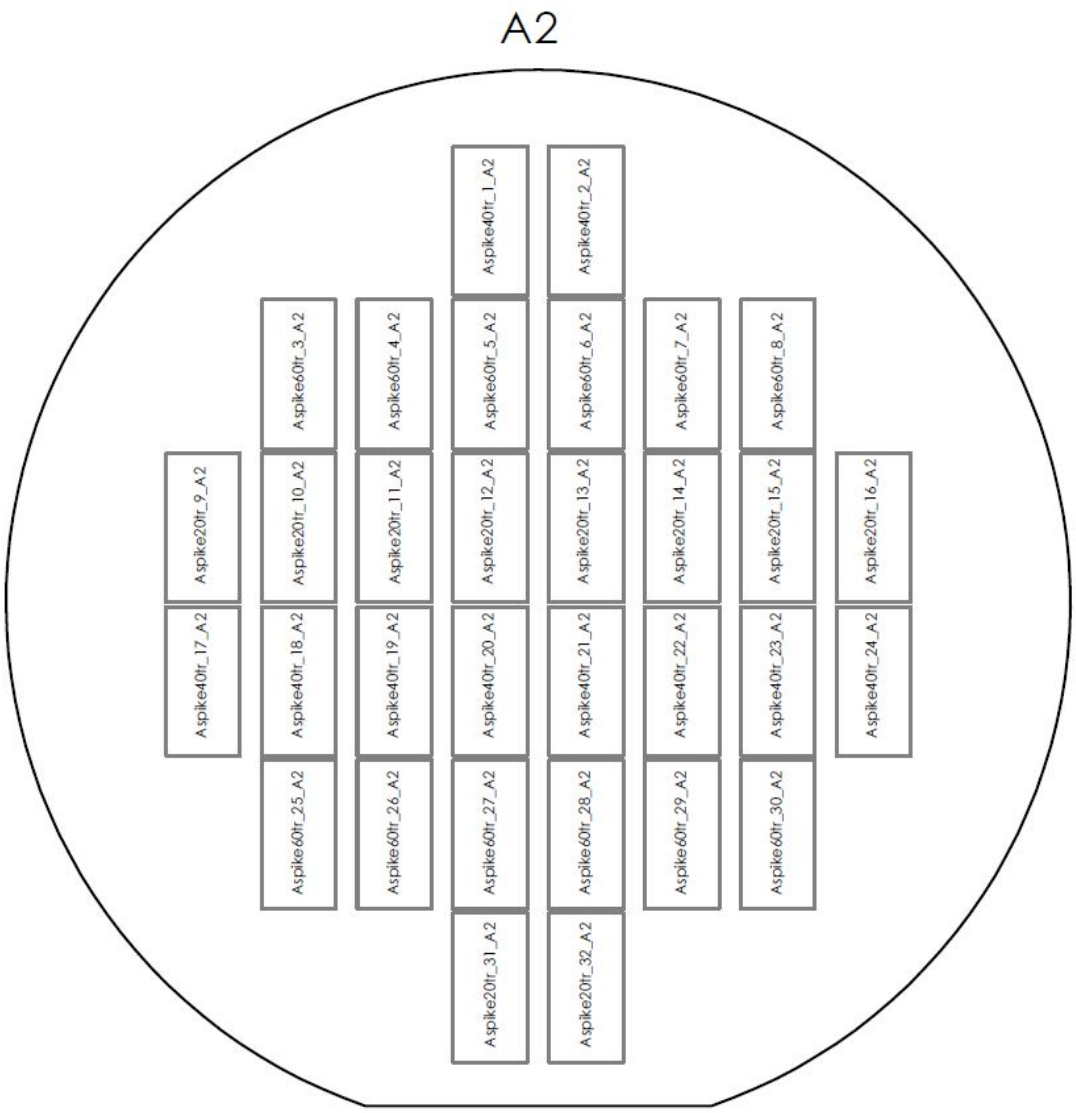

Figure E.2: Layout of A2 wafer

Table E.2: Measured dimensions of nozzles on A2 wafer

Name	throat width [µm]	throat depth [µm]	throat area [µm^2]	spike tip width [µm]	spike depth [µm]	inlet depth [µm]
Aspike40tr_1_A2	44.462	99.081	3868.996	283.301	97.947	101.657
Aspike40tr_2_A2	44.653	99.225	3793.989	283.748	98.664	102.989
Aspike60tr_3_A2	44.714	98.778	3640.441	109.845	98.978	101.693
Aspike60tr_4_A2	45.106	95.014	3684.911	110.130	95.822	99.061
Aspike60tr_5_A2	44.674	93.791	3543.483	110.455	94.605	98.209
Aspike60tr_6_A2	44.464	93.329	3490.987	110.110	94.785	98.266
Aspike60tr_7_A2	44.083	95.460	3583.479	110.967	95.516	99.657
Aspike60tr_8_A2	44.511	98.773	3811.867	110.685	98.390	103.220
Aspike20tr_9_A2	45.403	98.810	3833.432	602.403	100.028	102.018
Aspike20tr_10_A2	44.212	94.736	3608.935	602.943	96.172	98.690
Aspike20tr_11_A2	44.527	92.429	3436.312	603.140	94.453	96.822
Aspike20tr_12_A2	44.261	92.488	3419.606	603.682	93.900	96.818
Aspike20tr_13_A2	44.570	91.974	3491.186	603.132	93.925	96.688
Aspike20tr_14_A2	44.594	92.459	3437.890	602.707	94.334	97.106
Aspike20tr_15_A2	44.612	95.120	3664.906	602.828	95.903	99.513
Aspike20tr_16_A2	44.436	100.182	3771.732	602.406	99.838	103.800
Aspike40tr_17_A2	45.230	100.493	3866.310	283.800	104.206	103.376
Aspike40tr_18_A2	45.106	95.859	3699.043	282.490	97.571	99.514
Aspike40tr_19_A2	45.266	93.524	3483.780	283.343	95.004	97.602
Aspike40tr_20_A2	44.723	93.413	3523.268	284.282	94.783	97.643
Aspike40tr_21_A2	44.503	93.031	3535.220	283.510	94.931	97.484
Aspike40tr_22_A2	44.684	94.004	3618.576	283.587	95.570	98.503
Aspike40tr_23_A2	44.583	96.844	3655.550	283.207	97.679	101.142
Aspike40tr_24_A2	44.565	101.297	3905.965	284.413	102.923	107.441
Aspike60tr_25_A2	45.179	101.178	3954.537	109.626	105.115	104.590
Aspike60tr_26_A2	45.440	97.781	3850.642	110.881	101.689	102.030
Aspike60tr_27_A2	45.014	96.424	3689.299	109.551	98.746	100.640
Aspike60tr_28_A2	45.323	96.420	3624.296	110.145	98.058	100.742
Aspike60tr_29_A2	45.757	98.728	3792.003	110.399	101.907	103.216
Aspike60tr_30_A2	44.701	102.147	3945.089	109.655	104.394	106.786

Aspike20tr_31_A2	45.495	100.251	3762.987	603.894	102.495	104.015
Aspike20tr_32_A2	45.426	101.384	3882.144	602.819	101.482	104.712
μ	**44.821**	**96.701**	**3683.464**	**318.378**	**98.119**	**100.801**
σ	**0.427**	**3.171**	**160.890**	**208.081**	**3.405**	**3.009**
$\mu_{20\%}$	**44.754**	**95.983**	**3630.913**	**602.995**	**97.253**	**100.018**
$\sigma_{20\%}$	**0.493**	**3.781**	**177.120**	**0.490**	**3.357**	**3.306**
$\mu_{40\%}$	**44.778**	**96.677**	**3695.070**	**283.568**	**97.928**	**100.735**
$\sigma_{40\%}$	**0.305**	**3.161**	**156.693**	**0.551**	**3.301**	**3.240**
$\mu_{60\%}$	**44.914**	**97.319**	**3717.586**	**110.204**	**99.000**	**101.509**
$\sigma_{60\%}$	**0.474**	**2.753**	**152.614**	**0.484**	**3.603**	**2.623**

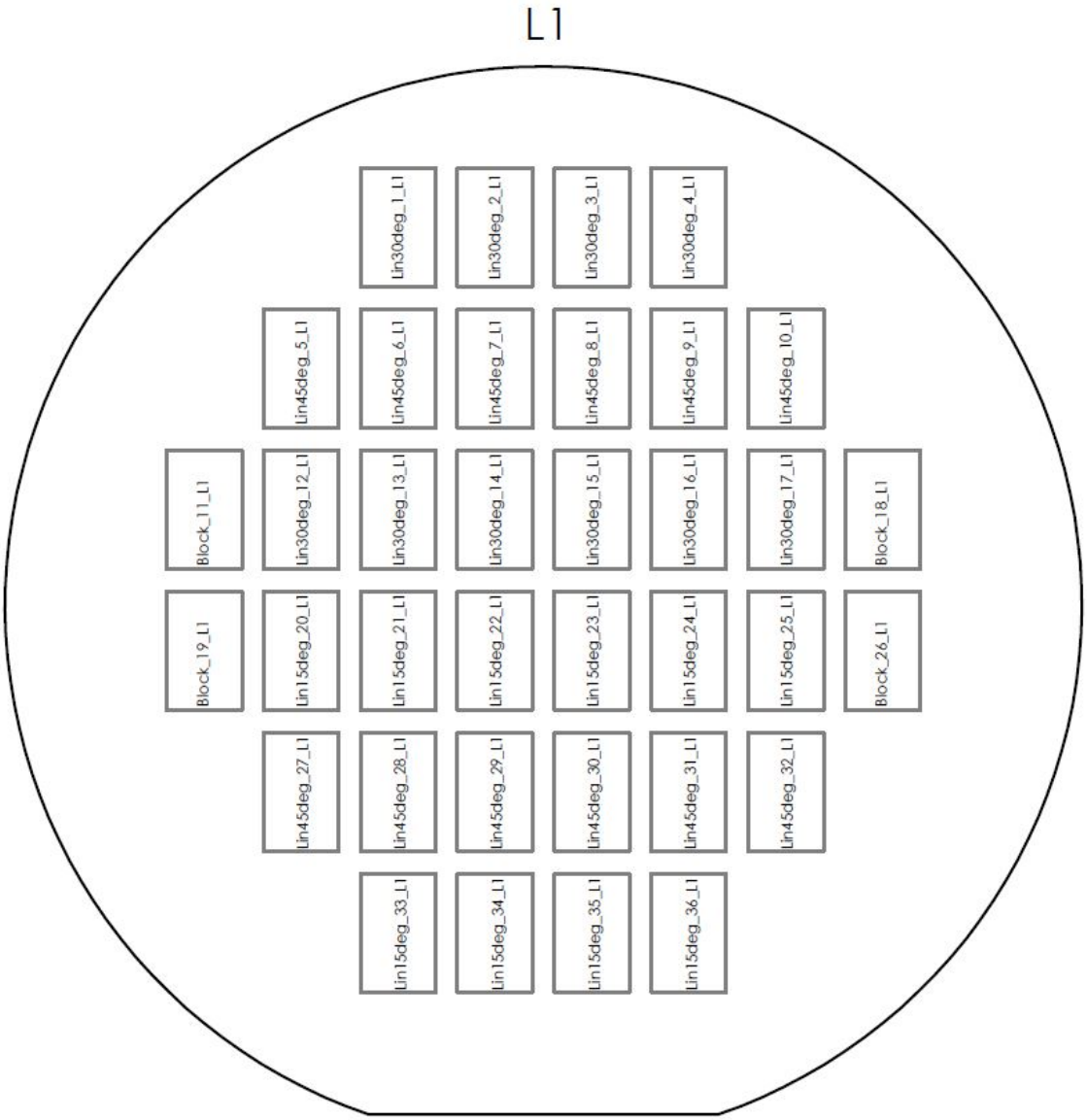

Figure E.3: Layout of L1 wafer

Table E.3: Measured dimensions of nozzles on L1 wafer

Name	throat width [µm]	throat depth [µm]	throat area [µm^2]	exit width [µm]	exit depth [µm]	inlet depth [µm]
Lin30deg_1_L1	45.163	102.221	3908.405	756.888	106.761	103.699
Lin30deg_2_L1	45.303	101.645	3911.793	756.441	106.623	103.709
Lin30deg_3_L1	44.788	101.780	3705.147	756.253	106.244	103.387
Lin30deg_4_L1	44.690	102.839	3761.035	756.081	106.566	103.913
Lin45deg_5_L1	44.788	104.050	3531.296	755.050	107.694	105.190
Lin45deg_6_L1	44.719	101.751	3898.261	756.035	106.945	104.327
Lin45deg_7_L1	43.762	102.141	3807.718	756.081	107.032	104.359
Lin45deg_8_L1	44.911	101.740	3723.501	756.595	106.678	104.117
Lin45deg_9_L1	44.177	102.424	3814.005	755.222	106.768	104.363
Lin45deg_10_L1	45.306	103.668	3722.853	756.304	107.859	105.954
Lin30deg_12_L1	44.788	103.125	3744.596	755.926	108.684	105.483
Lin30deg_13_L1	44.788	102.078	3881.575	755.394	108.360	104.915
Lin30deg_14_L1	44.479	102.428	3707.936	755.565	108.466	105.025
Lin30deg_15_L1	44.788	101.317	3885.118	756.882	108.317	105.014
Lin30deg_16_L1	44.273	102.331	3842.194	756.082	108.225	104.999
Lin30deg_17_L1	45.303	103.671	3835.315	755.738	108.914	106.063
Lin15deg_20_L1	45.306	105.002	3832.784	757.769	111.207	106.919
Lin15deg_21_L1	44.273	102.923	3781.450	755.395	110.159	106.187
Lin15deg_22_L1	45.306	102.662	3728.400	755.737	110.194	106.075
Lin15deg_23_L1	44.276	102.358	3809.614	757.282	109.857	106.080
Lin15deg_24_L1	45.303	102.975	3862.087	757.625	110.099	106.274
Lin15deg_25_L1	44.788	103.981	3796.558	755.738	111.468	107.936
Lin45deg_27_L1	45.303	107.770	4204.020	756.253	111.637	108.832
Lin45deg_28_L1	44.791	105.106	3922.493	755.909	109.348	106.843
Lin45deg_29_L1	44.788	104.090	3742.884	756.648	109.007	106.504
Lin45deg_30_L1	45.818	104.505	3722.373	756.939	109.488	106.755
Lin45deg_31_L1	45.303	105.429	3775.975	755.222	110.194	107.736
Lin45deg_32_L1	45.303	108.510	3876.062	756.940	112.809	110.287
Lin15deg_33_L1	45.818	107.411	3957.530	756.252	112.040	109.163
Lin15deg_34_L1	45.306	106.839	3995.853	757.111	112.983	108.698

Lin15deg_35_L1	45.303	107.294	3838.318	756.080	113.250	108.774
Lin15deg_36_L1	45.306	107.844	3881.529	757.110	112.750	109.776
$\boldsymbol{\mu}$	**44.947**	**103.872**	**3825.271**	**756.267**	**109.270**	**106.167**
$\boldsymbol{\sigma}$	**0.475**	**2.116**	**115.339**	**0.706**	**2.135**	**1.905**
$\boldsymbol{\mu_{15°}}$	**45.099**	**104.929**	**3848.412**	**756.610**	**111.401**	**107.588**
$\boldsymbol{\sigma_{15°}}$	**0.498**	**2.221**	**80.524**	**0.865**	**1.303**	**1.443**
$\boldsymbol{\mu_{30°}}$	**44.836**	**102.344**	**3818.311**	**756.125**	**107.716**	**104.621**
$\boldsymbol{\sigma_{30°}}$	**0.336**	**0.713**	**81.571**	**0.507**	**1.031**	**0.887**
$\boldsymbol{\mu_{45°}}$	**44.914**	**104.265**	**3811.787**	**756.100**	**108.788**	**106.272**
$\boldsymbol{\sigma_{45°}}$	**0.554**	**2.204**	**161.284**	**0.654**	**2.004**	**1.964**

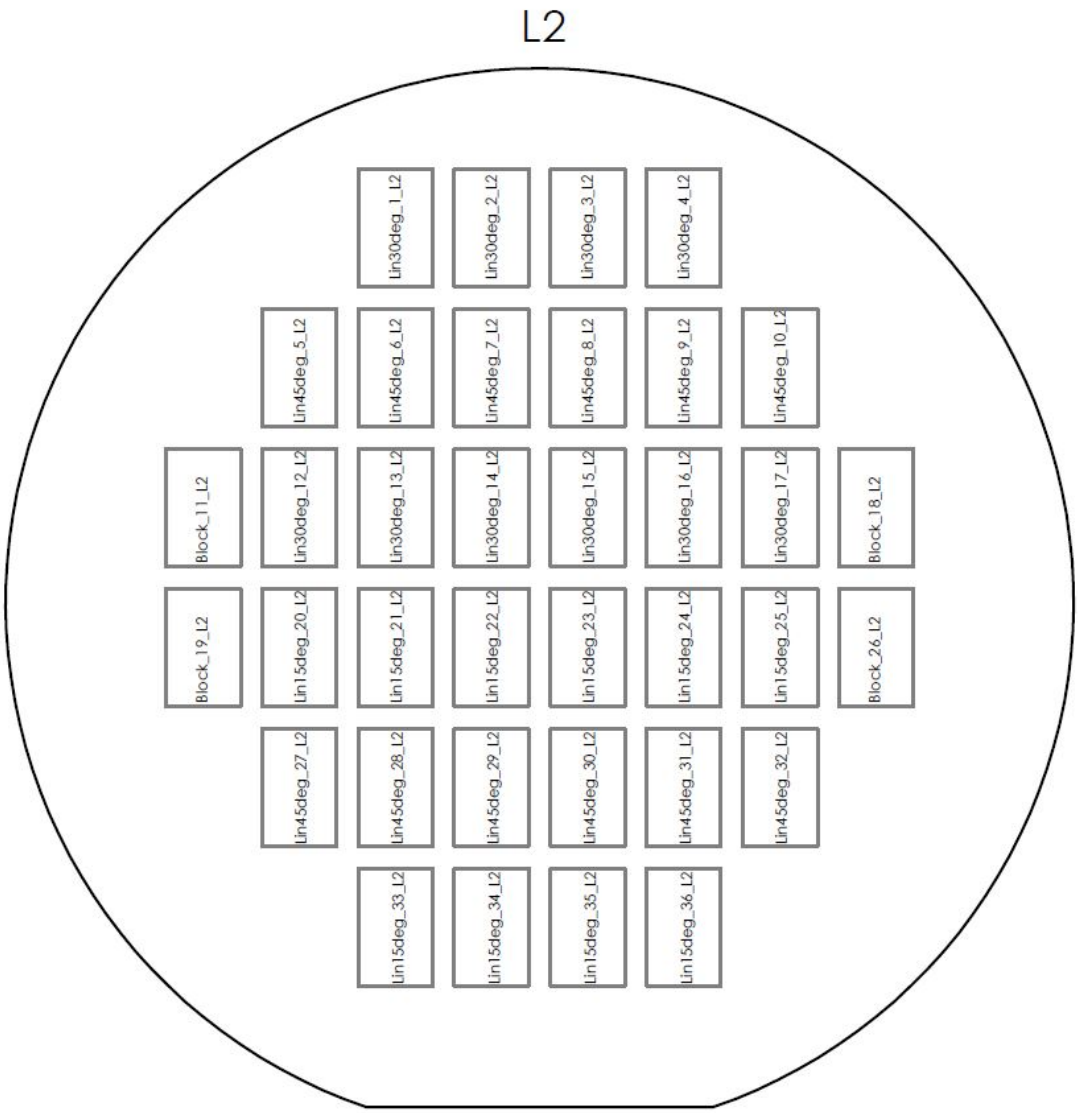

Figure E.4: Layout of L2 wafer

Table E.4: Measured dimensions of nozzles on L2 wafer

Name	throat width [µm]	throat depth [µm]	throat area [µm^2]	exit width [µm]	exit depth [µm]	inlet depth [µm]
Lin30deg_1_L2	44.519	103.711	3762.738	756.150	107.622	104.641
Lin30deg_2_L2	45.018	103.213	3926.790	756.087	107.597	104.714
Lin30deg_3_L2	45.066	102.576	3839.259	755.856	107.248	104.262
Lin30deg_4_L2	45.306	103.804	3757.471	755.226	107.913	105.005
Lin45deg_5_L2	44.791	105.122	3971.302	755.597	108.899	106.359
Lin45deg_6_L2	45.266	103.432	3880.327	756.085	107.969	104.964
Lin45deg_7_L2	45.046	103.153	3845.198	755.705	107.913	105.407
Lin45deg_8_L2	45.303	102.606	3802.285	756.232	107.733	105.021
Lin45deg_9_L2	45.234	103.398	3754.199	756.088	108.035	105.606
Lin45deg_10_L2	45.103	105.439	3823.678	755.446	109.245	107.032
Lin30deg_12_L2	44.791	103.592	3660.819	755.290	109.834	106.906
Lin30deg_13_L2	45.405	102.819	3830.806	756.802	109.207	105.781
Lin30deg_14_L2	44.788	103.768	3781.750	754.712	102.447	106.011
Lin30deg_15_L2	45.303	103.707	3726.769	755.473	109.677	105.710
Lin30deg_16_L2	45.140	103.095	3874.356	756.088	109.168	106.142
Lin30deg_17_L2	44.815	104.760	3731.995	755.571	110.272	107.330
Lin15deg_20_L2	45.303	105.509	3984.409	756.155	112.101	108.101
Lin15deg_21_L2	45.821	103.724	3829.722	755.565	110.830	106.659
Lin15deg_22_L2	45.818	103.259	3742.791	756.360	108.200	106.563
Lin15deg_23_L2	45.303	102.836	3854.056	756.713	111.074	106.678
Lin15deg_24_L2	45.303	103.455	3736.118	755.867	111.105	107.109
Lin15deg_25_L2	44.927	105.852	3767.975	755.468	112.646	108.886
Lin45deg_27_L2	45.306	108.992	3872.191	755.575	112.883	109.711
Lin45deg_28_L2	44.788	105.804	3681.154	754.885	110.592	107.574
Lin45deg_29_L2	45.303	104.737	3867.015	756.109	109.925	107.283
Lin45deg_30_L2	44.934	104.822	3856.786	755.202	110.447	107.766
Lin45deg_31_L2	43.852	106.494	3634.660	754.792	110.715	108.240
Lin45deg_32_L2	44.870	109.691	3980.381	755.395	113.724	111.112
Lin15deg_33_L2	45.501	107.745	3720.635	756.001	113.024	109.184
Lin15deg_34_L2	44.890	107.766	3957.572	755.511	113.898	109.568

Lin15deg_35_L2	45.384	107.753	3938.207	756.251	114.654	109.777
Lin15deg_36_L2	45.215	108.651	4100.562	755.722	114.219	110.877
$\boldsymbol{\mu}$	**45.107**	**104.853**	**3827.937**	**755.749**	**110.026**	**107.062**
$\boldsymbol{\sigma}$	**0.372**	**2.041**	**105.677**	**0.507**	**2.577**	**1.851**
$\boldsymbol{\mu_{15°}}$	**45.347**	**105.655**	**3863.205**	**755.961**	**112.175**	**108.340**
$\boldsymbol{\sigma_{15°}}$	**0.313**	**2.224**	**127.719**	**0.410**	**1.950**	**1.540**
$\boldsymbol{\mu_{30°}}$	**45.015**	**103.505**	**3789.275**	**755.726**	**108.099**	**105.650**
$\boldsymbol{\sigma_{30°}}$	**0.284**	**0.616**	**78.764**	**0.594**	**2.255**	**1.002**
$\boldsymbol{\mu_{45°}}$	**44.983**	**105.308**	**3830.765**	**755.593**	**109.840**	**107.173**
$\boldsymbol{\sigma_{45°}}$	**0.409**	**2.219**	**102.723**	**0.480**	**1.959**	**1.892**